Investigation of Natural Circulation Instability and Transients in Passively Safe Small Modular Reactors

Reactor Concepts
Research Development and Demonstration

Mamoru Ishii
Purdue University

Brian Robinson, Federal POC
Adrian Tentner, Technical POC

NEUP Nuclear Energy University Programs

U.S. Department of Energy

PURDUE
UNIVERSITY

INVESTIGATION OF NATURAL CIRCULATION INSTABILITY AND TRANSIENTS IN PASSIVELY SAFE SMALL MODULAR REACTORS –FINAL REPORT

November 2016

Prepared by

M. Ishii, W. S. Yang, S. Shi, Y. Yan, G. Wang, F. Odeh, Y.C. Lin, Z. Dang, X. Yang, J.P. Schlegel, C. Brooks, Y. Liu

School of Nuclear Engineering
Purdue University
ishii@purdue.edu

Prepared for

EXECUTIVE SUMMARY

The NEUP funded project, NEUP-3496, aims to experimentally investigate two-phase natural circulation flow instability that could occur in Small Modular Reactors (SMRs), especially for natural circulation SMRs. The objective has been achieved by systematically performing tests to study the general natural circulation instability characteristics and the natural circulation behavior under start-up or design basis accident conditions. Experimental data sets highlighting the effect of void reactivity feedback as well as the effect of power ramp-up rate and system pressure have been used to develop a comprehensive stability map. The safety analysis code, RELAP5, has been used to evaluate experimental results and models. Improvements to the constitutive relations for flashing have been made in order to develop a reliable analysis tool. This research has been focusing on two generic SMR designs, i.e. a small modular Simplified Boiling Water Reactor (SBWR) like design and a small integral Pressurized Water Reactor (PWR) like design.

A BWR-type natural circulation test facility was firstly built based on the three-level scaling analysis of the Purdue Novel Modular Reactor (NMR) with an electric output of 50 MWe, namely NMR-50, which represents a BWR-type SMR with a significantly reduced reactor pressure vessel (RPV) height. The experimental facility was installed with various equipment to measure thermal-hydraulic parameters such as pressure, temperature, mass flow rate and void fraction. Characterization tests were performed before the startup transient tests and quasi-steady tests to determine the loop flow resistance. The control system and data acquisition system were programmed with LabVIEW to realize the real-time control and data storage.

The thermal-hydraulic and nuclear coupled startup transients were performed to investigate the flow instabilities at low pressure and low power conditions for NMR-50. Two different power ramps were chosen to study the effect of startup power density on the flow instability. The experimental startup transient results showed the existence of three different flow instability mechanisms, i.e., flashing instability, condensation induced flow instability, and density wave oscillations. In addition, the void-reactivity feedback did not have significant effects on the flow instability during the startup transients for NMR-50.

Several initial startup procedures with different power ramp rates were experimentally investigated to eliminate the flow instabilities observed from the startup transients. Particularly, the very slow startup transient and pressurized startup transient tests were performed and compared. It was found that the very slow startup transients by applying very small power density can eliminate the flashing oscillations in the single-phase natural circulation and stabilize the flow oscillations in the phase of net vapor generation. The initially pressurized startup procedure was tested to eliminate the flashing instability during the startup transients as well. The pressurized startup procedure included the initial pressurization, heat-up, and venting process. The startup transient tests showed that the pressurized startup procedure could eliminate the flow instability during the transition from single-phase flow to two-phase flow at low pressure conditions. The experimental results indicated that both startup procedures were applicable to the initial startup of NMR. However, the pressurized startup procedures might be preferred due to short operating hours required.

In order to have a deeper understanding of natural circulation flow instability, the quasi-steady tests were performed using the test facility installed with preheater and subcooler. The effect of system pressure, core inlet subcooling, core power density, inlet flow resistance coefficient, and void reactivity feedback were investigated in the quasi-steady state tests. The experimental stability boundaries were determined between unstable and stable flow conditions in the dimensionless stability plane of inlet subcooling number and Zuber number.

To predict the stability boundary theoretically, linear stability analysis in the frequency domain was performed at four sections of the natural circulation test loop. The flashing phenomena in the chimney section was considered as an axially uniform heat source. And the dimensionless characteristic equation of the pressure drop perturbation was obtained by considering the void fraction effect and outlet flow resistance in the core section. The theoretical flashing boundary showed some discrepancies with previous experimental data from the quasi-steady state tests. In the future, thermal non-equilibrium was recommended to improve the accuracy of flashing instability boundary.

As another part of the funded research, flow instabilities of a PWR-type SMR under low pressure and low power conditions were investigated experimentally as well. The NuScale reactor design was selected as the prototype for the PWR-type SMR. In order to experimentally study the natural circulation behavior of NuScale

reactor during accidental scenarios, detailed scaling analyses are necessary to ensure that the scaled phenomena could be obtained in a laboratory test facility. The three-level scaling method is used as well to obtain the scaling ratios derived from various non-dimensional numbers. The design of the ideally scaled facility (ISF) was initially accomplished based on these scaling ratios. Then the engineering scaled facility (ESF) was designed and constructed based on the ISF by considering engineering limitations including laboratory space, pipe size, and pipe connections etc.

PWR-type SMR experiments were performed in this well-scaled test facility to investigate the potential thermal hydraulic flow instability during the blowdown events, which might occur during the loss of coolant accident (LOCA) and loss of heat sink accident (LOHS) of the prototype PWR-type SMR. Two kinds of experiments, normal blowdown event and cold blowdown event, were experimentally investigated and compared with code predictions.

The normal blowdown event was experimentally simulated since an initial condition where the pressure was lower than the designed pressure of the experiment facility, while the code prediction of blowdown started from the normal operation condition. Important thermal hydraulic parameters including reactor pressure vessel (RPV) pressure, containment pressure, local void fraction and temperature, pressure drop and natural circulation flow rate were measured and analyzed during the blowdown event. The pressure and water level transients are similar to the experimental results published by NuScale [51], which proves the capability of current loop in simulating the thermal hydraulic transient of real PWR-type SMR. During the 20000s blowdown experiment, water level in the core was always above the active fuel assemble during the experiment and proved the safety of natural circulation cooling and water recycling design of PWR-type SMR. Besides, pressure, temperature, and water level transient can be accurately predicted by RELAP5 code. However, the oscillations of natural circulation flow rate, water level and pressure drops were observed during the blowdown transients. This kind of flow oscillations are related to the water level and the location upper plenum, which is a path for coolant flow from chimney to steam generator and down comer.

In order to investigate the transients start from the opening of ADS valve in both experimental and numerical way, the cold blow-down experiment is conducted. For the cold blowdown event, different from setting both reactor

iii

pressure vessel (RPV) and containment at high temperature and pressure, only RPV was heated close to the highest designed pressure and then open the ADS valve, same process was predicted using RELAP5 code. By doing cold blowdown experiment, the entire transients from the opening of ADS can be investigated by code and benchmarked with experimental data. Similar flow instability observed in the cold blowdown experiment. The comparison between code prediction and experiment data showed that the RELAP5 code can successfully predict the pressure void fraction and temperature transient during the cold blowdown event with limited error, but numerical instability exists in predicting natural circulation flow rate. Besides, the code is lack of capability in predicting the water level related flow instability observed in experiments.

TABLE OF CONTENTS

LIST OF FIGURES

LIST OF TABLES

NOMENCLATURE

Latin

A	flow area ratio
	area
a	cross-sectional area
c	specific heat
C_k	kinematic wave velocity
c_p	specific heat at constant pressure
d	diameter
D	hydraulic diameter
f	friction factor or Frequency
F	friction number
g	gravitational acceleration
G	mass flux
h	heat transfer coefficient
i_{fg}	latent heat of vaporization
j	volumetric flux or center-of-volume velocity
k	conductivity
K	K factor (Minor loss coefficient)
K_α	void reactivity coefficient
K_D	Doppler-reactivity coefficient
l	length
L	axial length scale
$\dot{m}$	mass flow rate
N	dimensionless number
N_β	thermal expansion number
N_{Bi}	Biot number
N_d	drift number
N_{Eu}	Euler number
N_{Fo}	Fourier number
N_{Fr}	Froude number
N_f	friction number

N_{fl}	flashing number
N_{Pe}	Peclet number
N_{pr}	Prandtl number
N_{Re}	Reynolds number
N_{Ri}	Richardson number
N_{ρ}	density ratio number
N_{St}	modified Stanton number
N_{sub}	subcooling number
$N_{sub,d}$	departure subcooling number
N_T	time ratio number
N_{th}	thermal inertia ratio number
N_q	heat source number
N_{We}	Weber number
N_{Zu}	Zuber (phase change) number
$n(t)$	neutron amplitude function
	heater power
$n_E(t)$	heater power input for the control system
p	pressure
q	power
q''	heat flux
q'''	volumetric heat generation rate
s	complex number
t	time
T	temperature
u	velocity
U	overall heat conductance
v	specific volume
	velocity
V	volume
V_{gj}	drift velocity
x	flow quality
x_e	thermodynamic equilibrium flow quality
z	axial coordinate

Greek

α	void fraction
	thermal diffusivity
Γ_g	mass generation for the vapor phase
β	volumetric thermal expansion coefficient
	effective fraction of delayed neutrons
δ	conduction thickness
Δ	difference
λ	precursor decay constant
$\bar{\lambda}$	one group decay constant
Λ	neutron generation time
Λ_n	various transfer function
μ	dynamic viscosity
ν	kinematic viscosity
ξ	perimeter
ξ_i	reduced precursor concentration
ρ	density
ρ	total reactivity
ρ_α	void reactivity
ρ_D	doppler reactivity
ρ_{ext}	external reactivity
τ	time scale
τ_{AD}	artificial time delay
τ_c	fuel element time constant
$\tau_{12,23,34,13}$	residence time in (B), (C), (D), and in the heated region
ϕ, ψ	neutron flux
Ω	reaction frequency
ω	frequency

Superscripts

V	volume-averaged void fraction
A	area-averaged void fraction
$*$	dimensionless

Subscripts

D	doppler effect
e	equivalent or equilibrium
	region (D)
F	fuel element
F_∞	fuel element to coolant
f	liquid
	flashing
g	gas
h	heated
i	*i*th component
	*i*th group of precursor
	inlet
in	inlet
M	model
me	mixture in (D)
p	impedance void meter port
	pellet
P	prototype
o	reference point/component
R	ratio of model over prototype
S	solid structure
s	saturation
sub	subcooling
w	*w*etted
3	bottom of region (D)
4	top of region (D)
12	region (B)
23	region (C)
34	region (D)

Operators

$\langle \ \rangle$	area averaging ($\langle F \rangle = \dfrac{1}{A} \iint_A F dA$)

1. INTRODUCTION

Small modular reactor (SMR) designs, such as Mitsubishi's Integral Modular Reactor (IMR), Purdue University's Novel Modular Reactor (NMR) [1], and the NuScale Power Reactor, have simplified the reactor system and integrated the passive safety systems by removing the primary coolant pumps. Most SMRs are designed to operate and manage design basis accidents under natural circulation cooling instead of conventional forced circulation cooling.

Under natural circulation conditions, a two-phase coolant flow may become unstable. This can lead to control and safety problems in nuclear power plants. Instabilities in boiling systems occur due to disturbances in various parameters affecting the heat transfer. These disturbances can come from fluctuations in inlet enthalpy, flow regime transition, steam demand, etc. Particularly at low pressure, boiling systems are prone to static and dynamic thermal-hydraulic instabilities which can challenge reactor safety and control. Static instabilities such as flow excursion (Ledinegg) instability [2] and flow pattern transition instability [3], as well as dynamic instabilities such as density wave instability [4][5] and flashing/condensation instability [6] pose a significant challenge in two-phase natural circulation systems. The current research focuses on the natural circulation instabilities present in passively safe small modular reactors.

2. NEUTRONICS DESIGN AND ANALYSIS OF THE NMR-50

Neutronics design studies continued to optimize the core design for a 50 MWe novel modular boiling water reactor (NMR-50) that incorporates new passive safety features along with modern BWR technologies and to demonstrate its performance and safety characteristics [7]. The key design objective of the NMR-50 core design is to be able to achieve a 10-year cycle length while satisfying thermal hydraulics and materials related design criteria as well as minimizing the fuel cost.

In FY 2014, the reference fuel assembly design developed in FY 2013 was improved through systematic parametric studies. In order to minimize the fuel cost, the pin cell design was optimized to minimize the U-235 enrichment while maintaining the targeted cycle length of 10 years and satisfying the design constraints on reactivity feedback coefficients. Preliminary parametric studies were performed to determine an optimum assembly configuration to minimize the local power peaking. The resulting assembly design reduces the average U-235 enrichment to 4.5% from 4.75% of the reference design. The safety margin was also increased by increasing the minimum critical power ratio (MCPR) during the 10-year cycle from 1.84 to 2.0. However, while developing improved analysis models to be discussed below, it was found that xenon/samarium cross sections were improperly handled in the GenPMAXS code [12] run to prepare the cross section set for these calculations. Since the equilibrium concentrations of xenon and samarium were not included, the average U-235 enrichment would be higher than the calculated value of 4.5%.

In order to deliver an optimum core design for the NMR-50, the core design developed in FY 2014 was further optimized based on the coupled, whole-core neutronics and thermal-hydraulics calculations. The fuel assembly design was optimized by incorporating a simulated annealing (SA) based optimization method. The analysis models were also improved by refining the depletion and void branching calculations in CASMO-4 [8] lattice physics calculations to prepare the cross section data library for the core simulator PARCS [9]. The thermal feedback calculation was improved by extending the RELAP5 [10] model from the core to the entire primary loop. Furthermore, the peak fast fluence of the fuel assembly

channel box was investigated to examine the feasibility of a 10-year cycle length from the irradiation damage point of view.

2.1. DESIGN OBJECTIVES AND CONSTRAINTS

The main design objectives and constraints were discussed in detail in the FY 2014 annual report [6]. In order to examine the feasibility to achieve a 10-year cycle length from the structure integrity point of view, an additional design constraint was further imposed on the peak fast fluence of the fuel assembly channel box.

This design constraint takes into account the effect of a 10-year cycle length on the performance and integrity of structural material. Since irradiation damage strongly depends on fast neutron fluence, the peak fast fluence was limited to the current BWRs standards. A value of $2 \times 10^{22} \, \mathrm{n/cm^2}$ was used based on typical operational peak conditions of structural components, such as the channel box [11].

2.2. DESIGN ANALYSIS TOOLS

The lattice physics code CASMO-4 was used in the parametric studies to develop an optimized fuel assembly design and in the generation of cross section data for the core calculations using the PARCS code. The thermal feedback calculations were performed by coupling the PARCS code with the RELAP5 thermal-hydraulics system code. The computational models used in FY 2013 and FY 2014 were refined to enhance the simulation fidelity. The previous RELAP5 calculations were performed with a multi-channel model of the core with the boundary conditions on the inlet flow rate, inlet coolant temperature, and outlet pressure. This RELAP5 model was extended to include the entire primary loop. In addition, the cross section generation scheme was improved to enhance the interpolation accuracy by refining the depletion and coolant void branching calculations. The computational methods and models are discussed briefly in this section, focused on the modeling improvements.

2.2.1. CASMO-4

CASMO-4 is a well-established, industry-standard lattice physics code. It was used to perform pin cell [1] and assembly calculations during the assembly design optimization and to prepare the burnup dependent cross section libraries for the core calculations. The optimum assembly enrichment split was determined using simulated annealing optimization approach. In addition, the optimum amount of burnable poison (BP) and number of BP pins were determined.

2.2.2. PARCS

A core simulator PARCS was used to perform whole-core depletion calculations in order to determine the cycle length and to ensure no thermal design violation due to power peaking. A single-batch fuel management scheme was selected in FY 2013 to maximize the cycle length. A full core radial schematic view of the NMR-50 is shown in Figure 2-1, which consists of 256 fuel assemblies, 57 control rod blades, and reflectors. In PARCS, individual fuel and reflector assemblies were modeled, including the top and bottom axial reflectors. The model was constructed using 1 node per fuel assembly in the radial direction and 11 nodes per assembly in the axial direction. Thermal-feedback was considered separately for each PARCS node through a mapping to the respective thermal-hydraulics nodes. The adopted PARCS solver was a hybrid of analytic nodal method and nodal expansion method.
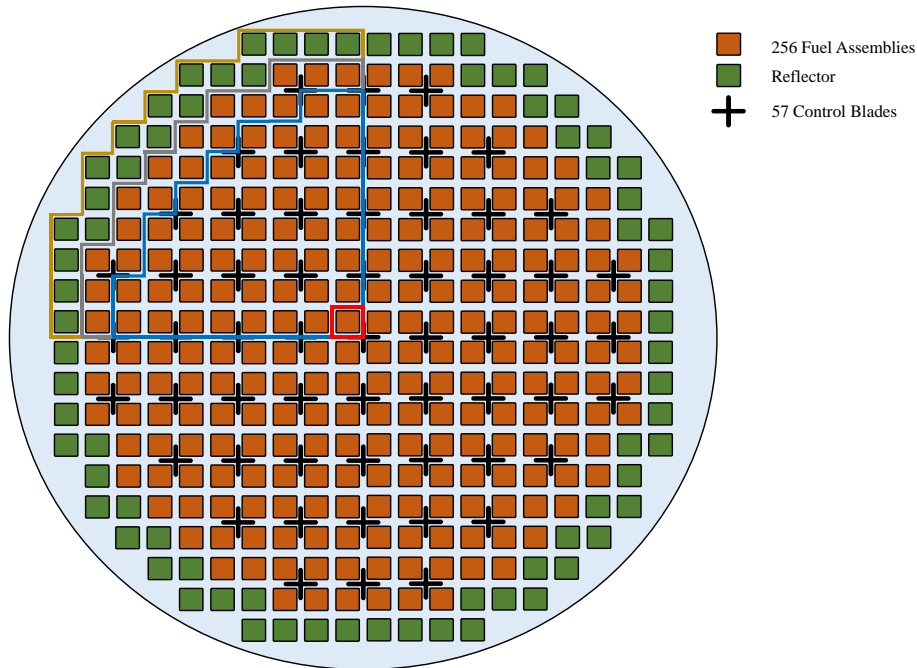
Figure 2-1 A schematic view of NMR-50 Core layout

2.2.3. RELAP5

A best estimate thermal hydraulics code RELAP5 was coupled, via parallel virtual machine, with PARCS to consider the local thermal feedback effects that are vital in BWR's. The Hench-Gillis correlation (Hench and Gillis, 1981) for critical quality boiling length was used to determine the minimum critical power ratio (MCPR). The reactor core was divided into four flow regions as defined in FY14. The RELAP5 now features the entire primary system. A simplified RELAP5 full primary system nodalization model of the NMR-50 is shown in Figure 2-2. This model includes the lower plenum, four core channels, chimney, separator, dry well, downcomer, feedwater tank, steam line outlet and turbine. Note that in the actual RELAP5 model, the downcomer and chimney are separated. The inlet flow rate, inlet coolant temperature, and outlet coolant pressure were used as the boundary conditions for the RELAP5 calculations. A semi-implicit scheme was adopted in RELAP5 to advance the hydrodynamics.

4 Channel Model (Quarter-Core Symmetric)

10 Axial Nodes

Pressure Vessel

Steam Line Outlet

11

Drywell

Separator

8

18

10

Turbine

16

Downcomer

Chimney

12

Core Channels

17

1

Feedwater Tank

Inlet

Tank
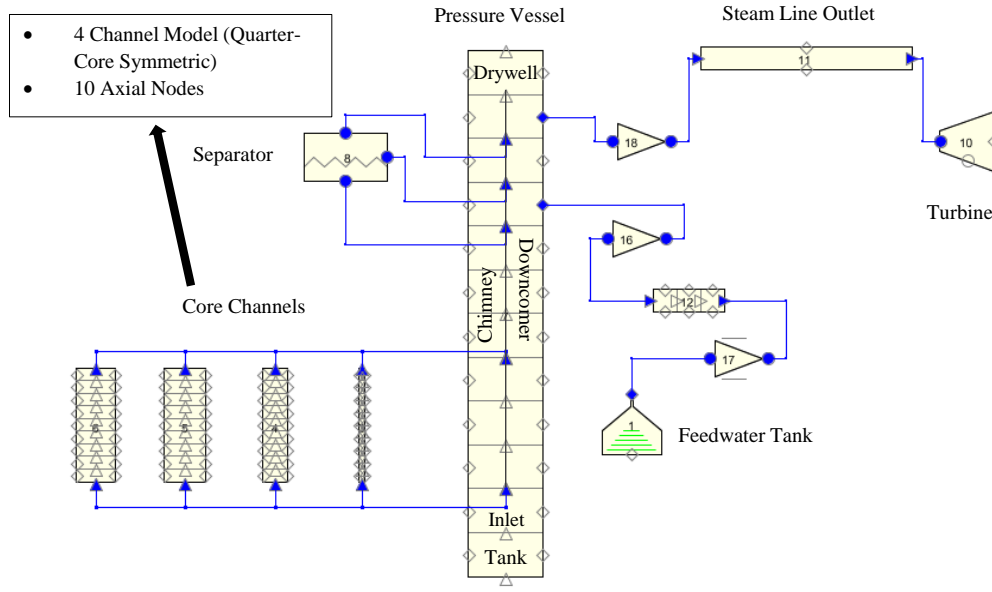
Figure 2-2 RELAP5 nodalization diagram (simplified) for the NMR-50 primary system using Symbolic Nuclear Analysis Package

2.2.4. Cross Section Generation Scheme Refinement

The computer code named Generation of Purdue Macroscopic Cross-Sections (GenPMAXS) is an interface between lattice physics code and whole core simulator that provides Purdue Macroscopic cross section (PMAXS). A PMAXS file includes macroscopic and microscopic cross-sections, discontinuity factors, kinetic data, and yields for the poisons. The cross sections are linearized as a function of state variables except for the moderator density and void fraction that use a quadratic variation. PARCS depletion calculation performs a multi-dimensional piecewise linear interpolation to obtain the partial derivatives.

The efficiency of the functionalization scheme in PMAXS and the accuracy of the cross section linear interpolation scheme were assessed. Considering a piecewise linear interpolation scheme, sufficient cross section database is required to reduce the error in the computation of partial derivatives. Error in calculating partial derivatives would affect the whole core eigenvalue and depletion calculation, which could result in a cycle length that is off by weeks or even months. Thus, a

sensitivity study of the branching calculation on the computation of eigenvalue was performed.

Voiding is the predominant factor in moderator density changes in BWR's, so void branching calculation was examined in detail. A reference case with a nominal thermal-hydraulics operating conditions were first established, followed by a case with a reduction in void; both cases are summarized in Table 2.1. The procedure to assess the accuracy of the cross section interpolation scheme was done by analyzing the difference in the k_{inf} eigenvalue from PARCS single assembly depletion with reflective boundary condition and PMAXS file obtained by performing branching calculation versus the reference CASMO-4 depletion results.

Table 2.1 Thermal-hydraulics operating conditions of the test cases.

Case	Fuel Temperature (K)	Moderator Temperature (K)	Void (%)
Reference	900	560	40
Reduced Void	900	560	5

Figure 2-3 compares the k-inf values obtained from the PARCS calculations with different cross section sets with the CASMO-4 reference solution. When the conventional branching calculation procedure derived from the SIMULATE-3 case matrix (S3C), the $k\infty$ of the reduced void case shows a maximum difference around 100 pcm. To reduce this large error, the branching calculation procedure was refined until the eigenvalue difference was within 10 pcm. Both depletion and void step size were refined, as shown in Table 2.2

Table 2.2 Depletion and void branch comparison between refined and conventional method.

	Refined	Conventional (S3C Case Matrix)
Depletion Branch	0 0.1 0.5 1 1.5 … 20 25 30 … 60	0 0.5 2.5 4 5 6 7.5 9 10 11 12.5 15 17.5 … 60
Void Branch	0 10 20 30 … 80 100	0 40 80 100

The depletion branching calculation was refined in the first 15 GWd/tU where gadolinium content is burned out. This refinement reduced the deviation in eigenvalue to below 35 pcm. Furthermore, the void branching calculation was refined. This refinement reduced the deviation in eigenvalue to below 10 pcm, which is an acceptable level of deviation in eigenvalue.

Note that cross section library generation is the most time-consuming procedure in the overall neutronics simulation. This is taken into consideration when the simulated annealing algorithm is devised.
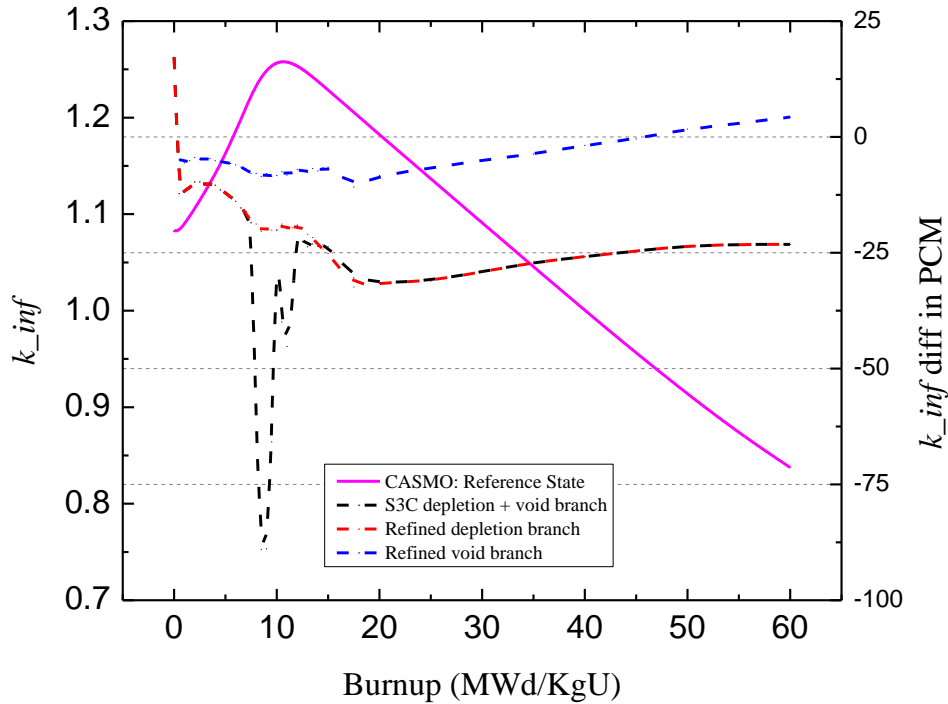
Figure 2-3 k-inf vs. burnup results for case problem with the high moderator density

2.3. NMR-50 CORE DESIGN OPTIMIZATION

The focus of optimization is to achieve the targeted 10-year cycle length with a minimum fissile loading. This optimization process was taken by a systematic three-step approach to reduce the design domain. Simulated annealing based optimization method was used in deriving an optimized assembly and burnable poison axial zoning designs.

In FY 2014, using CASMO-4, pin cell calculations were performed to determine the optimum pin size, moderator-to-fuel ratio, and average enrichment. Void coefficient (VC) was calculated by performing a branching calculation at different void fraction. While some modifications were made to this pin design, work focused on optimizing the fuel assembly design. Using an SA optimization algorithm, the enrichment split among fuel pins were optimized to minimize the local power peaking. Moreover, the number of burnable poison pins and its concentration were optimized to hold down the excess reactivity so that a sufficient cold shutdown margin (SDM) can be obtained without modifying the control blade design. The axial zoning design of the burnable poison fuel rods was optimized such that axial power peaking factor is minimized. The axial peaking factors were evaluated from PARCS/RELAP-5 calculations.

2.3.1. Fuel Pin Cell

Fuel pin-cell models were developed to represent the average assembly behavior. Pin cell depletion calculations were performed and the critical burnup that represents the cycle burnup of single-batch scheme was determined. The critical burnup was estimated by imposing a conservatively assumed leakage fraction of 7%.

The critical cycle burnup was calculated at a fixed enrichment by varying the pin outside diameter and the water-to-fuel volume ratio. The critical cycle burnup corresponding to a 10-year cycle length was determined.

Then the pin diameter and water-to-fuel volume ratio to yield a 10-year cycle length was determined for different fuel enrichments. The contour lines of 10-year cycle length for five different enrichments are shown in Figure 2-4 as dotted lines. The color plot in Figure 2-4 is the contour plot of VC including a line showing negative VC cutoff. Figure 2-4 also shows the critical heat flux (CHF) limits (solid horizontal line) for two different assembly lattices, which was determined by the smallest pin diameter for a given assembly lattice and a conservative three-dimensional power peaking factor (FQ) of 3.5. The dashed lines show the pin diameter versus water-to-fuel volume ratio for four different assembly lattices.
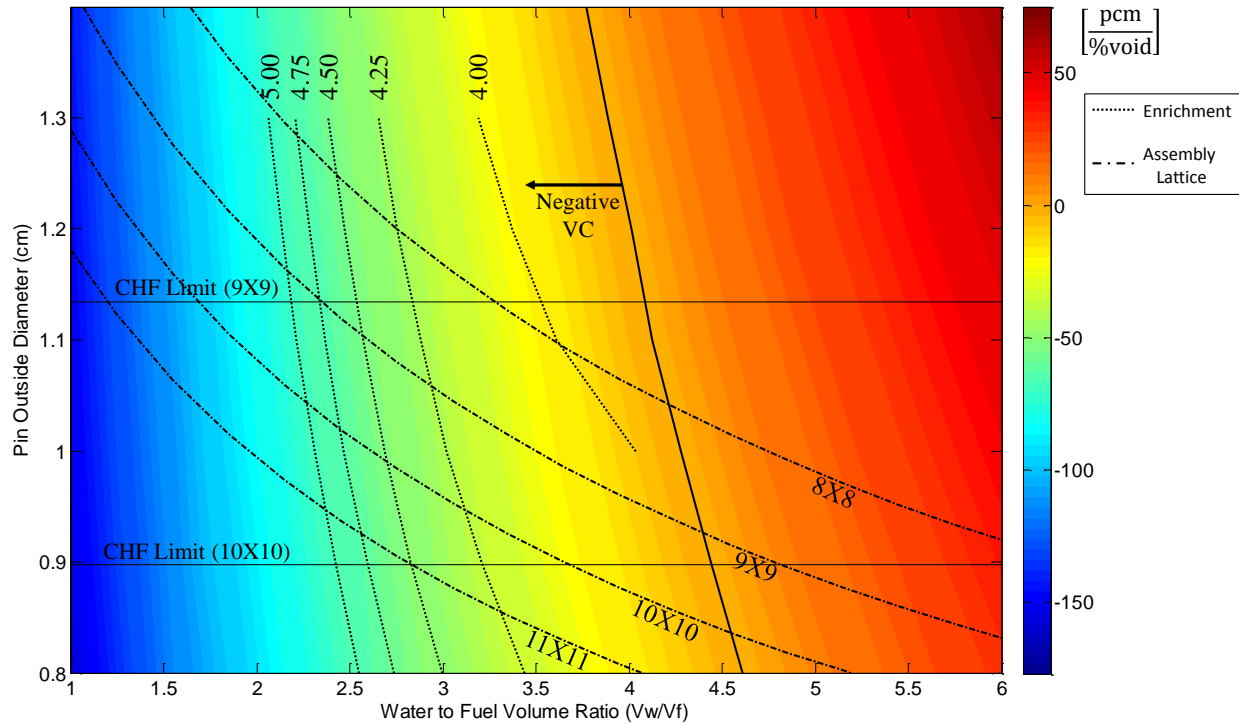
Figure 2-4 Void Reactivity Coefficient (pcm/%void) as a function of both water-to-fuel volume ratio and pin outside diameter at fixed enrichment of 4.5%

From Figure 2-4, it can be seen that with increased water-to-fuel volume ratio, the average enrichment required for a 10-year cycle length decreases. However, the imposed VC constraint yields a minimum average enrichment around 4.5 wt%. Since a smaller sized pin is desirable from a standpoint of minimizing the fissile loading, a 1.05 cm fuel pin diameter, water-to-fuel volume ratio of 2.7, and an average enrichment of 4.5 wt% were chosen for an optimum average fuel-pin design.

2.3.2. Fuel Assembly

2.3.2.1. Enrichment Split

Fuel enrichment distribution within assembly allows a better fuel utilization (fuel cost), more even burnup, and lower local power peaking. The presence of water rods and inter-assembly gap provides more moderation for the fuel pins

adjacent to them and thus would cause significant power increases in these pins if a single enrichment were used for all the fuel pins. In FY 2014, it was found that a near linear relationship exists between relative fuel pin power and local water-to-fuel volume ratio (local moderation). This behavior was utilized in a way to determine an optimum fuel enrichment split by correlating individual pin enrichment and local water-to-fuel volume ratio. Therefore, fuel pins with high local water-to-fuel volume ratio were assigned a lower enrichment, while pins with low local water-to-fuel volume ratio were assigned a higher enrichment. The optimum enrichment domain for an individual pin, within an assembly, can be determined by analyzing the local pin relative power as a function of both the designated pin and its surrounding pins enrichments, which is shown in Figure 2-5 for four different fuel pins. The primary purpose of an enrichment split is to reduce the power peaking factor, in order to flatten the power/burnup distribution and ensure thermal margins are not violated. Hence, it is desirable to target a local power peaking factor of unity. However, with a targeted average assembly enrichment of 4.6 wt%, the central fuel pin cannot achieve a local pin relative power of unity. This analysis, summarized in Figure 2-5, was used to set a tight enrichment domain on the different fuel type such that the local pin relative power is approximately unity.
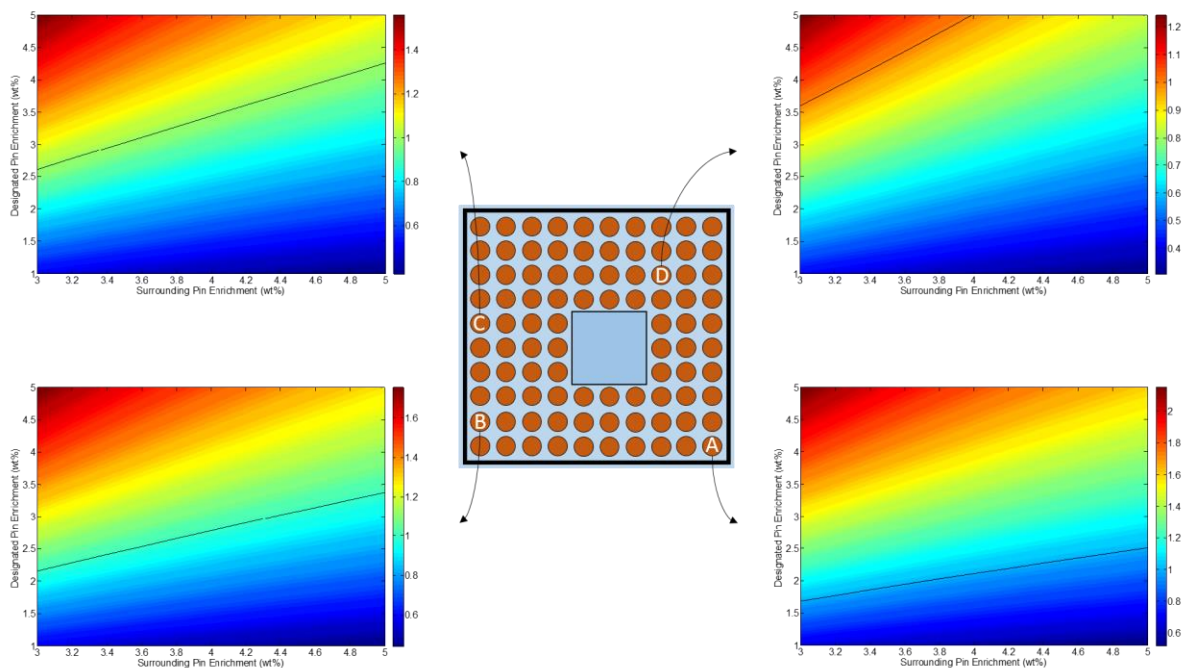
Figure 2-5 Local pin relative power at different designated pins and its surrounding pins enrichments

Typical practice in the industry involves maintaining the number of different fuel pin enrichments within an assembly to a minimum [13]. However, some assembly designs, such as AREVA Atrium 10B, have many more types of fuel pins within an assembly. This increases the degrees of freedom when searching for an optimum enrichment split. The NMR-50 assembly design employs seven different types of fuel (enrichment) pins within its assembly along with a centered water rod that occupies nine fuel pins.

2.3.2.2. Burnable Absorber

The type, number, and amount of burnable poison (BP) rods required within an assembly were determined. The main purpose of introducing BP is to hold down the excess reactivity and to reduce the local power peaking. There are numerous BP types studied, tested, and used [14], however, three primary BPs are industrially used that includes: boron, erbium, and gadolinium (Gd). Boron has a high absorption cross section, no significant self-shielding effects, and no other absorbing boron isotopes. Therefore, boron tends to burn out rapidly, which does not make it suitable for a long life core. Gadolinium and erbium are similar in terms of their isotopic chain in which both include isotopes with a reasonable absorption cross section. In addition, both gadolinium and erbium have significant self-shielding effects, which allow for slow burn out. This means that both are suitable for long life core. Furthermore, it was found that Gd is more beneficial on the basis of residual absorber penalty [14]. Since NMR-50 cannot use boric acid, a larger burden is placed on control rod blades and BP for excess reactivity hold-down. Therefore, gadolinium that has a relatively a higher absorption than erbium, was chosen. Gadolinium is used in the form of Gd_2O_3 with a specified enrichment of Gd that is mixed with fuel, also known as gadolinia fuel rods.

The optimum gadolinium amount and the number of pins were determined to hold down the excess reactivity so that the required cold shutdown margin can be obtained with the current control blade design. Gadolinium is also used to suppress the power peaking factor, but it requires a large amount of Gd than the amount

required for reactivity hold down. Since the primary purpose of Gd is to control excess reactivity, fewer number of Gd fuel pins with higher Gd concentration are favorable. That is because the higher concentration reduces the decreasing rate of reactivity worth with fuel burnup, due to increased neutron self-shielding [15]. This is shown in Figure 2-6, where the gadolinium amount is conserved in all three cases. It can be noted that the assembly with a lower number of Gd fuel pins and higher concentration yields a lower residual neutron absorption content. This indicates that the residual penalty is reduced, which yields a longer cycle length. In particular, the difference in cycle length between seven and fifteen Gd fuel pin designs is approximately 2 weeks. Seven Gd fuel pin design was chosen. With the current control rod blade design, 6.2 wt% enriched Gd2O3 is required to hold down the required excess reactivity, while maintaining sufficient cold shutdown margin.
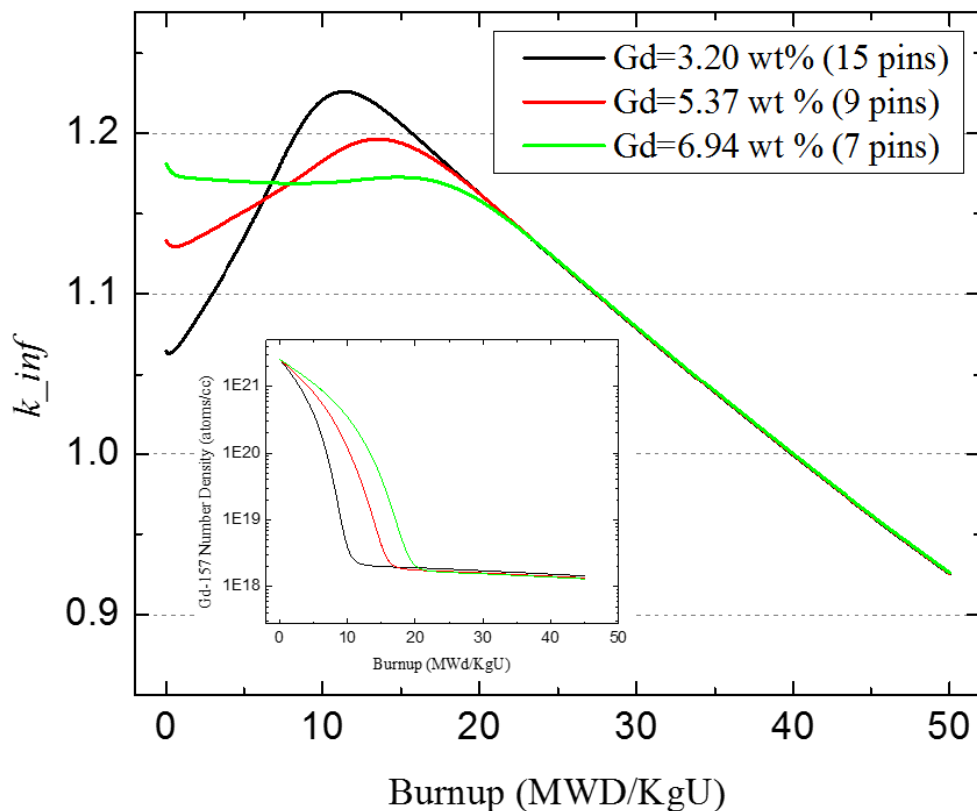
Figure 2-6 Excess reactivity and Gd-157 number density behavior for three different Gd fuel pin designs

2.3.2.3. Simulated Annealing

Simulated annealing (SA) based optimization method [16] was used in deriving an optimized fuel assembly (FA) design. The focus was on determining an optimum fuel enrichment split within an assembly. This method of optimization is highly regarded in nuclear fuel management due to its attributes such as non-linear dependence on objective function, many local minima of the objective function, and a large domain space [15]. The simulated annealing main engine was based on the Metropolis algorithm [17]. The concept of simulated annealing is an analogy to the annealing process in metallurgy in which the process involves heating a metal to an elevated temperature and then cooled gradually. Similarly, SA algorithm utilizes an artificial temperature variable to control the rate of convergence. This temperature variable provides a distinctive feature of the SA algorithm regarding a minimization or maximization problem. It allows for the acceptance of a new solution even though its objective function is worse than the previous solution. This ensures that the new solution is not confined to a local minimum via extending the searching domain.

In the overall SA FA optimization algorithm a FA proposal logic, an objective-function, an acceptance probability, an initial temperature, a temperature reduction scheme, and a termination criterion are required. Each feature will be discussed in the following paragraphs.

To propose a new FA from the current FA, two random numbers are used. The first random number is used to determine the fuel pin type, were NMR-50 FA is composed of seven different fuel types. The second random number is used to determine the new fuel pin enrichment given an enrichment domain. Then the average FA enrichment is analyzed and adjusted by a factor such that the average assembly enrichment is approximately 4.6 wt%. The series of proposed FA constitutes a Markov chain because each successive solution depends only on the preceding solution and random numbers. The SA algorithm is divided into stages and samples. Each stage is composed of a number of FA samples, where the samples refer to the number of neighboring FAs possible from the current FA.

The objective function defined is the cycle length, however, since this evaluation requires CASMO-4 cross section library generation for each newly accepted FA design that is extremely time consuming, the objective function is simplified to k-inf at BOC. This was done in order to improve the overall

efficiency of the optimization code. Once the objective function is maximized, the top 10% proposed FAs are selected. The selected FAs are then evaluated using CASMO-4 depletion calculation where the cycle length can be determined. Then, the optimum mutually undominated FAs are determined and the best candidates are evaluated using full core PARCS/RELAP5 coupled calculation.

The acceptance probability of the proposed FA is determined according to the Metropolis algorithm, which is computed using an exponential function similar to that of the Arrhenius equation.

$$
P_{acceptance} = \begin{cases} \exp\left(-\dfrac{O(X_m)-O(X_n)}{T_s}\right); \text{if } O(X_m) < O(X_n) \\ 1; \text{otherwise} \end{cases}
\tag{2.1}
$$

Where X_m and X_n represent the new and current FA, respectively. $O(X)$ is the objective function and T_s is the temperature variable at stage s. The initiation of the initial temperature is important in order to allow for efficient FA search. The temperature must be high enough in order to accept all neighboring FA proposed from the current FA, while not too high to avoid a completely random search. The initial temperature is determined by running an initialization, which consists of a number of randomly proposed FAs, and determining the average objective function and the standard deviation. As the temperature decreases, the acceptance probability decreases. The temperature reduction scheme adopted in this study uses a polynomial time annealing schedule [18], determined as

$$
T_{s+1} = \alpha_s T_s
\tag{2.2}
$$

$$
\alpha_s = \dfrac{1}{1 + \dfrac{T_s \ln(1+\delta)}{3\sigma_s}}
\tag{2.3}
$$

Where α_s is the quality factor (thoroughness of optimization), σ_s is the standard deviation of the objective function values at stage s, and δ is the distance parameter.

The termination criteria used is based on the number of accepted FAs per stage. At any given temperature and stage, if the number of accepted FAs is less than a user defined value, then a signal for termination is sent.

The search for an optimum enrichment split was performed using the SA optimization method. At first, the simulation consists of a CAMSO-4 BOC calculation with 800 samples (FAs) per stage. The simulation was terminated at stage 110, where 88,000 FAs were generated. Of these proposed FAs, around 27,000 of them were accepted.

From this data, the top 15% FAs, based on maximizing kinf, were chosen for the CASMO-4 depletion calculation. Figure 2-7 shows the local power peaking factor as a function of cycle length. Since a maximum cycle length with minimum local power peaking factor is desired, there are only 12 mutually un-dominated FA designs.

To determine an optimum candidate, the present value of the fuel assembly cost was considered. The fuel cost was determined by adding the known costs incurred in the front-end cycle. This included the cost of uranium ore, conversion, enrichment, fabrication, and gadolinia fuel rods. The cost of each seven fuel pin type was considered explicitly due to the enrichment split. Then, the ratio of the assembly cost and the cycle length is established as a unit cost. By minimizing the assembly unit cost, five optimum FA candidates were chosen. The lowest unit cost corresponded to the FA design with the largest cycle length, which was chosen as the optimum design for full core coupled calculation.
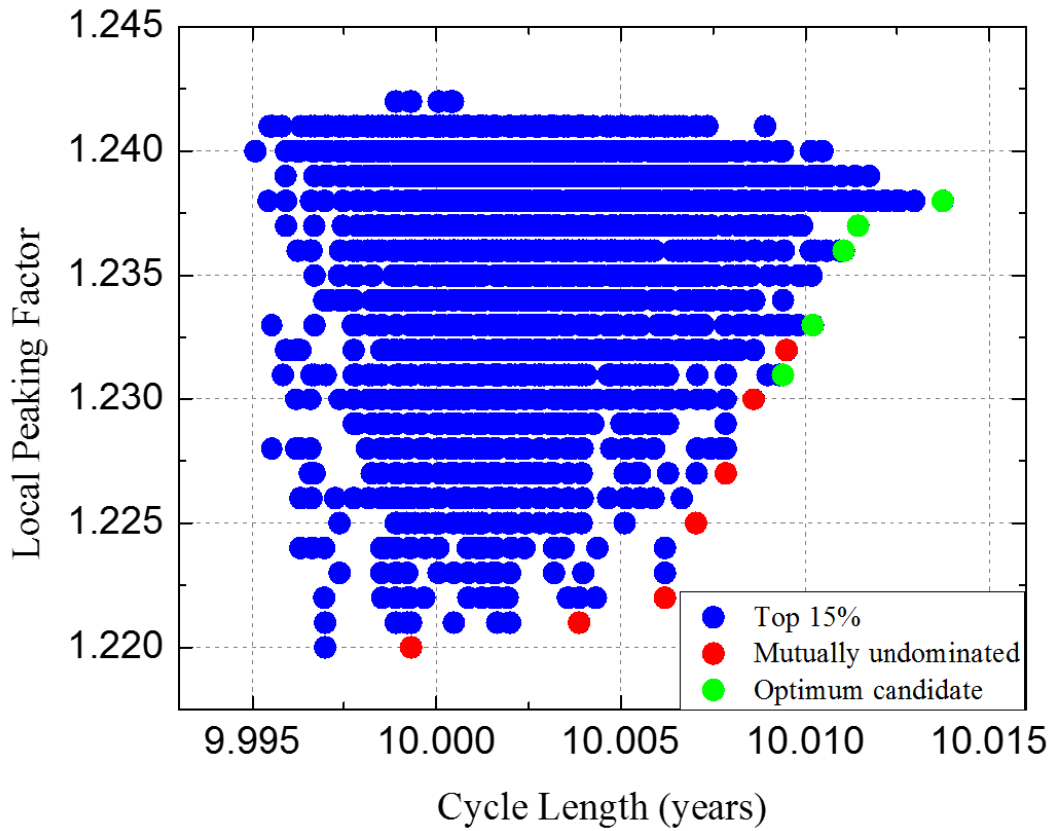
Figure 2-7 Local power peaking factor versus fuel cycle length

The optimum assembly design deduced from the above step-wise optimization process is illustrated in Figure 2-8. The optimized design parameters for NMR-50 FA are summarized in Table 2.3. The average assembly enrichment was 4.61 wt% and the local power peaking factor was 1.232.

Type	Enrichment/Gd (wt%)
Fuel 1	2.59
Fuel 2	3.58
Fuel 3	4.20
Fuel 4	4.60
Fuel 5 (BP)	4.94/6.2
Fuel 6	4.7
Fuel 7	4.98
Water Rod	
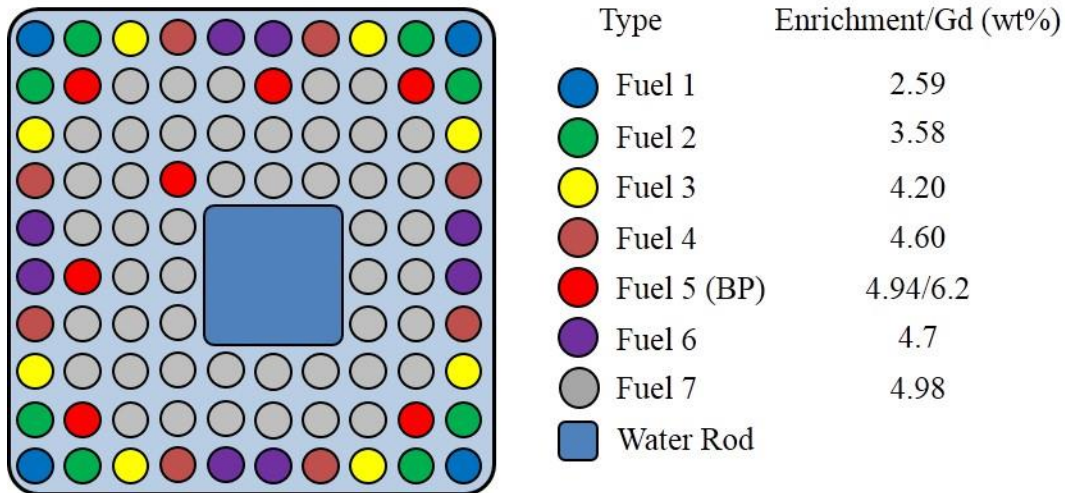
Figure 2-8 The optimum fuel assembly design layout

2.3.3. Whole Core

Axial zoning of fuel assemblies, typically with different burnable poison loading, is used to counteract the reactivity penalty imposed by boiling in the upper regions of the core, which is inevitable in BWR systems. Without axial zoning, the power profile is heavily bottom skewed, which leads to uneven axial power distribution. This induces uneven fuel burnup and large spatial xenon changes. Uneven fuel burnup is uneconomical while large spatial xenon variation leads to power oscillation. An assessment of the asymmetry of power profile as well xenon induced reactivity in NMR-50 will be discussed in the following section.

Axial zoning of Gd content is optimized such that axial power peaking factor (F_z) is minimized while maintaining a hold down of excess reactivity so that the required cold shutdown margin can be achieved with the current control blade design. In the previous section, it was found that an average of 6.2 wt% enriched Gd_2O_3 is required to hold down the required excess reactivity.

The gadolinia fuel rod was divided into two axial zones. The total height of the active fuel was divided into 9 axial segments. The search for optimum axial zoning design involved varying the number of axial meshes per zone. In addition, the Gd concentration in the respective axial zone was varied while maintaining an overall

average concentration that is in the vicinity of the established requirement (6.2 wt%).

PARCS full core model was developed from the optimum assembly design determined earlier. PARCS was coupled with RELAP5 for local thermal feedback. Depletion calculation was performed for the different possible axial zoning assembly design. Discrete axial zone heights and Gd content were set for this optimization.

Throughout the depletion cycle, the maximum axial power peaking factor as well as maximum keff was recorded. Maximum Fz versus maximum keff for the different possible zoning design is shown in Figure 2-9.
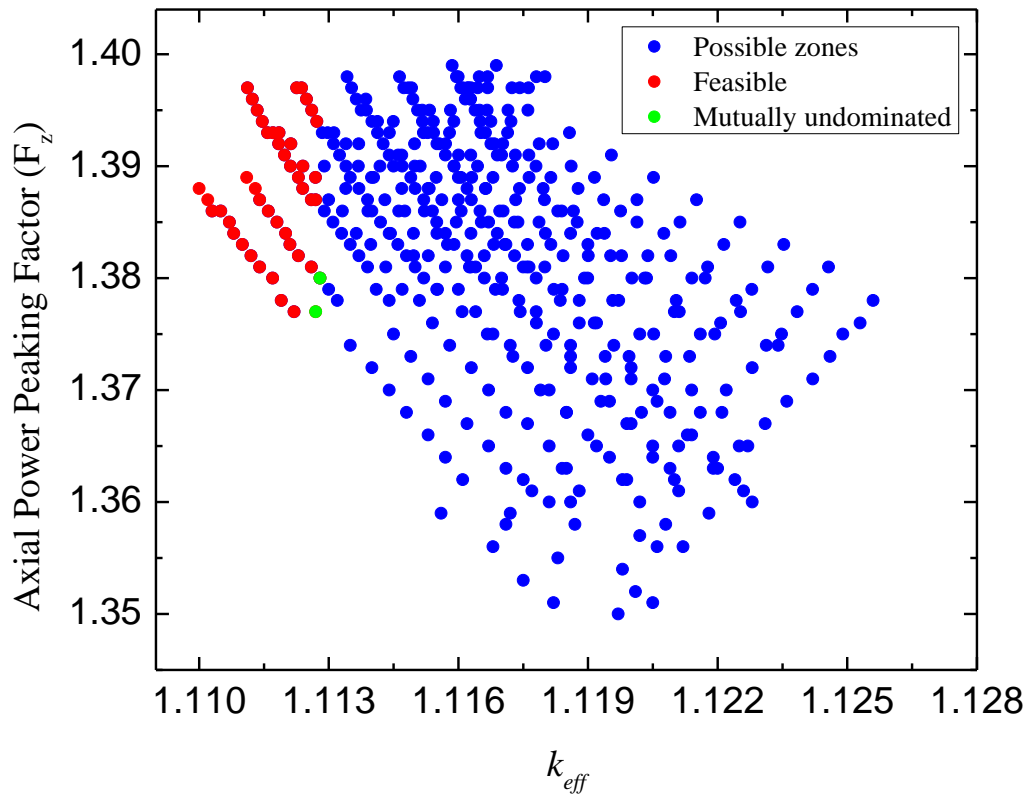
Figure 2-9 Axial power peaking factor versus keff

Figure 2-9 shows all possible zones of the burnable poison fuel rod in which the average Gd concentration is around 6.2 wt%. Given the current NMR-50 control rod blade worth, a maximum allowable k_{eff} is defined in order to ensure

sufficient cold shutdown margin. This results in certain feasible zoning designs. With a goal of minimizing axial power peaking factor and maximizing k_{eff}, there are two mutually un-dominated zoning designs. The lower axial power peaking factor was chosen as the optimum axial zoning design. The geometry and material distribution of the optimized axial zoning of the NMR-50 gadolinia fuel rod is shown in Figure 2-10. The average Gd concentration was 6.17 wt%, with 6.7 wt% and 5.1 wt% in the bottom and top zone, respectively. The gadolinia fuel rod design in FY 2014, which is comprised of 15 gadolinia fuel pins, had a larger total amount of gadolinia. Considering that the cost of gadolinia fuel rod with 6 wt% enriched gadolinium is around $400/rod [19], cost saving is in the order of $0.3 million in the reactor core.
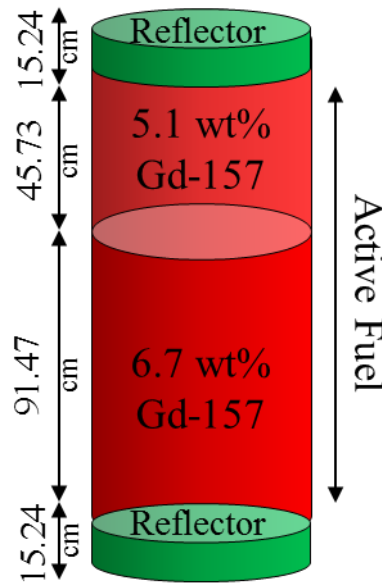
Figure 2-10 Axial zoning of the NMR-50 integral fuel burnable absorber design

NMR-50 is split into 4 flow regions, where typically, a core is divided into 3-4 orifice zones [20]. Regarding orifice design and flow allocation, the inlet loss coefficient (K_{loss}) was previously determined, FY 2013, for the four flow regions such that the power to flow ratio are identical.

Regarding the control rod programming, the Control Cell Core approach was used. The Control Cell Core minimizes the impact of control-rod blade movement

on the radial power distribution [21] and the buildup of burnup shadowing [15]. Only two group of control rod blades in a control cell, also known as the control bank, were utilized and interchanged during the reactor operation.

Table 2.3 Parameters of the optimized NMR-50 core.

Parameters	Values
Fuel pin parameters	
Fuel rod outside diameter	10.5 mm
Fuel rod cladding thickness	0.6058 mm
Gap	0.0851 mm
Fuel characteristics	
Moderator-to-fuel volume ratio	2.38
Fuel density at 20°C	10.45 g/cm^3
Average U-235 enrichment	4.61 wt%
Average gadolinium enrichment	6.17 wt%
Fuel material	
Cladding material	Zircaloy-2
Fuel pellet materials	UO2
Burnable poison	Gd2O3
Fuel assembly	
Fuel rod array layout	10x10
Pitch of square rod array	13.1 mm
Number of fuel rods per assembly	91
Number of fuel pin with burnable poison	7
Number of water rods per assembly	9
Fuel type	Fuel enrichment (wt%)
1	2.59
2	3.58
3	4.2
4	4.6
5	4.94
6	4.7
7	4.98

2.4. NMR-50 DESIGN AND PERFORMANCE

Using the optimum fuel assembly design illustrated in Figure 2-8 and Figure 2-10, a full core PARCS/RELAP5 depletion calculation were performed to

determine the cycle length and to evaluate the thermal safety margins. Moreover, the reactivity feedback coefficients and cold shutdown margin were evaluated. A preliminary study on the NMR-50 vulnerability to xenon induced-power oscillations was assessed. Finally, the potential consequences of long life core on structural material is addressed from a radiation damage stand point.

2.4.1. Cycle Length and Thermal Safety Margins

Performance and safety margins are determined during depletion in order to ensure safe operation throughout the 10-year cycle length. At each time point, the criticality was maintained by adjusting the control blade bank position. The core depletion calculation yielded a cycle length of 10.2 years. Fuel cycle depletion characteristics are summarized in Table 2.4. The control blade insertion position is represented by notch values, between 0 and 3192 that represent the fully inserted and the fully withdrawn states, respectively. The indicated thermal margins are in terms of the MCPR and MFLPD respectively. Note that both MFLPD and MCPR satisfy the imposed design constraints with large margins throughout the 10-year cycle. This is due to the reduction in power density that provides an increased thermal safety margin when compared to SBWR-200.

Table 2.4 Fuel cycle performance of the NMR-50.

Years	Average burnup (GWd/tU)	k_{eff}	Control blade notch	Overall power peak	Radial power peak	Axial power peak	Axial offset (%)	MFLPD (kW/m)	MCPR
0.0	0.00	0.99998	25296	2.099	1.518	1.302	-10.96	13.50	2.22
1.0	3.05	1.00036	30241	1.773	1.32	1.215	-9.81	11.70	2.19
2.0	6.11	1.00014	30796	1.791	1.311	1.231	-8.51	11.74	2.14
3.0	9.16	1.00010	31351	1.669	1.288	1.231	-7.85	11.78	2.10
4.0	12.21	1.00002	30846	1.482	1.3	1.198	-9.35	10.91	2.12
5.0	15.27	1.00002	28767	1.591	1.208	1.188	-9.33	10.48	2.07
6.0	18.32	1.00020	25679	1.887	1.33	1.376	-0.41	12.61	2.03
7.0	21.37	1.00004	20300	1.644	1.234	1.158	-1.84	10.57	2.28
8.0	24.43	1.00017	13008	1.765	1.23	1.155	-12.50	11.35	2.22
9.0	27.48	1.00003	7472	1.97	1.366	1.308	-14.80	12.67	2.14
10.0	30.53	0.99998	1428	2.766	1.669	1.564	-17.62	18.25	1.99
10.2	31.04	0.99977	848	2.654	1.628	1.543	-17.70	17.60	2.00

The axial power profile is of significant importance, especially in BWRs, due to two-phase flow nature. It is necessary to limit overall power tilting for safe reactor operation [20]. The behavior of the axial power profile, at the hottest fuel assembly, as a function of the reactor operation time is shown in Figure 2-11. It can be seen that the axial power profile is bottom skewed, especially during the early stage of the cycle. The degree of axial power asymmetry is represented by the axial offset (AO), which is defined as

$$AO = \left(\frac{P_U - P_L}{P_U + P_L} \right) \cdot 100 \qquad (2.4)$$

In which P_U and P_L are the total power at the upper half and lower half of the reactor core, respectively. The AO indicates the spatial non-uniformity presence of 135Xe. From Figure 2-11, it can be observed that the axial offset varies during the reactor operation. Large AO causes large spatial xenon changes that may induce a large power oscillation. This could threaten the safety of reactor operation. Spatial xenon effect on NMR-50 will be discussed.
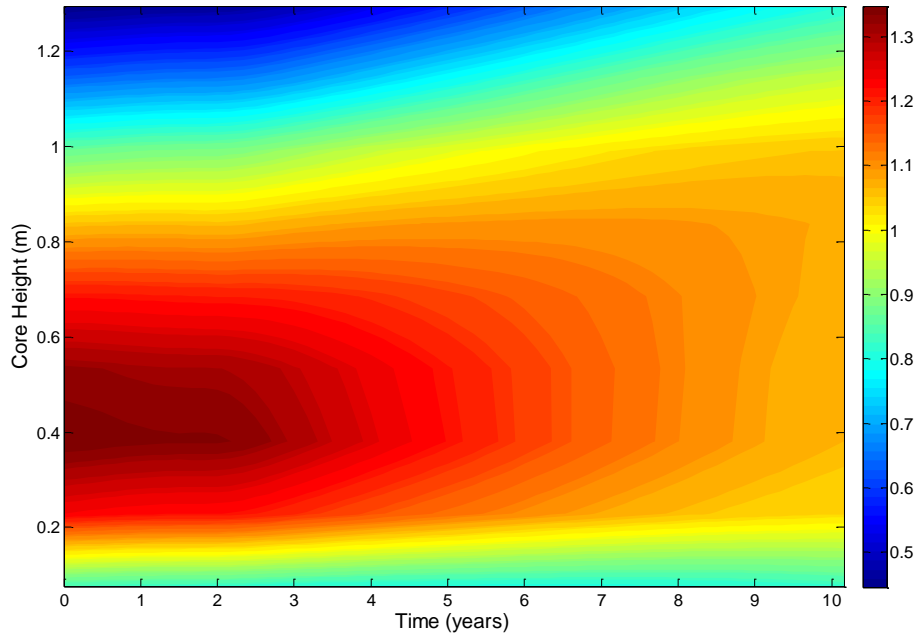
Figure 2-11 NMR-50 temporal axial power profile at the hottest assembly

24

As a confirmation of proper coupling calculation between PARCS and RELAP5, the core coolant mass flow rate response to power changes was analyzed. The flow rate variation within the hottest and peripheral assemblies during the reactor operation is shown in Figure 2-12. As power increases in certain fuel assemblies, the void fraction increases and the coolant flow rate increases such that the exit pressure equals to the pressure boundary condition. The core thermal hydraulics performance of NMR-50 design is summarized in Table 2.5.
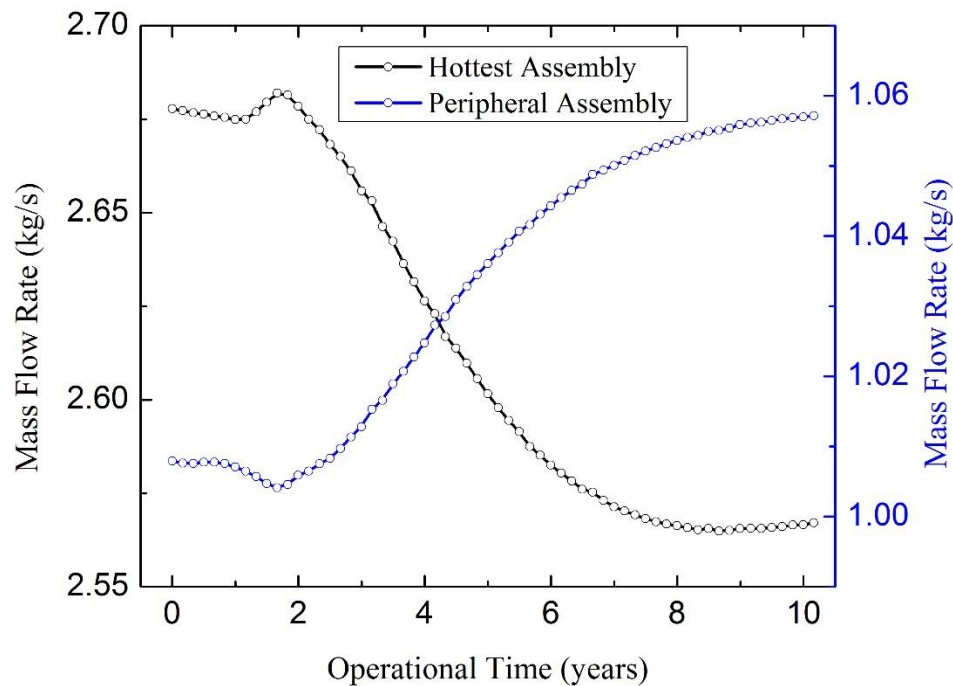
Figure 2-12 Core coolant zonal flow variation during NMR-50 operation

Table 2.5 Core thermal hydraulics performance of the NMR-50.

Parameter	Value
Core pressure drop	29.4 kPa
Average core void fraction	0.428
Maximum exit void fraction	0.750
Core average exit quality	0.144

2.4.2. Reactivity Safety Margin

Especially in BWRs, Doppler and void reactivity coefficients are the main feedback mechanism. The Doppler reactivity coefficient is the most significant quenching mechanism in short term transients due to its instantaneous reactivity feedback. Such a scenario is evident in the rapid power excursion by means of control blade ejection [20]. During NMR-50 operation, the production of, mainly, ^{240}Pu contributes to a more negative Doppler reactivity coefficient as illustrated in Figure 2-13.

Void reactivity feedback is most important in stabilizing and controlling the reactivity during reactor operation. During the NMR-50 operation, the production of plutonium as well as fission products results in a more negative void reactivity coefficient [22] as illustrated in Figure 2-14.
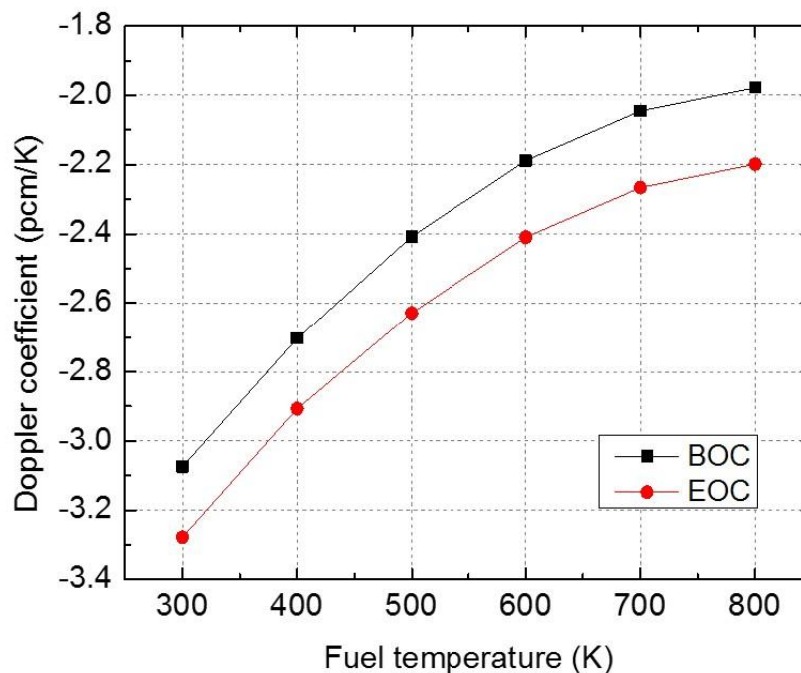
Figure 2-13 Fuel temperature (Doppler) coefficient as a function of fuel temperature at BOC and EOC
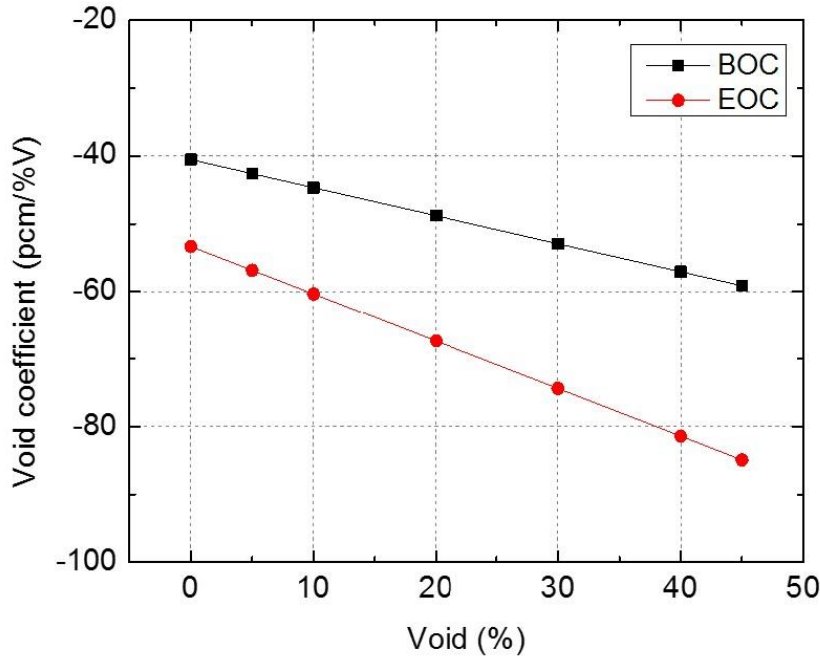
Figure 2-14 Void coefficient as a function of coolant void fraction at BOC and EOC

To ensure safe reactor operations, the reactor should be shut down from the most reactive state during the life cycle, with a sufficient margin. For a conservative measure of cold shutdown margin, the "stuck-rod criterion" was used. This method involves the calculation of the total control blade reactivity worth, excluding the most reactive control blade (stuck out of the core). The shutdown margin was evaluated at the cold and xenon-free reactor condition at peak excess reactivity and EOC. At EOC, the reactivity feedback coefficients are most negative. However, the most limiting SDM was found to be at peak excess reactivity. The control reactivity balance is shown in Table 2.6. The result shows that NMR-50 reactor design provides a sufficient cold shutdown margin.

Table 2.6 Control reactivity balance and SDM at most reactive state.

Reactivity Component	Value (%ρ)
Temperature and Power Defect	9.148
Equilibrium Xe/Sm to HFP[a]	2.070
HFP to HZP[b]	5.054
HZP to CZP[c]	2.023
Excess Reactivity	10.170
Control Blade	21.091
SDM	**-1.773**

[a]Hot full power; [b]hot zero power; [c]cold zero power

2.4.3. Vulnerability to Xenon Oscillation

In the current LWR community, xenon oscillation phenomenon is most significant in PWRs due to the large height of the reactor core that allows for little flux coupling between regions, thus enhancing the vulnerability of a spatial power oscillation. This phenomenon becomes less significant in BWR's due to the large void reactivity effect. It provides an abundance of damping to suppress power oscillations, hence, a high xenon stability characteristic [23]. Since xenon induced power oscillations become less important in smaller size core, NMR-50 could exhibit an enhanced xenon stability characteristic compared to current BWRs [13]. To provide a constructive analysis, the magnitude of xenon induced reactivity worth is calculated for both NMR-50 and a conventional BWR, Oskarshamn-2 (O-2), in Sweden. The reactors condition was considered at around one fourth of the cycle length, which is when the burnable absorber is burnt out leading to the largest axial power peaking factor and relative power.

The upper and lower limit of AO during the NMR-50 cycle of operation does not violate the standards set in the LWR industry. In practice, AO limits are bound between -18% to 2% at 100% full power.

The 3-D spatial xenon concentration was computed using PARCS at equilibrium state. Axial thermal neutron flux accompanied by the Xe-135

concentration for both NMR-50 and O-2 is shown in Figure 2-15. In addition, the xenon induced reactivity worth for both NMR-50 and O-2 is shown in Figure 2-16. This study is not a transient; however, it gives a relative evaluation of xenon induced reactivity worth in NMR-50.

A key take out point is the relative magnitude of xenon induced reactivity worth in NMR-50 compared to conventional BWR. Around two fold reduction in xenon reactivity worth in NMR-50 compared to O-2 is observed. This reduction in reactivity worth owes to the significant reduction in thermal flux, by a factor of four.
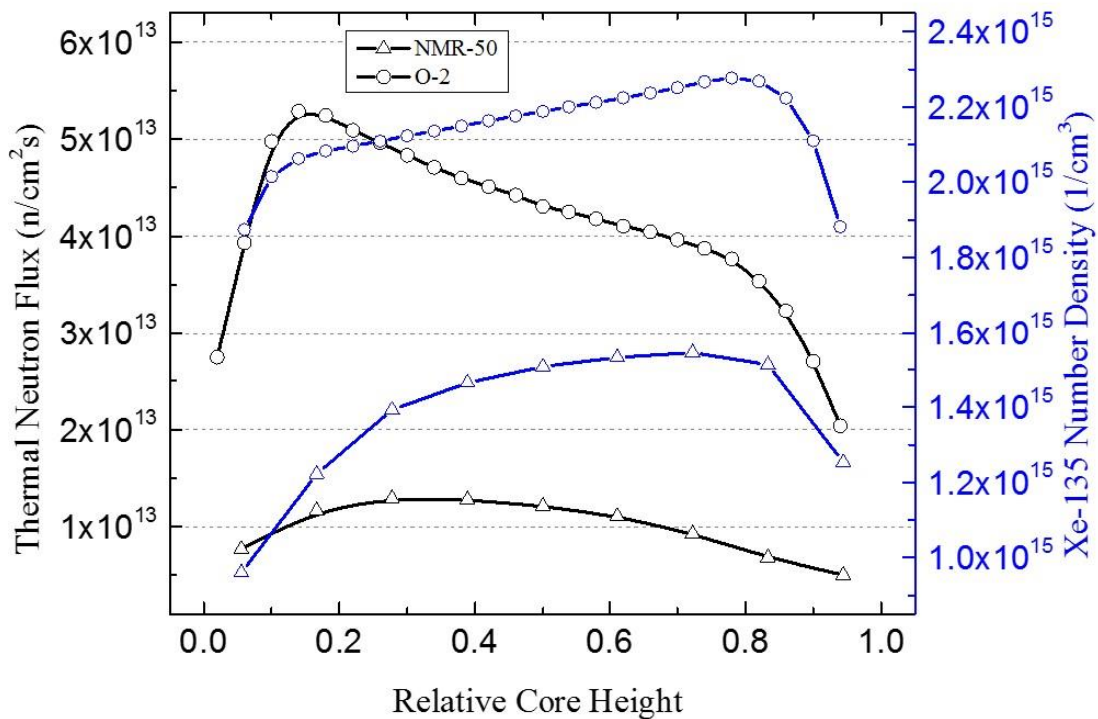
Figure 2-15 Thermal neutron flux and xenon concentration axial distribution of NMR-50 and Oskarshamn-2 at one fourth of cycle
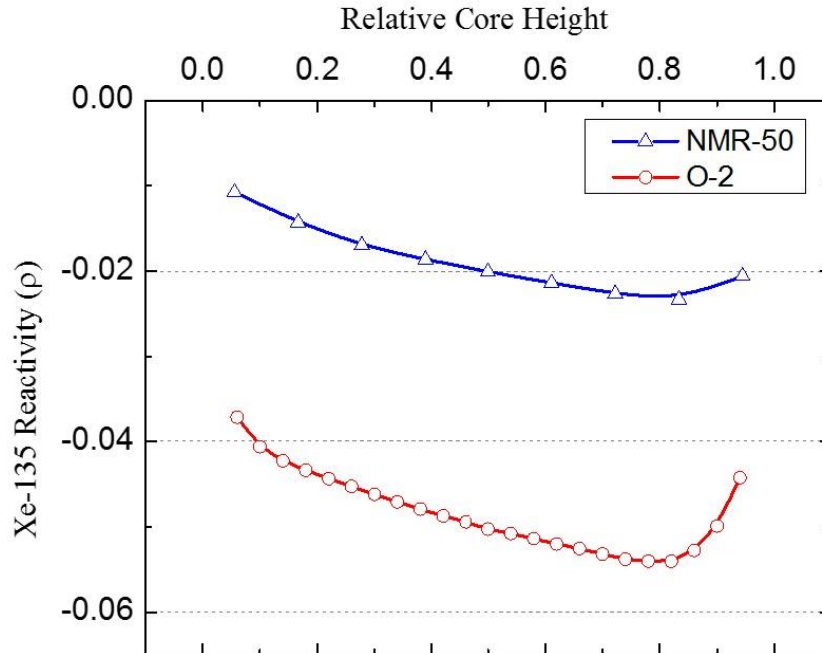
Figure 2-16 Local xenon-135 induced reactivity in the axial direction

2.4.4. Potential Consequences of Long Life Core on Structural Material

With almost half a century of operational experience in BWRs, the main consideration of increased fuel cycle length is channel distortions [24]. The BWRs fuel assembly channel box may experience dimensional deformation that could induce control blade friction and even, in the worst case, prevent control blade insertion. There are three major distortion phenomena: bulging, bowing, and twisting. It was found that channel bowing is the major concern and is mainly due to what is so-called shadow corrosion-induced. The shadow corrosion-induced enhances the hydrogen content on the surface of the channel box due to the galvanic effect of two dissimilar metals when control blade are inserted. Therefore, the differential hydrogen content of the two channel faces leads to a shadow corrosion-induced channel bow; due to the larger specific volume of ZrH compared of zircaloy-2 [11].

Material irradiation growth is strongly dependent on the fast neutron fluence. With NMR-50 operating at a low power density and with a relatively lower

neutron flux, the fast neutron fluence on the channel box at EOC is significantly lower than current BWRs. Research showed that significant growth was observed at fast fluence greater than $1 \times 10^{22} \, \text{n}/\text{cm}^2$. Moreover, from extensive plant data on measured channel bow as a function of burnup, it was found that channel bow occurred at burnup levels around 40 GWd/tU and greater [19]. Therefore, realizing that NMR-50 EOC peak fast neutron fluence is $8.8 \times 10^{21} \, \text{n}/\text{cm}^2$ and that average and maximum cycle burnup is around 32 and 40 GWd/tU, it can be concluded that NMR-50 could exhibit less of a concern over its 10-year cycle length from a radiation damage point of view. Moreover, utilizing the control cell core approach, control blades are not inserted in the center of core, hence, reducing the possibility of a shadow corrosion-induced bow.

3. NEUTRON KINETICS

In the thermal hydraulic startup transients that do not consider the reactivity feedback, the power curve is set as an input to the control system. However, the transient behavior of core power for the nuclear coupled startup transients is determined by neutron kinetics. The neutron flux can be calculated by solving the neutron diffusion equations along with the rate equations for precursors. Since the stability analysis for BWR startup is complicated due to its nature, the Point Kinetics Model (PKM) is chosen for the power calculation for the nuclear coupled startup transient tests.

3.1. POINT KINETICS MODEL

The diffusion theory balance equation for the time-dependent neutron flux depends on space and energy [25]. For the BWR startup tests, it is neither necessary nor feasible to solve a complicated set of equations including the space-dependent precursor equations. The PKM only solves the time dependent equations by considering the reactor as a point. This model gives a good estimate for the core-wide oscillations in the NCBWR where the whole core oscillation is in phase [26].

The PKM was previously derived by assuming that the time dependency of flux is separable from its space and energy dependence.

$$\phi(r,E,t) = n(t)\psi(r,E) \tag{3.1}$$

Furthermore, the PKM equations are derived from weighted integration of time-dependent neutron balance equations by choosing proper initial adjoint flux. Two sets of ordinary differential equations ban be obtained for the neutron amplitude function $n(t)$ and the six group reduced precursor concentration ξ_i as [25]

$$\frac{dn(t)}{dt} = \frac{\rho(t) - \beta}{\Lambda} n(t) + \frac{1}{\Lambda} \sum_{i=1}^{6} \lambda_i \xi_i \tag{3.2}$$

$$\frac{d\xi_i(t)}{dt} = -\lambda_i \xi_i(t) + \beta_i n(t) \tag{3.3}$$

where β_i is the delayed neutron yield of the i_{th} group, λ_i is the decay constant of i_{th} group reduced precursor, ξ_i is the i_{th} group reduced precursor concentration, $\rho(t)$ is the dynamic reactivity expressed by $(k-1)/k$, and Λ is the neutron generation time.

Reactivity feedback is the phenomenon that occurs when an originally applied reactivity changes the state of the system [25]. As a simple reactivity model to analyze the NMR50 startup transient behavior, the dynamic reactivity $\rho(t)$ can be decomposed into several components:

$$\rho(t) = \rho_{ext}(t) + \rho_{\alpha}(t) + \rho_D(t) \tag{3.4}$$

where

$\rho_{ext}(t)$: reactivity due to control rods or other control elements,

$\rho_{\alpha}(t)$: reactivity due to void fraction change or moderate density change,

$\rho_D(t)$: reactivity due to fuel pellet temperature change or the Doppler effect.

External reactivity due to control rod movement can be calculated from the power ramp excluding the feedback reactivity. The nuclear reactor startup procedure usually takes hours to days, so it belongs to the medium time phenomena in nuclear reactor dynamic analysis. The moderator density change due to void fraction and nuclear fuel temperature change can also affect the reactivity in the reactor. In current startup experiment for the BWR test facility, the void reactivity feedback is the most dominant feedback mechanism compared to the Doppler-reactivity. The Doppler-reactivity becomes important when there are large amplitude power oscillations causing significant fuel temperature change. The two reactivity coefficients are defined by

$$K_{\alpha} = \frac{\partial \rho}{\partial \langle \alpha \rangle} \tag{3.5}$$

$$K_D = \frac{\partial \rho}{\partial \langle T \rangle_p} \tag{3.6}$$

33

where $\langle\alpha\rangle$ is the volume-averaged void fraction, and $\langle T\rangle_p$ is the averaged fuel pellet temperature.

3.2. REACTIVITY CALCULATION

In the simulation of the nuclear-coupled startup transient, the external reactivity can be calculated from the given power ramp. The expression for $\rho(t)$ can be derived from the expression for $n(t)$ by solving the inverse problem of the PKM.

In order to further simply the research, the one group reduced precursor concentration for the delayed neutron source is utilized in PKM with void reactivity.

$$\frac{dn(t)}{dt} = \frac{\rho(t) - \beta}{\Lambda} n(t) + \frac{1}{\Lambda} \bar{\lambda}\xi(t) \tag{3.7}$$

$$\frac{d\xi(t)}{dt} = -\bar{\lambda}\xi(t) + \beta n(t) \tag{3.8}$$

$$\rho(t) = \rho_{ext}(t) + \rho_\alpha(t) \tag{3.9}$$

with the steady state initial conditions:

$$n(0) = n_0 \tag{3.10}$$

$$\xi(0) = \xi_0 = \frac{\beta}{\bar{\lambda}} n_0 \tag{3.11}$$

$$\alpha(0) = \alpha_0 \tag{3.12}$$

$$\rho(0) = 0 \tag{3.13}$$

where $n(t)$ and $\xi(t)$ are neutron and reduced precursor concentration respectively. β is the total delayed neutron yield for six groups

$$\beta = \sum_{i=1}^{6} \beta_i \tag{3.14}$$

and $\bar{\lambda}$ is the one group effective precursor group decay constant defined as follows

$$\frac{1}{\bar{\lambda}} = \frac{1}{\beta} \sum_{i=1}^{6} \frac{\beta_i}{\lambda_i} \tag{3.15}$$

$\bar{\lambda}$ highlights the importance of the long-live precursor groups. This gives accurate results in medium term slow transients such as reactor start-up. And $\rho_{ext}(t)$ is the

external reactivity accounting for the reactivity changes due to the external control elements (such as control rods) intervenes.

Using the initial conditions in Eq. (3.10) to Eq. (3.13), the reduced precursor concentration of Eq. (3.8) can be integrated as follows

$$\xi(t) = \frac{\beta}{\bar{\lambda}} n_0 e^{-\bar{\lambda}t} + \beta \int_0^t n(t') e^{-\bar{\lambda}(t-t')} dt' \tag{3.16}$$

Therefore, by inserting Eq. (3.16) into the first equation of Eq. (3.7), the reactivity for a known power transient $\tilde{n}(t)$ can be determined as

$$\tilde{\rho}(t) = \Lambda \frac{d}{dt}\{\ln[\tilde{n}(t)]\} + \beta\left[1 - \frac{\tilde{n}_0}{\tilde{n}(t)} e^{-\bar{\lambda}t} - \frac{\bar{\lambda}}{\tilde{n}(t)}\int_0^t \tilde{n}(t')e^{-\bar{\lambda}(t-t')}dt'\right] \tag{3.17}$$

Assume the known power transient $\tilde{n}(t)$ can be expressed linearly with time as

$$\tilde{n}(t) = a_1 t + a_0 \tag{3.18}$$

The reactivity in Eq. (3.17) can be calculated as

$$\tilde{\rho}(t) = \beta + \Lambda \frac{a_1}{\tilde{n}(t)} - \frac{\beta}{\tilde{n}(t)}\left[e^{-\bar{\lambda}t}a_0 + (a_1 t - \frac{a_1}{\bar{\lambda}} + a_0) + e^{-\bar{\lambda}t}(\frac{a_1}{\bar{\lambda}} - a_0)\right] \tag{3.19}$$

If the void fraction transient corresponding to the power transient $\tilde{n}(t)$ is given by $\tilde{\alpha}(t)$, the reactivity in Eq. (3.19) represents the sum of the external reactivity and the void reactivity feedback:

$$\tilde{\rho}(t) = \rho_{ext}(t) + \rho_{\tilde{\alpha}}(t) \tag{3.20}$$

Consequently, if the external reactivity insertion in Eq. (3.17) is to be simulated using a known power transient $\tilde{n}(t)$ with the associated void fraction transient $\tilde{\alpha}(t)$, the reactivity in Eq. (3.7) should be evaluated as

$$\rho(t) = \rho_{ext}(t) + \rho_\alpha(t) = \tilde{\rho}(t) - \rho_{\tilde{\alpha}}(t) + \rho_\alpha(t) \tag{3.21}$$

where $\tilde{\rho}(t)$ is given by Eq. (3.17) and the void coefficient $\rho_\alpha(t)$ can be obtained through a perturbation approach with the core simulation. The detailed procedure of generating void coefficients for this study can be found in Section 3.1.2.

4. SCALING AND EXPERIMENTAL FACILITY DESIGN FOR NMR-50

Scaling approach has been widely used not only in nuclear engineering but also in other fields dealing with the fluids movement. An appropriate scaling method can largely simplify the analysis for the prototype, which means smaller size facility, reduced operational pressure, and velocity scale for the model. In this chapter, scaling methods specially used in nuclear engineering will be discussed. The goal of scaling is to make sure that the flow phenomena in the model can reflect what really happens in the prototype. Therefore, the key technique for the scaling analysis is to obtain the appropriate similarity groups between the prototype and the model. Good similarity groups can maintain the similarity in geometry, kinematics, and dynamics between two systems. Generally, two methods are used to get the similarity groups for scaling down the prototype to the model. One is to get the dimensionless parameters from dimensionless field equations; the other is to get dimensionless parameters from dimensionless characteristic equations in frequency domain analysis. The dimensionless parameters can be utilized as similarity groups for the scaling analysis.

4.1. SCALING METHODS

The classification of general scaling methods is given by Ishii and Jones [52] and it is summarized as following:

1. Scaling methods based on Buckingham's π Theorem: This method can solve the dimensionless parameters from the given variables, even if the field equations and physical laws governing the phenomena are unknown. The Buckingham's π Theorem is especially suitable for the scaling analysis of pressure drop, heat transfer, and critical heat flux, where the number of governing parameters is not large.

2. Scaling methods based on field equations: The phenomena of interest can be described by series of field equations including continuity equation, momentum equation and energy equation. The field equations can then be non-dimensionalized by introducing reference value as proper scale for key parameters such as length, area, velocity etc. Similarity groups including geometrical

similarity and physical similarity can be derived from the dimensionless field equations through the order of magnitude analysis. Since a variable could be governed by several different mechanisms, the choosing of proper scale is important and might be complicated.

3. *Scaling methods based on small perturbation analysis:* When a dynamic system is specified by field equations, constitutive equations, boundary conditions and initial conditions, scaling methods can be derived from using small perturbation analysis. A small perturbation is introduced on one variable such as a disturbance in the duct inlet velocity or on multiple variables. Then frequency response function for other variables can be derived from the field equations with constitutive equations, initial conditions, and boundary conditions. The similarity groups can be acquired from dimensionless characteristic equations in frequency transfer equations. Apart from getting the similarity groups, the stable boundary of a dynamic system can be approached from frequency domain analysis.

Ishii et al. [28] developed a three level scaling approach for the design of Purdue University Multi-dimensional Integral Test Assembly (PUMA).

1. *First level (Integral system scaling):* In a BWR type nuclear reactor, various parts might work under both single-phase and two-phase flow conditions. Therefore, the scaling criteria should meet the similarity requirements of single-phase flow and two-phase flow. For single-phase flow, the similarity groups are derived from the integral effects of the local conservation equation of mass, momentum and energy. However, for two-phase flow the similarity groups are obtained from frequency domain analysis or one-dimensional drift flux model.

2. *Second level (Mass and energy inventory and boundary flow scaling):* The second level scaling is especially suitable for the accident analysis for BWR. For example, the water inventory is a very important parameter when LOCA happens. Then the mass flow rate of depressurization valve, inlet flow to Isolation Condensation System (ICS) and equalization line will determine the water level in the core after accidents. Control volume analysis is widely used at this level, which can make sure the parameter in the model can reasonably simulate what happens in the prototype.

3. *Third level (Local phenomena scaling):* There are a lot of local phenomena that happen under accident scenario for BWR, such as pipe break and ADS flow, flashing in chimney, and condensation in the suppression pool etc. For this level, different local phenomena might require different methods corresponding to the

identification of the physical process. Detailed scaling methods can be found in Ishii's report [28].

4.2. SIMILARITY GROUPS

The similarity groups for single-phase flow and two-phase flow have been developed by Ishii and Kataoka [47]. The similarity groups for single-phase flow are based on one-dimensional conservation law, which include Richardson number, friction number, modified Stanton number, time ratio number, heat source number, and Biot number etc. For two-phase flow, important dimensionless groups are derived from one-dimensional drift-flux model or small perturbation analysis, which include phase change number, subcooling number, Froude number, drift-flux number, time ratio number, thermal inertia number, friction number, and orifice number etc. Among them, the phase change number, which is also named as Zuber number, physically scale the amount of heating and phase change, and the subcooling number scale the cooling in the downcomer region.

1. Richardson number: The Richardson number scales the driving force for the single-phase natural circulation.

$$N_{Ri} = \frac{\beta g l_o \Delta T_o}{v_o^2} = \frac{buoyancy}{inertia} \tag{4.1}$$

2. Friction number: The friction number scales the flow resistance including friction and orifice resistance.

$$N_f = (\frac{f l_o}{D} + K)_i = \frac{friction}{inertia} \tag{4.2}$$

3. Modified Stanton number: This number scales the wall convection heat transfer in single-phase flow.

$$N_{St} \equiv \frac{\bar{h}_\infty \xi_h l_o}{\rho_f c_{pf} A_o v_o} = \frac{wall\ convection}{axial\ convection} \tag{4.3}$$

4. Time ratio number: This number scales the heat conduction inside the solid, so it reflects the inside temperature profile.

$$N_T \equiv \frac{\alpha_s l_o}{\delta_s^2 v_o} = \frac{transport\ time}{conduction\ time} \tag{4.4}$$

5. Heat source number: This number scales the heat generation inside the solid in the volumetric heat generation rate.

$$N_q \equiv \frac{q_s''' l_0}{(\rho c)_s v_0 \Delta T_0} = \frac{heat\ source}{axial\ energy\ change} \tag{4.5}$$

6. Biot number: The Biot number scales the ratio of inside heat conduction resistance and surface heat convection resistance.

$$N_{Bi} \equiv \frac{\bar{h}_\infty \delta_s}{k_s} = \frac{conductive\ resistance}{convective\ resistance} \tag{4.6}$$

7. Fourier number: The Fourier number scales the heat transferred from the solid to the energy storage in the solid.

$$N_{Fo} \equiv \frac{\bar{h}_\infty \xi_h l_0}{(\rho c)_s A_s v_0} = \frac{heat\ transferred\ from\ the\ solid}{heat\ stored\ in\ the\ solid} \tag{4.7}$$

8. Zuber number: The Zuber number is also known as phase change number, which is the most important dimensionless parameter governing the phase change in two-phase flow. The denominator of this number stands for the inlet flux of the system, while the numerator indicates the power level of the system.

$$N_{Zu} = \frac{\dot{Q}}{v_o A_o} \frac{\Delta v_{fg}}{\Delta i_{fg}} = q_o''' \frac{l_o}{v_o} \left(\frac{\Delta v_{fg}}{\Delta i_{fg}} \right)$$
$$= \frac{\dot{Q}}{\dot{m}_o} \frac{\Delta \rho}{\rho_g \Delta i_{fg}} \propto \frac{core\ enthalpy\ rise}{latent\ heat} \tag{4.8}$$

9. Subcooling number: The subcooling number scales the inlet subcooling of the heated section. This number actually provides the boundary conditions in the field energy equations.

$$N_{sub} = \Delta i_{sub} \frac{\Delta \rho}{\rho_g \Delta i_{fg}} \propto \frac{core\ inlet\ subcooling}{latent\ heat}$$
$$= \rho_f c_{pf} \Delta T_{sub} \left(\frac{\Delta v_{fg}}{\Delta i_{fg}} \right) \tag{4.9}$$

10. Reynolds number: The Reynolds number scales the ratio of the inertia force and the viscous force. This number can be used to determine the flow pattern, i.e. laminar flow and turbulent flow.

$$N_{Re} = \frac{\rho_f v_o D_e}{\mu_f} = \frac{inertia\ force}{viscous\ force} \tag{4.10}$$

11. Prandtl number: The Prandtl number scales the ratio of momentum transfer and heat transfer. Both this number and the Reynolds number are used to define the Peclet number.

$$N_{Pr} = \frac{\mu_f c_{pf}}{k_f} = \frac{momentum\ diffusivity}{thermal\ diffusivity} \tag{4.11}$$

12. Modified Peclet number:

$$N_{Pe} \equiv \left(\frac{\xi_w}{\xi_h}\right) N_{Re} N_{Pr} = \frac{G c_{pf} D_h}{k_f} \tag{4.12}$$

13. Departure subcooling number: This number is different from the subcooling number in the subcooling item. The departure subcooling is defined at point of the net vapor generation in a heated channel.

$$N_{sub,d} \equiv \Delta i_{sub,d} \frac{\Delta\rho}{\rho_g \Delta i_{fg}} \propto \frac{departure\ subcooling}{latent\ heat}$$

$$= \rho_f c_{pf} \Delta T_{sub,d} \left(\frac{\Delta v_{fg}}{\Delta i_{fg}}\right) \tag{4.13}$$

14. Density ratio number: This number plays an important role on the instability problem under low pressure. This number is a function of the system pressure only.

$$N_\rho \equiv \frac{\rho_g}{\rho_f} = \frac{gas\ density}{liquid\ density} \tag{4.14}$$

15. Drift number: This number scales the relative motion between the phases. Because the relative motion relies on the flow regimes, this number also characterizes the flow regimes.

$$N_d \equiv \frac{\overline{V}_{gj}}{v_o} \propto \frac{drift\ transport}{convective\ transport} \tag{4.15}$$

16. Froude number: The Froude number scales the ratio of gravity and the inertia in both single-phase and two-phase flow.

$$N_{Fr} \equiv \frac{gl_o}{v_o^2} = \frac{gravity}{inertia} \tag{4.16}$$

17. Thermal inertia number: This number scales the energy storage in the solid structure. This number is very important during the transients such as the reactor initial startup.

$$N_{th} \equiv \frac{(\rho c)_s A_s}{\rho_f c_{pf} A_o} = \frac{solid\ heat\ capacity}{liquid\ heat\ capacity} \tag{4.17}$$

In addition to the above introduced dimensionless parameters, several geometrical similarity groups are defined as follows:

$$\text{Length ratio: } L_i \equiv \frac{l_i}{l_o} = \frac{i\text{-}th\ section\ flow\ length}{reference\ length} \tag{4.18}$$

$$\text{Flow area ratio: } A_i \equiv \frac{a_i}{a_o} = \frac{i\text{-}th\ section\ flow\ area}{reference\ area} \tag{4.19}$$

$$\text{Structure area ratio: } A_h \equiv \frac{a_h}{a_o} = \frac{heat\ transfer\ area}{reference\ flow\ area} \tag{4.20}$$

4.3. GENERAL SIMILARITY LAWS

The similarity criteria between two systems can be obtained from the similarity groups and proper constitutive relations. A general scaling ratio between the model and prototype can be defined as follows:

$$\psi_R \equiv \frac{\psi_m}{\psi_p} = \frac{\psi\ in\ the\ model}{\psi\ in\ the\ prototype} \tag{4.21}$$

4.3.1. Single-phase Flow Similarity

Geometrical similarity is the most fundamental requirement between the model and the prototype. Thus, the scaling criteria can be derived from the geometrical groups.

$$\text{Length ratio: } L_{iR} = \left[\frac{l_i}{l_o}\right]_R = 1 \tag{4.22}$$

$$\text{Area ratio: } A_{iR} = \left[\frac{a_i}{a_o}\right]_R = 1 \tag{4.23}$$

$$\left[\sum_i \frac{F_i}{A_i^2}\right]_R = \left[\sum_i \left(\frac{f_i l_i}{d_i} + K_i\right) / \left(\frac{a_i}{a_o}\right)^2\right]_R = 1 \text{ for single-phase flow} \tag{4.24}$$

The hydraulic diameter d_i and the conduction depth δ_i are defined by

$$d_i = 4a_i / \xi_i \text{ and } \delta_i = a_{si} / \xi_i \tag{4.25}$$

where a_i, a_{si}, and ξ_i are the flow cross-sectional area, solid structure cross-sectional area, and wetted perimeter of ith section. For single-phase flow, the reference velocity v_0 in heated section is derived from the steady-state solution by integrating the momentum equation in the loop as follows.

$$v_o = \left[\left(4\beta g q_o''' l_o^2 / \rho_f c_{pf}\right)\left(a_{so} / a_o\right) / \sum_i \left(F_i / A_i^2\right)\right]^{1/3} \tag{4.26}$$

Equation (4.1) through (4.7) govern the similarity criteria for the single-phase flow system. So the following relations can be obtained for two similar systems:

$$(N_{Ri})_R = 1, (N_{St})_R = 1, (N_T)_R = 1, (N_{Bi})_R = 1, and\ (N_q)_R = 1 \tag{4.27}$$

By solving Eq. (4.27), the following similarity requirements should be satisfied:

$$(v_o)_R = \left[\beta q_o''' l_o^2 / (\rho c_p)_s\right]_R^{1/3} \tag{4.28}$$

$$(\delta_i)_R = (\alpha_s l_o / v_o)_R^{1/2} \tag{4.29}$$

$$(d_i)_R = \left[(\rho c)_s / \left(\rho_d c_{pf}\right)\right]_R (\alpha_s l_o / v_o)_R^{1/2} \tag{4.30}$$

4.3.2. Two-phase Flow Similarity

For the two-phase flow, the friction scaling criteria is satisfied with Eqs. (4.31) and (4.32) with other geometrical scaling criteria.

$$\left[\left(\frac{fl}{d}\right)_i\left[\frac{1+x\left(\Delta\rho/\rho_g\right)}{(1+x\Delta\mu/\mu_g)^{0.25}}\right]\bigg/\left(\frac{a_i}{a_o}\right)^2\right]_R=1 \tag{4.31}$$

$$\left[K_i\left[1+x^{3/2}\left(\Delta\rho/\rho_g\right)\right]\bigg/\left(\frac{a_i}{a_o}\right)^2\right]_R=1 \tag{4.32}$$

Equations (4.8) through (4.17) represent the dimensionless parameters governing the two-phase flow. These numbers should be equal between the prototype and model. Hence, the following conditions should be satisfied:

$$(N_{Zu})_R=1,(N_{sub})_R=1,(N_{fl})_R=1,(N_{Fr})_R=1,(N_{th})_R=1,and\,(N_d)_R=1 \tag{4.33}$$

The relation between the N_{Zu} and N_{sub} can be derived from the steady-state energy balance as

$$N_{Zu}-N_{sub}=x_e\frac{\Delta\rho}{\rho_g} \tag{4.34}$$

where x_e is the quality at the exit of the heated section. Considering the similarity of phase change number and subcooling number, the following similarity about exit quality can be obtained

$$\left(x_e\right)_R\left(\frac{\Delta\rho}{\rho_g}\right)_R=1 \tag{4.35}$$

Equation (4.35) indicates that the exit quality should be scaled by the density ratio. By solving the Eq. (4.33), the following similarity requirements for two-phase flow can be obtained:

$$\left(v_o\right)_R=\left(l_o\right)_R^{1/2} \tag{4.36}$$

$$\left(\Delta i_{sub}\right)_R=\left(\frac{\Delta i_{fg}\rho_g}{\Delta\rho}\right)_R \tag{4.37}$$

$$\left(q_0'''\right)_R=\left[(\rho_f\rho_g\Delta i_{fg}/\Delta\rho)(d/\delta)\right]_R\left(l_o\right)_R^{-1/2} \tag{4.38}$$

$$\left(\delta_i\right)_R=\left(l_{oR}\right)^{1/4}\left(\alpha_{sR}\right)^{1/2} \tag{4.39}$$

$$(d_i)_R = \left[(\rho c)_s / (\rho_f c_{pf})\right]_R (l_{oR})^{1/4} (\alpha_{sR})^{1/2} \qquad (4.40)$$

The time scale for the two-phase flow is defined as

$$\tau_R = \left(\frac{l_o}{v_o}\right)_R = \sqrt{l_{oR}} \qquad (4.41)$$

The time scale indicates that the time events for a reduced height system are shortened by a factor of $\sqrt{l_{oR}}$.

Single-phase flow and two-phase flow sometimes exist in a same system. Based on the principle of scaling analysis, similarity groups from both single-phase flow and two-phase flow should be satisfied, which is actually very difficult to get realized. It is important to point out that the geometrical similarity requirements become the same if the Eq. (4.36) is used in the single-phase geometrical similarity requirements. Kocamustafaogullari and Ishii [53] discussed this issue and proposed two alternatives. One method is time scale simulation, and the other is power scale simulation. Time scale simulation imposes additional power density ratio for the transition from single-phase flow to two-phase flow, which can be attained by using the same fluid in some cases. However, problems will be met for the time scale simulation in simulating the high pressure system with low pressure system using the same fluid as the prototype. Consequently, the power scale simulation has been recommended for reduced pressure scaling with distortions in the time scale, which can be accounted for the system.

4.4. DESIGN OF IDEALLY SCALED FACILITY

The three-level scaling methodology developed for the NRC and applied for the design of a BWR integral test facility [28] is utilized in this chapter to design a modern well-scaled experimental facility to perform the instability tests for the NMR-50. This practical methodology is important for obtaining justifiable results and ensures that components and conditions are properly simulated. By using the three-level scaling methodology, an ideally scaled facility (ISF) is developed from the NMR-50 without considering any physical constraints. Then an engineering scaled facility (ESF) is designed based on the geometry of the ISF, but the design of ESF takes into account physical limitations and engineering requirements.

Scaling distortions between the ISF and the ESF need to be reduced as much as possible.

4.4.1. Scaling Laws for the ISF

Prototypic pressure scaling scales the model and the prototype under the same pressure using the same fluid (Ishii & Kataoka, 1984). Thus, all the fluid properties can be considered identical for the prototype and the model:

$$\rho_{fR} = \rho_{gR} = \beta_R = c_{pR} = k_R = \mu_R = \Delta i_{fgR} = 1 \tag{4.42}$$

Then the length ratio and the area ratio for the core geometrical scaling are selected based on current core design from a previous test loop [29]. The natural circulation rate (velocity scale), which is defined as the single-phase velocity at the core inlet, can be derived from the Froude number. From the phase change number, the power ratio has the same value as the mass flow rate ratio. Another important number is the hydraulic diameter ratio, which comes from the time ratio number accounting for the transport time over conduction time. Under these scaling ratios, the time scale of events are shortened in the scaled-down ISF by a factor of $L_{o,R}^{1/2}$. Ratios for the ISF prototype pressure scaling are given as follows:

$$\text{Length ratio: } L_{o,R} = \frac{l_{o,ISF}}{l_{o,NMR-50}} = \frac{1}{1.214} \tag{4.43}$$

$$\text{Area ratio: } A_{o,R} = \frac{a_{o,ISF}}{a_{o,NMR-50}} = \frac{1}{1164} \tag{4.44}$$

$$\text{Volume ratio: } V_R = \frac{V_{ISF}}{V_{NMR-50}} = \frac{1}{1413} \tag{4.45}$$

$$\text{Velocity ratio: } u_{o,R} = \frac{u_{o,ISF}}{u_{o,NMR-50}} = \sqrt{L_{o,R}} = \frac{1}{1.1} \tag{4.46}$$

$$\text{Mass flow rate ratio: } \dot{m}_R = \frac{\dot{m}_{ISF}}{\dot{m}_{NMR-50}} = \rho_R u_{o,R} A_{o,R} = \frac{1}{1280} \tag{4.47}$$

$$\text{Power ratio: } q_R = \frac{q_{ISF}}{q_{NMR-50}} = \frac{1}{1280} \tag{4.48}$$

Core hydraulic diameter ratio: $D_R = \dfrac{D_{ISF}}{D_{NMR-50}} = \sqrt{\dfrac{L_{o,R}}{u_{o,R}}} = \dfrac{1}{1.05}$ (4.49)

Time scale: $\tau_R = \dfrac{\tau_{ISF}}{\tau_{NMR-50}} = L_{o,R}^{1/2} = \dfrac{1}{1.1}$ (4.50)

4.4.2. Geometrical Dimensions of the ISF

The design of the ISF is scaled exactly from the NMR-50 design [54] based on the previous scaling analysis without considering any engineering constraints (i.e. the ISF may have a pipe with 10.35 cm hydraulic diameter but area of 0.002 m², even though such a pipe cannot exist). The materials are all identical between the ISF and the NMR-50. Based on this information, the design parameters for the ISF are given in Table 4.1.

Table 4.1 Ideally Scaled Facility Design Characteristics

Design Characteristics	Units	NMR-50	ISF	Ratio (N50/ISF)
Thermal and Hydraulic				
Rated power	MWt	165	0.129	1280
Steam flow rate	kg/h	3.19×10^5	249	1280
Core coolant flow rate	kg/h	2.23×10^6	1742	1280
Feedwater flow rate	kg/h	3.19×10^5	249	1280
Absolute pressure in steam dome	MPa	7.17	7.17	1
Average linear heat generation rate	kW/m	7.8	0.0084	1054
Average heat flux	kW/m^2	203.1	0.19	1054
Core average exit quality	% steam	14.3	14.3	1
Feedwater temperature	℃	215.6	215.6	1
Fuel assembly				
Number of fuel assemblies		256	256	1
Fuel rod array size		10×10	10×10	1
Overall length	cm	170.6	140.5	1.214
Fuel Rods				
Number of fuel rods per assembly		91	91	1
Outside diameter	mm	10.55	10.55	1
Cladding thickness	mm	0.6058	0.6058	1
Cladding material		Zircaloy-2	Zircaloy-2	

4.4.3. RELAP5 Analysis of the ISF

In order to assure accurate and scalable experimental results, the behavior of the flow in the ISF must be analyzed in detail by RELAP5 simulation to determine if any scaling distortions result from using the scaling ratios mentioned above. To evaluate the hydrodynamic characteristics such as pressure drop and driving head for natural circulation, as well as the power scaling and other criteria, a steady-state RELAP5 analysis is performed at full-power operation. The coolant mass flow rate predicted by RELAP5 analysis of the two systems is shown in Figure 4-1, with the results plotted according to time scale (1/1.1) and mass flow rate ratio (1/1280). As the figure shows, the scaled mass flow rate matches well between the ISF and the NMR-50. Additionally the RELAP5 analysis gives a core exit quality of 14.3% for the ISF, which is identical to the design value for NMR-50 [54].
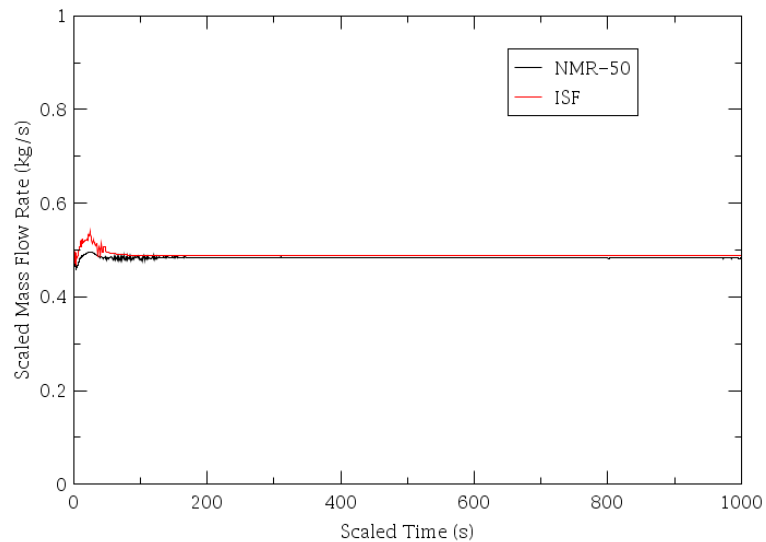
Figure 4-1 Mass Flow Rate of the ISF and the NMR-50 by RELAP5 Analysis

In addition to the steady-state analysis for the ISF, a simulation of the startup transients using RELAP5, with the startup power curve being properly scaled, is performed to evaluate the scaling distortions of the

components related to heat transfer. The mass of the system structure and the initial coolant inventory should be properly scaled by the volume ratio based on energy balance as shown in Table 4.2. During the startup transients, the heat produced by the fuel rods in the core is transferred to the coolant and structure to increase the system pressure. Single-phase natural circulation at low pressure occurs until the coolant reaches the saturated condition in the core. Then steam generation in the core initiates two-phase natural circulation. The system pressure increases due to coolant thermal expansion and net vapor generation rate in the reactor dome. The detailed startup procedure for the NMR-50 is similar to that of the SBWR-600 design [27] and the startup power ramp rate is given in Figure 4-2. For benchmarking the scaling distortions, the same power ramp is used to simulate the startup transient in the ISF.

Table 4.2 Wall Thickness of Heat Structure (Unit: mm)

Components	NMR-50	ISF	Ratio (N50/ISF)
Core fuel can	2.5	0.07	34
Fuel cladding	0.8	0.02	34
Chimney partition	9.0	0.27	34
Standpipe wall	3.4	0.10	34
Separator wall	3.1	0.09	34
Dryer skirt	7.0	0.21	34
Dryer wall	5.0	0.15	34
Upper-Head	147.0	4.32	34
Chimney/Upper DC Wall	50.0	1.47	34
Lower DC wall area	50.0	1.47	34
Bottom-Head	147.0	4.32	34
CRD housing tubes	13.0	0.38	34
Vessel wall	89.0	2.62	34
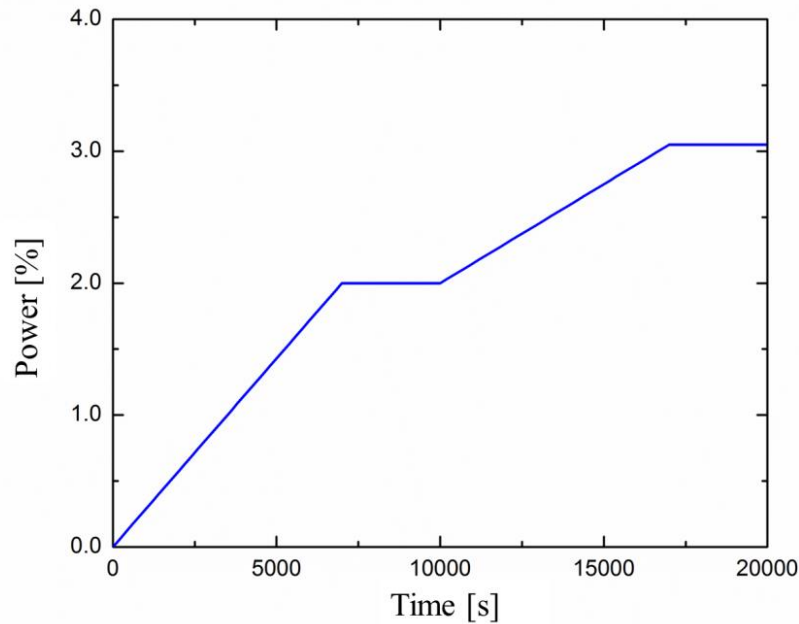
Figure 4-2 Startup Power Ramp.

Figure 4-3 and Figure 4-4 present the important results of the startup analysis for the ISF. The time and mass flow rate for the NMR-50 prediction are scaled by the time scale (1/1.1) and mass flow rate ratio (1/1280). The ISF startup RELAP5 analysis uses full pressure scaling, so no scaling adjustment of the pressure is needed. As can be seen in Figure 4-3, the pressure responses in the NMR-50 and the ISF under both single-phase and two-phase natural circulation (before 20000 s) have a discrepancy of less than 0.1 %. The pressure spikes during two-phase natural circulation are due to the removal of water during heat-up to control the water level.

The coolant mass flow rate prediction during startup is displayed in Figure 4-4. In the initial phase (0-1000 s), the mass flow rate increase linearly, and then it decreases slightly due to the heat transported to the downcomer, which reduces the driving head. However, the mass flow rate increases gradually because of continuous heat-up from the fuel. Some fluctuations can be seen after 3000 seconds as well as before the whole system fully goes into two-phase natural circulation. In this phase, the coolant in the chimney may still be subcooled. The steam generated in the core could then condense in chimney, which might initiate certain type of flow instability. Later the core inlet subcooling becomes smaller,

51

the two-phase mixture leaving the core is saturated, and the steam generated in the core cannot be condensed. Low pressure density wave oscillations could happen during startup transients for natural circulation system.
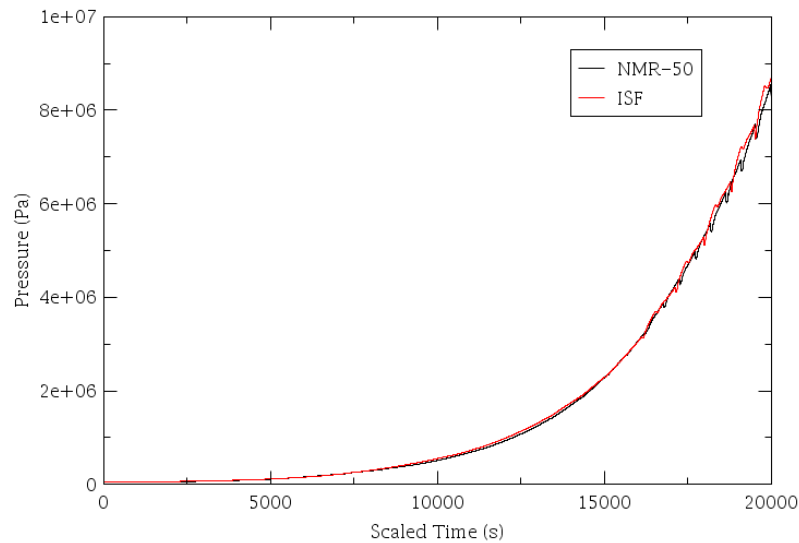
Figure 4-3 Pressure during Startup for the ISF and the NMR-50 by RELAP5 Analysis
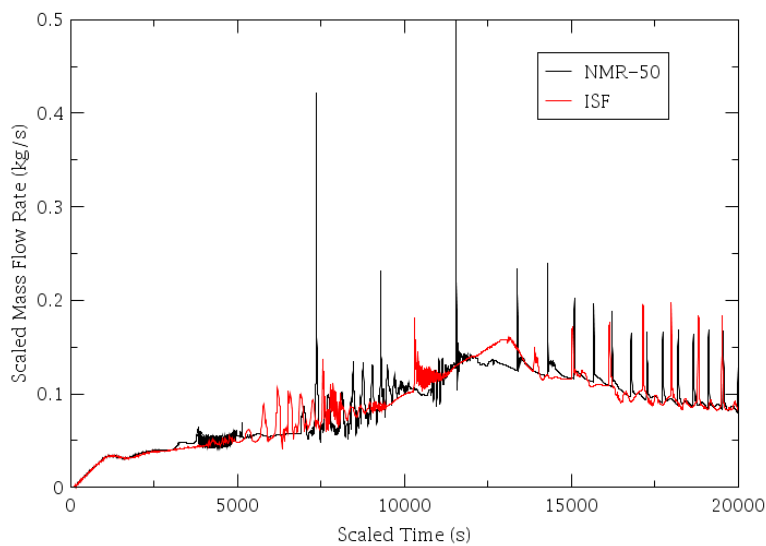
Figure 4-4 Mass Flow Rate during Startup for the ISF and the NMR-50 by RELAP5 Analysis

4.5. DESIGN OF ENGINEERED SCALED FACILITY

4.5.1. Facility Design

While the ISF is a scaling exercise to confirm that the results of the scaled-down facility should be applicable to the full-scale prototype, it is generally not possible to build an exactly ideally scaled facility. Thus, the Engineered Scaled Facility (ESF) is built based on the scaling of the ISF, but it uses components that can actually be obtained or constructed. In general, the scaling ratios for the ESF are identical to those for the ISF with some unavoidable distortions due to engineering considerations. For instance, the engineering facility uses four larger electric heated rods to simulate the fuel assembly in the core region, since it is impossible to construct a small-scale reactor core with thousands of heater rods with diameters on the order of a few microns.

4.5.2. Separator/Dryer Assembly Design

In addition, the steam separator and dryer assembly cannot realistically be scaled down exactly for the ESF. The steam separator assembly, located directly above the chimney shroud, is designed to efficiently remove entrained water from the steam-water mixture entering the separators. This provides moist steam to the dryer assembly, which then undergoes additional separation to provide dry steam for the turbine generators. The pressure drop scaling across the separator has been detailed for the separator used in the PUMA facility at TRSL [28]. However, for the ESF a simpler procedure of direct flow area scaling is used. According to the flow area scaling ratio, the standpipe flow area for ESF is about 0.0013 m^2. Due to physical and engineering limitations, only one thin-wall tube of 1-1/2 inch nominal size is used for the ESF separator tubes.

The ESF steam separator design is based on flow area similarity with the NMR-50 separator assembly. Therefore, the elevation of the first level of pick-off ring openings in the NMR-50 stand pipes must be scaled for the ESF based on the length scaling. In the case of significant water inventory swelling in the downcomer region, these openings will be the first access points for water to flow back into the standpipes and down into the chimney region. To simulate this, holes can be made in the ESF separator tube walls. The elevation of these holes is based

on length scaling of the elevation given for the lowest level of pick-off ring openings in the NMR-50 standpipes.

In order for water collected on the upper steam separator plate to drain back down through skimmer tube, a single vertical tube is connected beneath the upper steam separator plate. The length of the tube is based on length scaling so that its bottom end is positioned accurately with respect to the nominal water level.

Figure 4-5 shows the ESF separator engineering design. The outermost pipe simulates the upper vessel wall of NMR-50. A smaller pipe inside the vessel wall acts as the dryer skirt with openings at the bottom. Inside the dryer skirt, there is one separator tube with 4 holes at the top representing the pick off rings. The second stage of the separator contains two pipes on top of the upper separator plate with flow area identical to the single separator tube. The length of the skimmer tube is based on length scaling and the nominal operating water level.
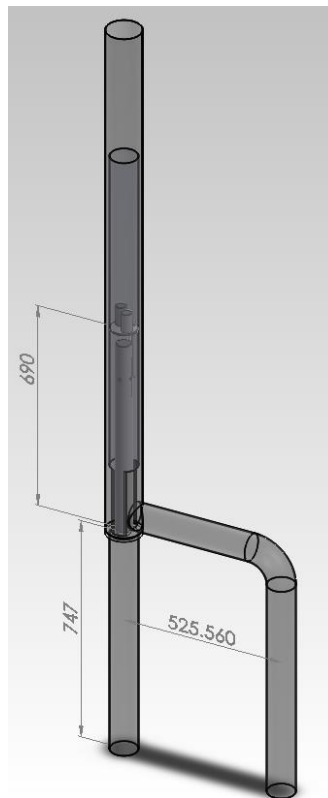
Figure 4-5 ESF Separator Engineering Design (units: mm)

The engineered facility must be built finally to study the flow instability that could happen in the NMR-50 during steady state operation or startup procedure.

Because pipes and other components are not available with arbitrary diameters, commercially available components must be selected for construction. These components should be chosen to minimize the scaling distortions in the ESF. However, some distortions in the flow area and hydraulic diameter of the various components are unavoidable. Detailed design data based on the components selected for the ESF are presented in the DOE annual report [1], along with the values for the NMR-50 and the ISF.

4.5.3. REALP5 Analysis of the ESF

Although some limitations cannot be avoided, the specified natural circulation rate at steady state determined by the scaling analysis must be preserved. This is generally done by adjusting the flow restrictions, as the natural circulation flow rate is dependent on the driving head and the pressure drop in the system. The pressure drop across a flow restriction is given by

$$\Delta P = K \frac{\rho v^2}{2} \qquad (4.51)$$

where K is a factor that depends on the geometrical design of the flow restriction. The pressure drop can therefore be adjusted by modifying the value of K at various locations in the system. For the ESF, the values of K at various locations within the core region are listed in the DOE annual report [1]. The mass flow rate at steady state calculated by RELAP5 analysis of the steady-state behavior of the ESF is shown in Figure 4-6. The results show that if the inlet K factor of ESF is chosen accurately, then the scaled mass flow rate can be obtained exactly for the steady state analysis.
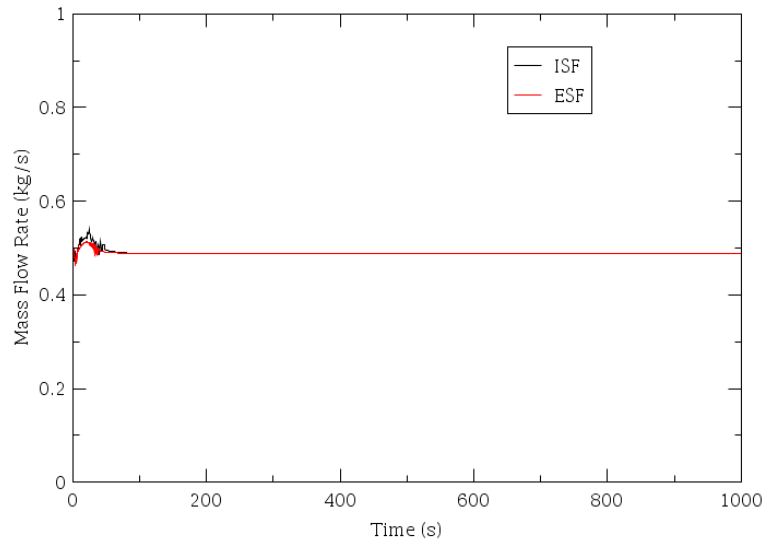
Figure 4-6 Mass Flow Rate of the ESF and the ISF by RELAP5 Analysis

As with the ISF, a startup analysis of the ESF is performed to evaluate the thermal inertia of the system and its transient response characteristics. As the ESF geometry is not exactly identical to the ISF, there might be some discrepancies in the mass of the structure and in the coolant inventory. The comparison of the values important to the heat transfer characteristics is given in Table 4.3. The table shows that the initial coolant inventory in the ESF is a little bigger than in the ISF, and there is much more structural mass in the ESF. The ESF has a much smaller fuel mass than the ISF due to the use of stainless steel heater rods rather than uranium fuel.

In the RELAP5 analysis for the ESF startup transient, the power ramp used is identical to that for the ISF. The pressure during startup for both the ISF and ESF is shown in Figure 4-7. As can be seen, the pressure response is slower in the ESF than in the ISF due to larger initial water inventory and additional structural mass. An analysis of the total energy inventory of the ISF and ESF, based on the heat capacity of the coolant and structure and the masses given in Table 4.3, shows an expected discrepancy of 13% at $t =$17000 seconds. This is due to less production of steam in the ESF, as more energy is required to reach saturation conditions due to the additional mass. The actual discrepancy is 14%, indicating that other scaling distortions have minimal effect. The mass flow rate during startup is shown in

56

Figure 4-8. The mass flow rate is determined by the driving head and the flow resistance. The RELAP5 analysis shows a discrepancy of less than 1% in the initial startup and long-term behavior of the two cases. There is some discrepancy in the oscillatory behavior between 7000 seconds and 14000 seconds, which is likely due to the error in the numerical scheme. However, the scaling implications of these oscillations are small and the results indicate that the dynamic scaling distortions between the ISF and ESF are negligible.

Table 4.3 Comparison of Initial Water Mass and Heat Structure Mass (kg)

	ESF	**ISF**
Initial water inventory	54	52
Structure (except fuel assembly)	84	79
Fuel	15	23
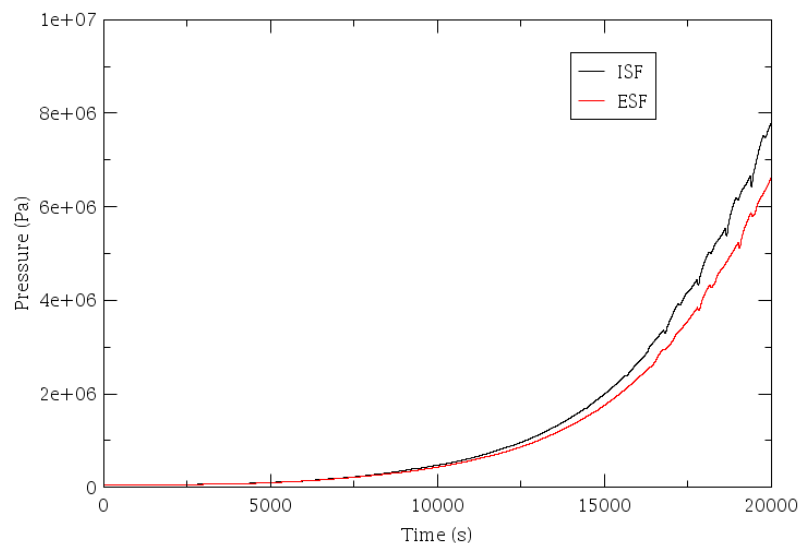
Figure 4-7 Pressure during Startup for the ISF and the ESF by RELAP5 Analysis
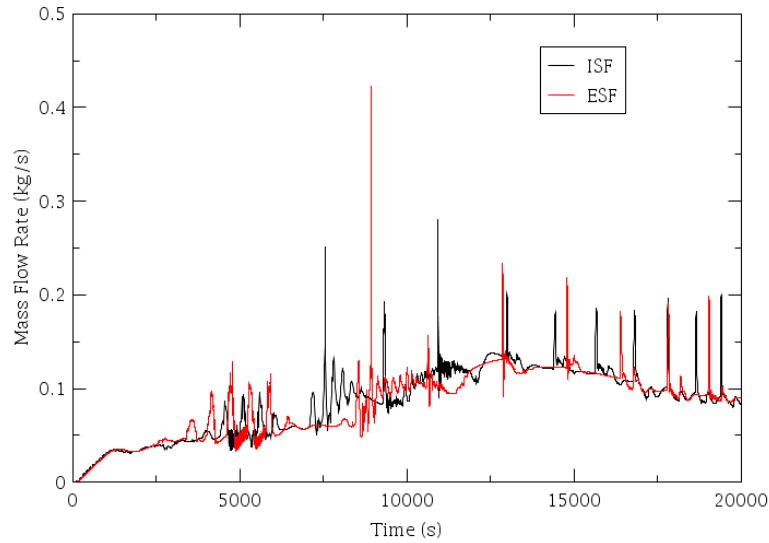
Figure 4-8 Mass Flow Rate during Startup for the ISF and the ESF by RELAP5 Analysis

4.5.4. Discussion on the Scaling Distortions

The ideally scaled facility is free of any scaling distortions based on the scaling analysis. However, the scaling distortions widely exist in the engineered scaled facility due to various limitations of construction. Some scaling distortions can be compensated by other designs, while the others can never be avoided. The scaling distortions of the test facility and influence on the flow instability results for the NMR-50 are summarized in Table 4.4.

Table 4.4 Summary of Scaling Distortions

Scaling Distortions	Cause	Influence on the Results
Design of downcomer using a single tube instead of annular channel	Installment of various instruments in the core section	Minimal impact
Hydraulic diameter of the core	The difference between commercial electric heater rods and reactor fuel assembly	Minimal impact
Mass of structure of pipe connections	Pipe connections using flanges	Minimal impact after temperature compensation
Number of flow channels of the core	Simplified design of the core	More conservative test results
Elimination of the bypass channel in the test facility	Simplified design of the core	More conservative test results

The first three scaling distortions listed in Table 4.4 are very well handled to minimize the impact on the test results. However, test results are expected to be conservative due to the scaling distortions caused by the number of flow channels and elimination of bypass channel. In a BWR, several channels including the bypass channel have different power densities and mass flow rates due to the radial power distribution. Therefore, the flow instability could be less significant on average than that in current experimental test facility.

4.6. EXPERIMENTAL FACILITY

4.6.1. Description of Experimental Facility

A new well-scaled experimental facility is built based on the scaling approach in the previous sections. The detailed schematics of the facilities for the startup transient tests are shown in Figure 4-9. In addition, a picture of the BWR-type natural circulation test facility before insulation is shown in Figure 4-10. The main structure material of this test facility is 304 and 316 stainless steel. The facility includes similar structures as the prototype (NMR-50) such as

1. Lower plenum housing the unheated section of electric heater rods,
2. Core section with four electric heater rods simulating the fuel assembly,
3. Chimney section with a single pipe,
4. Simplified separator and steam dome section, and
5. Downcomer.

As shown in Figure 4-9, the core section has four cartridge heaters with a layout of 2×2. The total length of the heater rod is about 1.3 m with unheated part in both ends and the outer diameter of the rods is 19.05 mm. The total maximum power output of the four electric heater rods are 20 kW, which is controlled by commercial WATLOW SCR power controller with an accuracy of $\pm 0.5\%$ of the power output. The chimney section and downcomer section are simply built with 304 stainless steel pipes available in the market. Moreover, this test facility has two heat exchangers. One is for the degassing to remove noncondensible gases before both startup and quasi-steady tests, while the other is a heat sink for quasi-steady tests, where the steam coming out from the steam dome condenses and is then fed back to the test inlet with the separated water from the downcomer.
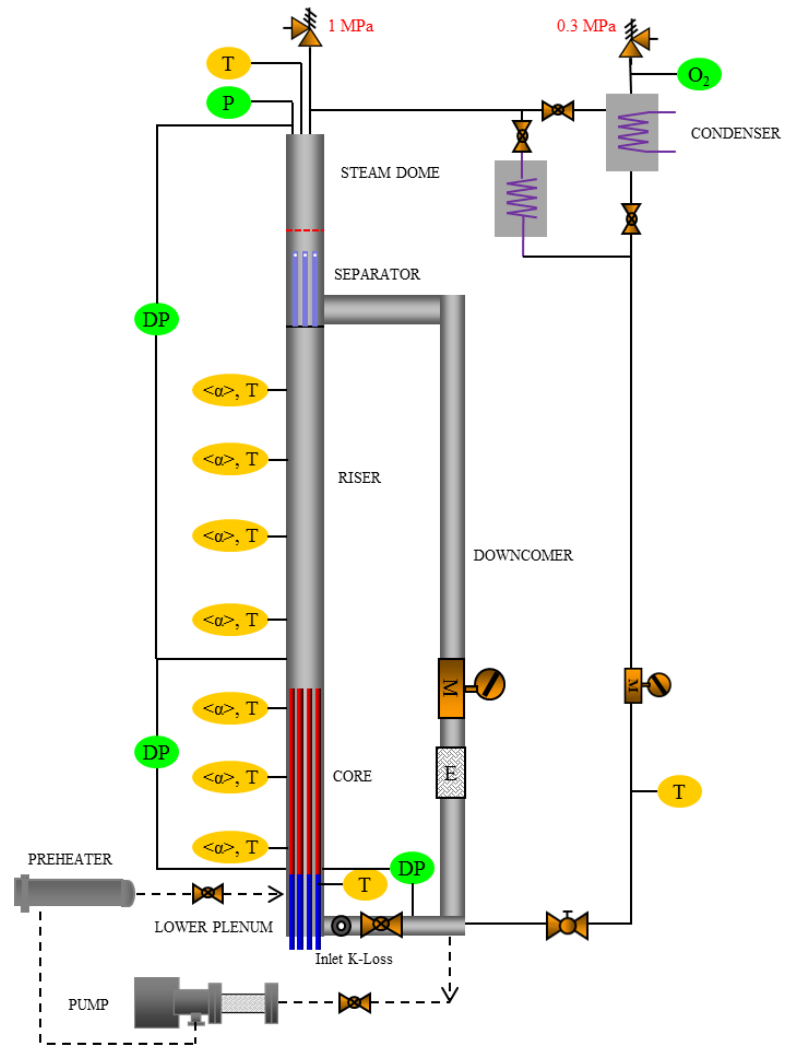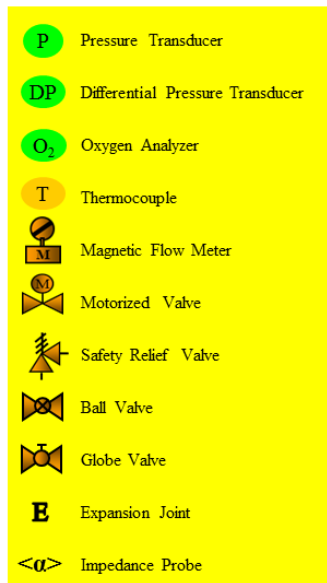
Figure 4-9 Schematic of the Test Facility

Figure 4-10 Natural Circulation Instability Facility before Insulation

4.6.2. Instruments and Data Acquisition System

The new natural circulation test facility is designed to perform startup transient tests and quasi-steady state tests. The determination of flow instability relies on the measurements of various thermal-hydraulic parameters, i.e., absolute pressure,

differential pressure, flow velocity, temperature, and void fraction. As can be seen in Figure 4-9, pressure transducers, magnetic flow meters, thermocouples, and home-made impedance void meters are installed. The detailed introduction and calibration of these instruments have been detailed [26].

Seven instrument ports are installed in the core and chimney to measure different thermal-hydraulic parameters. Two Honeywell pressure transducers are installed at the bottom of the inlet and top of the steam dome, respectively, to measure the system pressure. Three differential pressure (DP) transducers are installed to measure the pressure differences for the following purposes: DP1 measures the inlet loss between the bottom of the downcomer and the core inlet; DP2 measures the pressure difference between the core inlet and core exit; DP3 measures the pressure difference between the chimney inlet and the steam dome. All the HONEYWELL ST3000 Smart Pressure Transmitters 100 series can provide an accuracy of ±0.0375% of the span.

Two Honeywell magnetic flow meters are installed in the downcomer and condensation line to measure the liquid flow rate. The natural circulation rate, which is defined as the single-phase velocity at the core inlet, of the test facility can be measured from the magnetic flow meter in the downcomer section with an accuracy of ±0.5% of the readings. Several T-type thermocouples are embedded in the test section to measure the temperatures at different locations with an uncertainty of 1 ℃. The impedance void meter is a key instrument for void fraction measurements. The void fraction can be obtained by measuring the electrical impedance of two-phase flow [26]. There are three impedance meter probes (IMP01 - IMP03) in the core part, and four (IMP04 - IMP07) in the chimney part. The calibration of the home-made impedance void meters is included in the next section.

Experimental data are acquired from the instruments using a Lab computer and a set of data acquisition system. The data acquisition board is a National Instruments AT-MIO-64E3 with thirteen 5B37 Thermocouple Input Modules and 5B39-01 Current Output Modules [26, 29]. The operation and control of the test facility are realized using LabVIEW for both the startup transient tests and quasi-steady tests. A detailed DAS display in LabVIEW for the thermal hydraulic startup transient test is shown in Figure 4-11. Similarly, the display for the nuclear coupled test is shown inFigure 4-12. The experimental data is saved in a PC during the tests.
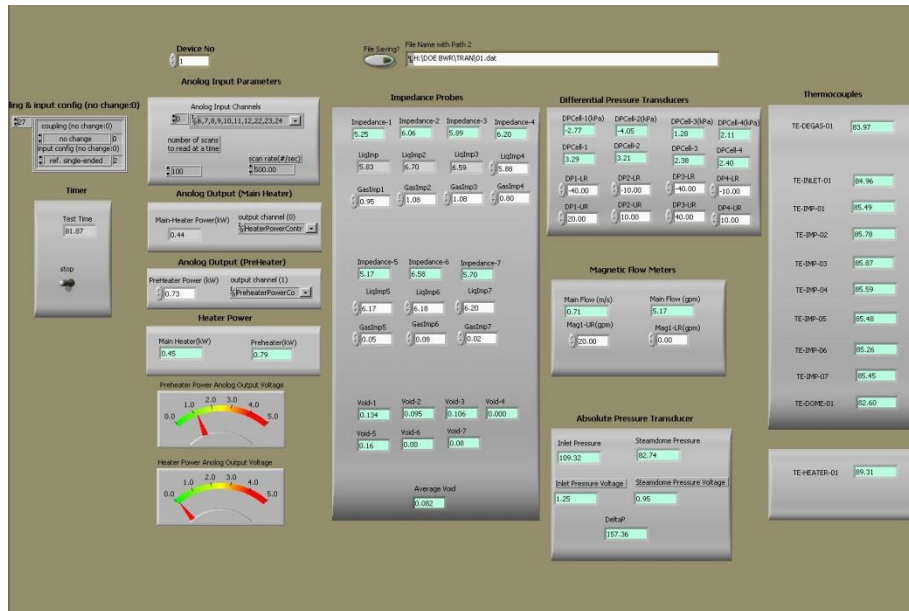
Figure 4-11 Display Panel for the Thermal Hydraulic Test.
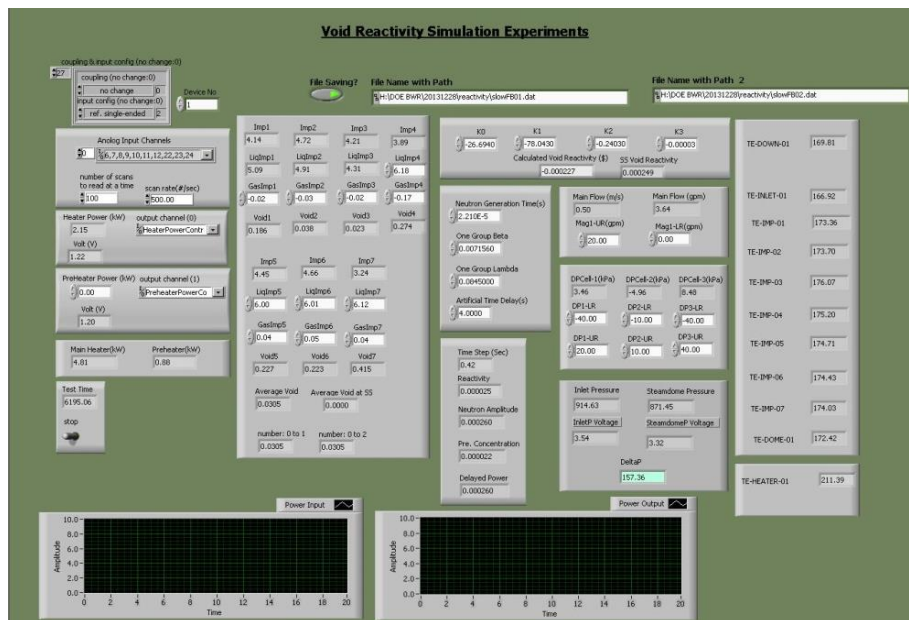
Figure 4-12 Display Panel for the Nuclear Coupled Test.

4.6.3. Calibration of Impedance Void Meter

During the startup transient and quasi-steady tests with nuclear coupling, core void reactivity is a key input for the point kinetics model to calculate the required power output. So the impedance void meter is a key instrument for void fraction

measurements [26, 29]. The home-made impedance void meter generally consists of two major components, i.e., a probe and an electronic circuit. The design of the impedance probe is required to withstand higher temperatures up to 200 °C. For good mechanical and noncorrosive properties, 316 stainless steel is chosen as the material for the impedance electrodes. In addition, Teflon is selected as an electrical insulator between two electrodes, and between the electrodes and outer shell of the probe. Two types of impedance void meter design are used in the current facility to obtain required measuring accuracy. One design in the heated section (core part) uses four heater rods with one stainless steel ring and the partition plate as electrodes as shown in Figure 4-13. The other design for the unheated section (chimney part) uses two stainless steel rings as electrodes as shown in Figure 4-14. The two rings are mounted inside the wall and insulated from each other.

There are three impedance void meters (01- 03 upwards) in the core section, and four (04 - 07 upwards) in the chimney section. Calibration data for each impedance void meter are shown in Figure 4-15 to Figure 4-21. A third order polynomial is used to determine the impedance void meter calibration.
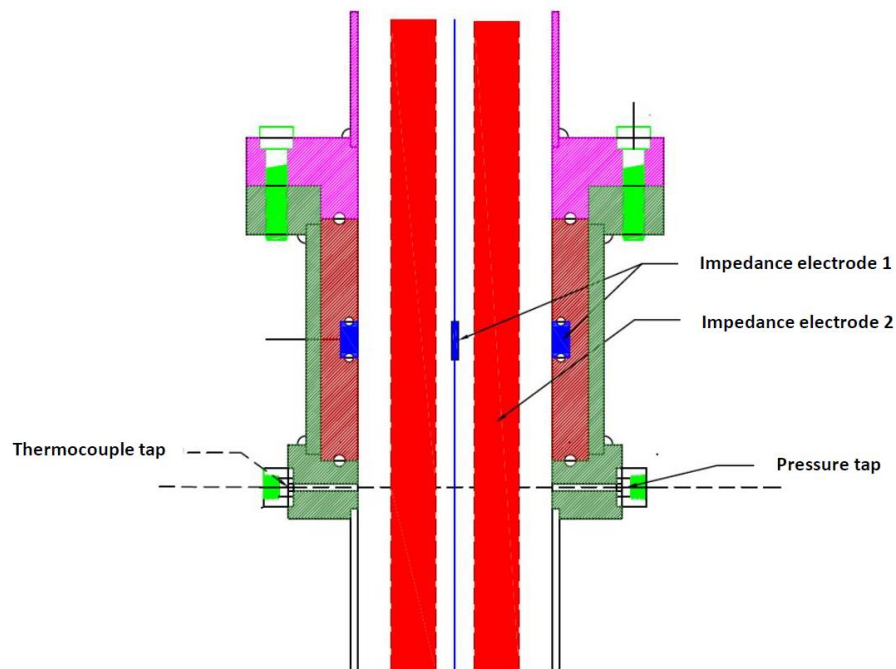
Figure 4-13 Instrumentation Ports on the Heated Section [29]
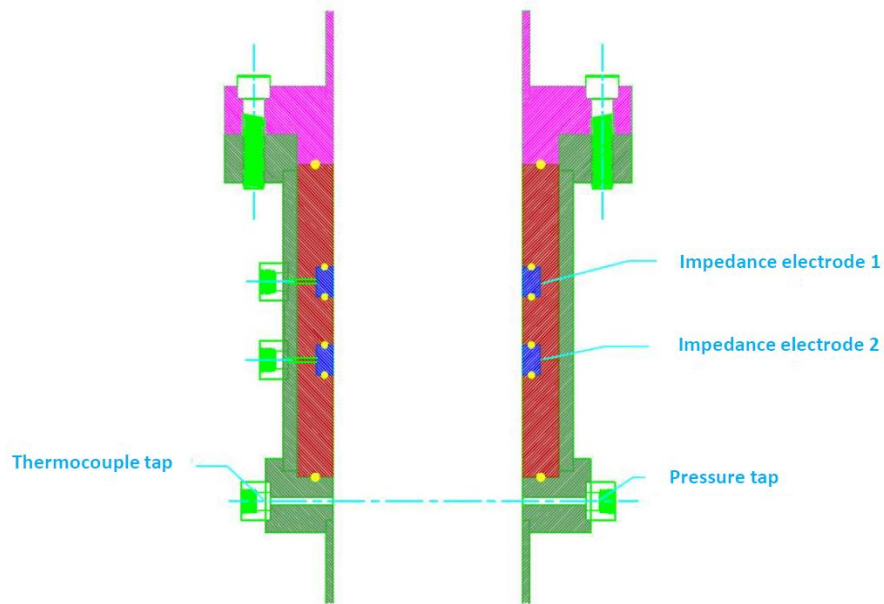
Figure 4-14 Instrumentation Ports on the Unheated Section [29]
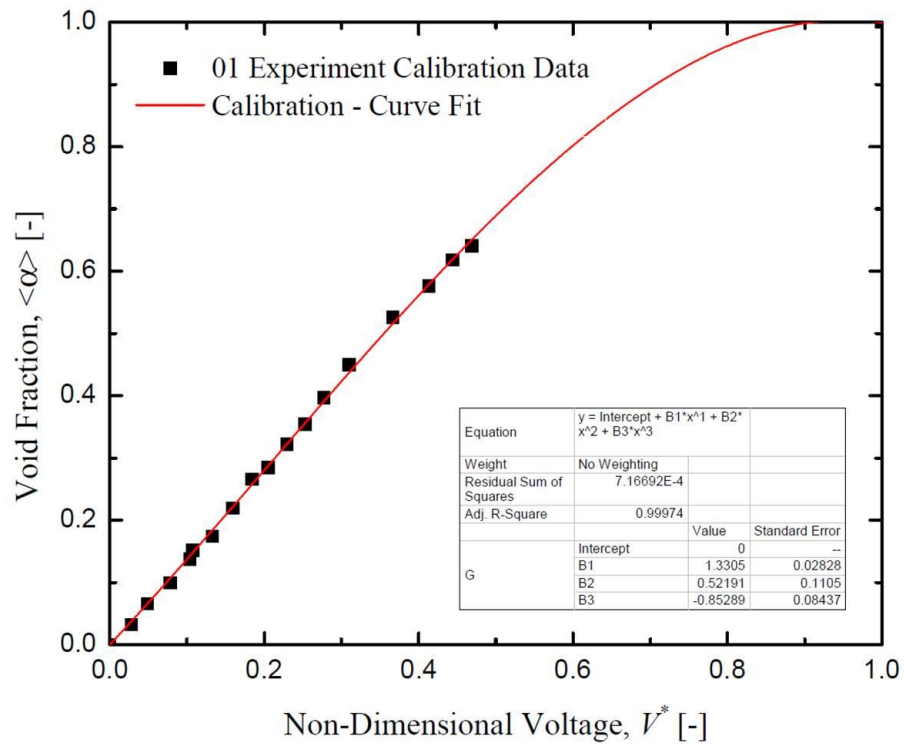
Figure 4-15 Calibration of Impedance Void Meter 01

66
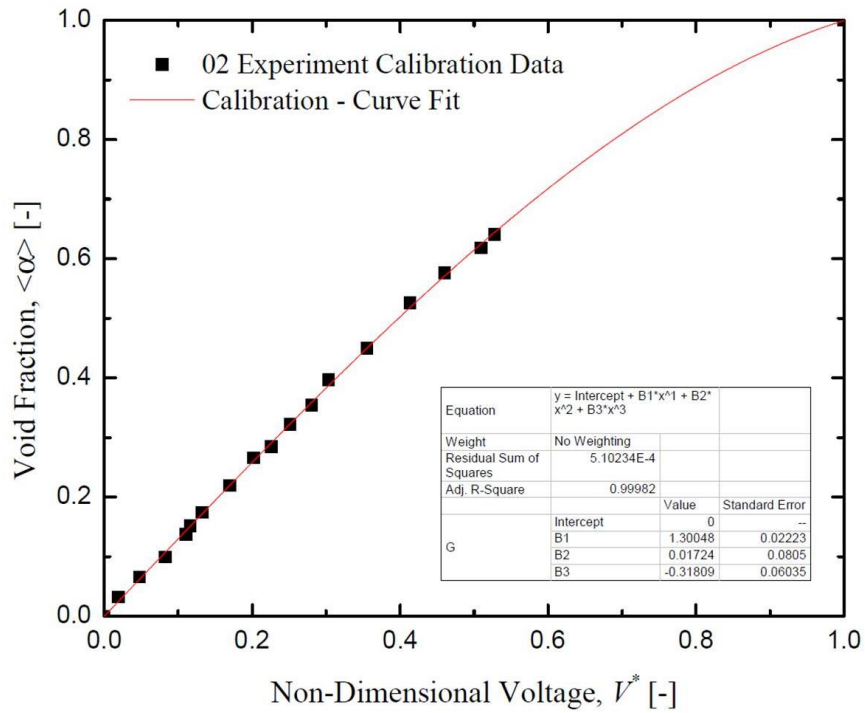
Figure 4-16 Calibration of Impedance Void Meter 02
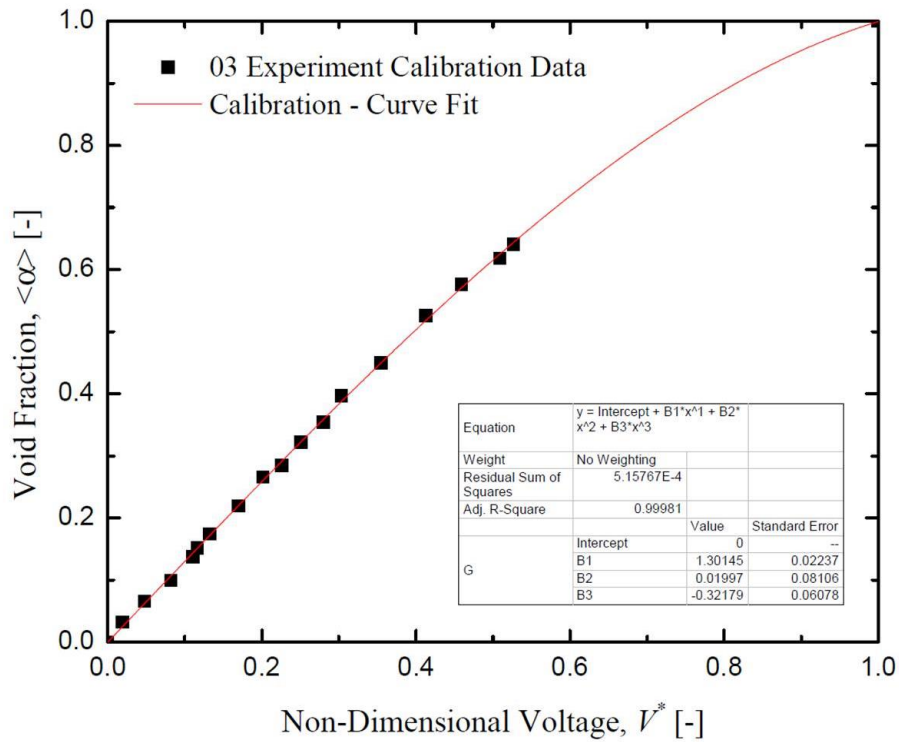
Figure 4-17 Calibration of Impedance Void Meter 03
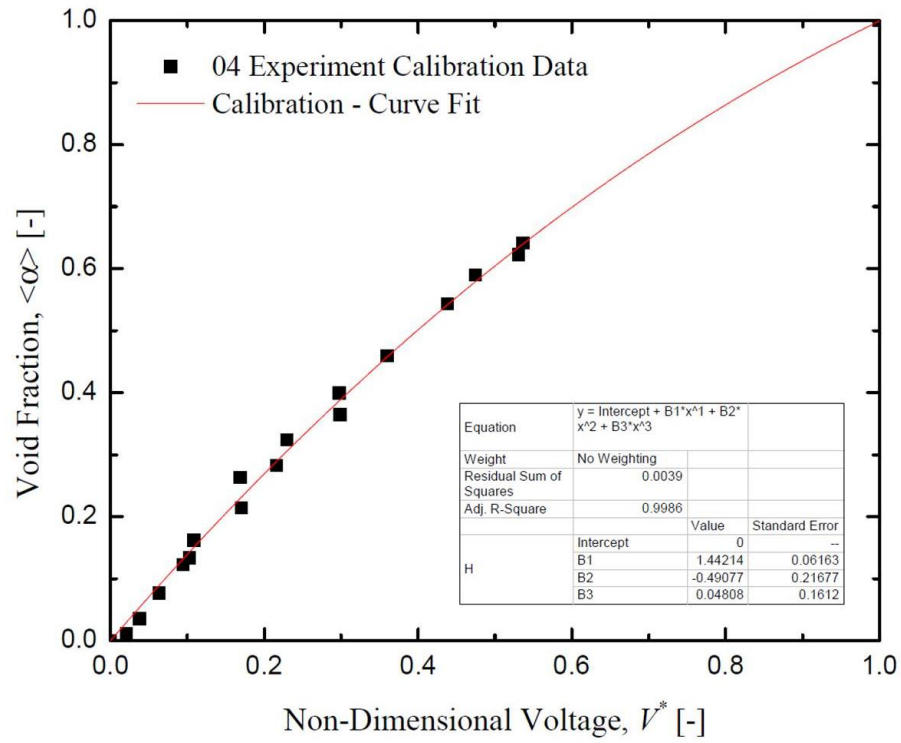
Figure 4-18 Calibration of Impedance Void Meter 04
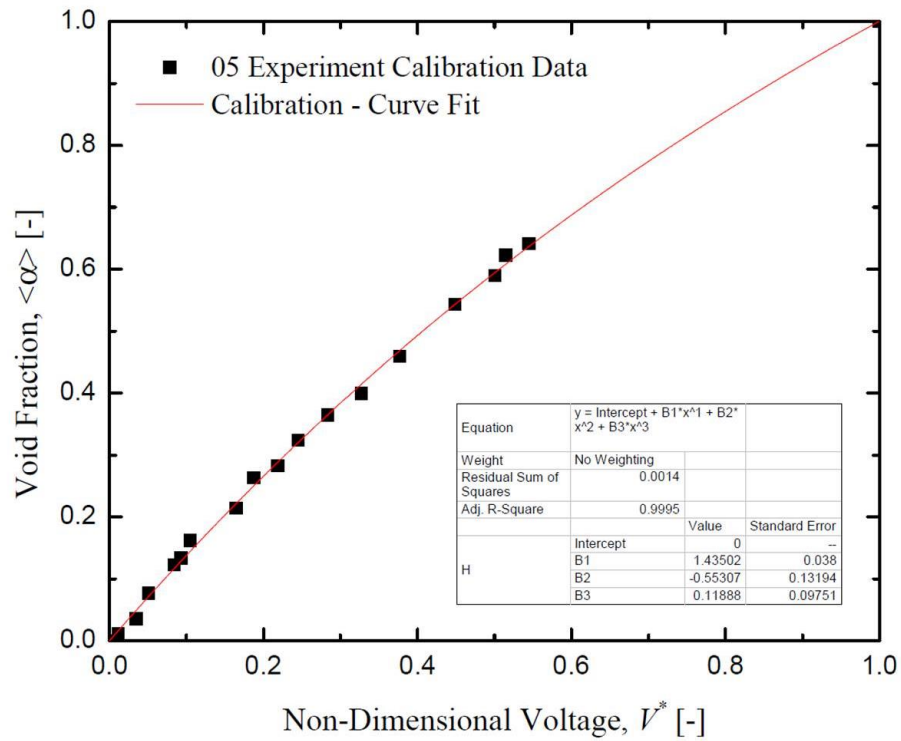
Figure 4-19 Calibration of Impedance Void Meter 05
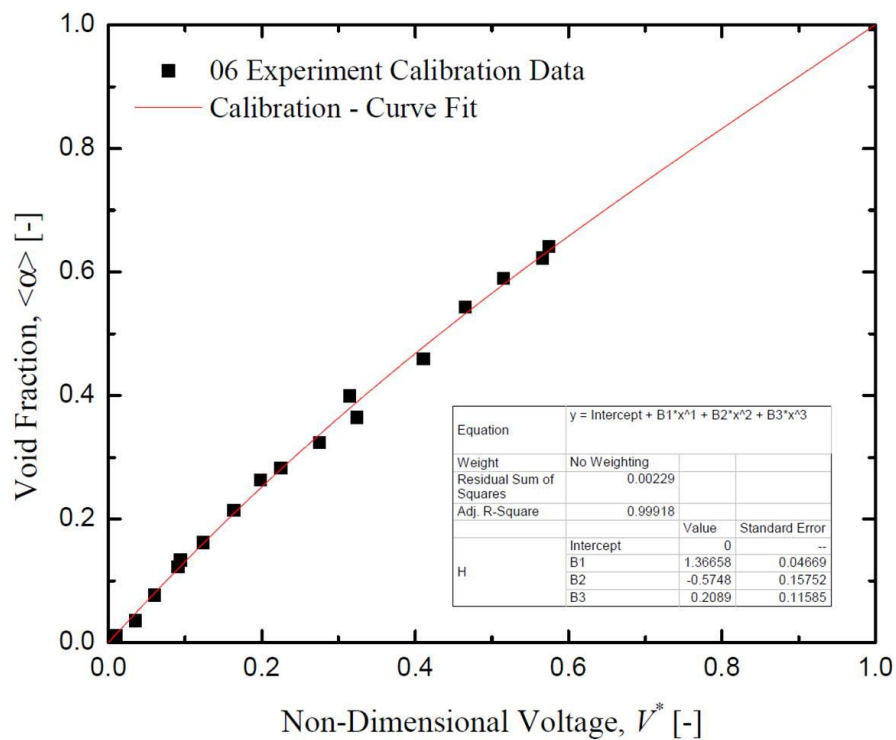
Figure 4-20 Calibration of Impedance Void Meter 06
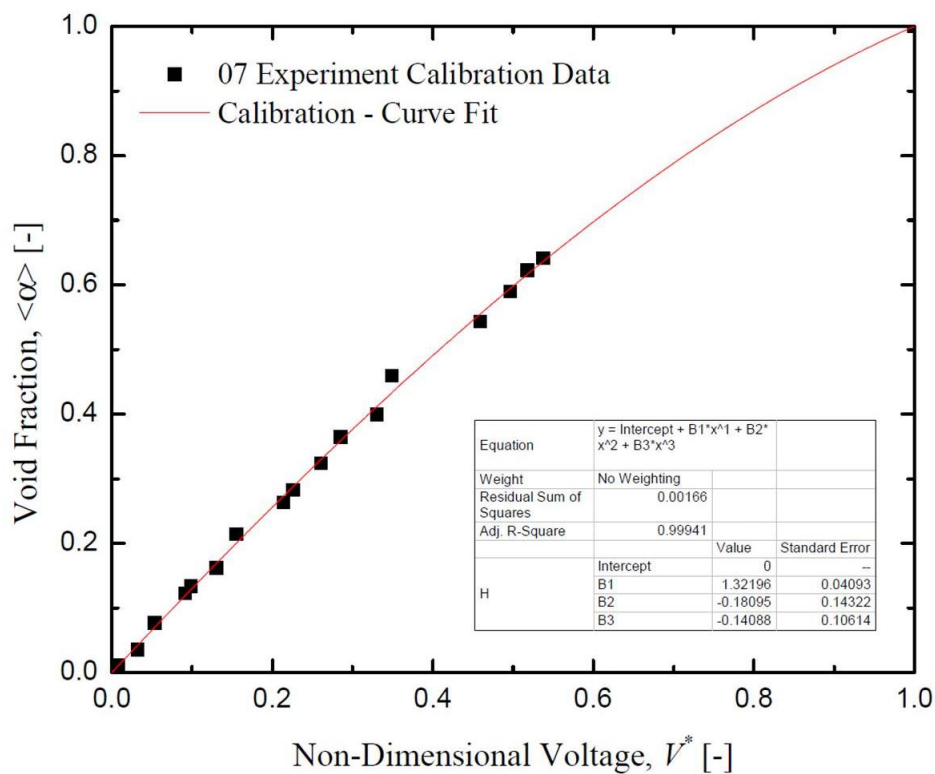
Figure 4-21 Calibration of Impedance Void Meter 07

4.6.4. Calibration of Loop Inlet Loss Coefficient

Another important parameter is the core inlet loss coefficient, which determines the natural circulation rate for the loop. For natural circulation boiling water reactor, most flow resistance is at the inlet of the core. A two inch ball valve and two perforated plates are used to distribute the inlet loss coefficient of the test facility. The loss coefficient range of a ball valve is from 0 to 1500 calculated based on the core flow area. Each thin perforated plate has seven holes with a diameter of about 7 mm and contributes a loss coefficient of 300 calculated based on the core flow area. The total inlet loss coefficient of the facility should be around 1100 based on the scaling analysis [31].

Before the startup transient test, inlet loss coefficient is calibrated by measuring pressure difference and flow rate with HONEYWELL pressure transducers and magnetic flow meter. A protractor is mounted on the panel with the ball valve lever. The inlet loss coefficient is calibrated at Reynolds numbers of 3000 to 15000. Figure 4-22 displays the relation between the inlet loss coefficient and ball valve lever position. As can be seen, the flow resistance increase slowly before 60 degrees and then increases sharply. In order to ensure stability and accuracy of the loss coefficient, the ball valve should be adjusted between 50 and 60 degrees.
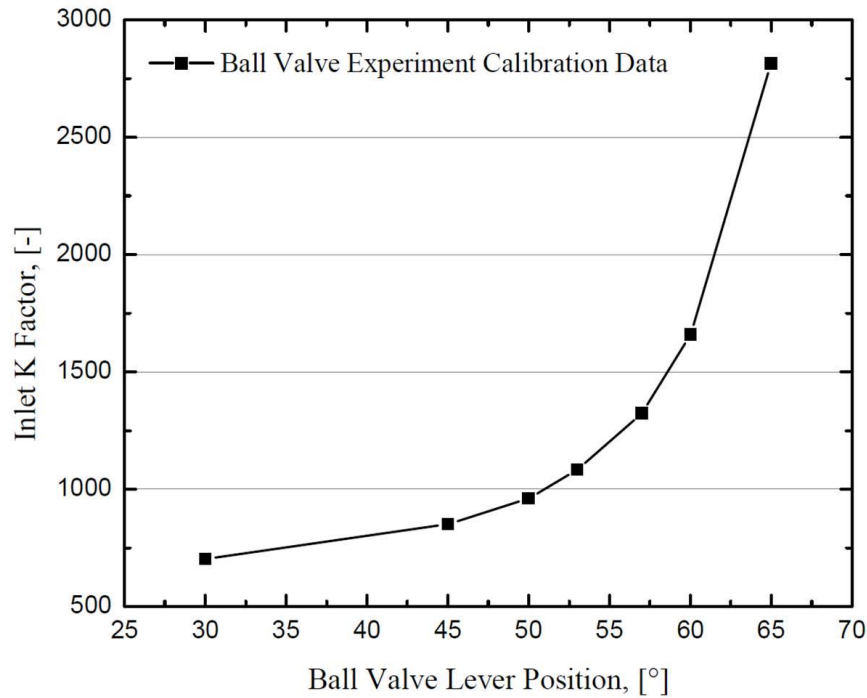
Figure 4-22 Ball Valve Inlet Loss Coefficient Calibration at Re = 8000

The loop inlet flow resistance coefficient can be calibrated by injecting air uniformly to simulate the void fraction of the prototype at steady state operating conditions. Figure 4-23 shows that the liquid velocity measured by the magnetic flow meter increases with the void fraction. The natural circulation rate for the test loop is 0.185 m/s at the average void fraction of 0.43. From ESF Relap5 analysis shown in Figure 4-6 and duplicated in Figure 4-23, 0.18 m/s is the steady state liquid velocity at full power, and the void fraction at the core outlet and chimney are 0.52 and 0.40, respectively. The void fraction distribution is nearly uniform axially during the calibration test, which is different from the void fraction distribution in the real boiling water reactor. However based on the average void fraction in the chimney the error between the RELAP5 analysis and the experimental measurement is only 3%, which means the loop flow resistance is well scaled and simulated.
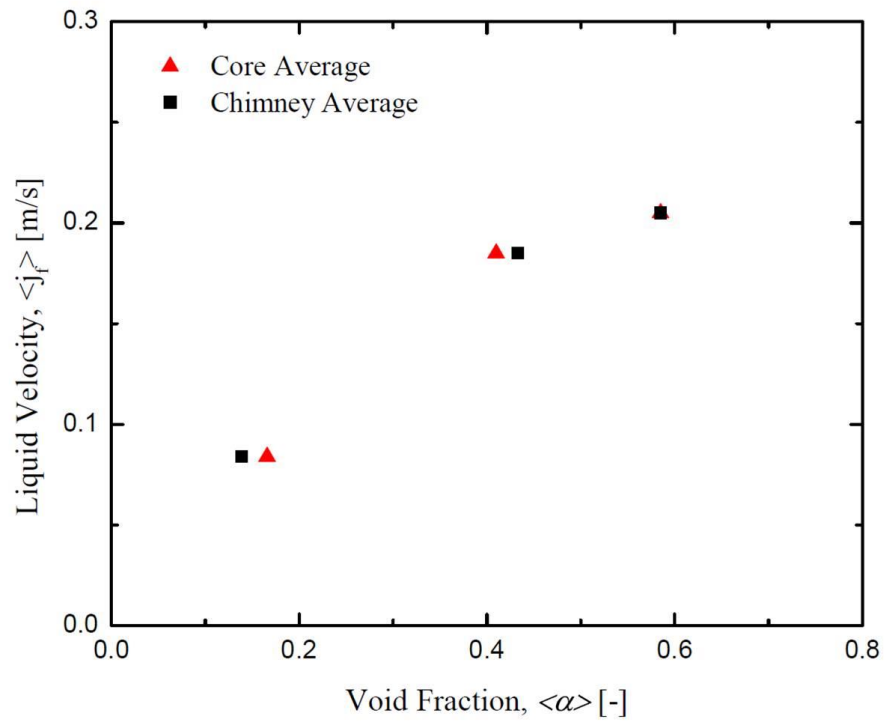
Figure 4-23 Loop Loss Coefficient Calibration with Lever at 56 °
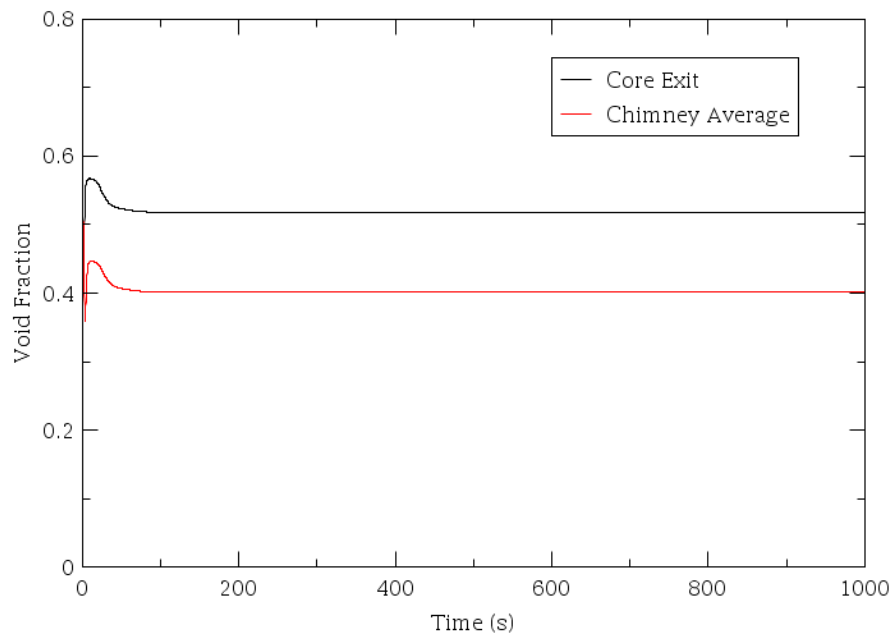
Figure 4-24 ESF Void Fraction RELAP5 Analysis

72

4.6.5. Test Procedures

Startup transient test procedure consists of a degassing procedure and heat-up test procedure. Before each test, general checks are performed. The steps are summarized as follows.

(1) Check all valves positions

(2) Turn on the power for the DPs, P-cells, and impedance circuits

(3) Check differential pressure transducer settings

(4) Purge each differential pressure transducer

(5) Check various instruments

(6) Check the data acquisition system

(7) Set up the initial water level for the degassing procedure

(8) Turn on the power supply for main heater and pump (for degassing)

(9) Remove the noncondensable gases completely by heating the loop to 100 ℃

(10) Separate the degassing tank with the test loop

(11) Set up the initial water level for the startup transient test

(12) Cool the test loop down to 85 ℃

(13) Perform the final valve position for the inlet flow resistance

(14) Check the nuclear constants (for nuclear coupled test)

(15) Start the experiment applying the prescribed power curve

5. EXPERIMENTAL STUDY OF STARTUP TRANSIENT FOR NMR-50

In this section, the experimental results for the startup transients of NMR-50 are presented. Several flow instabilities (i.e. flashing instability, condensation caused instability, and density wave oscillations) can occur during the NCBWR startup transients. Rohatgi et al [27] simulated the startup using RAMONA-4B and therefore divided the startup procedure into four phases related to flow instabilities:

1. Phase Ⅰ - Single phase natural circulation. Control rods are withdrawn in the nuclear reactor plant to increase the power and system pressure. At the beginning of the startup, the steam dome pressure is set at a vacuum of 55 kPa. Due to the height of the chimney, the coolant at the bottom of the core is subcooled. When the subcooled coolant is heated up at the core, the density difference between the riser (core and chimney) and downcomer initiates the single phase natural circulation.

2. Phase Ⅱ - Net vapor generation in the core. During the startup process, the subcooled boiling boundary will move towards the core inlet. Then Net Vapor Generation (NVG) means sustainable bubble concentration in the core. The subcooling along the chimney decreases with the elevation due to bubble condensation in the chimney.

3. Phase Ⅲ- Saturated chimney. The power and pressure continuously increase with the pulling of the control rods. The bubble condensation at the chimney inlet continuously reduces the chimney subcooling. During this phase, both flashing and condensation can occur in the chimney.

4. Phase Ⅳ- Power ascension at full pressure. From phase Ⅱ and Ⅲ, the vapor generated is collected inside the steam dome. The pressure of the steam dome will increase much faster than that in the first phase. The water level is maintained by feedwater flow controller.

5.1.1. Initial and boundary conditions

The thermal hydraulic startup instability experiments without considering the void reactivity feedback are currently performed at two different power ramp rates. The initial conditions can be seen in Table 5.1. The startup transient tests start from about half atmospheric vacuum pressure, which can be obtained by cooling down the test facility after degassing procedure. The initial water level for startup transient is set at 5.85 m, which is close to the first level pick off ring at separator [28]. Two linear power curves in Figure 5-1 are used to test slow heat-up, and fast heat-up thermal hydraulic startup transients.

Table 5.1 Initial conditions for the startup transient

Pressure (kPa)	Coolant Temp. (℃)	Coolant Level (m)	Core Inlet Subcooling (℃)
55	85	5.85	18
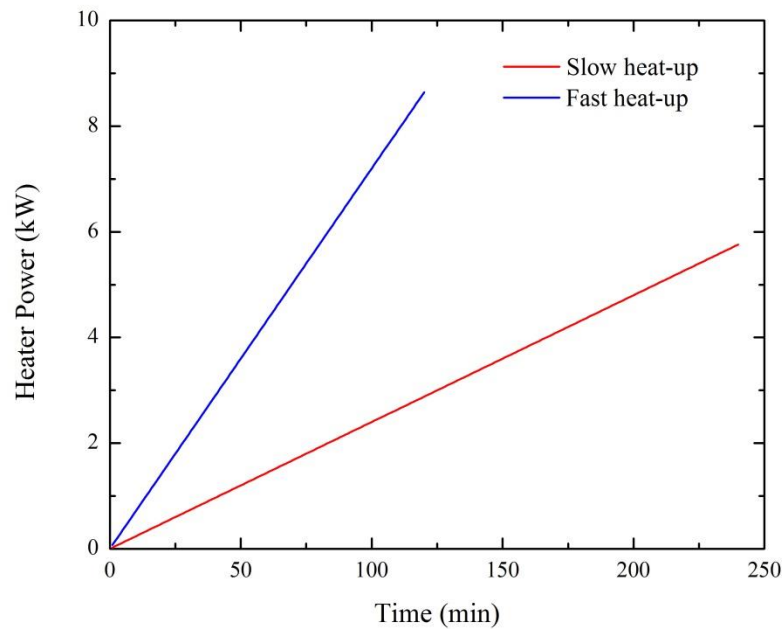
Figure 5-1 Power Curves for Startup Transients

5.1.2. Nuclear-Coupled Simulation

Void reactivity feedback is an influential mechanism to the stability of the natural circulation boiling reactor. However, the moderator density change due to void fraction changes the reactivity in the real reactor. The power ramp is given in the thermal –hydraulic startup tests. From the thermal hydraulic startup transient, the reactivity generated by the control rod movement can be determined by the PKM for certain power ramp. The external reactivity and void reactivity feedback determine the transient behavior of power.

The void reactivity coefficient for NMR-50 at different void condition is obtained by using the reference NMR-50 core design based on CASMO/PARCS code system. The steady state calculations for the reference core are performed with power rate being perturbed at a different level. The core average void and effective eigenvalue associated with different power rate is shown in Table 5.2.

Table 5.2 Core average void fraction and eigenvalue with different power level.

Power rate (%)	α (%)	k-eff
14.3	0.00	1.040491
17.5	1.53	1.038895
20.0	3.28	1.037384
22.5	5.03	1.035934
25.0	6.95	1.034255
30.0	10.49	1.03116
35.0	14.01	1.028007
40.0	17.21	1.025111
45.0	20.10	1.022455
50.0	23.06	1.019754
100.0	42.59	1.001043
150.0	54.60	0.988946

As shown in Table 5.2, the averaged void for the power rate at 14.3% is close to zero, hence the coolant density distribution of this case is assumed to be reference state for the coolant density. The reactivity variation with corresponding

perturbation of the coolant density can be evaluated by PARCS in restart calculation mode. The resulting reactivity variation curve as a function of void (which is related to the corresponding coolant density) is illustrated in Figure 5-2 below. The red dash line in Figure 5-2 is the trend line of the reactivity variation curve obtained by using standard polynomial fitting approach with up to a third order of polynomials. Hence the polynomial form of the reactivity change as a function of the void fraction can be expressed as follows

$$\Delta\rho(\alpha) = -26.694 - 78.043\alpha - 0.2403\alpha^2 - 3\text{E-}05\alpha^3 \quad [\text{pcm}] \tag{5.1}$$
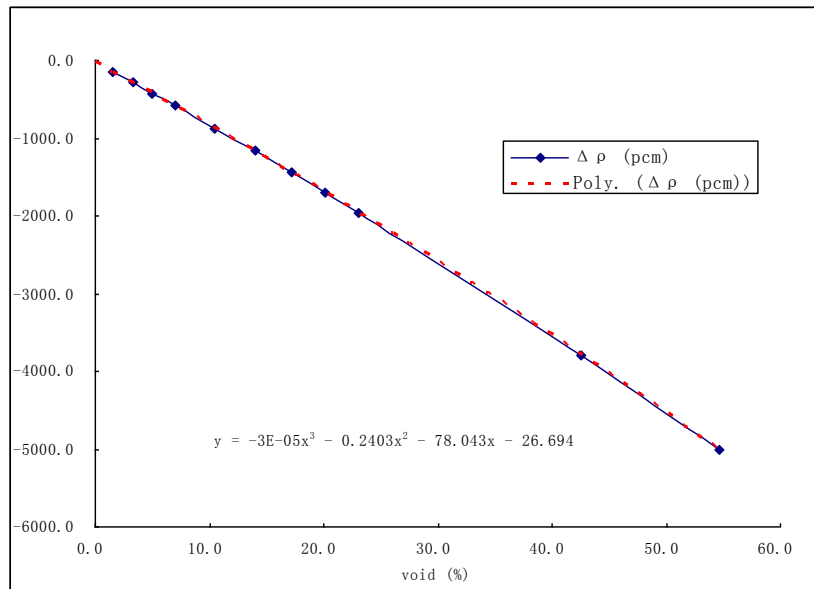
Figure 5-2 The reactivity variation with the change of averaged void in the core at BOC

To obtain the void reactivity change by using the formula in Eq. (5.1), reactivity feedback model in Eq. (3.21) can be written as

$$\rho(t) = \tilde{\rho}(t) + \Delta\rho[\alpha(t)] - \Delta\rho[\tilde{\alpha}(t)] \tag{5.2}$$

where $\tilde{\rho}(t)$ and $\tilde{\alpha}(t)$ are the reactivity and average void fraction for the reference state, which is the startup transients without considering the void reactivity. The second term on the right hand side of Eq. (5.2) is the reactivity change caused by real time core void fraction. The third term on the right hand side is calculated based on the smoothed out $\tilde{\alpha}(t)$ excluding flow oscillations caused by thermal hydraulic instabilities. The polynomial formulation of the reactivity variation due

77

to the void change can be incorporated into the reactivity model. In order to simulate the void reactivity using current test section, volume averaged void fractions measured over the core part are used as an input of the control program, which is compiled using Labview. The one group PKM given by Eq. (3.7) and Eq. (3.8) are solved numerically by assuming the neutron concentration is piece linear, that is

$$n(t) = \frac{n_{i+1} - n_i}{\Delta t}(t - t_i) + n_i \tag{5.3}$$

where Δt is the time step and i is the time index starting from 0. The reduced precursor concentration is given as

$$\xi_{i+1} = \xi_i e^{-\bar{\lambda}\Delta t} + \beta e^{-\bar{\lambda}t_{i+1}} \int_{t_i}^{t_{i+1}} n(t') e^{\bar{\lambda}t'} dt' \tag{5.4}$$

By inserting Eq. (5.3) into Eq. (5.4),

$$\xi_{i+1} = \xi_i e^{-\bar{\lambda}\Delta t} + \beta e^{-\bar{\lambda}t_{i+1}} \left[\frac{n_{i+1} - n_i}{\Delta t} \int_{t_i}^{t_{i+1}} t' e^{\bar{\lambda}t'} dt' + \left(\frac{n_i t_{i+1} - n_{i+1} t_i}{\Delta t} \right) \int_{t_i}^{t_{i+1}} e^{\bar{\lambda}t'} dt' \right] \tag{5.5}$$

The above equation can be re-written as

$$\xi_{i+1} = \xi_i e^{-\bar{\lambda}\Delta t} + \gamma_1 n_{i+1} + \gamma_0 n_i \tag{5.6}$$

where

$$\gamma_1 = \frac{\beta}{\bar{\lambda}} \left(1 - \frac{1}{\bar{\lambda}\Delta t} + \frac{e^{-\bar{\lambda}\Delta t}}{\bar{\lambda}\Delta t} \right), \quad \gamma_0 = \frac{\beta}{\bar{\lambda}} \left(\frac{1}{\bar{\lambda}\Delta t} - e^{-\bar{\lambda}\Delta t} - \frac{e^{-\bar{\lambda}\Delta t}}{\bar{\lambda}\Delta t} \right). \tag{5.7}$$

The time derivative for the neutron concentration in Eq. (3.7) can be treated using the theta method, which is given as

$$\frac{n_{i+1} - n_i}{\Delta t} = \theta R_{i+1} + (1 - \theta) R_i \tag{5.8}$$

where

$$R_{i+1} = \frac{\rho_{i+1} - \beta}{\Lambda} n_{i+1} + \frac{\bar{\lambda}}{\Lambda} \xi_{i+1}$$

$$R_i = \frac{\rho_i - \beta}{\Lambda} n_i + \frac{\bar{\lambda}}{\Lambda} \xi_i \tag{5.9}$$

$$0 \le \theta \le 1$$

Eq. (5.8) is explicit method if $\theta = 0$ and it becomes full implicit Euler scheme if $\theta = 1$. If $\theta = 0.5$, Eq. (5.8) becomes the Crank-Nicholson scheme, which is second-order accurate and permits sufficiently large time step size in most transient

calculations. The theta method is unconditionally stable for $\theta \geq 0.5$. The expression for new time step values for the neutron amplitude can be expressed as

$$n_{i+1} = \frac{\left(\dfrac{1}{\Delta t} + \theta \dfrac{\bar{\lambda}}{\Lambda} \gamma_0 \right) n_i + \left(\theta \dfrac{\bar{\lambda}}{\Lambda} e^{-\bar{\lambda}\Delta t} \right) \xi_i + (1-\theta) R_i}{\dfrac{1}{\Delta t} - \theta \dfrac{\rho_{i+1} - \beta}{\Lambda} - \theta \dfrac{\bar{\lambda}}{\Lambda} \gamma_1} \tag{5.10}$$

5.1.3 Fuel Dynamics Simulation

In order to simulate the effect of void reactivity feedback in nuclear coupled tests, the differences between the electric resistance heaters and typical fuel element must also be considered. As can be seen in Figure 5-3, there are similarities between a SMR fuel element and commercial electric heater rods used in the test facility. Kuran [5] utilized the two-region lumped model to describe the fuel dynamics for both fuel element and electric heater rods in his Ph.D thesis. In a typical electric heater rod, the oxide central region, usually magnesium-oxide, is used for electric insulation. The heating coils are placed near the periphery of this region. The oxide-region is enclosed by a cladding material, which is normally stainless steel or Incoloy.
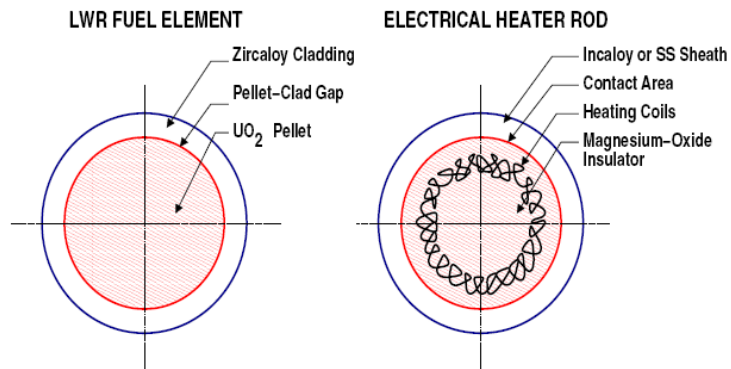
Figure 5-3 Fuel Element and Electric Heater Rod [5].

The fuel time constant, which characterizes the time needed to transfer the heat to the coolant, between the reactor fuel element and electric heater rods is different due to fuel geometry, structure and material. In nuclear coupled test considering the void reactivity feedback, the nuclear concentration for new step is calculated from Eq. (5.10). The similarity criteria for the fuel dynamics between the fuel element and electric heater rods is dominated by the Fourier number [5]. And a delay Eq. (4.11) is needed in addition to the equation for the neutron kinetics when calculating the heater power response in void-reactivity simulation.

$$\tau_{AD} \frac{dn_E(t)}{dt} = n(t) - n_E(t) \tag{5.11}$$

where $n(t)$ is the solution from the point kinetic equations and $n_E(t)$ is the signal which is sent to the heater power controller. The artificial time delay, τ_{AD}, can be determined as

$$\tau_{AD} = [\tau_c]_P \sqrt{l_{oR}} - [\tau_c]_M \tag{5.12}$$

where $\tau_c = \frac{\langle \rho c \rangle_F A_F}{U_{F\infty}}$ is the time constant of the fuel or the heater rod.

Table 5.3 gives the geometrical and thermo-physical information for the NMR-50 fuel elements and the facility electric heaters. The NMR-50 time constant ($[\tau_c]_P$) is about 6.7 seconds under 1000 W/m² of gap conductance [26]. The heater rod time constant ($[\tau_c]_M$) calculated based on the design parameter in the experiment is about 2.13 seconds. The artificial time delay enforced between the heater power and nuclear reactor power will be about 4.0 seconds. That is, τ_{AD} in Eq.(5.12) can be approximately set as 4.0 sec in the nuclear coupled startup transients.

Table 5.3 Geometrical data and thermo-physical properties of the NMR-50 Fuel Element and Facility Heaters

	NMR-50	Facility
Fuel Pellet Outer Radius (mm)	4.585	6.475
Cladding Outer Radius (mm)	5.276	9.475
Number of rods	23,296	4
Pellet Thermal Conductivity (W/m/K)	3.4	45
Cladding Thermal Conductivity (W/m/K)	14.3	13.85

Gap Conductance (W/m^2/K)	Varied	∞

5.2. STARTUP TRANSIENT TEST WITHOUT VOID-REACTIVITY FEEDBACK

5.2.1. Slow Startup Transient Test

The slow heat-up transients are simulated without considering the void reactivity feedback. The power curve tested is given in Figure 5-1. The minimum power of the main heater is 0.8%. Therefore, it takes about 6 minutes before the coolant can get heat from the heater rods under this condition. The initial water level for the startup transients is set at 5.9 m, which is scaled down from that of the NMR-50. The inlet K factor is set based on Relap5 analysis and the experimental calibration.

Figure 5-4 shows the steam dome pressure profile for the slow startup transient. For the initial 50 minutes, the steam dome pressure is pre-saturated and almost constant. The pressure increase in the steam dome is due to heating of coolant in the single phase natural circulation and boiling in the two phase natural circulation respectively. From 50 minutes to 150 minutes, the steam dome pressure begins to escalate with oscillations, which is caused by the flashing in the chimney. After 150 minutes, the steam dome pressure rises exponentially because of continuous vapor generated in two phase natural circulation.

Figure 5-5 shows the temperature profile at different axial locations including core inlet, core exit and the middle of the chimney. The temperature increasing rate is about 25°C/hr. There are about 5 degrees of temperature difference between the core inlet and the core exit. The general temperature profiles for three locations are similar to the steam dome pressure profile except the initial 50 minutes. The heating in the core generates the single phase natural circulation due to density difference. Once the flow is built, the subcooled coolant from downcomer goes into core and brings the temperature down temporarily. The temperature profile at the core exit and the middle of the chimney are important to pay attention to. The temperature oscillation reflects the fluctuation of the natural circulation rate, which can be caused by condensation and flashing in the chimney.

Figure 5-6 demonstrates the time trace of natural circulation rate for the slow startup transient. Combined with the void fraction profile shown from Figure 5-7 to Figure 5-10, the experimental thermal hydraulic startup transients can be divided into the following three phases.

81

1. Single phase natural circulation. The initial stage is from 0 to 100 minutes. At the beginning of the initial stage, there is no loop wise natural circulation due to imposed boundary conditions. Following this, the density difference caused by heating in the core initiates the single phase natural circulation. The thermal driving force and loop flow resistance determines the single phase natural circulation rate. The single phase flow velocity starts to increase at 40 minutes. The coolant is heated in the core and flows upwards into the subcooled chimney. Due to the decrease hydrostatic head along the chimney, coolant vaporizes in the chimney and the flow regime in the chimney is changed. There are several flow velocity oscillations observed from 50 to 100 minutes, which could be caused by the flashing in the chimney. However, these oscillations occur in single phase and are insignificant in amplitude with respect to the flow instability.

2. Net vapor generation phase. The second phase (transition) is from 100 minutes to 160 minutes, which is also the start of boiling. More bubbles in the core can be generated due to decreasing of the core inlet subcooling and increasing power density. As can be seen in Figure 5-6, the two-phase natural circulation has been established already. The average period of velocity fluctuations is about 6 minutes and becomes shorter with higher power density. During this period, the pressure and temperature have the same pattern of oscillations.

The time trace of void fraction at the core exit, chimney inlet, and chimney outlet are shown from Figure 5-7 to Figure 5-10. Due to continuous heating by the heater rods, bubbles are generated in the core and flow upward along the chimney. The bubbles diminish at the chimney inlet due to chimney inlet subcooling. Then, at certain distances from the core exit, the occurrence of flashing in the chimney can be observed from the change of void fraction at different axial locations. The flow regime is transferred from bubbly flow into bigger bubbles by very rapid growth of nucleated bubbles in the core. Similar phenomenon was also found by Lee and Ishii [6] in their Freon-113 loop. However, the slug flow regime was found in the chimney of their test section. The presence of bigger bubbles in the riser (chimney) induces the density difference and increases the natural circulation rate temporarily. Next, significant amounts of subcooled coolant in the downcomer flows into the core and leads to complete or partial suppression of boiling temporarily. The density difference between the riser and the downcomer is reduced so the flow velocity becomes small again. Several instances of flashing in

the chimney will result in a continuous natural circulation rate in the next stage. The fluctuation amplitude becomes smaller and ends at about 160 minutes.

3. Two phase natural circulation. After 160 minutes the oscillations induced by flashing are dampened and flow is stabilized due to less chimney inlet subcooling and increasing system pressure. The natural circulation rate grows smoothly with the increasing power density and void fraction. No flashing instabilities are observed at pressure larger than 0.3 MPa, which is also investigated by Woo [26] and Dixit [29]. However, sinusoidal oscillations are oberved from 170 minutes to 185 minutes, which can be seen from Figure 5-8. The amplitude of these sinusoidal oscillations can be considered as density wave oscillations (DWO) with a peroid of about 45 seconds. The DWO disappers or become negligble after about 190 minutes.

In general, three possible flow instabilitis can occur during the startup transient at low pressure and low power for a natural circulation nuclear reactor. The flashing oscillations can be found in the single phase natural circulation and net vapor generation phase. Furthermore, the flashing in the chimney occurs more frequently with the rising natural circulation rate. Flashing in the chimney can cause intermittent oscillations in the test loop. The condensation at the core exit can cause the flow oscillations in the chimney too. However, it is difficult to distinguish the condensation oscillations from the intermittent oscillations caused by flashing. The DWO is observed in the intial period of two phase flow and becomes negilible soon with the increasing power density and natural circulation rate for the slow startup transient.

Figure 5-4 Steam Dome Pressure for Slow Startup Transient

Figure 5-5 Temperatures for Slow Startup Transient

Figure 5-6 Natural Circulation Rate for Slow Startup Transient

Figure 5-7 Void Fraction at the Core Exit (IMP03) for the Slow Startup Transient

85

Figure 5-8 Detailed Void Fraction at the Core Exit (IMP03) for the Slow Startup Transient

Figure 5-9 Void Fraction at the Chimney Inlet (IMP04) for the Slow Startup Transient

Figure 5-10 Void Fraction at the Chimney Outlet (IMP07) for the Slow Startup Transient

5.2.2. Fast Startup Transient Test

The fast startup transient is simulated without considering the void reactivity feedback. The power curve tested is given in Figure 5-1. The initial and boundary conditions are the same as those in the slow startup transient.

The experimental results for the fast startup thermal-hydraulic are shown from Figure 5-11 to Figure 5-17. The general startup transients observed are similar to what occurs in the slow stratup transients. The three phases are the stable single phase natural circulation, net vapor generation and two phase natural circulation. And the instability behavior observed are the flashing in the single phase natural circulation, intermittent oscillations in the net vapor generation phase, and sinusoidal oscillations in the two phase natural circulation.

Figure 5-11 shows the steamdome pressure for the fast startup transients. The steam dome pressure increases slowly at the beginning and then rises exponentially after boiling starts. It takes about 120 minutes for the steamdome pressure to increase from partial vacuum pressure to 0.7 MPa. From the time trace of temperature demonstrated in Figure 5-12, the temperature increase rate is about 42 ℃ /hr, which is about twice as much as that of slow heat-up transients.

Figure 5-13 displays the natural circulation rate for the fast startup transients. The magnitude of the natural circulation rate for the fast startup transients is 20% larger that that in the slow startup transients. The single phase natural circulation phase is from 0 to 60 minutes with few velocity fluctuations during this phase. This instability is recognized as the flasing instability in the above section. Intermittent oscillations caused by flashing are continuously observed in the net vapor generation phase, which is from 60 minutes to 75 minutes. Compared to the slow startup transients, less oscillations are seen during this phase. The period of flashing oscillations is about 5 minutes, which is also smaller than that of slow heat-up transients because of increased power density. Higher power density during the startup procedure results in less time.

Combined with the void fraction shown in Figure 5-14 and Figure 5-15, density wave instabiliy (DWO) is observed from 85 to 100 minutes, which is in the two phase natural circulation phase. The sinual oscillations with the period of about 40 seconds are density wave instabilities. DWO is strongly related to the core power density and inlet subcooling conditions. So the magnitude of DWO is

larger for the fast startup transients than that in the slow startup transients. The void fraciton in the chimney part are shown in Figure 5-16 and Figure 5-17. As can be seen, void fraction peak means the flashing occur in the chimney.
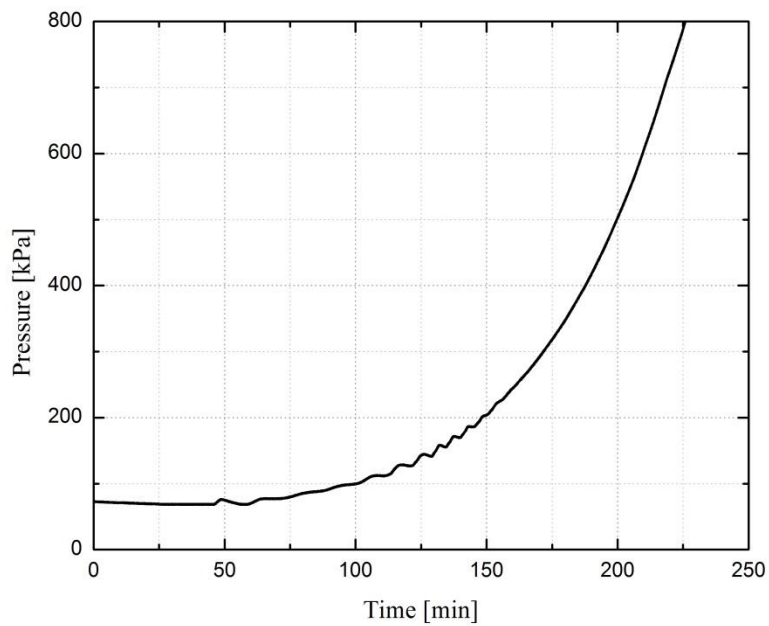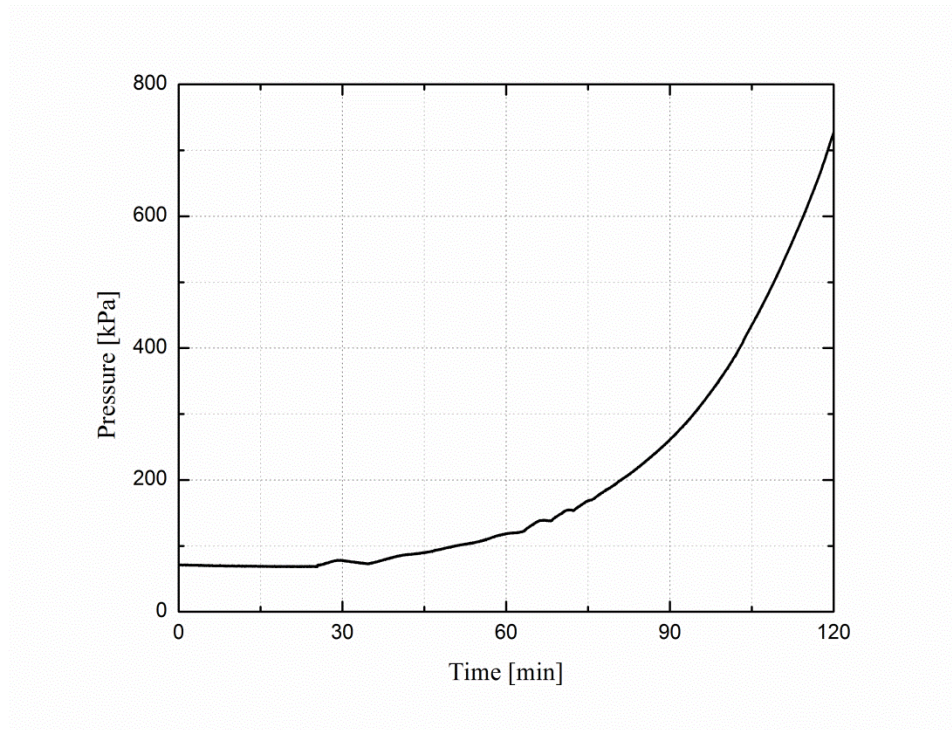

Figure 5-11 Steam Dome Pressure for the Fast Startup Transient
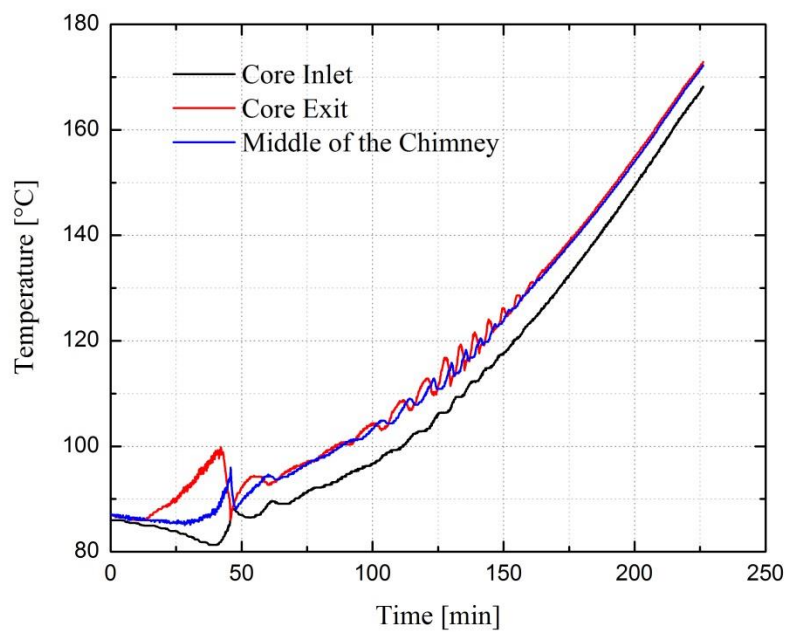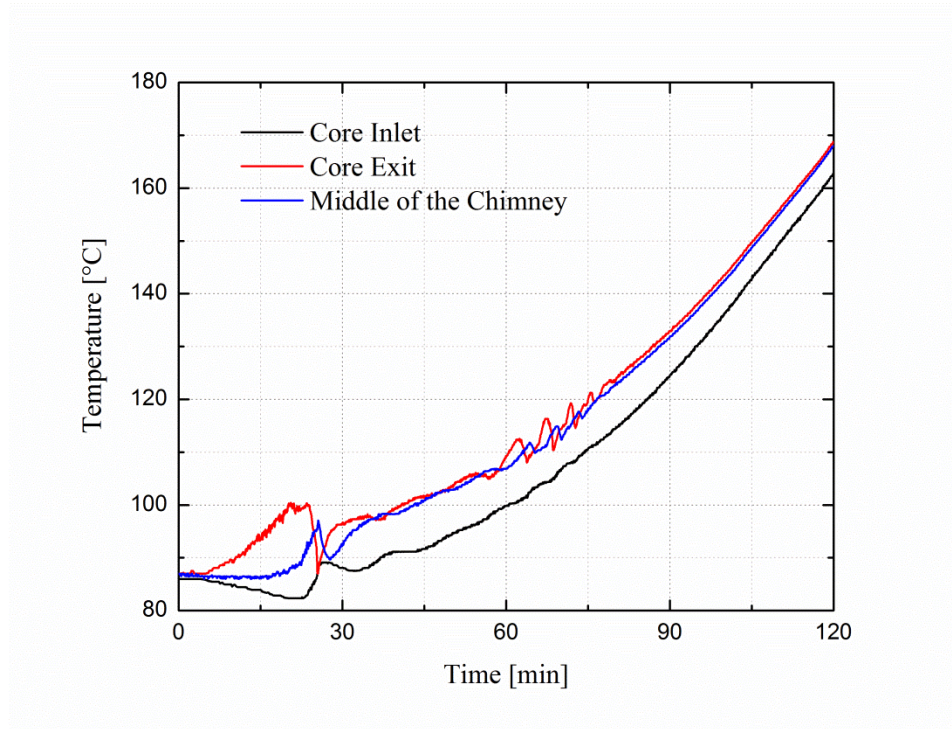
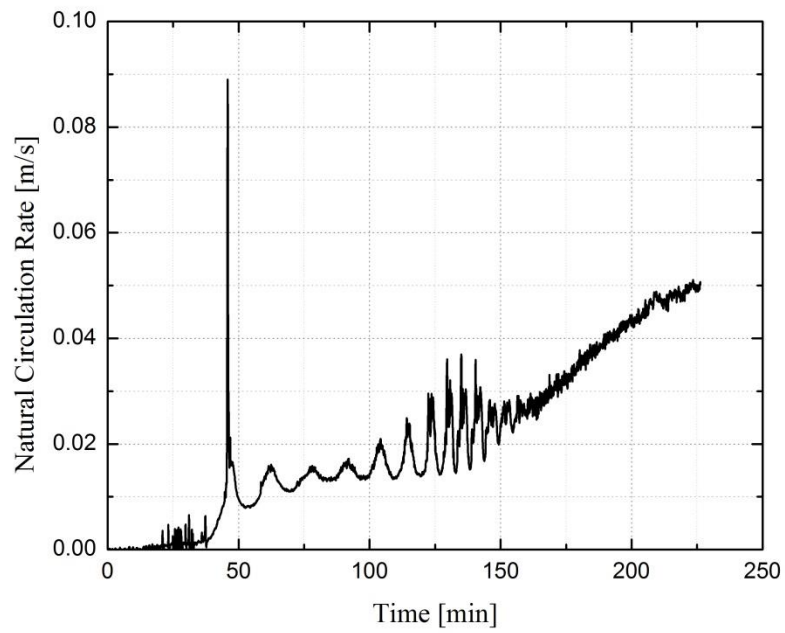*Figure 5-12 Temperatures for the Fast Startup Transient*
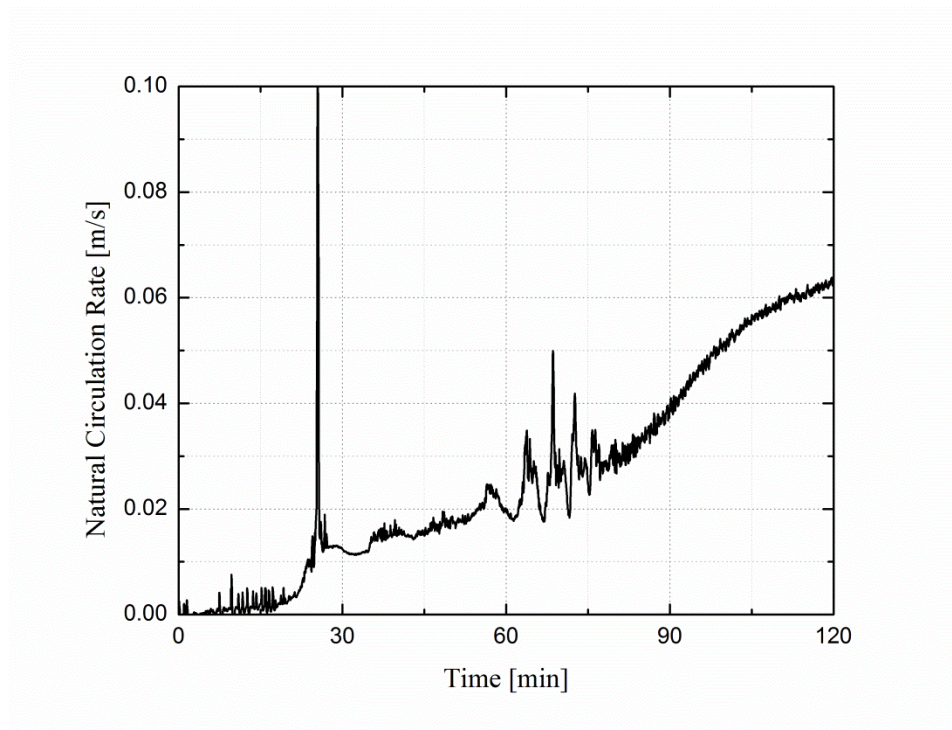
Figure 5-13 Natural Circulation Rate for the Fast Startup Transient
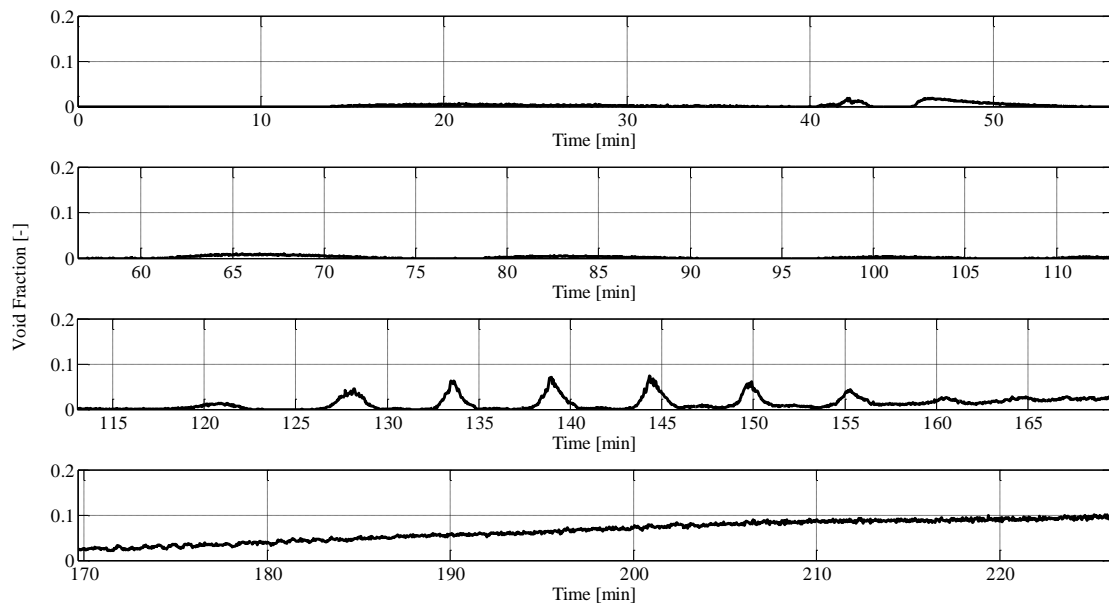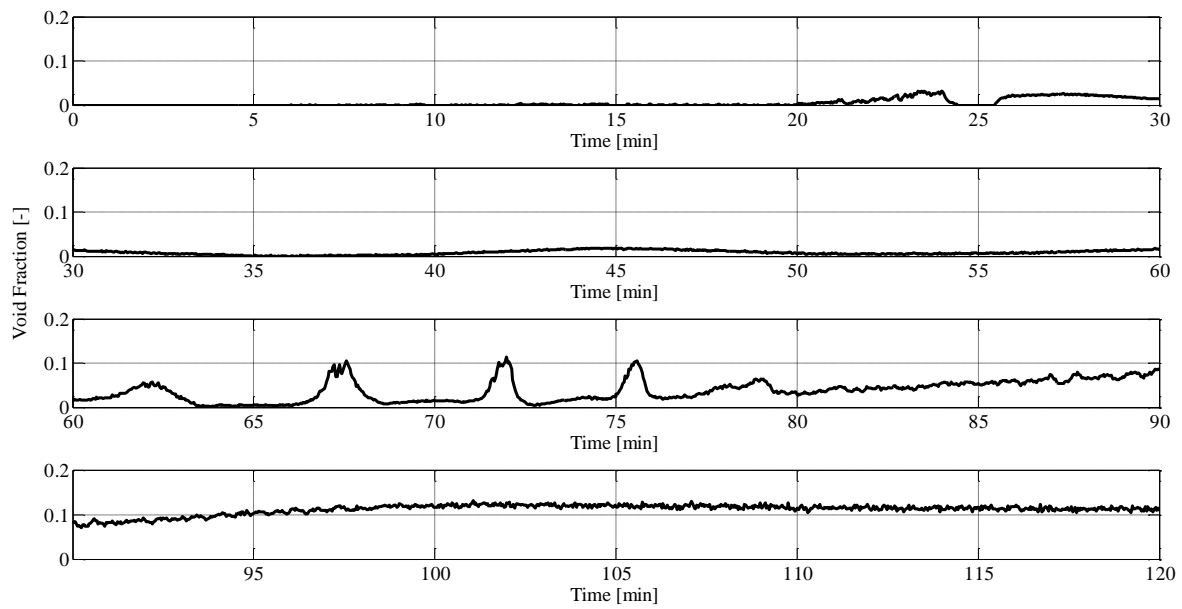
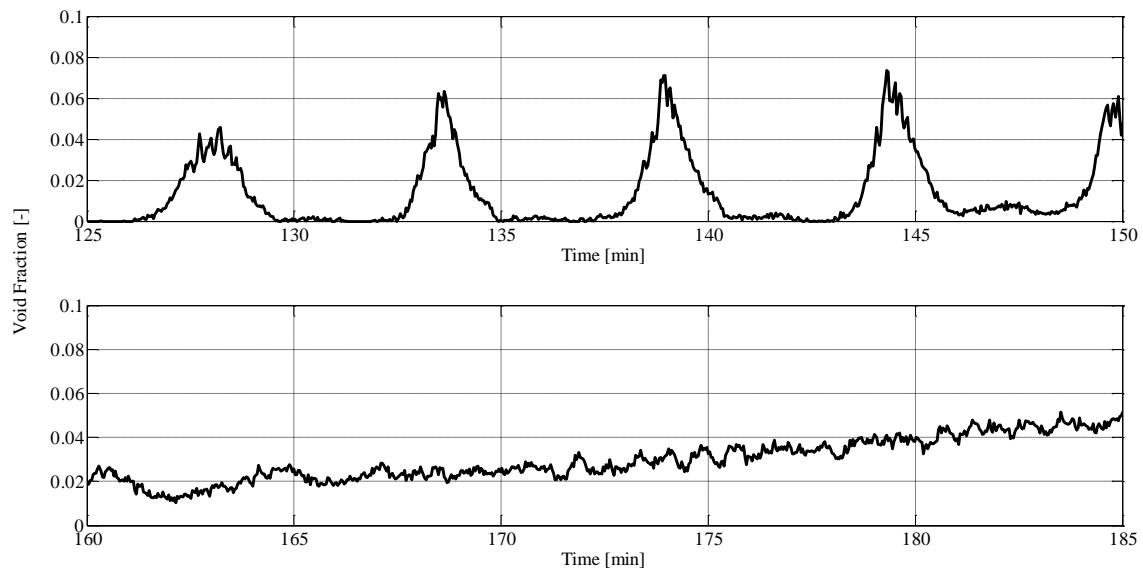*Figure 5-14 Void Fraction at the Core Exit (IMP03) for the Fast Startup Transient*
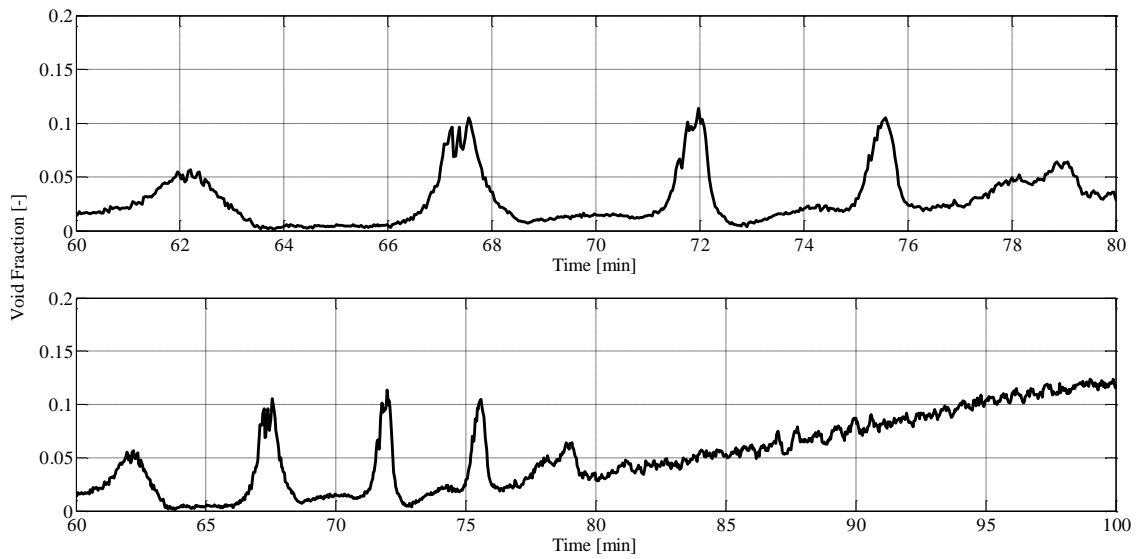
Figure 5-15 Detailed Void Fraction at the Core Exit (IMP03) for the Fast Startup Transient
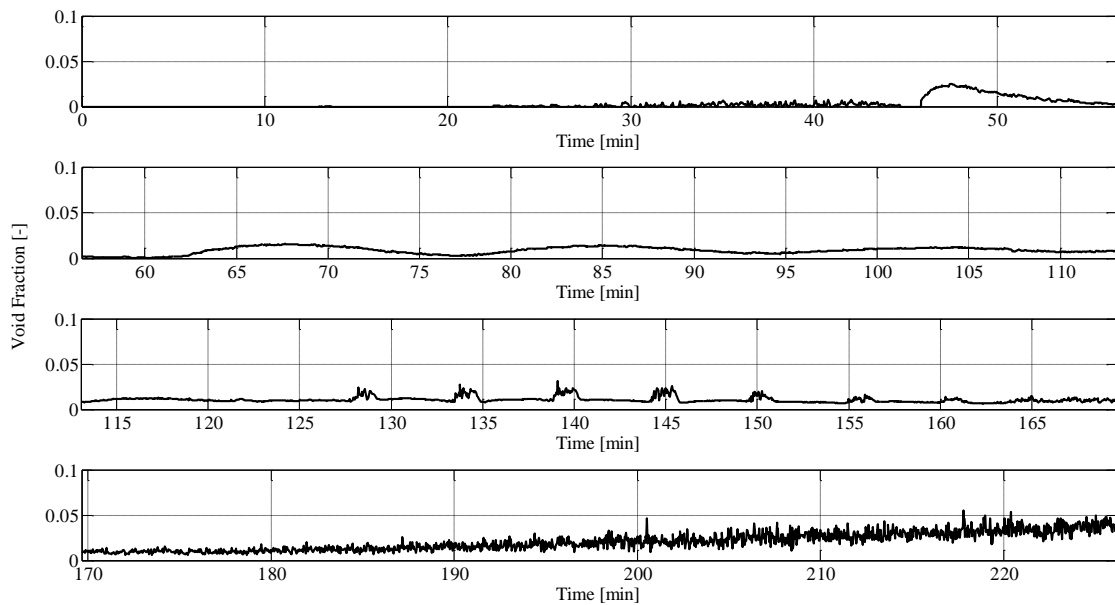
91

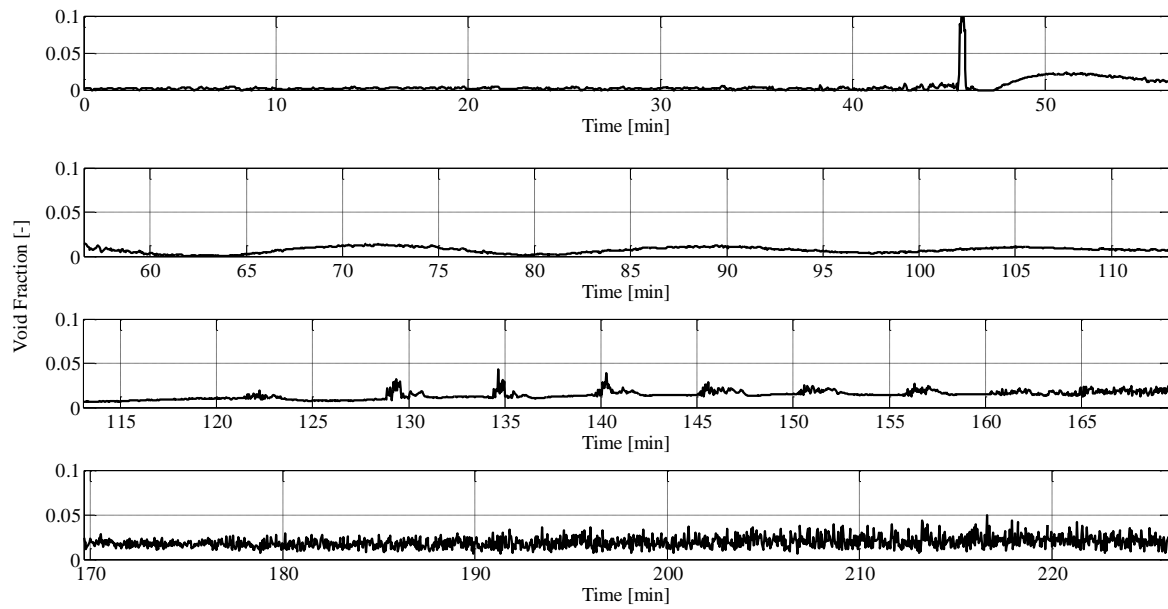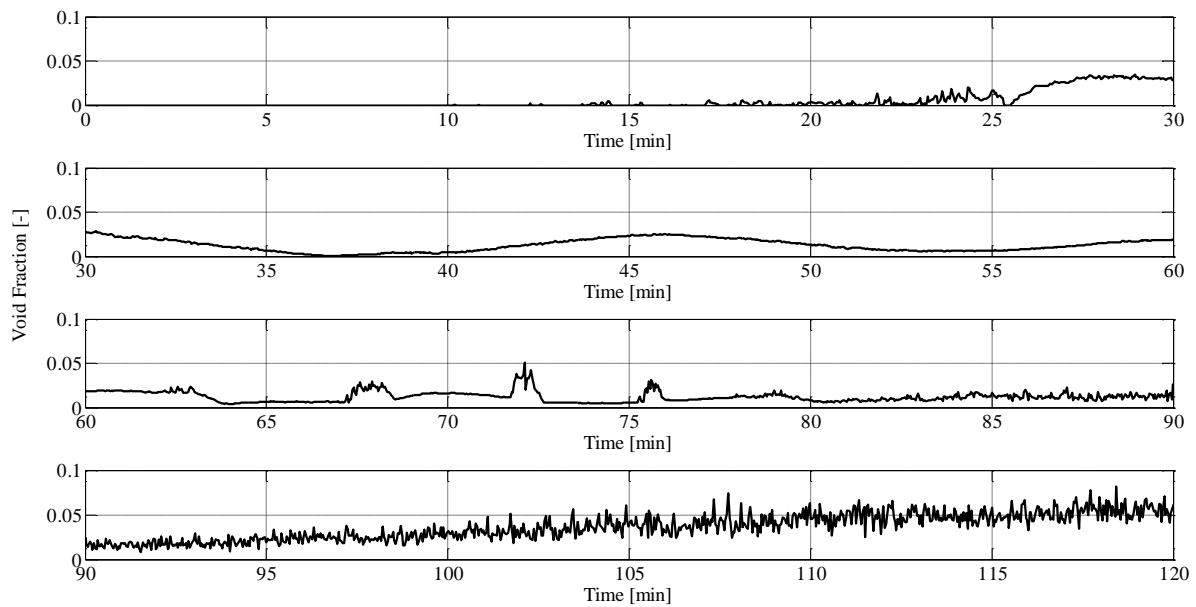*Figure 5-16 Void Fraction at the Chimney Inlet (IMP04) for the Fast Startup Transient*
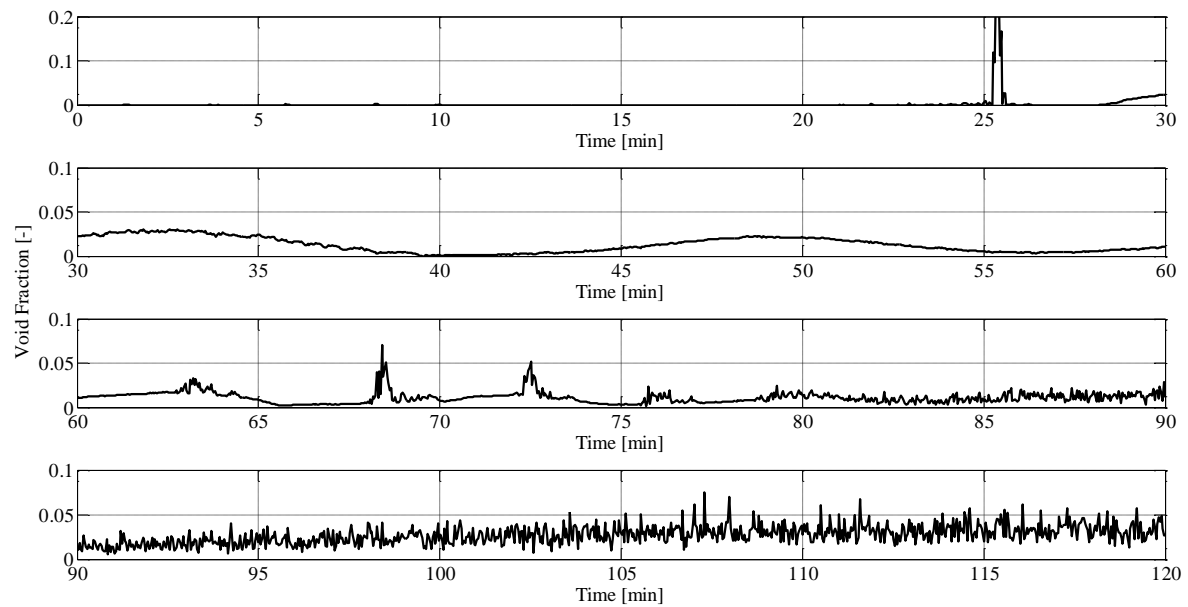
Figure 5-17 Void Fraction at the Chimney Outlet (IMP07) for the Fast Startup Transient

In the previous section, the startup transient tests are performed to investigate the thermal hydraulic instability in a natural circulation test loop. The power curve for the heat-up of the test section is set as input in LabVIEW. However, in the real reactor, the heat-up of a boiling water reactor is by means of nuclear fission and different feedbacks such as control rods, moderator density, and Doppler effect. Among these feedbacks, the void reactivity feedback coefficient is always negative for a natural circulation light water reactor. However, void reactivity feedback can be positive due to unstable flow oscillations and time lag in fuel conduction. In this section, the slow and startup transient test with void reactivity feedback is simulated based on the PKM. In other words, the system can have positive void feedback due to the control rods movement and void generation at that time.

The void fraction measurement in the core part is very important to the startup transient tests considering the void reactivity feedback. The information about the stability mechanism and natural circulation rate can be acquired from the void fraction measurement. In order to simulate the void reactivity feedback, three impedance void meters have been installed in the core region. Volume-averaged void fraction in the core region, α_{core}^{V}, has been used in current test as follows

$$\alpha_{core}^{V} = (\alpha_{p,1}^{A} + \alpha_{p,2}^{A} + \alpha_{p,3}^{A})/3 \tag{5.13}$$

where $\alpha_{p,1}^{A}, \alpha_{p,2}^{A}$, and $\alpha_{p,3}^{A}$ are the three area-averaged void fraction measure in the axial location. Since the flow area and distance between two impedance void meters are uniform. So above equation can be used to estimate the volume-averaged core void fraction.

The flow chart for the heater power control program for the void reactivity feedback startup transients is shown in Figure 5-18. The impedance void meter needs to be calibrated before the test due to the change of coolant conductivity with time. The volume-averaged void fraction in the core is then acquired from those three impedance void meters in the core. The point kinetics equations are solved numerically by using Eq. (5.5) and Eq. (5.10) with a time step of 0.5 second in LabVIEW. The new power calculated is sent to the power controller after considering the time difference between nuclear fuel and electric heater rods. In

this section, two power ramp rates corresponding to the thermal hydraulic tests are tested for the nuclear coupled tests.


```
┌─────────────────────────────────────┐
│        Initialize the DAS board       │
└─────────────────────────────────────┘
                   ⇩
┌─────────────────────────────────────┐
│          Start the simulation         │
└─────────────────────────────────────┘
                   ⇩
┌─────────────────────────────────────┐
│  Read void fraction from Impedance    │
│  Void Meters (IMP) in the core        │
└─────────────────────────────────────┘
                   ⇩
┌─────────────────────────────────────┐
│  •  Read the local temperature for IMP│
│  •  Calculate the liquid Impedance as a│
│     function of temperature            │
│  •  Calculate the volume-average void  │
│     fraction in the core               │
└─────────────────────────────────────┘
                   ⇩
┌─────────────────────────────────────┐
│  •  Solve the point kinetic equations  │
│     based on external reactivity and   │
│     void reactivity                    │
│  •  Calculate the new power and sent it│
│     to power controller after delay    │
└─────────────────────────────────────┘
```

Figure 5-18 Flow Chart of Heater Power Control Program for Void Reactivity Feedback

5.3.1. Slow Startup Transient Test with Void-Reactivity Feedback

Figure 5-19 shows the power curve used in thermal hydraulic test and recalculated power with only external reactivity, which does not include the void

reactivity. The external reactivity shown in Figure 5-20 is calculated by using Eq. (3.19). Then the new power curve is calculated by using Eq. (5.10).

The steam dome pressure during the slow startup transient with void reactivity feedback is demonstrated in Figure 5-21. The overall trend of the pressure response is very similar to the thermal-hydraulic startup simulation. At the beginning of the test, the steam dome pressure is almost constant and close to the saturated temperature in the steam dome. After the start of core boiling, the steam dome pressure rises exponentially with vapor generation. The total test time is about 220 minutes for this condition.

Figure 5-22 shows the axial temperature profile for the slow startup transients with void reactivity feedback. The temperature oscillations at the core exit and middle of the chimney reflects oscillations of the natural circulation rate caused by condensation and flashing in the chimney during the net vapor generation phase.

Figure 5-23 shows the natural circulation rate for the slow startup transients with void reactivity feedback. The oscillation pattern is pretty much similar to that of slow startup transients without considering the void reactivity feedback. Combined with the void fraction profile shown from Figure 5-25 to Figure 5-27, the void reactivity feedback has limited effects on the flow instability observed during the nuclear coupled slow startup transients.

Figure 5-24 displays the power curve for the nuclear coupled test. The first 100 minutes belong to the single phase natural circulation, where the void reactivity is zero. The void reactivity affects the power when there is void fraction in the core. The output power has certain oscillations from 100 minutes to 150 minutes. These oscillations are caused by the intermittent void fraction oscillations when the core starts boiling. Due to the unstable flow conditions and heat conduction at the point of adding void reactivity, the system can have either positive feedback or negative feedback initially such as the power ascension at 100 minute in Figure 5-24. However, the nuclear coupled power curve is able to fluctuate around the reference power curve used in the thermal-hydraulic test. The power oscillation has little effect on the natural circulation rate due to its small magnitude. Because the test section still has a large amount of subcooling needs to be removed during the phase of net vapor generation. And the base power and fluctuations are not large enough to alter the flow regime in a short period. Because of the limitation of the experimental conditions, the experiments stop at 220 minutes. However, it can be

expected that the power increases continuously with some oscillations but still follows the linear power curve with the reactivity feedback model.
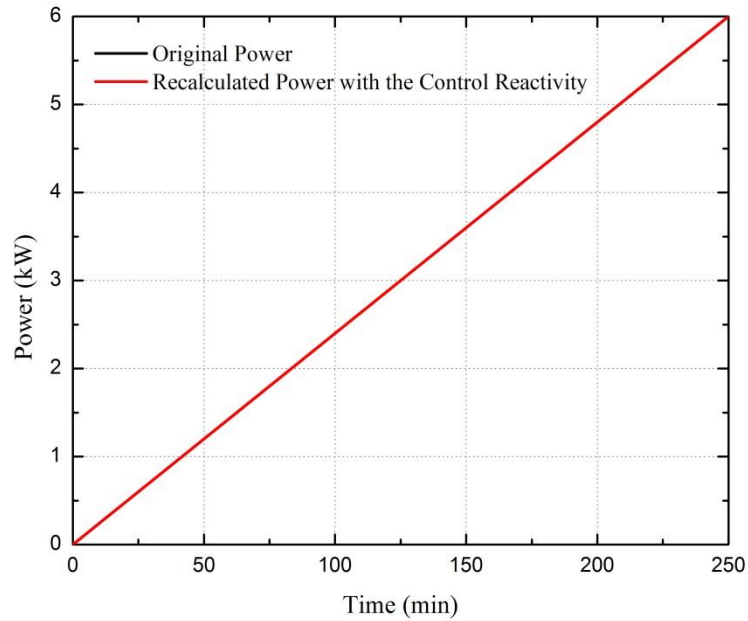
Figure 5-19 Validation of Point Kinetics Model for the Slow Startup Transient
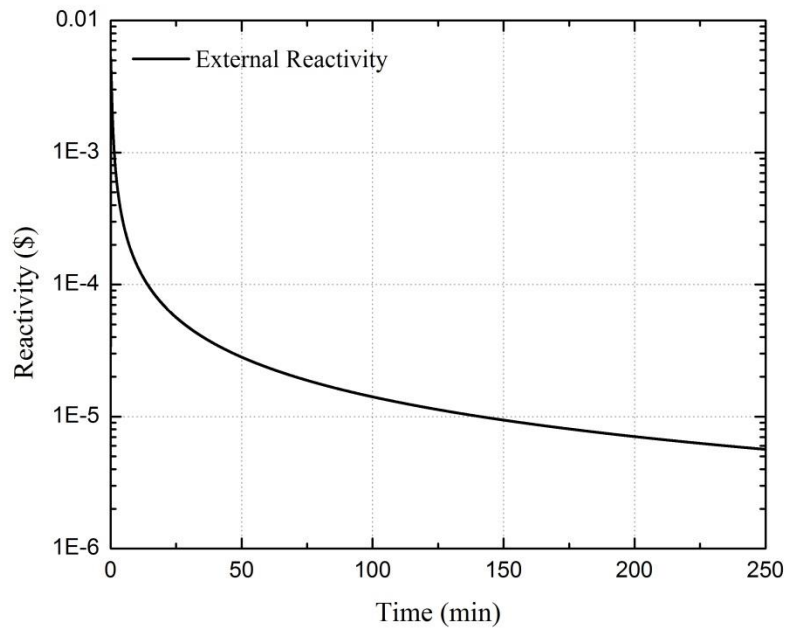
Figure 5-20 External Reactivity Calculated for the Slow Startup Transient

96
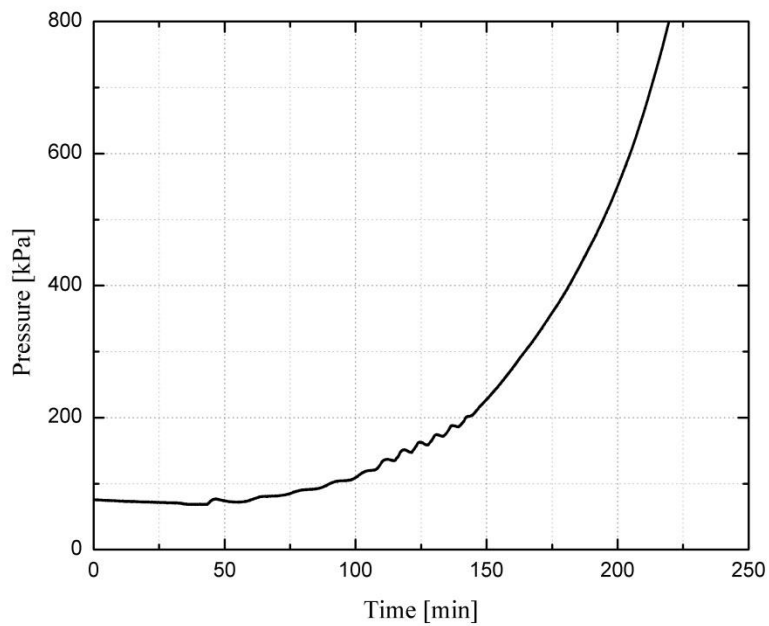
Figure 5-21 Steam Dome Pressure for the Slow Startup Transient with Void Reactivity Feedback
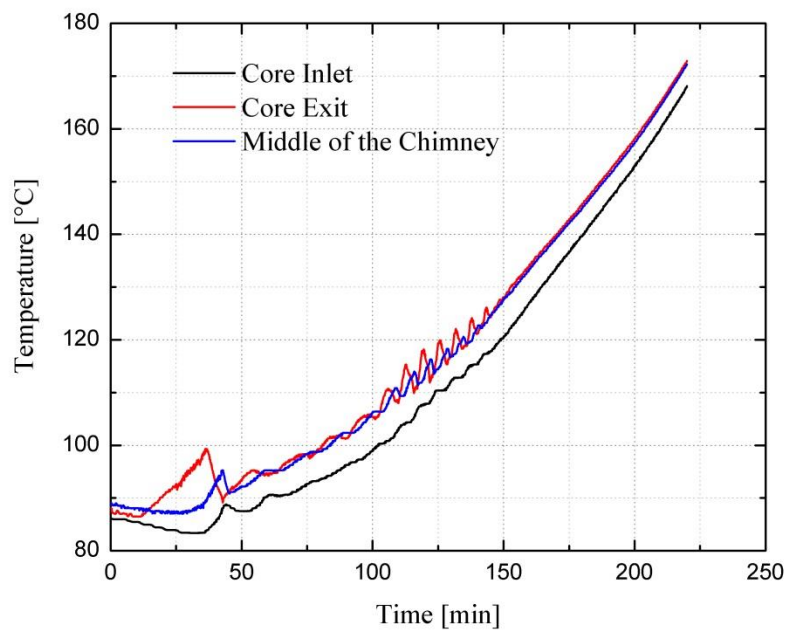
Figure 5-22 Temperatures for the Slow Startup Transient with Void Reactivity Feedback
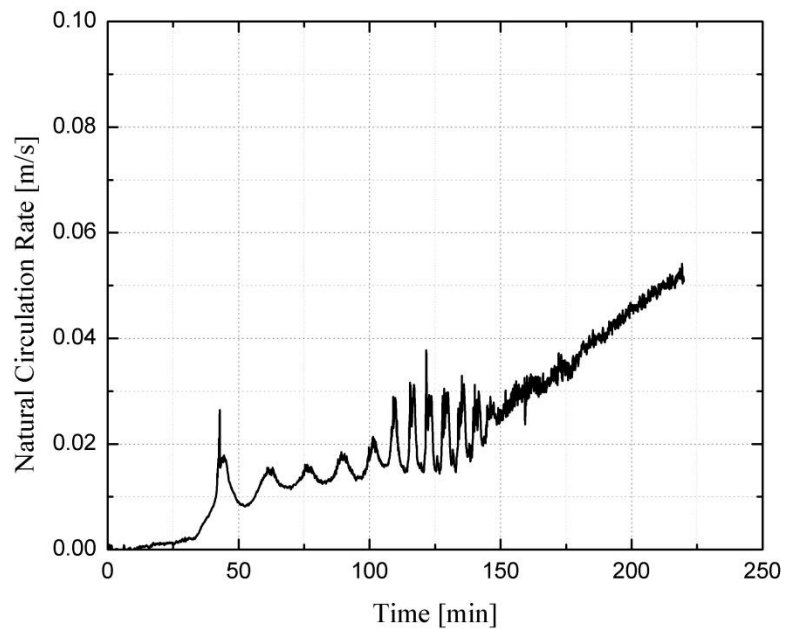
Figure 5-23 Natural Circulation Rate for the Slow Startup Transient with Void Reactivity Feedback
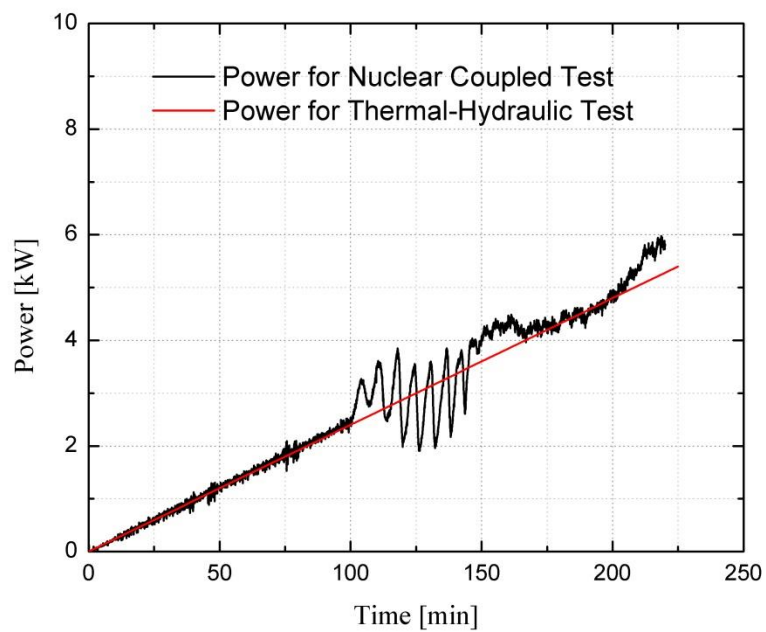
Figure 5-24 Main Heater Power for the Slow Startup Transient with Void Reactivity Feedback

98
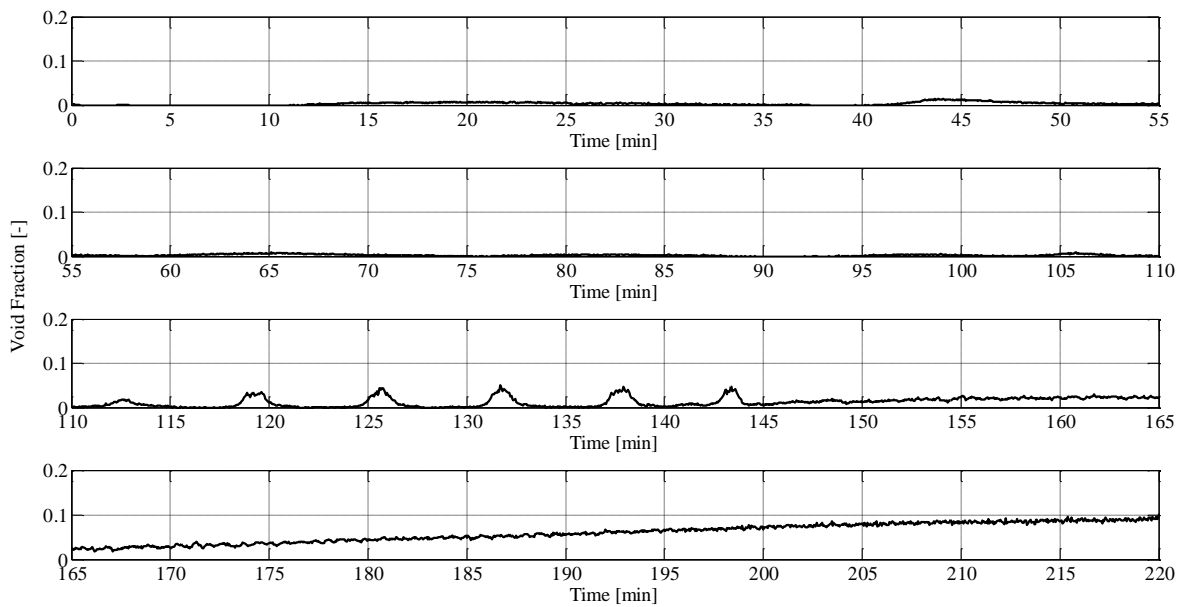
Figure 5-25 Void Fraction at the Core Exit (IMP03) for the Slow Startup Transient with Void Reactivity Feedback
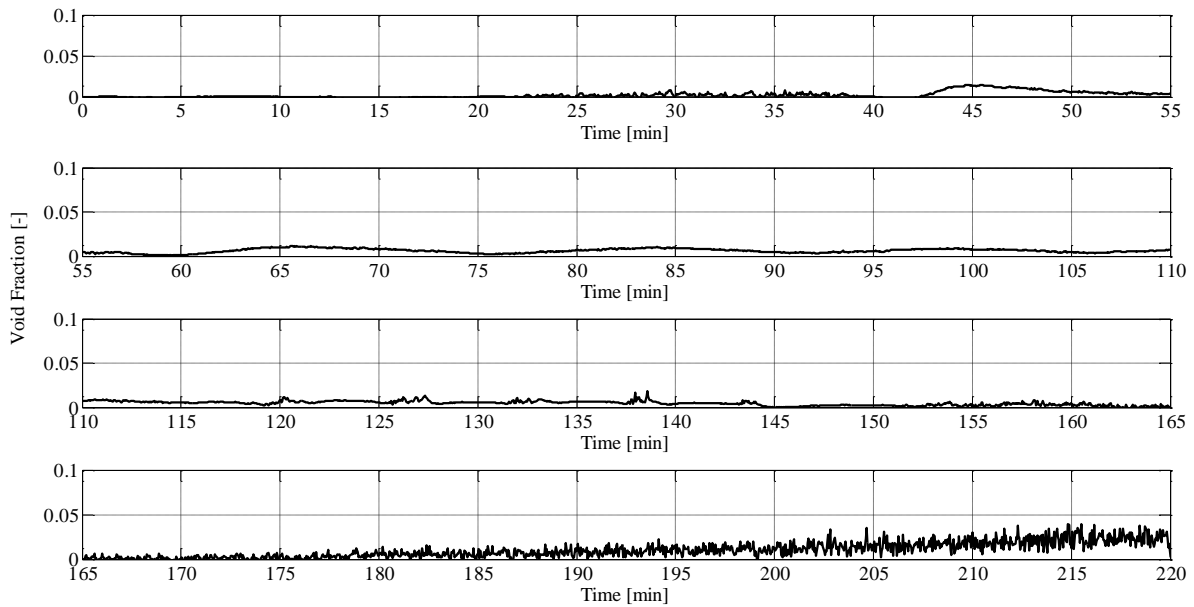
Figure 5-26 Void Fraction at the Chimney Inlet (IMP04) for the Slow Startup with Void Reactivity Feedback

99
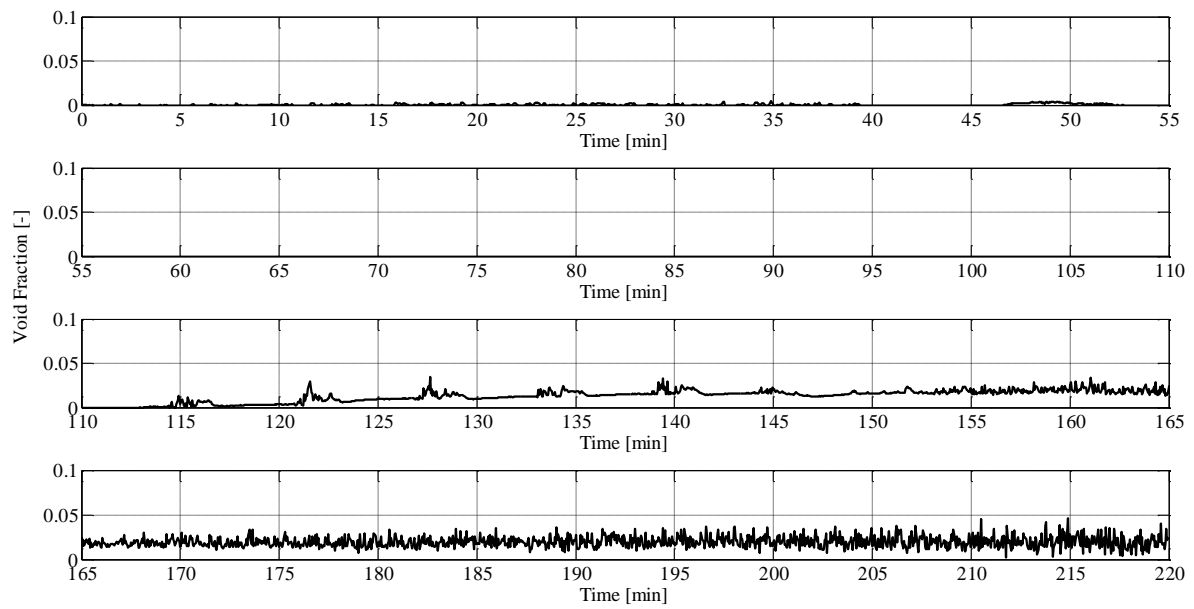
Figure 5-27 Void Fraction at the Chimney Outlet (IMP07) for the Slow Startup with Void Reactivity Feedback

5.3.2. Fast Startup Transient Test with Void-Reactivity Feedback

The fast startup transient test is performed by considering the void reactivity feedback. This test is intended to investigate the heat-up effect on the flow instability for the nuclear coupled test.

Figure 5-28 shows the steam dome pressure profile for the fast startup transient test with void reactivity feedback. The total test time for this condition is about 120 minutes.

Figure 5-29 shows the axial temperature profile during the test. Compared to the nuclear-coupled slow startup transients, fewer oscillations are observed during the phase of net vapor generation due to larger heat flux.

Figure 5-30 displays time trace of the natural circulation rate during this test. Flashing occurs in the phase of single phase natural circulation increases the loop flow velocity. In the phase of net vapor generation, condensation at the chimney inlet and flashing near the top of the chimney can cause the intermittent oscillations from 50 minutes to 70 minutes. Density wave oscillations can be observed in the earlier period of two phase natural circulation and diminish with the power density continuously rises. Figure 5-32 to Figure 5-34 shows the time trace of void fraction during the nuclear-coupled fast startup transients. They do not show too much difference with those of the thermal-hydraulic fast startup transients.

Figure 5-31 displays the nuclear-coupled power curve calculated numerically from PKM. As can be seen, the power fluctuates during the phase of net vapor generation due to unstable flow conditions. In the late phase of two phase natural circulation, the power curve increases and follows the linear fast thermal-hydraulic power curve. The bias of void fraction measurement can cause certain fluctuations in the nuclear coupled power curve due to its complexity in controlling.
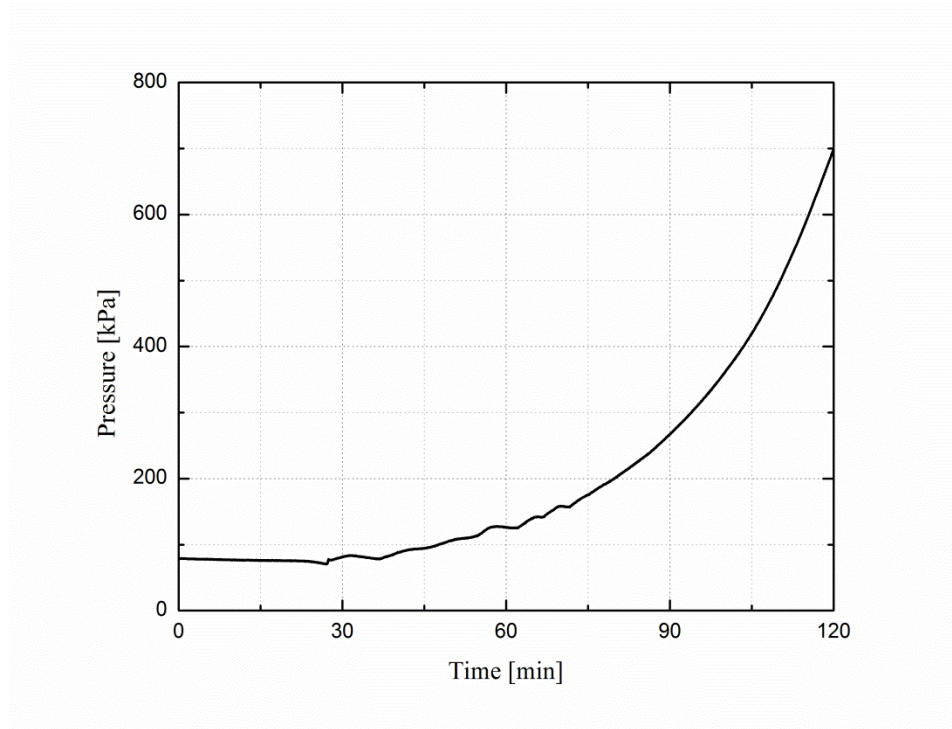
Figure 5-28 Steam Dome Pressure for the Fast Startup Transient with Void Reactivity Feedback
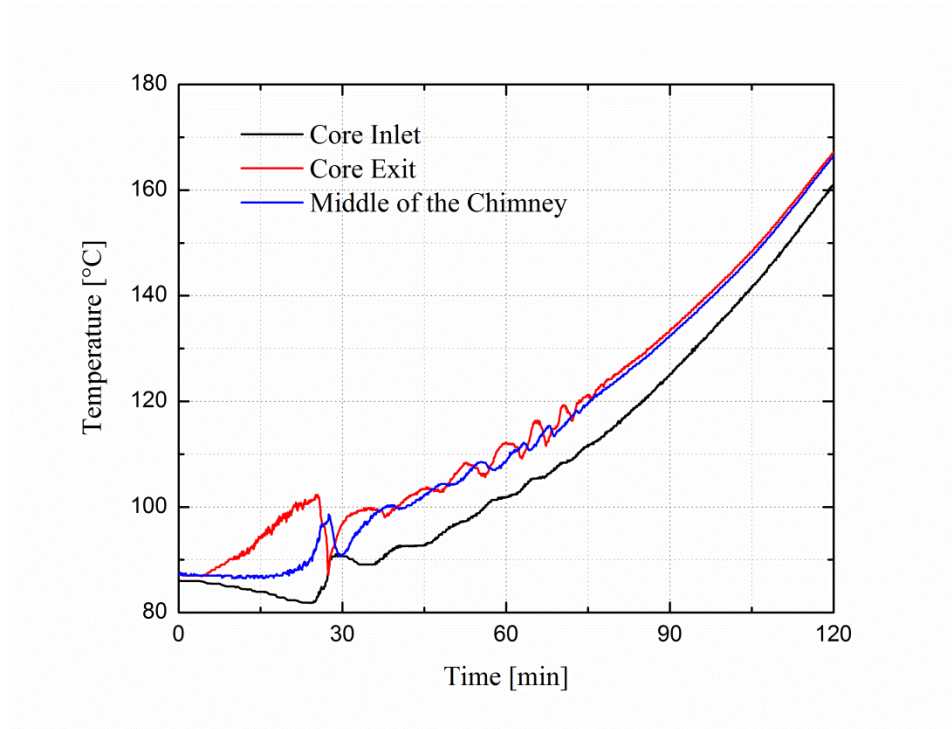
Figure 5-29 Temperatures for the Fast Startup Transient with Void Reactivity Feedback

102
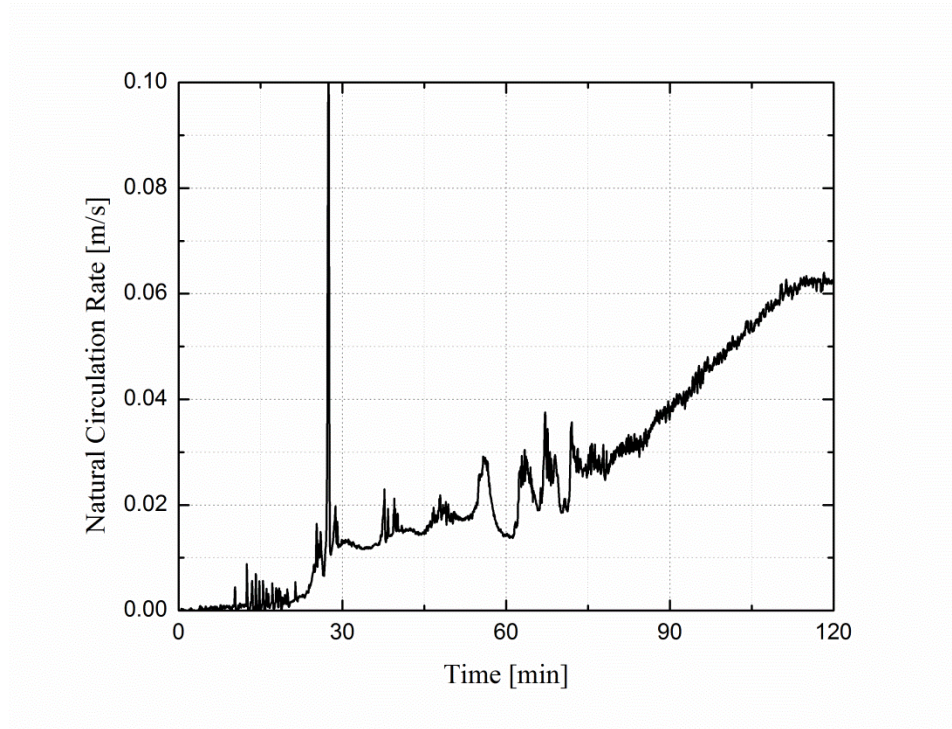
Figure 5-30 Natural Circulation Rate for the Fast Startup Transient with Void Reactivity Feedback
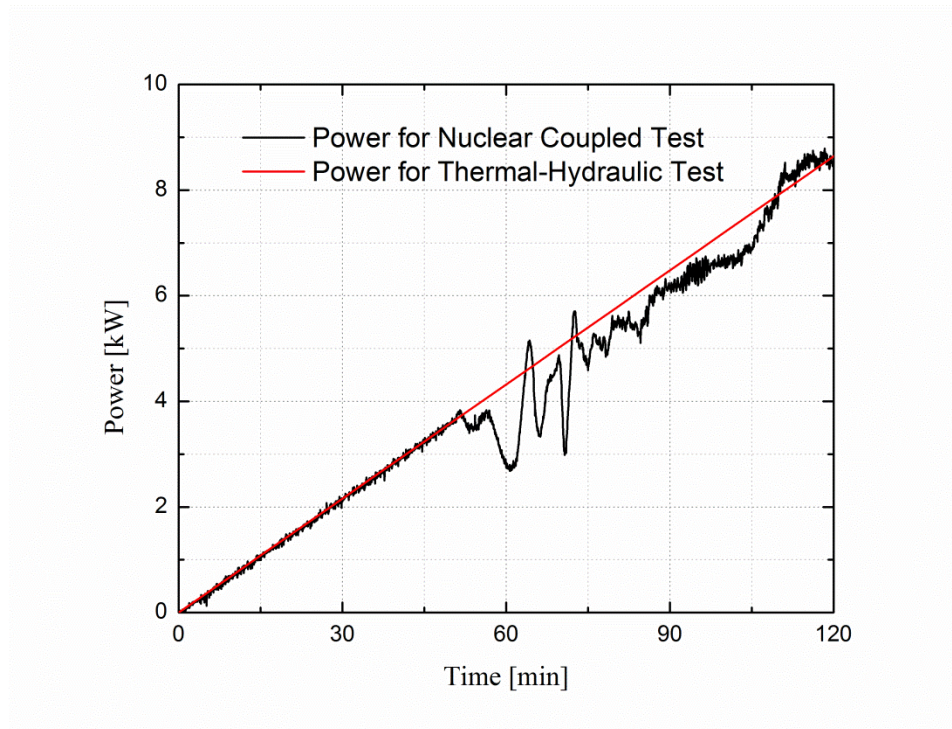
Figure 5-31 Main Heater Power for the Fast Startup Transient with Void Reactivity Feedback
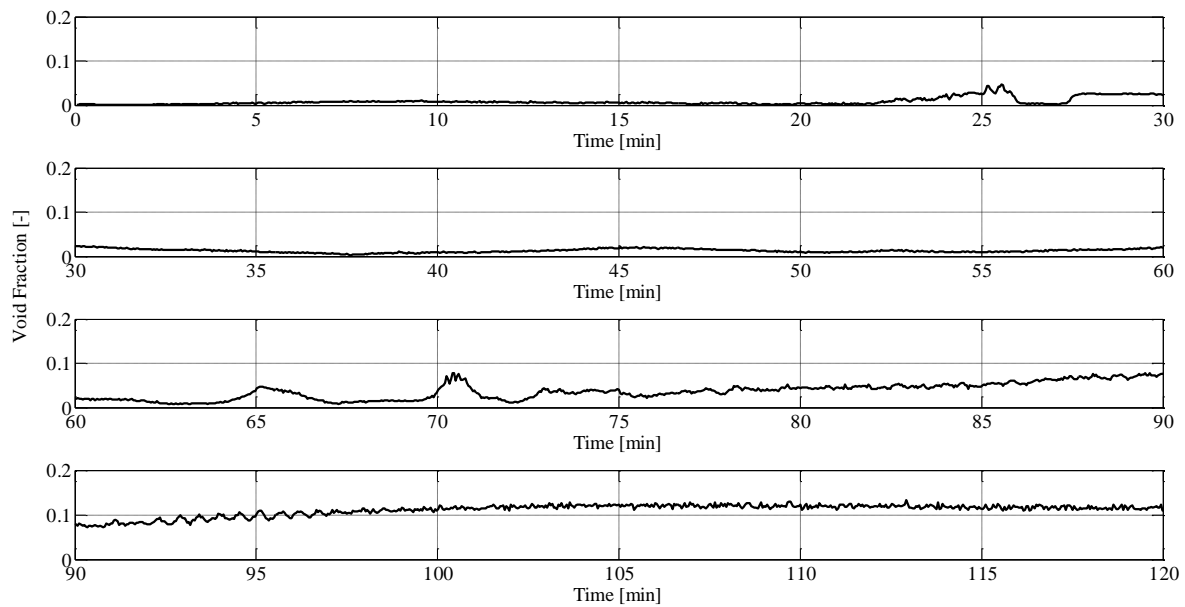
Figure 5-32 Void Fraction at the Core Exit (IMP03) for the Fast Startup Transient with Void Reactivity Feedback
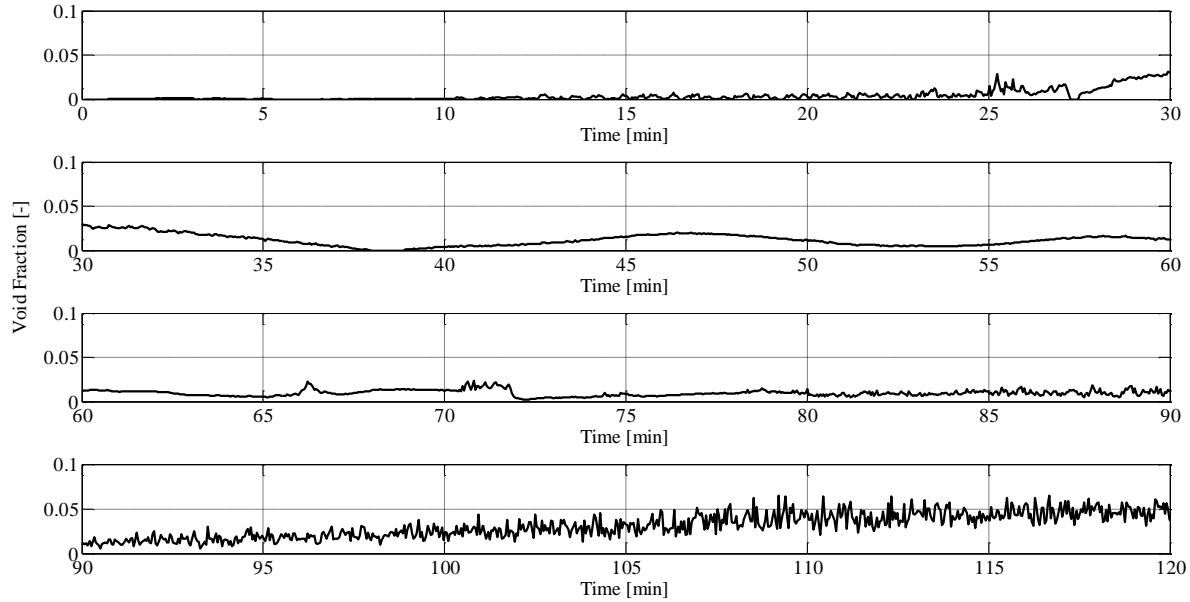
Figure 5-33 Void Fraction at the Chimney Inlet (IMP04) for the Fast Startup Transient with Void Reactivity Feedback
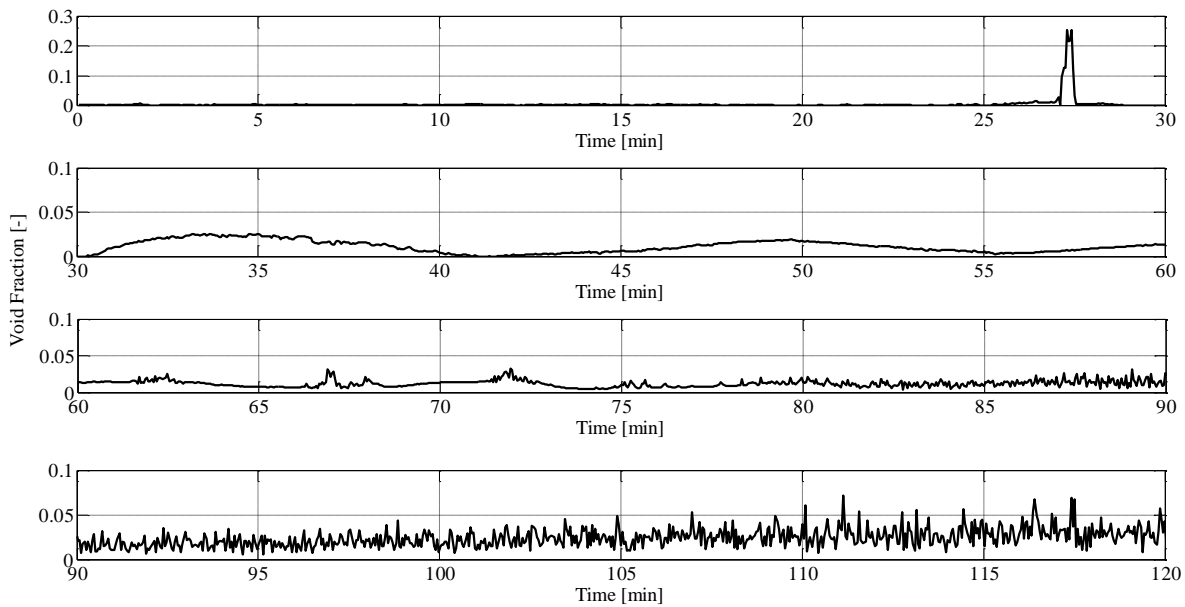
Figure 5-34 Void Fraction at the Chimney Outlet (IMP07) for the Fast Startup Transient with Void Reactivity Feedback

5.4. FURTHER INVESTIGATION INTO STARTUP PROCEDURE ON NATURAL CIRCULATION BOILING WATER REACTOR

In previous sections, the experimental results for startup transients with and without the reactivity feedback are discussed. The flashing oscillations, which occurs in the single phase natural circulation and net vapor generation phase, is the most dominant flow instability in the startup procedure for natural circulation facility. In this section, extra experimental results are performed to study the flashing oscillations. In order to examine the power density on the startup procedure, only thermal hydraulic startup transients are investigated. A very slow variable power ramp shown in Figure 5-35 is applied to the thermal hydraulic startup transients. This variable power curve can be divided into three regions. The first and second phase last longer compared to previous power ramp used in the slow thermal hydraulic startup transients. In the first four hours the power increases at a rate of 5×10^{-5} kW/s to initiate the single phase natural circulation and eliminate flashing. In the net vapor generation phase, the power maintains constant

at 0.99 kW for about 14 hours. At the later phase, the power increases at a rate of 2×10^{-4} kW/s. The purpose of using variable power ramp is to stabilize the flow oscillations by heating at very small power density.
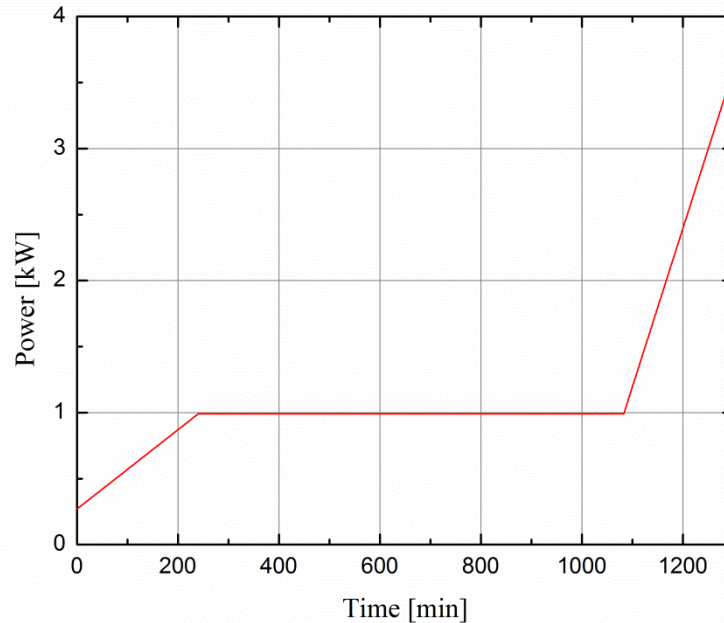

Figure 5-35 Power Curve for Very Slow Startup Transients

Figure 5-36 shows the steam dome pressure profile for the very slow startup transients. The pressure oscillation starts at 380 minute and ends at about 1180 minute at 0.35 MPa. The temperature profiles at different elevations are presented in Figure 5-37. As can be seen, the core temperature increase is about 3 degrees and the chimney has a very uniform temperature distribution along the chimney through the tests. The uniform temperature in the chimney can stabilize the flow oscillations under non-equilibrium conditions. Figure 5-38 shows the inlet subcooling ($\triangle T=T_{sat}-T_{inlet}$) during the startup procedure. Due to the effects of the chimney hydro-static head and heating removal, the inlet subcooling decreases from 16 degrees at the beginning to 4 degrees at the end. Less inlet subcooling means smaller non-boiling length if the same core power density is given [30]. So when the inlet subcooling is reduced to less than 5 degrees, two-phase natural circulation system can be generated in the later phase of startup transients.

However, the oscillations of inlet subcooling also leads to the flow ocillations during the net vapor generation phase.

Figure 5-39 shows the time trace of natural circulation rate for the very slow startup transient. As can be seen, the single phase natural circulation rate is stabilized largely by very slow heating up. The big peak flow shown in slow and fast startup transients is not observed at this power ramp. The net vapor generation starts at about 350 minutes and ends at 1200 minutes. During this period, there are continuous oscillations with a period of about 15 minutes because of very small power density. However, the pattern of intermittent oscillations shown in Figure 5-40 much more uniform than that shown in Figure 5-41 for the slow startup transient. After 1200 minutes, the flow oscillations reduced and the system is dominated by the two phase natural circulation. The void fraction profiles at different level are shown in Figure 5-42 to Figure 5-44. The void fraction measurement is not so accurate for the very slow startup transient due to difficulties in long time calibration of impedance void meter. The magnitude of intermittent flow oscillations caused by flashing is much smaller than that in the slow startup transients.

Based on the experimental results and above analysis, the power ramp with very small heating rate and long period of heating can stabilize the startup transients for the natural circulation boiling water reactor. In real reactor, core power is divided into several regions, i.e., hot channel, average channel and periphery channel. The coolant from different channels mixes each other at the core exit and goes upwards into the chimney. So the flow oscillations observed in the test facility can be further reduced. However, it is very difficult and might be impossible to avoid the flow oscillations caused by flashing when the nuclear reactor is started from half atmospheric temperature. After comparing all the startup tests, it can be found that the flow oscillations caused by flashing disappear at about 0.3 MPa. It is easy to postulate that pressure can suppress the flashing oscillations. The reactor can be pressurized to 0.3 MPa using nitrogen after degassing procedure. When the reactor is heated up to 0.5 MPa, the test section needs to degas again to remove the nitrogen through top vent line. This pressurized startup procedure will be tested in the next phase of project.
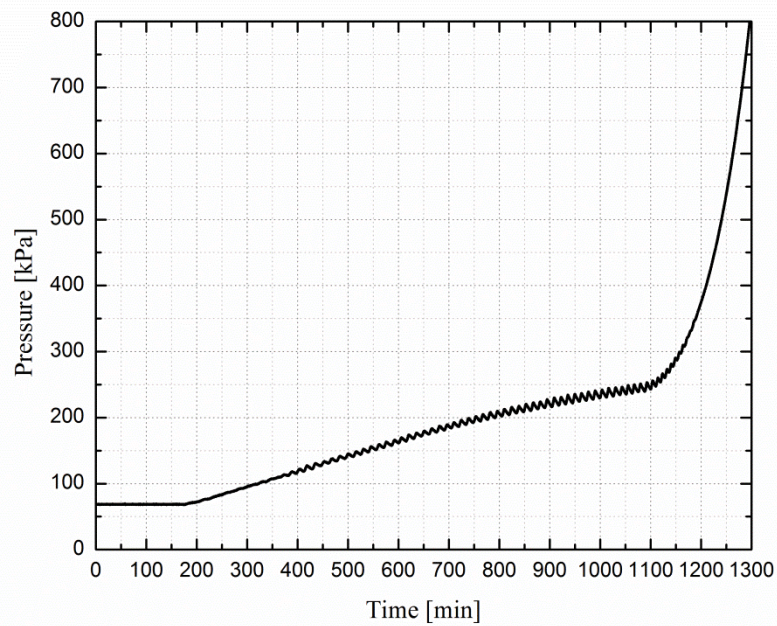
Figure 5-36 Steam Dome Pressure for Very Slow Startup Transient
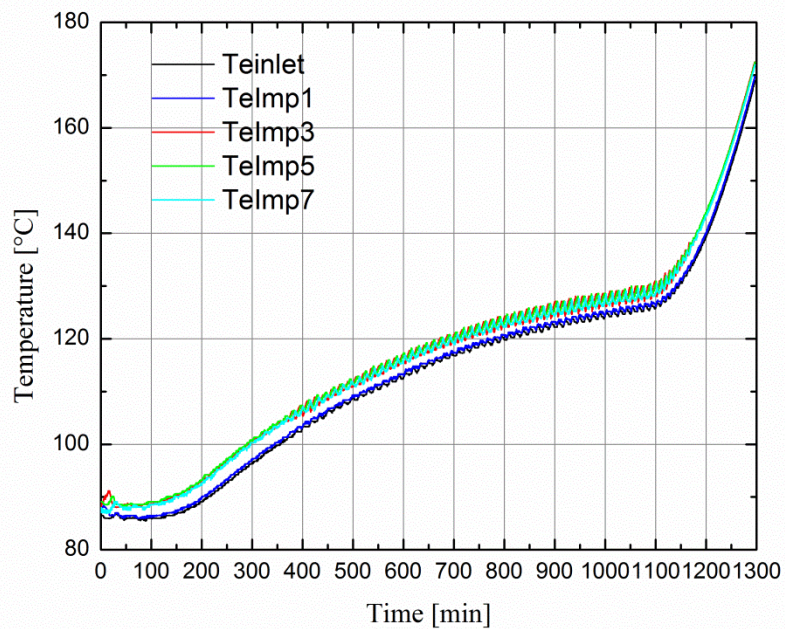
Figure 5-37 Temperatures for Very Slow Startup Transient

108
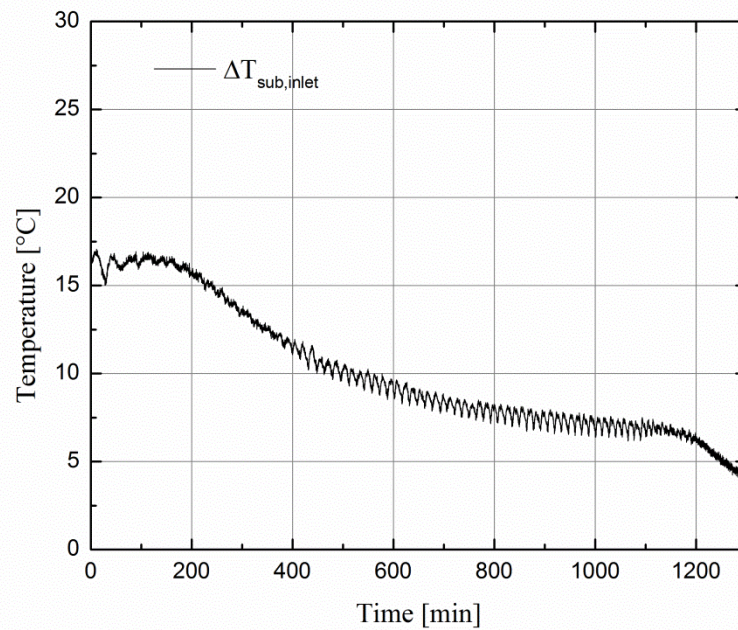
Figure 5-38 Inlet Subcooling Temperature for Very Slow Startup Transient
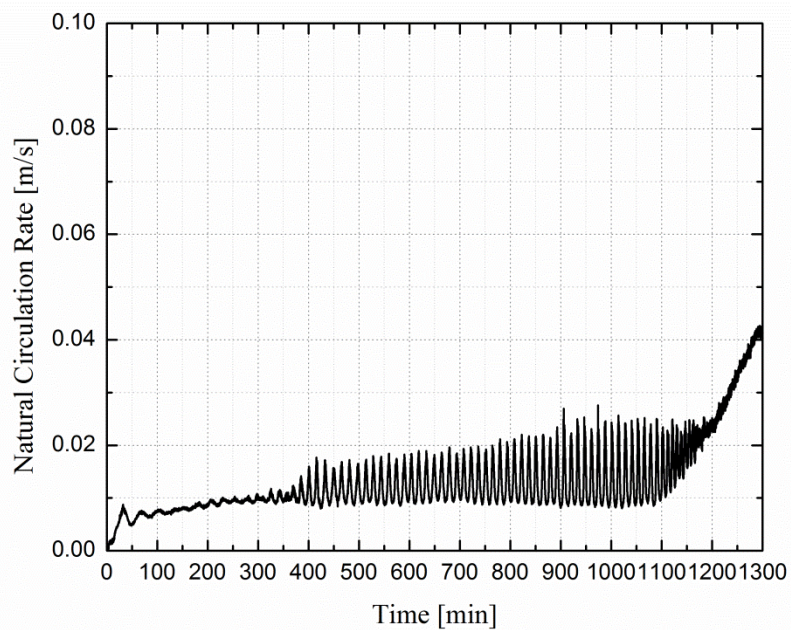
Figure 5-39 Natural Circulation Rate for Very Slow Startup Transient

109
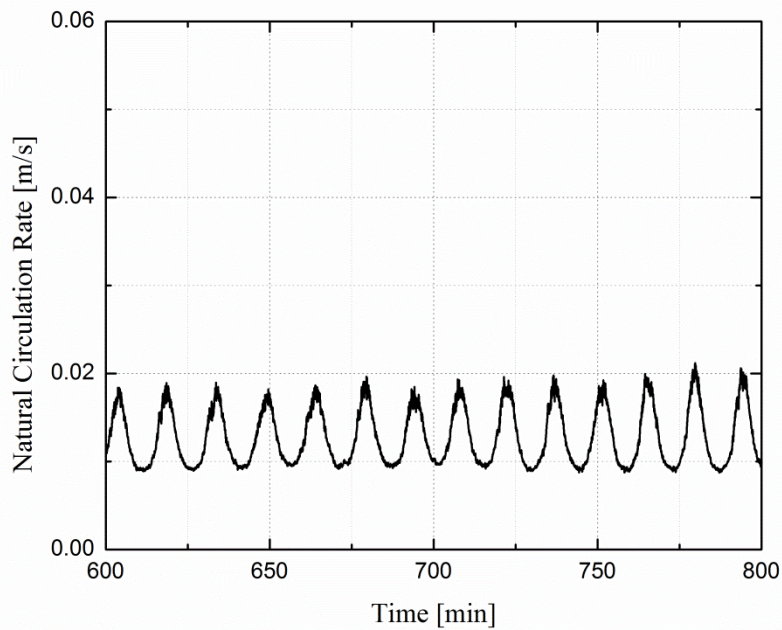
Figure 5-40 Detailed Natural Circulation Rate for Very Slow Startup Transient
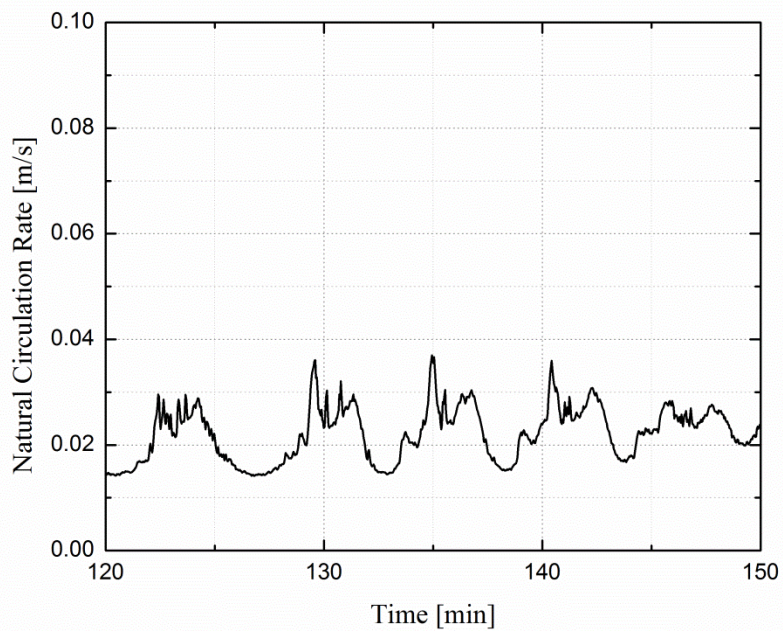
Figure 5-41 Detailed Natural Circulation Rate for Slow Startup Transient

110
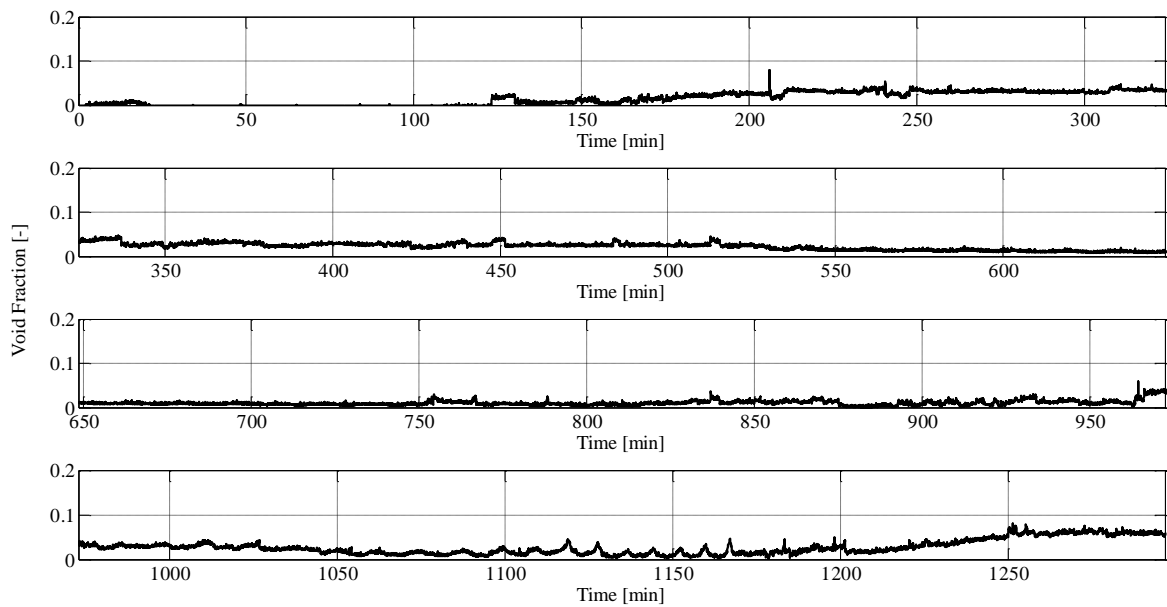
Figure 5-42 Void Fraction at the Core Exit (IMP03) for the Very Slow Startup Transient
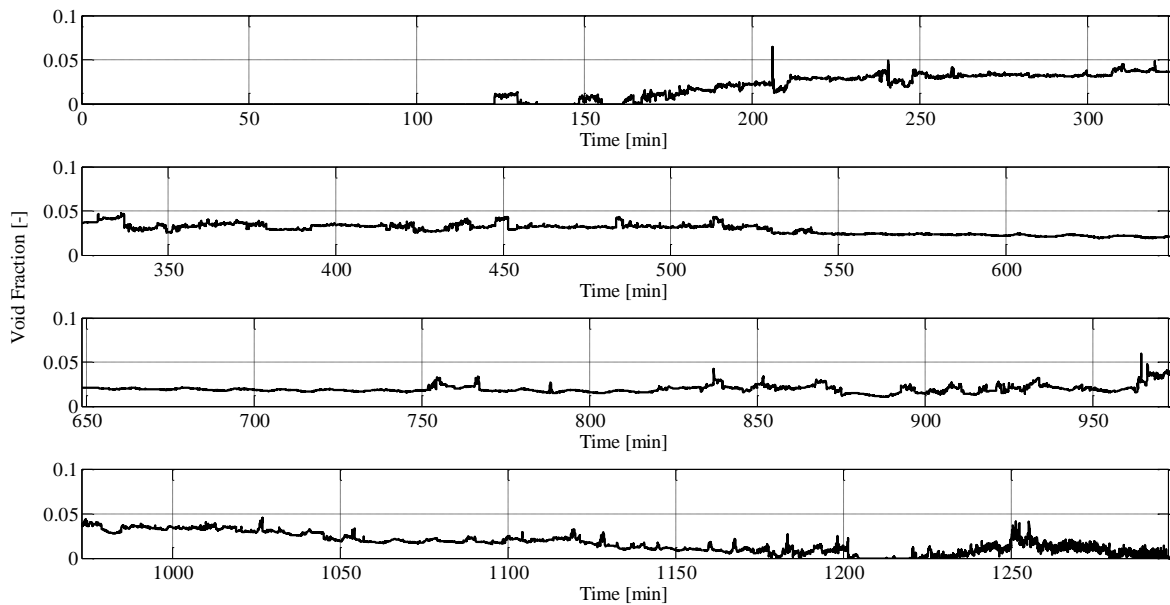
Figure 5-43 Void Fraction at the Core Exit (IMP04) for the Very Slow Startup Transient

111
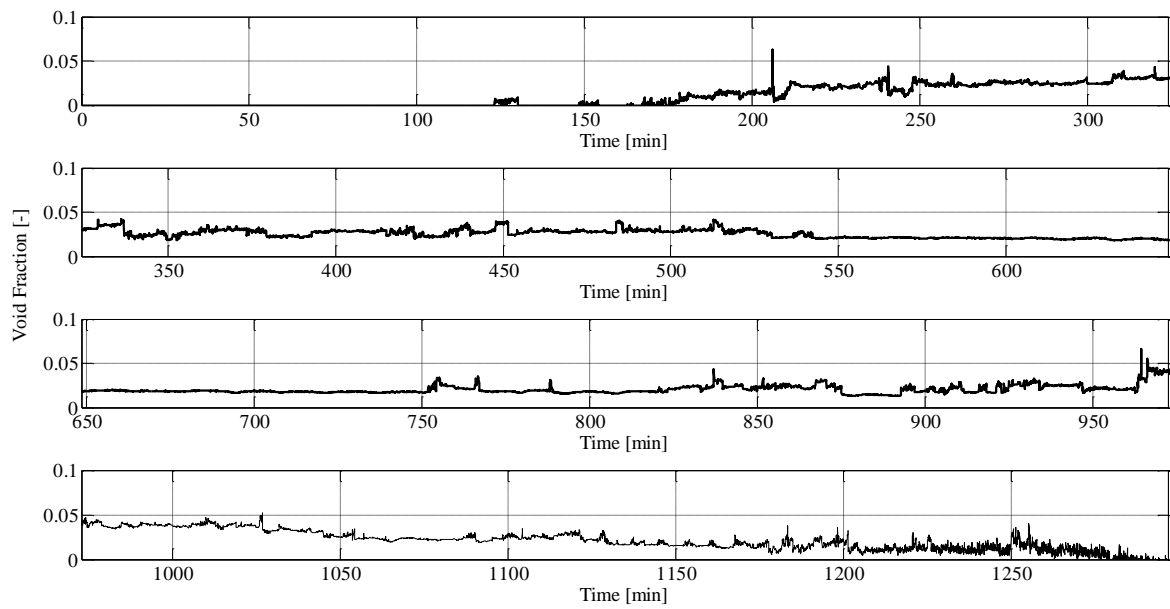
Figure 5-44 Void Fraction at the Core Exit (IMP07) for the Very Slow Startup Transient

112

6. PRESSURIZED STARTUP TRANSIENT TEST FOR NMR-50

The natural circulation boiling water reactors are prone to various instabilities at low pressure and low power conditions. The initial startup procedure is one of the three phases of the normal operation of a reactor. And the initial startup procedure for a natural circulation reactor must go through the low pressure and low power conditions. Normal initial startup procedure for NMR-50 starts from about half atmospheric pressure by vacuuming the steam dome to remove the non-condensable gas. Previous research found that flashing instability occurs more often than other flow instabilities due to the reduced head in long chimney, which is the essential characteristic of long chimney in the natural circulation boiling reactors. Although the flashing instability can be reduced to a small extent by using very small power ramp to heat up, the flashing instability cannot be avoid completely by using normal initial startup procedure. In this report, the pressurized startup procedure will be applied for the startup procedure of the natural circulation boiling water reactor. In this section, the experimental results for the pressurized initial startup transients of NMR-50 are presented. Three power curves

6.1. SIMULATION STRATEGY
6.1.1. Initial and boundary conditions

The thermal hydraulic pressurized startup instability experiments without considering the void reactivity feedback are currently performed at three different power ramp rates. The initial conditions can be seen in Table 6.1. The startup transient tests start from 300 kPa by filling the steam dome with the non-condensable gas i.e. nitrogen after degassing procedure. The initial water level for startup transient is set at 5.85 m. Three linear power curves in Figure 6-1 are used to test slow heat-up, medium heat-up and fast heat-up thermal hydraulic pressurized startup transients.

Table 6.1 Initial Conditions for the Startup Transient

Pressure (kPa)	Coolant Temp. (℃)	Coolant Level (m)	Core Inlet Subcooling (℃)
300	85	5.85	53
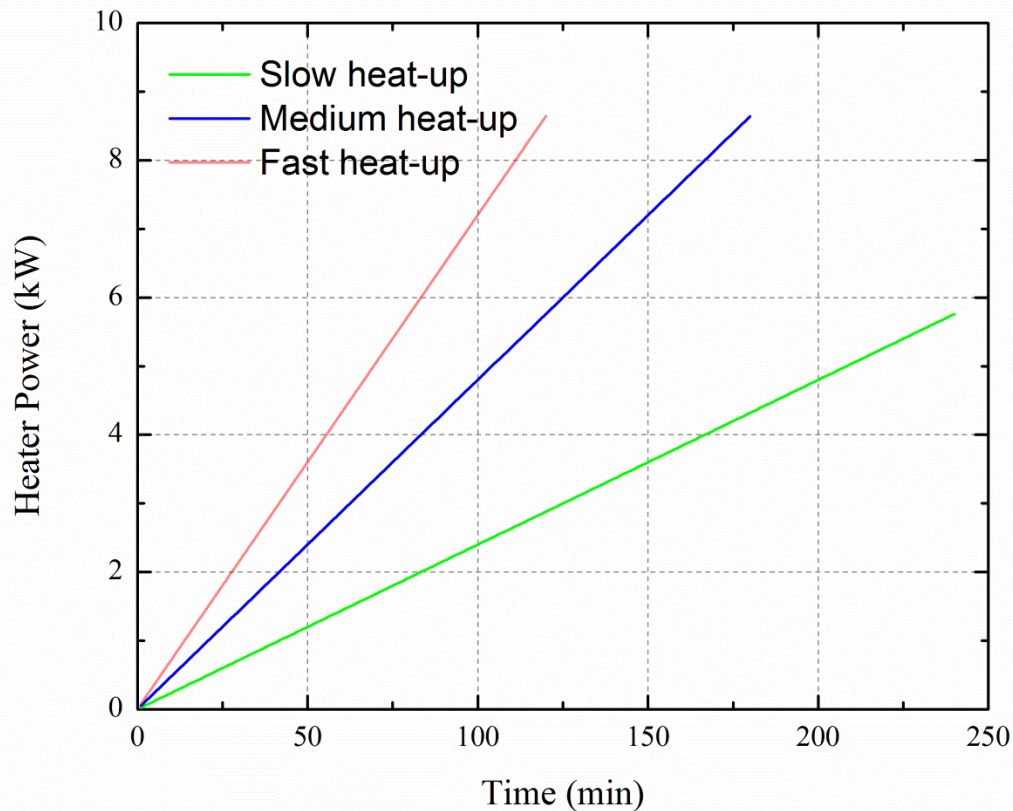
Figure 6-1 Power Curves for Pressurized Startup Transients

6.1.2. Test Procedure

Pressurized startup transient test procedure consists of a degassing procedure, pressurized procedure, vent procedure and heat-up test procedure. Before each test, general checks are performed. The steps are summarized as follows.

(1) Check all valves positions
(2) Turn on the power for the DPs, P-cells, and impedance circuits
(3) Check differential pressure transducer settings

114

(4) Purge each differential pressure transducer

(5) Check absolute pressure transducer setting

(6) Check magnetic flow meter

(7) Check the thermocouples

(8) Check the data acquisition system

(9) Set up the initial water level for the degassing procedure

(10) Turn on the power supply for main heater and pump (for degassing)

(11) Remove the noncondensable gases completely by heating the loop to 100 ℃

(12) Separate the degassing tank with the test loop

(13) Set up the initial water level for the startup transient test

(14) Cool the test loop down to 85 ℃

(15) Fill the test section with nitrogen gas to 3 bar

(16) Perform the final valve position for the inlet flow resistance

(17) Check the nuclear constants (for nuclear coupled test)

(18) Start the experiment applying the prescribed power curve

(19) Open the vent line when steam dome pressure reaches 5 bar

(20) Close the vent valve when steam dome saturated pressure and temperature match each other

(21) Shutdown the test section when system pressure reaches 8 bar

Compared to the normal startup procedure, the pressurized startup procedure includes pressurization with nitrogen gas after degassing procedure. The steam dome is filled with nitrogen to 3 bar from the vent line. Previous research shows that flashing instability disappears after system pressure reaches 5 bar. Then the non-condensable gas needs to be vent when the system pressure reaches 5 bar after startup procedure starts. The saturated P-T curve can be used to determine if there is non-condensable gas inside the steam dome. If there is non-condensable gas exists inside the steam dome, the steam dome temperature is lower than the saturated temperature corresponding to the steam dome pressure. When the vent procedure is done, the vent valve will be closed and the heating continues until the system pressure reaches the targeted value.

The slow pressurized startup transients are simulated by filling the steam dome with non-condensable gas after degassing procedure. The power curve tested is given in Figure 6-1. The initial water level for the startup transients is set at 5.9 m, which is scaled down from that of the NMR-50. The inlet K factor is set based on RELAP5 analysis and the experimental calibration.

Figure 6-2 shows the steam dome pressure profile for the pressurized slow startup transient. The pressure drops little due to cooling down effect in the steam dome. It starts to increase at about 75 minutes and reaches 0.5 MPa at about 175 minutes, when the vent line is open. In the first three minutes, the pressure decreases because of venting. Then the pressure increases again due to coolant vaporization and boiling in the test section. The vent process lasts about 15 minutes. After that the steam dome pressure continues to increase under the startup power ramp.

Figure 6-3 shows the temperature profile at different axial locations including core inlet, core exit and the middle of the chimney. As can be seen, the temperatures at the core exit and middle of the chimney are almost the same. However, there are about 5 degrees difference between the core inlet and the core exit. This temperature difference increases to about 10 degrees before the vent process and decreases to 4 degrees after the vent process. Figure 6-4 shows the steam dome temperature profile and saturated temperature under the steam dome pressure. Before the vent, the saturated temperature is much larger than the real-time temperature due to partial pressure of non-condensable gas i.e. nitrogen. When the test section is free of any non-condensable gas, two temperatures should be repeated.

Figure 6-5 shows the time trace of natural circulation rate for the pressurized slow startup transient. The single phase natural circulation rate is about 2 cm/s. When the vent valve is open, the steam dome pressure drops immediately. The critical flow occurs in the vent line. Then the two phase natural circulation is generated due to coolant evaporation. In a few minutes, the vaporization decreases and boiling increases, which cause the steam dome pressure increases again. And the natural circulation rate increases from 2 cm/s to 8 cm/s. At the beginning of the vent process, the velocity increases to 6 cm/s in a short time. The sudden increased velocity brings subcooled coolant into the core and chimney, which reduces the

116

natural circulation rate due to density difference. However, the natural circulation rate increases immediately because of increased evaporation. Figure 6-6 to Figure 6-8 show the local area-averaged void fraction profile at the core exit, chimney inlet and chimney exit. As can be seen, the void fraction is zero before the vent process. The void fraction at the core exit shown in Figure 6-6 starts to increase after the vent process. Few oscillations are observed during the vent process and cause small flow oscillations. The void fraction in the chimney is smaller than that at the core exit due to bubble condensation. There is more evaporation at the chimney exit than that at the chimney inlet during the vent process. After the vent process, the void fraction at the core exit tends to be stabilized. At this time, the two phase natural circulation is generated and the void fraction increases with power.
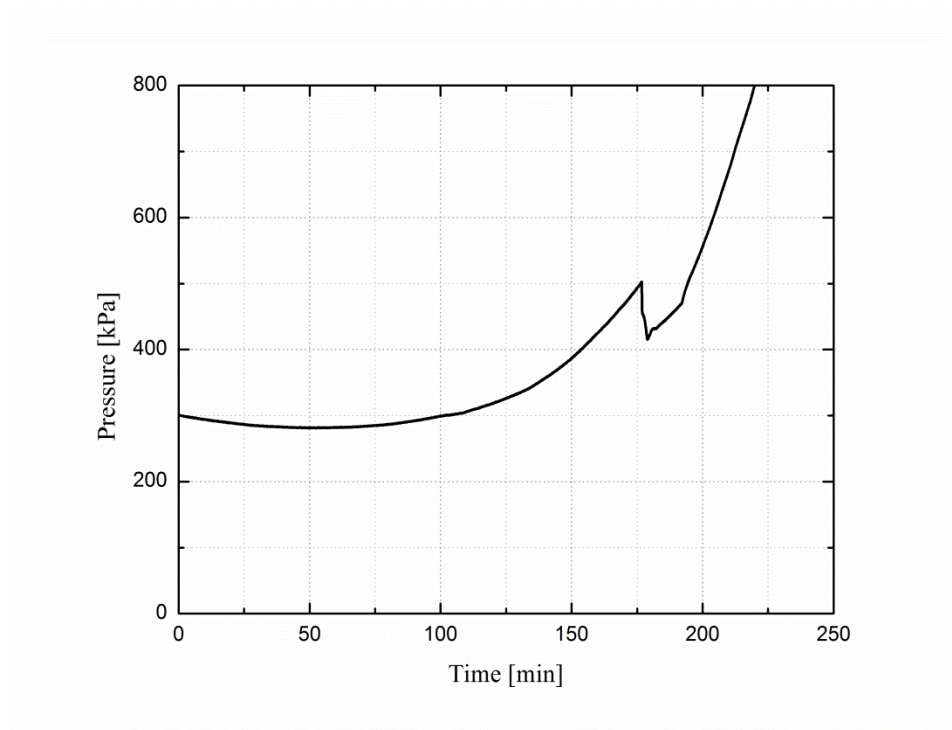
Figure 6-2 Steam Dome Pressure for Pressurized Slow Startup Transient

117
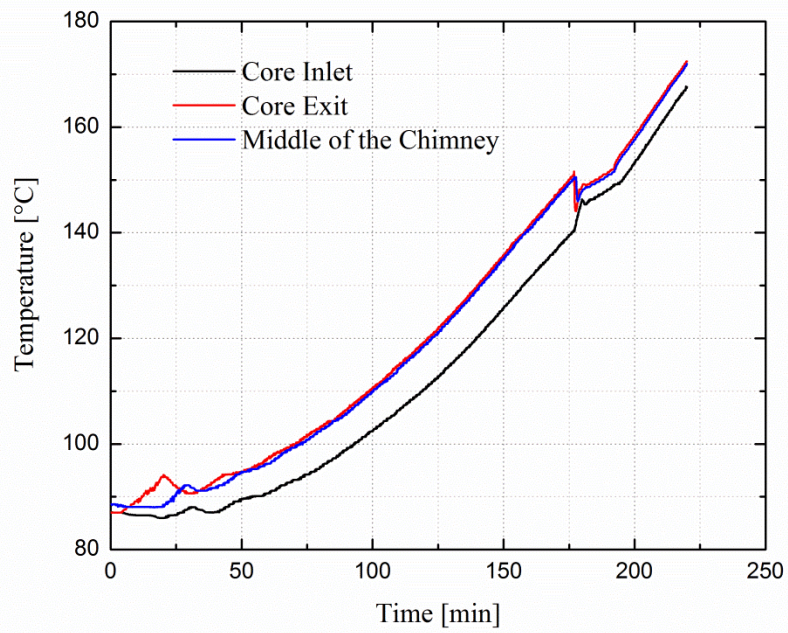
Figure 6-3 Temperatures for Pressurized Slow Startup Transient
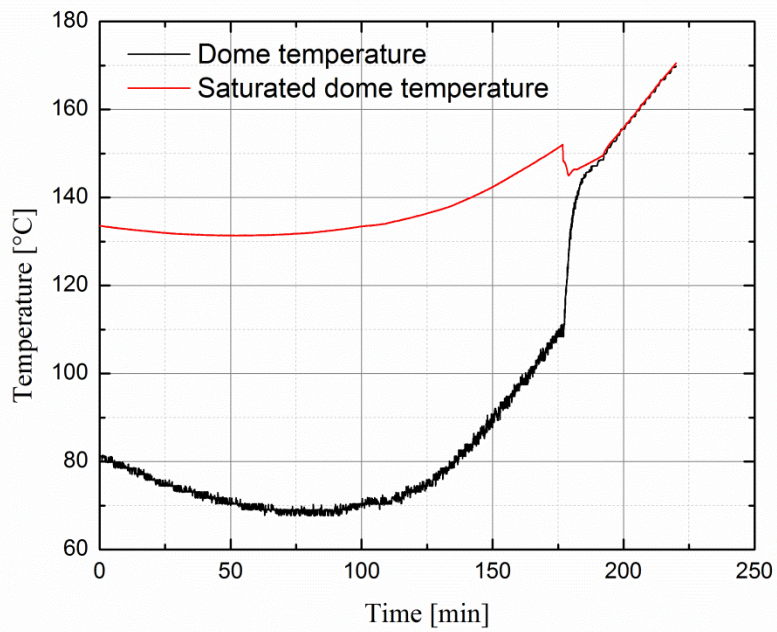
Figure 6-4 Steam Dome Temperatures for Pressurized Slow Startup Transient
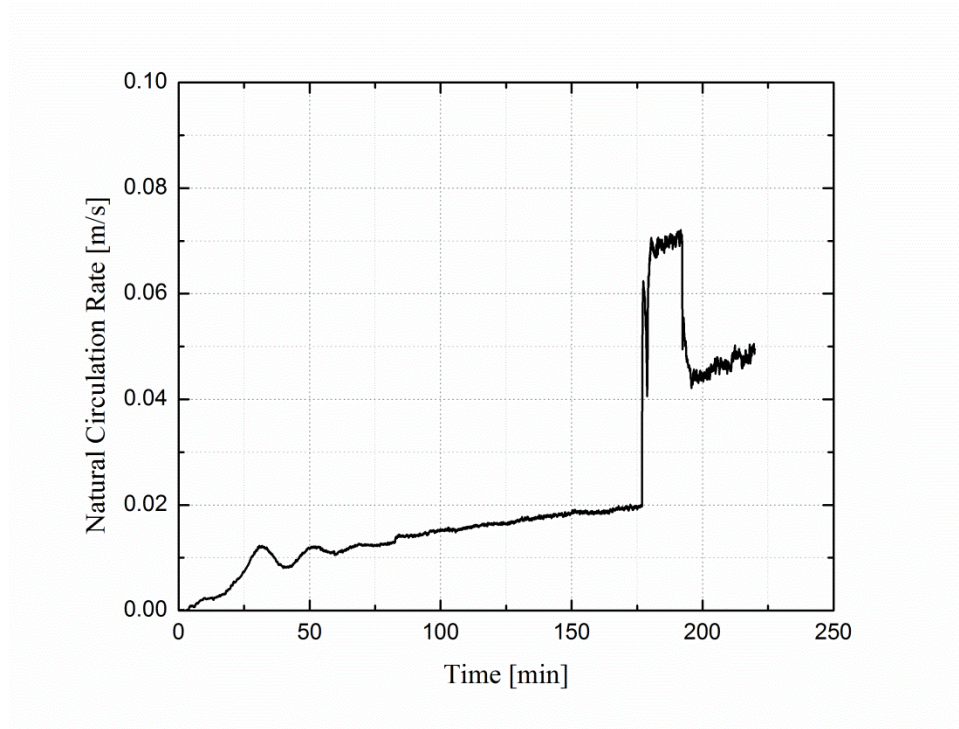
Figure 6-5 Natural Circulation Rate for Pressurized Slow Startup Transient
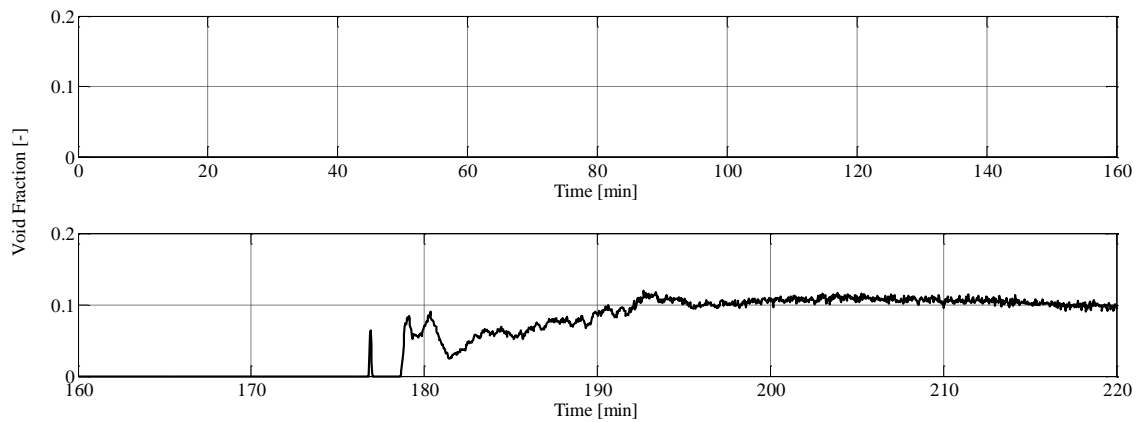
Figure 6-6 Void Fraction at the Core Exit (IMP03) for the Pressurized Slow Startup Transient

119
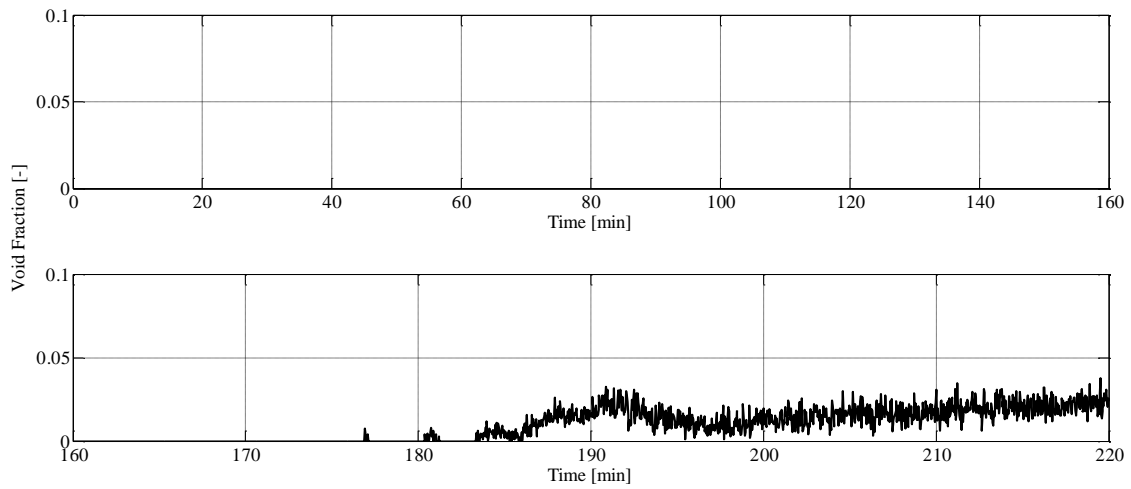
Figure 6-7 Void Fraction at the Chimney Inlet (IMP04) for the Pressurized Slow Startup Transient
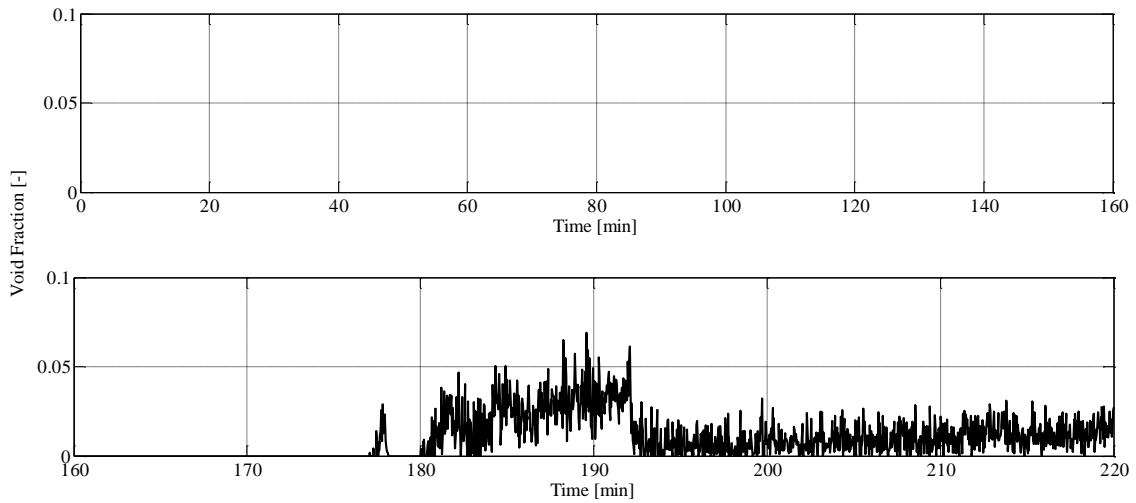
Figure 6-8 Void Fraction at the Chimney Outlet (IMP07) for the Pressurized Slow Startup Transient

6.3. MEDIUM PRESSURIZED STARTUP TRANSIENT TEST

The medium pressurized startup transient is simulated without considering the void reactivity feedback. The power curve tested is given in Figure 6-1. The initial and boundary conditions are the same as those in the pressurized slow startup transient.

The experimental results for the medium startup thermal-hydraulic are shown from Figure 6-9 to Figure 6-14. The general startup transients observed are similar to what occurs in the pressurized slow stratup transients. The three phases are the stable single phase natural circulation, coolant evaporation and two phase natural circulation.

Figure 6-9 shows the steam dome pressure for the fast startup transients. The steam dome pressure increases slowly at the beginning and then rises exponentially after boiling starts. It takes about 150 minutes for the steam dome pressure to increase from initial 0.3 MPa to 0.7 MPa. There is slight pressure drop when the vent valve is open. As can be seen in Figure 6-10 the temperature increases at a rate of about 40 ℃/hr.

Figure 6-11 displays the natural circulation rate for the fast startup transients. The single phase natural circulation phase is from 0 to 130 minutes. The natural circulation rate incrases from 3 cm/s to 8 cm/s during the vent process. After the vent, the velocity decreases to two phase natural circultion rate, which is 6 cm/s.

Combined with the void fraction shown in Figure 6-12, the coolant starts to boiling before the vent process. The void fraction decreases at the beginnging of the vent process and soon increases again. The reason is sudden increased natural circulation rate will compress the boiling in a short time. Later the void fraction raises again due to both evaporation and heating.
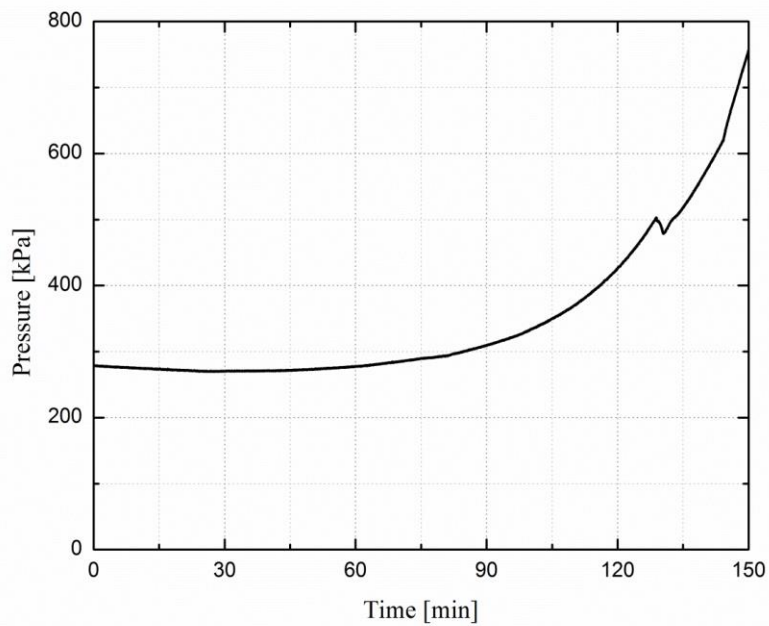
Figure 6-9 Steam Dome Pressure for Pressurized Medium Startup Transient
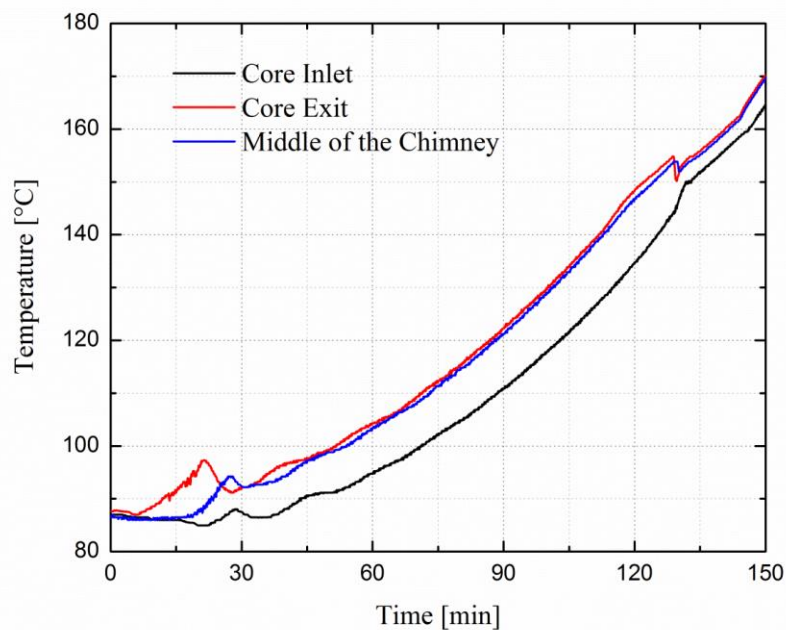
Figure 6-10 Temperatures for Pressurized Medium Startup Transient

122
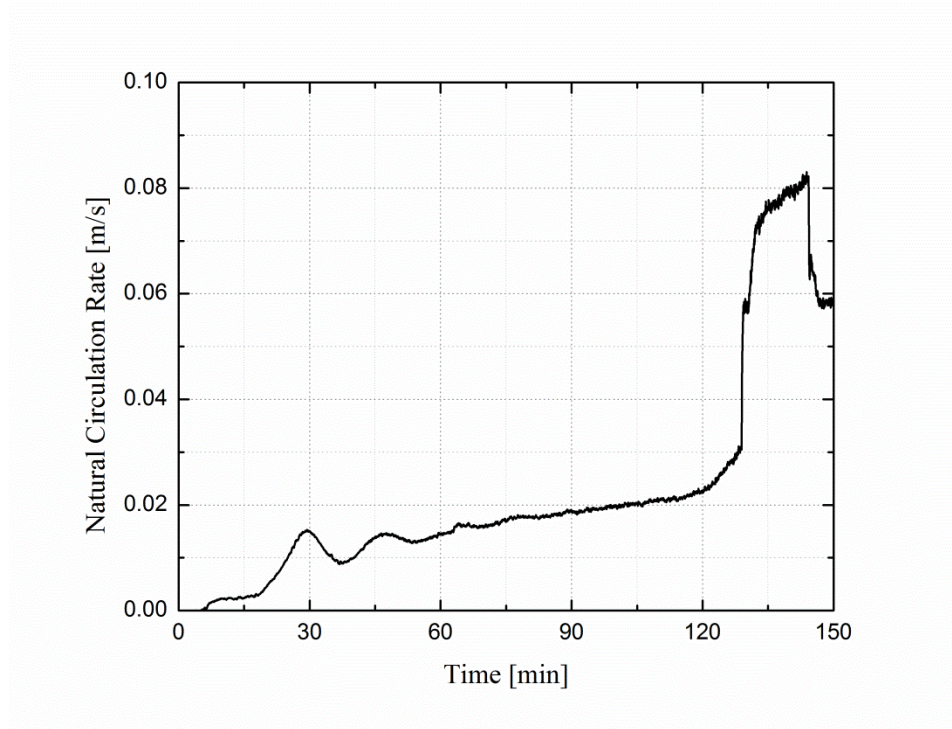
Figure 6-11 Natural Circulation Rate for Pressurized Medium Startup Transient
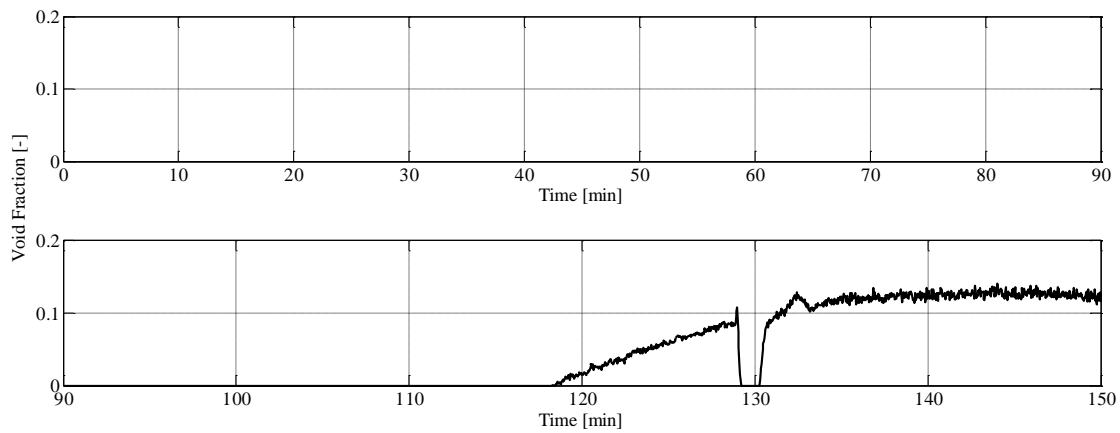
Figure 6-12 Void Fraction at the Core Exit (IMP03) for the Pressurized Medium
Startup Transient
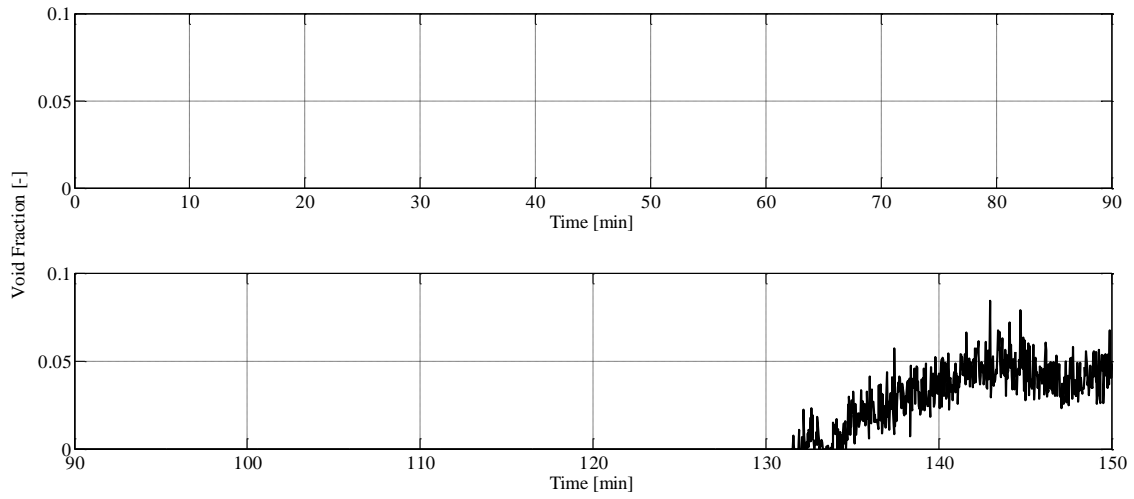
Figure 6-13 Void Fraction at the Chimney Inlet (IMP04) for the Pressurized Medium Startup Transient
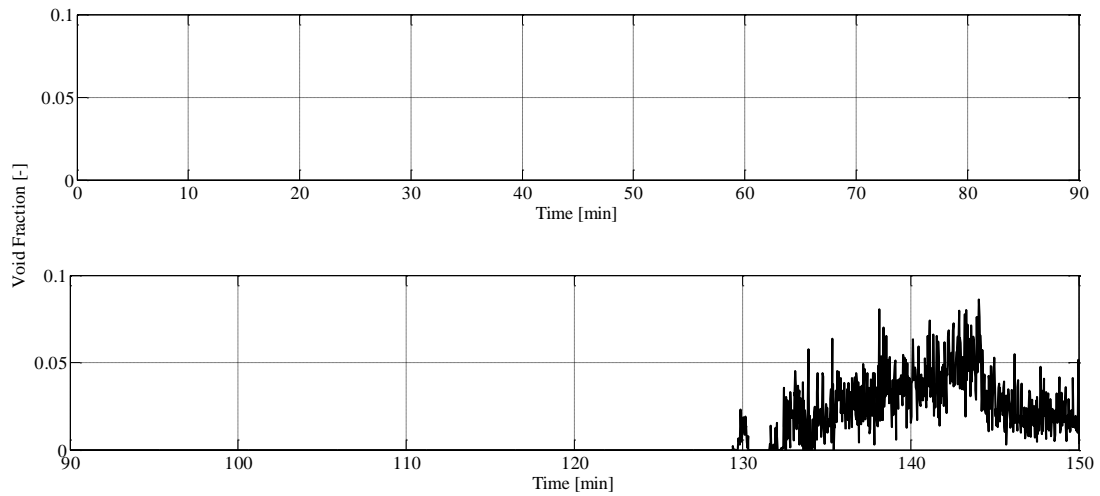
Figure 6-14 Void Fraction at the Chimney Outlet (IMP07) for the Pressurized Medium Startup Transient

6.4. FAST PRESSURIZED STARTUP TRANSIENT TEST

The fast pressurized startup transient is simulated without considering the void reactivity feedback. The power curve tested is given in Figure 6-1. The initial and boundary conditions are the same as those in the pressurized slow startup transient.

The experimental results for the pressurized fast startup thermal-hydraulic are shown from Figure 6-15 to Figure 6-20. The general startup transients observed are similar to what occurs in the pressurized slow stratup transients. The three phases are the stable single phase natural circulation, coolant evaporation and two phase natural circulation.

Figure 6-15 shows the steam dome pressure for the fast startup transients. The steam dome pressure increases slowly at the beginning and then rises exponentially after boiling starts. It takes about 120 minutes for the steam dome pressure to increase from initial 0.3 MPa to 0.7 MPa. There is very small pressure drop when the vent valve is open. As can be seen in Figure 6-16 the temperature increases at a rate of about 45 ℃/hr.

Figure 6-17 displays the natural circulation rate for the fast startup transients. The single phase natural circulation phase is from 0 to 90 minutes. The natural circulation rate incrases from 4 cm/s to 8 cm/s during the vent process. After the vent, the velocity decreases to two phase natural circultion rate, which is 6 cm/s.
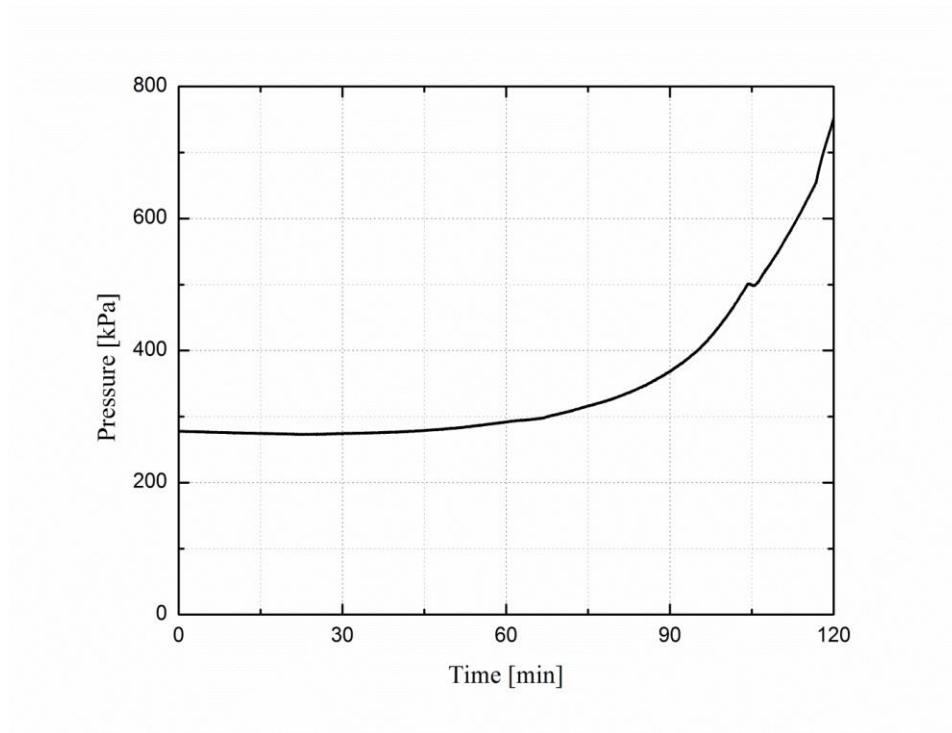
Figure 6-15 Steam Dome Pressure for Pressurized Fast Startup Transient
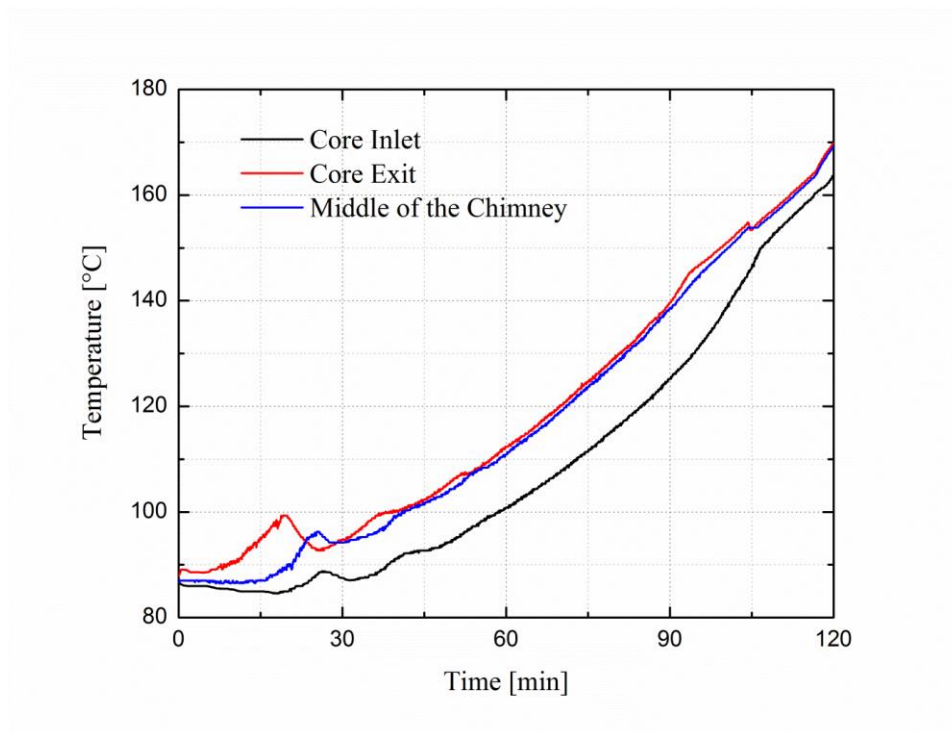
Figure 6-16 Temperatures for Pressurized Fast Startup Transient

126
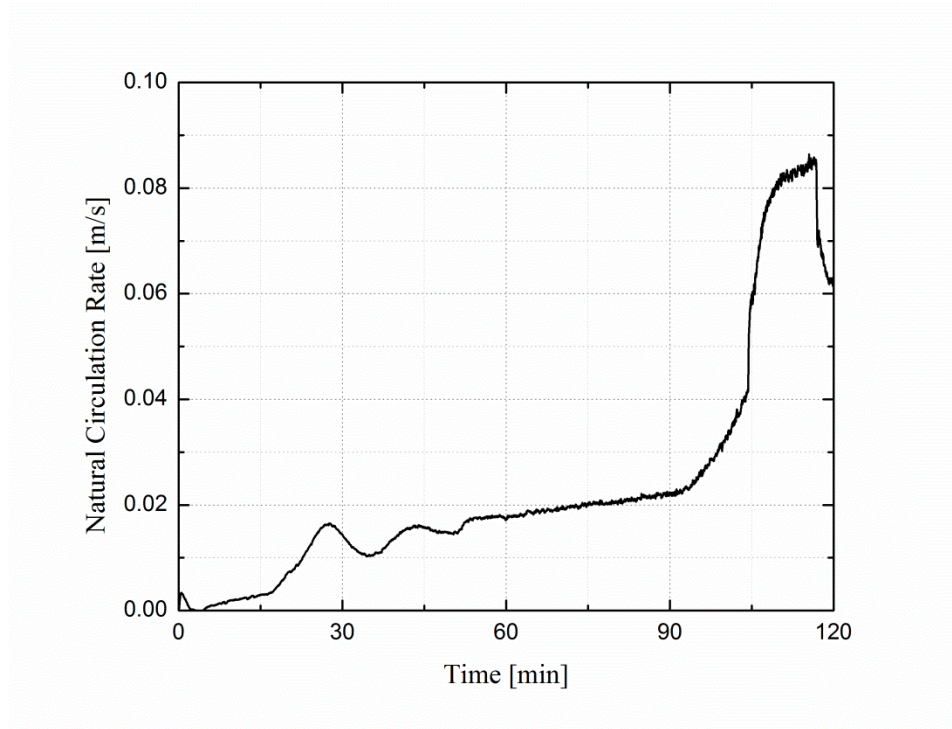
Figure 6-17 Natural Circulation Rate for Pressurized Fast Startup Transient
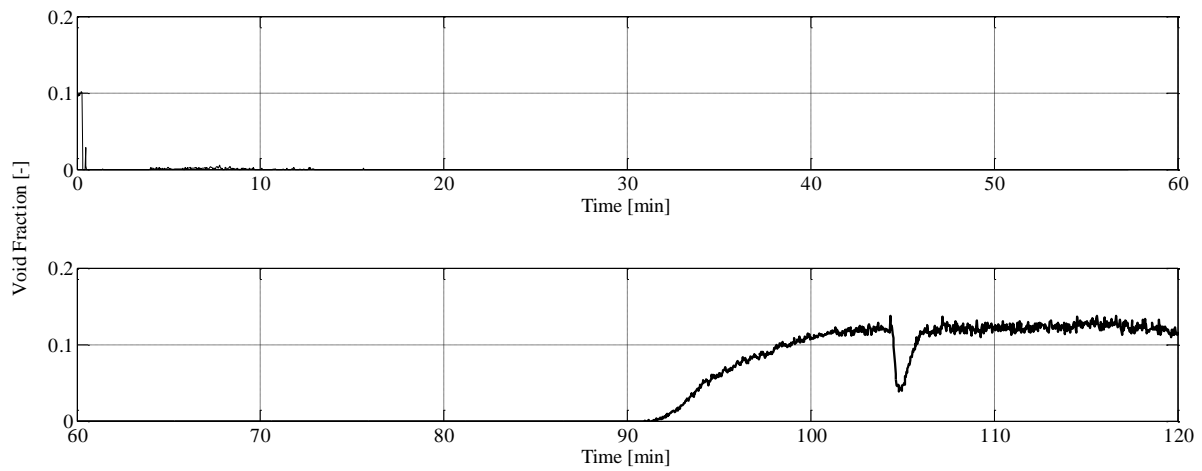
Figure 6-18 Void Fraction at the Core Exit (IMP03) for the Pressurized Fast Startup Transient
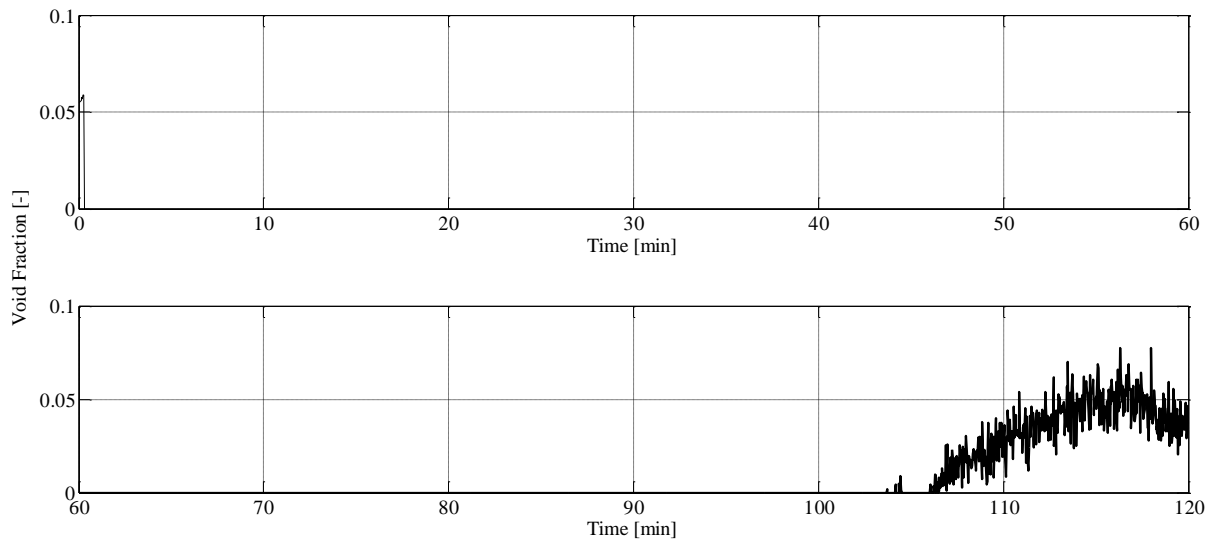
Figure 6-19 Void Fraction at the Chimney Inlet (IMP03) for the Pressurized Fast Startup Transient
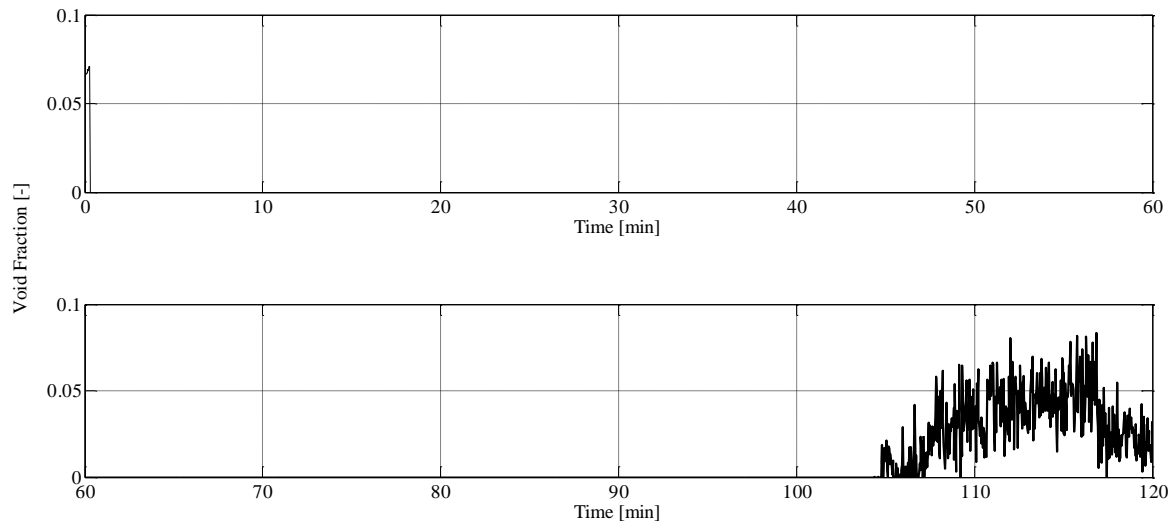
Figure 6-20 Void Fraction at the Chimney Outlet (IMP03) for the Pressurized Fast Startup Transient

7. LOW PRESSURE STEADY STATE TESTS

Flashing instability is the main flow instability observed from previous startup experiments. The flashing instability is caused by the vapor generation in the chimney due to the reduced hydrostatic head at low pressure conditions. Then sudden increased void fraction in the chimney enhances the driving force of natural circulation and therefore increases the mass flow rate. Flashing instability usually occurs during the transition phase, when inlet mass flow rate oscillates between the single-phase natural circulation and the two-phase natural circulation.

The quasi-steady tests are performed at low pressures to obtain the stability maps for the natural circulation boiling water reactor. The system pressure, core heat flux, and void reactivity feedback are investigated on the flow instability for the NMR-50. In order to draw the stability map, the core inlet subcooling and heat flux needs to be controlled to obtain the stable and unstable operating conditions under different flow conditions.

7.1. DESCRIPTION OF EXPERIMENTAL FACILITY

The steady state experimental facility is similar to that of startup transient tests, which is built based on the three level scaling methodology in the previous report submitted to DOE [31]. The detailed schematics of the facilities for the quasi-steady tests are shown in Figure 7-1. In addition, this test facility has another three-phase 18 kW preheater installed at the upstream of the core inlet and another pipe subcooler in the downcomer section. The preheater and subcooler are used to change the inlet subcooling during the tests.
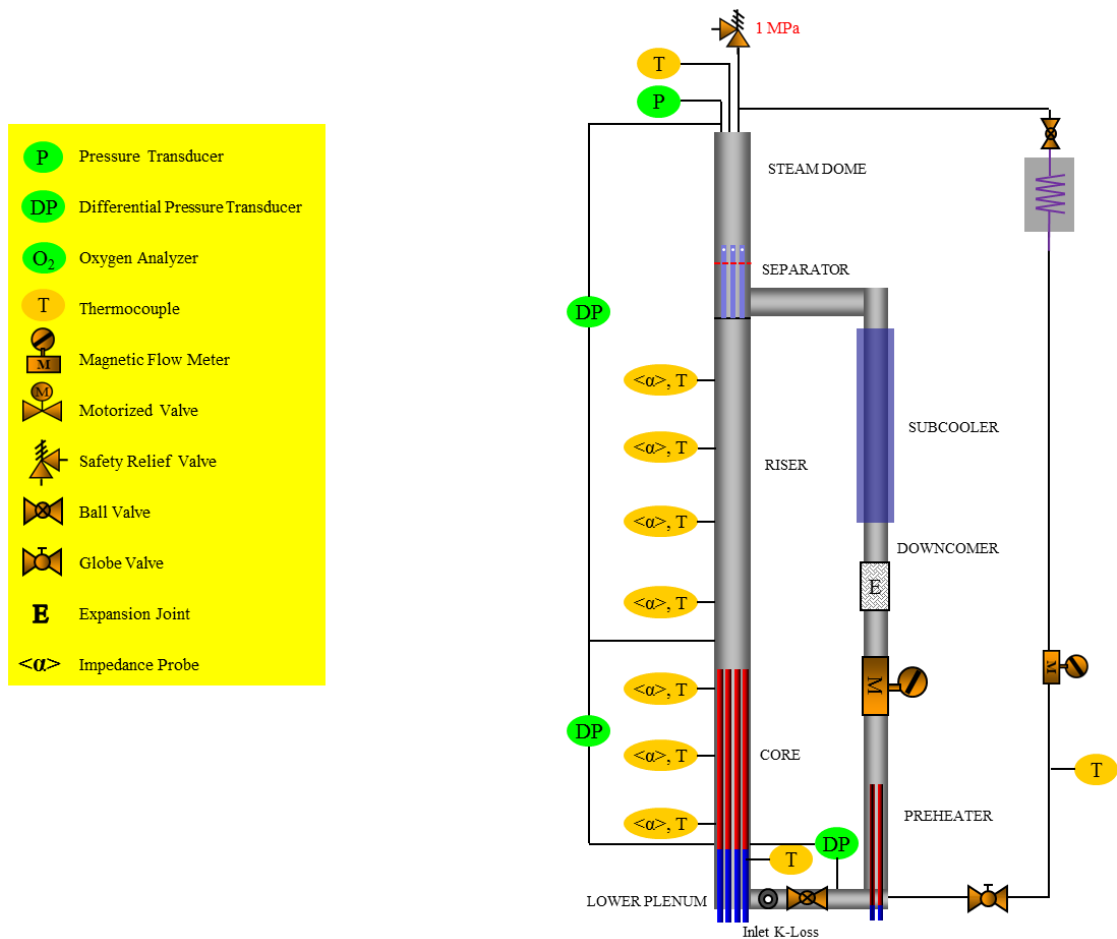
Figure 7-1 Schematic of the Steady State Test Facility

7.2. TEST PROCEDURE

Quasi-steady test procedure consists of a degassing procedure and quasi-steady test procedure. Before each test, general checks are performed. The steps are summarized as follows.

  (1) Check all valves positions
  (2) Turn on the power for the DPs, P-cells, and impedance circuits
  (3) Check differential pressure transducer settings
  (4) Purge each differential pressure transducer
  (5) Check absolute pressure transducer setting
  (6) Check magnetic flow meter
  (7) Check the thermocouples
  (8) Check the data acquisition system

(9) Set up the initial water level for the degassing procedure

(10) Turn on the power supply for main heater and pump (for degassing)

(11) Remove the non-condensable gases completely by heating the loop to 100 ℃

(12) Separate the degassing tank with the test loop and involve the condenser

(13) Set up the initial water level for the quasi-steady test

(14) Perform the final valve position for the inlet flow resistance

(15) Pressurize the test section to certain pressure by heating

(16) Use subcooler to generate single-phase natural circulation

(17) Gradually increase the power of preheater to reduce core inlet subcooling

(18) Stop the tests until stale two-phase natural circulation is reached

7.3 QUASI STEADY STATE TEST FOR NMR-50

In this section, the experimental results for the quasi-steady tests of NMR-50 are presented. The system pressure is defined as the pressure of the core inlet. The tests are performed at system pressure of 200, 400 kPa. The inlet flow resistance is set at $K_{in} = 1200$, which is the value for the normal operating conditions [1].

7.3.1. Stability Criteria

The measured time trace signals can be obtained from the quasi-steady test under different operational conditions. Two main flow instabilities, i.e. flashing instability at low pressure and DWO, can be categorized on the stability map by controlling the inlet subcooling and heat flux. The core inlet flow rate is analyzed to determine if the flow is stable or unstable. And the statistical root mean squared error (RMSE) along with the mean inlet velocity are obtained as

$$\bar{v}_{in} = \frac{1}{n} \sum_{i=1}^{n} v_{in,i}$$

$$v_{in,RMSE} = \sqrt{\frac{\sum_{i=1}^{n} (v_{in,i} - \bar{v}_{in})^2}{n}} \tag{7.1}$$

Furthermore, the frequencies of the flashing instability and DWO are different based on previous results of startup transients. Two criteria are used to classify the flow condition into unstable and stable condition.

1. Flow is stable if the RMSE of the inlet flow velocity is less than 10 % of the mean inlet flow velocity.

2. The unstable boundary can be determined if the amplitude of the flow oscillation starts increasing exponentially rather than keep constant in stable region.

7.3.2. Stability Map

The stability map developed by Ishii [4] using dimensionless subcooling and phase change numbers is now a standard tool to analyze the flow instability. The subcooling number and phase change number indicates the subcooling and the heat input to the system. From the non-dimensionalized steady-state energy equation, the subcooling and heat input to the system can have the relations as

$$N_{Zu} - N_{sub} = x_e \frac{\Delta\rho}{\rho_g}$$

$$\frac{\dot{Q}\Delta\rho}{\dot{m}\Delta i_{fg}\rho_g} - \frac{\Delta i_{sub}\Delta\rho}{\Delta i_{fg}\rho_g} = x_e \frac{\Delta\rho}{\rho_g} \tag{7.2}$$

In the quasi-steady tests, the subcooling number is directly determined by the core inlet temperature and system pressure. And the phase change number is determined by the heat flux and mass flow rate for the natural circulation boiling water reactor, which is quite different from the forced circulation reactor. In natural circulation test facility, the increased heat flux might generate void fraction to increase the natural circulation rate.

7.3.3. Stability Maps at 200 kPa of System Pressure

The stability map at 200 kPa is shown from Figure 7-2 to Figure 7-3. The testing points are plotted in the plane of heat flux and core inlet subcooling number in Figure 7-2, while in the non-dimensional plane of N_{sub}-N_{pch} in Figure 7-3. As

can be seen in Figure 7-2, the testing conditions change from stable single-phase natural circulation to stable two-phase natural circulation. Between two stable phases, the flashing induced intermittent oscillations occur during the transition phase. One stability boundary is drawn between the stable and unstable conditions. The first boundary between the single-phase natural circulation and the transition phase shows linear characteristic. However, the second boundary between the transition phase and the two-phase natural circulation shows non-linear characteristic.

The same amount of testing points is plotted in the non-dimensional plane with the zero quality line at the core exit in Figure 7-3. From Eq. (6.2), the subcooling number is equal to the phase change number in the zero quality line at the core exit. Most testing points are above the zero quality line except few unstable transient points, which means the testing points are in the thermal non-equilibrium conditions. The subcooled boiling induced by flashing in the chimney leads to the intermittent oscillations.

As can be seen in Figure 7-3, the change of phase change number is not sensitive to the decreasing of subcooling number during the single-phase. However, the phase change number reduces substantially when the water in the test section starts to boil. The boundary in the green line between the single-phase and the two-phase is clear shown in the stability map. The two-phase natural circulation points are in the low phase change number region due to larger natural circulation rate compared to single-phase natural circulation rate. The time trace of natural circulation rate at three phases can be seen in Figure 7-4. For both single-phase and two-phase natural circulation, the core inlet flow velocities are stable. However, the flow velocity shows a big peek during the transition phase due to the flashing instability.
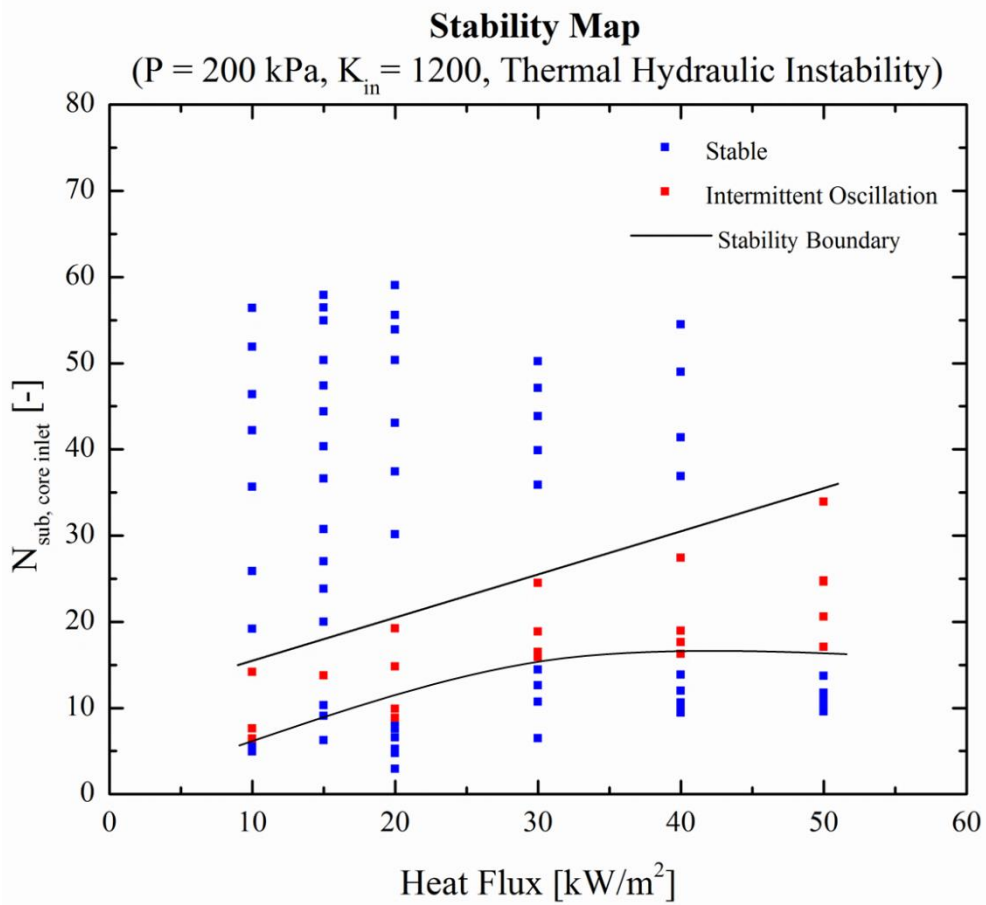
Figure 7-2 Stability Map at 200 kPa (K_{in} = 1200)
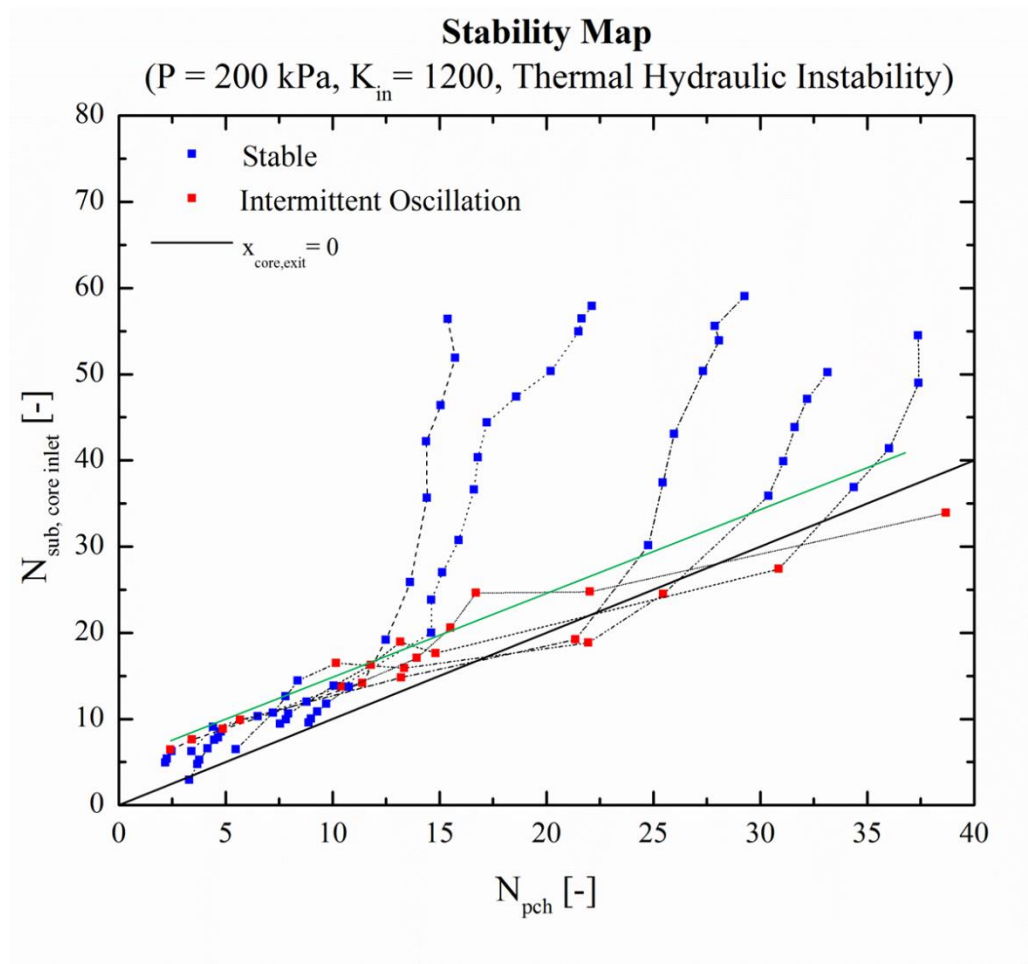
Figure 7-3 Stability Map with Non-dimensional plane (N_{sub}-N_{pch}) at 200 kPa (K_{in} = 1200)
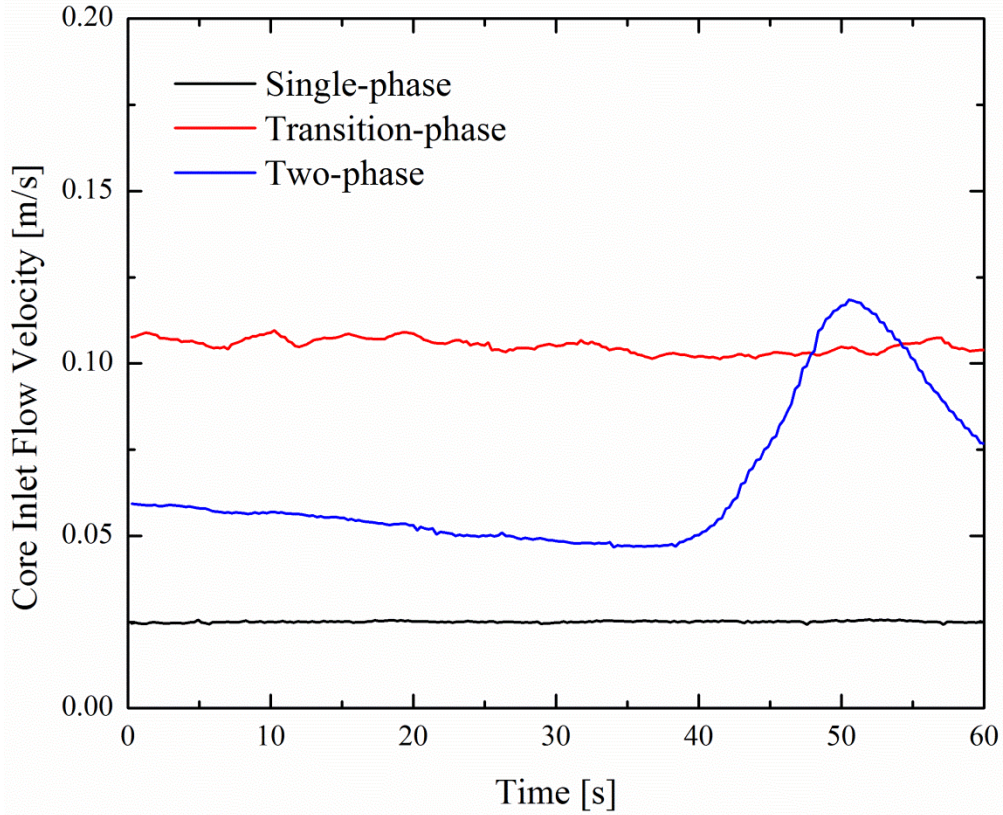
Figure 7-4 Core Inlet Flow Velocity Profile at Different Phases

7.3.4. Stability Maps at 400 kPa of System Pressure

The flashing instability is the main flow instability mechanism observed at the pressure of 200 kPa. In order to investigate the pressure effect on the flow stability, the stability maps at 400 kPa is shown in Figure 7-5. Compared to the stability map at the pressure of 200 kPa, the single-phase stable region is moving toward to the low subcooling area, which means the single-phase stable region is enlarged at the pressure of 400 kPa. And the unstable region of flashing instability is reduced due to the suppression of flashing at higher pressure.

The stability map plotted in the non-dimensional plane of N_{pch}-N_{sub} is shown in Figure 7-6. As can be seen, the general map is similar to the map under 200 kPa. However, the stability boundary between the single-phase natural circulation and

transition phase moves to the zero quality line at the core exit. In other words, the subcooled boiling occurs at low pressure is largely reduced, which moves the boundary to the zero quality line calculated in thermal equilibrium conditions. And the whole unstable region of the transition phase is very thin at this pressure.
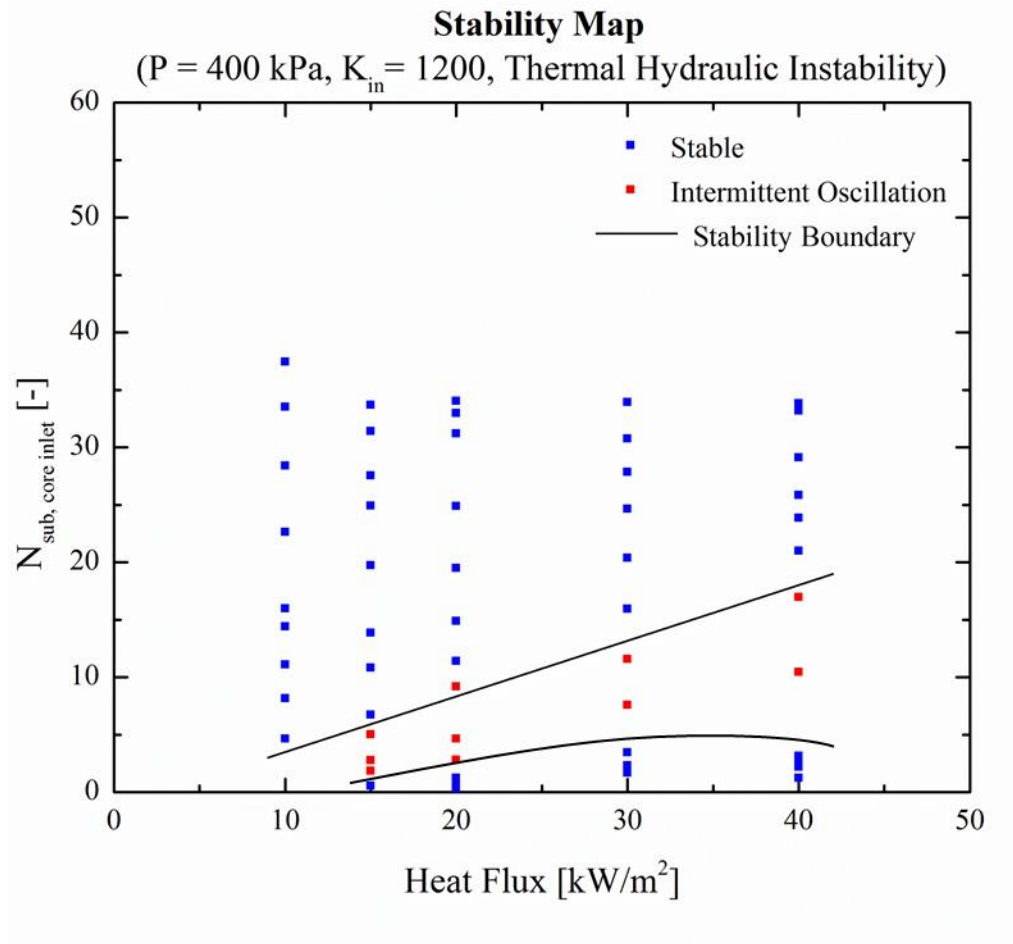
Figure 7-5 Stability Map at 400 kPa

Stability Map
(P = 400 kPa, K_{in} = 1200, Thermal Hydraulic Instability)
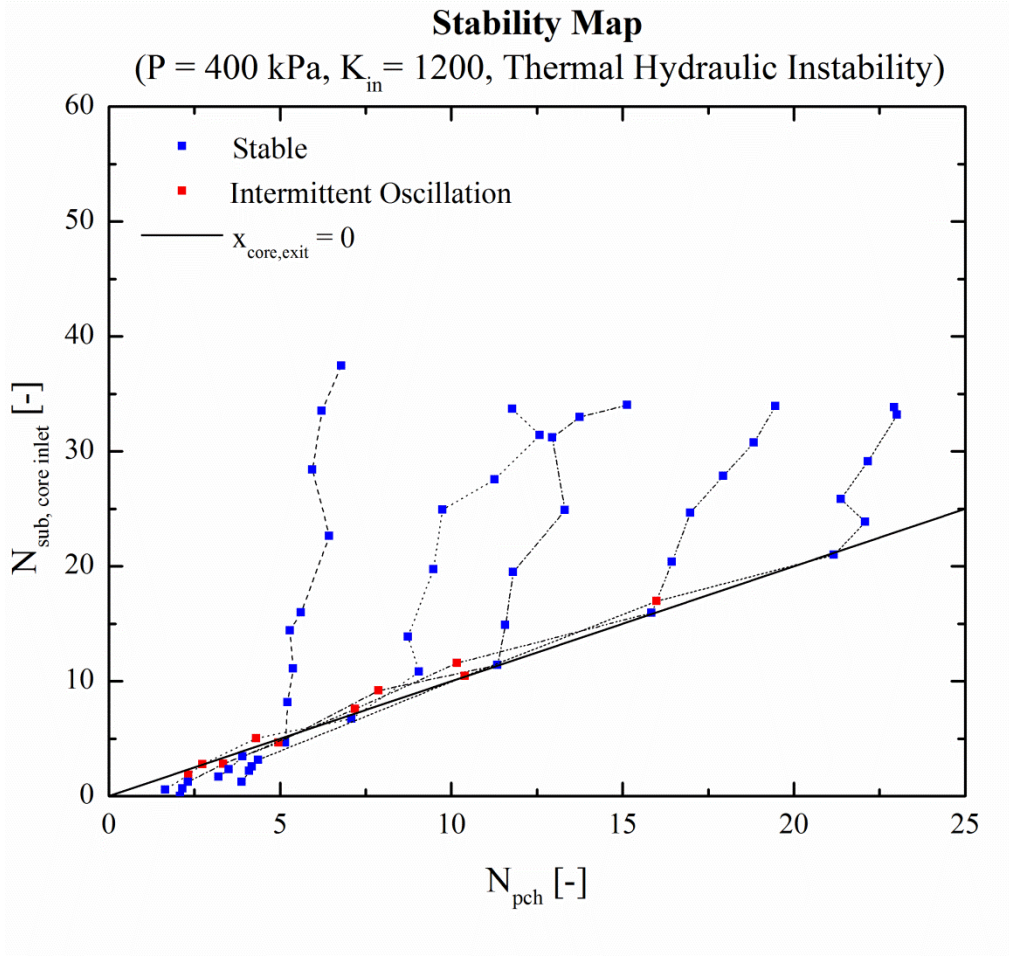
Figure 7-6 Stability Map with Non-dimensional plane (N_{sub}-N_{pch}) at 400 kPa

7.3.5. Stability at different Inlet Flow Resistance

The increase of inlet flow resistance, i.e., inlet K factor, can effectively stabilize the density wave oscillations in a two-phase flow system [4]. However, for a natural circulation system, the increase of the inlet flow resistance brings down the natural circulation rate, which is not beneficial for a natural circulation system. And the effect of increasing inlet flow resistance on the flashing instability boundary is not very clear. In this section, three inlet K factors are investigated on the stability map at the system pressure of 200 kPa. The nominal inlet K factor is 1200 for this test facility based on the experimental calibration. And the inlet K factor can be set at another two values of 600 and 1800 through the ball valve

installed. Figure 7-7 and Figure 7-8 shows the standard stability maps in the dimensionless plane (Nsub-Npch) at another two inlet K factor at the system pressure of 200 kPa.
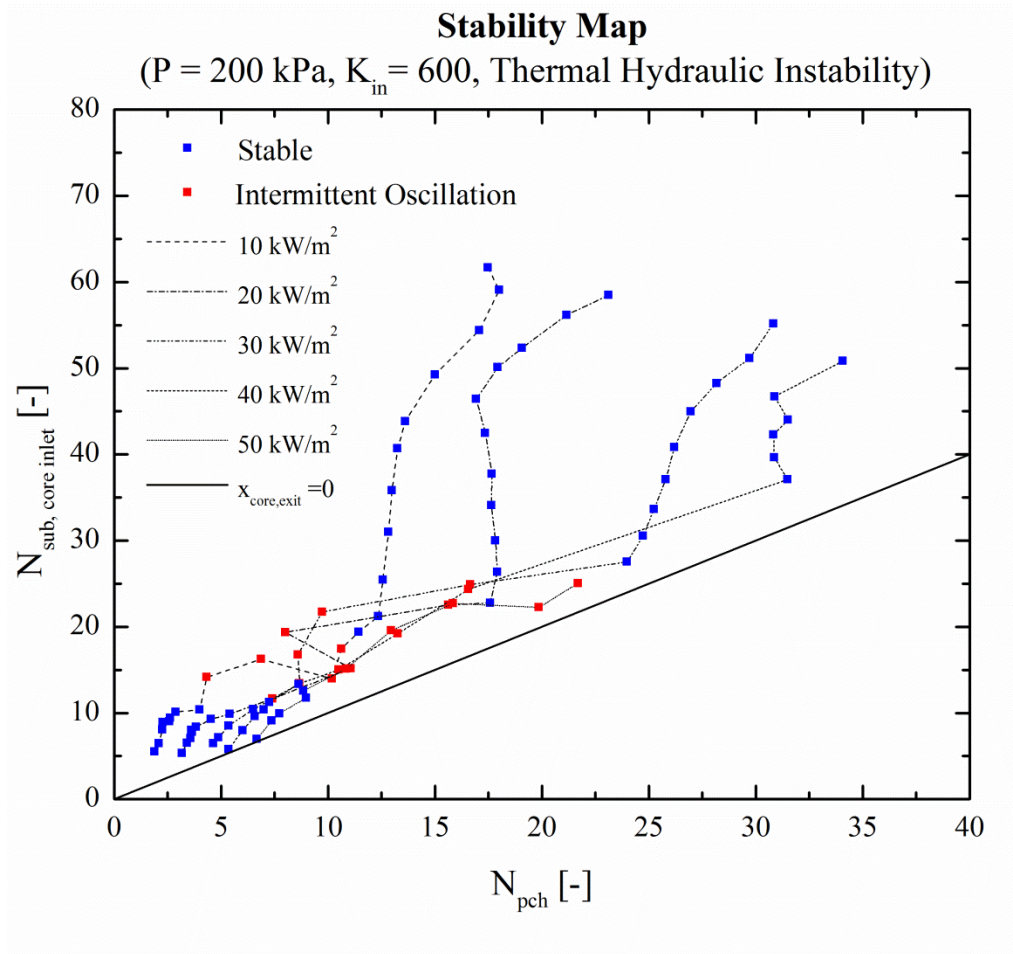
Figure 7-7 Stability Map with Dimensionless Plane (N_{sub}-N_{pch}) at 200 kPa (K_{in} = 600)

Stability Map
(P = 200 kPa, K_{in} = 1800, Thermal Hydraulic Instability)
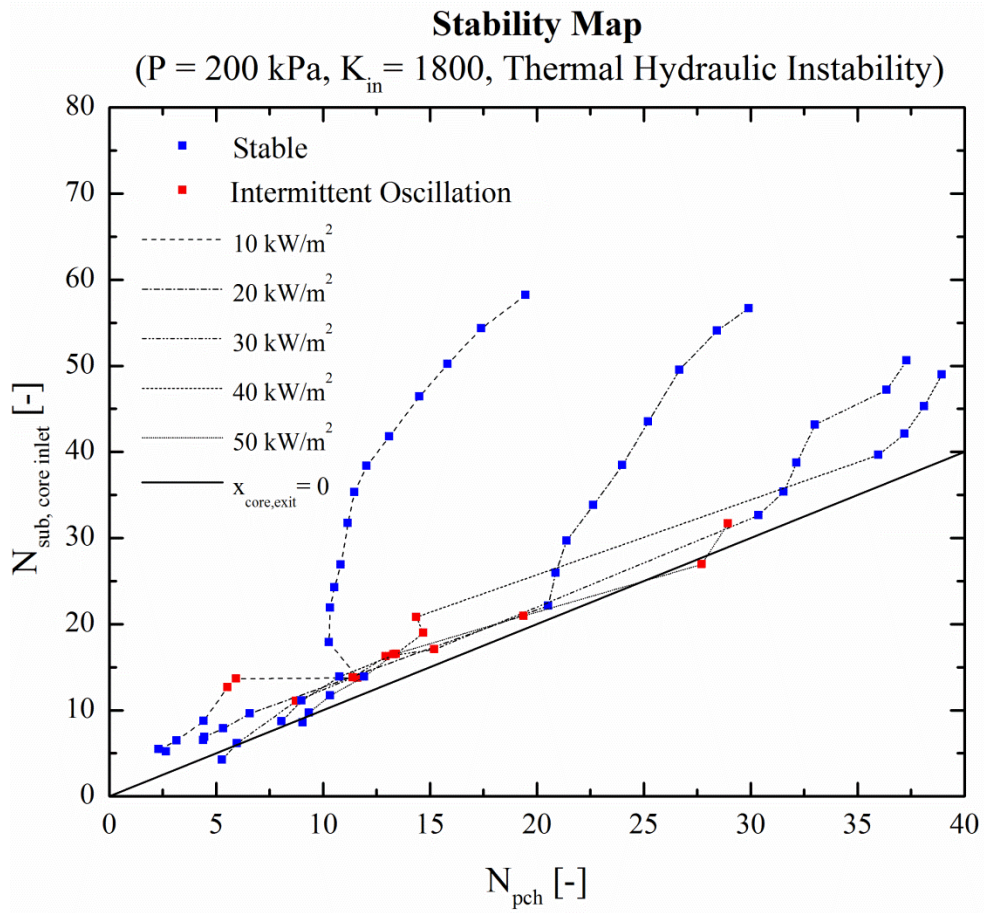
Figure 7-8 Stability Map with Dimensionless Plane (N_{sub}-N_{pch}) at 200 kPa (K_{in} = 1800)

Compared with Figure 7-3, by increasing inlet K factor, the flow system is stabilized in both single-phase and two-phase natural circulation region by comparing the trend of stable points (marked by blue color) at different core power densities. And the transition between the single-phase and two-phase natural circulation flow region becomes much smoother, which can be verified from the distribution of unstable points (marked by red color) in the stability map. Smaller flow velocity means longer residence time in the heated section for the coolant. So the coolant is more uniformly heated in the core section and the system is closer to the equilibrium conditions. However, the increase of inlet pressure drop is not necessarily three times if inlet K factor is increased by three times because velocity would be reduced for natural circulation. So that is why the effect of increasing

inlet flow resistance is not as significant as that in the forced circulation system, where the inlet flow velocity is more or less constant.

7.3.6. Stability Maps for Core-Wide Nuclear Coupling at 400 kPa of System

Pressure

In the previous section, the void reactivity feedback is investigated on the flow instability during the startup transient for different power ramp rate. The conclusion is that the void reactivity feedback has trivial effects on the flow instability during the transition phase, when the flashing instability occurs. The void reactivity feedback might induce the density wave oscillation (DWO) due to power oscillation during the two-phase natural circulation. The flashing induced flow instability has low frequency while the DWO has high frequency owing to conditions of inlet subcooling. In other words, the power oscillations caused by void fraction fluctuation in the core cannot alter the flow regime from transition phase to two-phase natural circulation unless inlet subcooling stabilizes. However, the power oscillations might have influence on the high frequency oscillation.

In order to investigate the void reactivity feedback on the stability map, the quasi-steady tests at 400 kPa are performed by considering the void reactivity feedback. Figure 7-9 shows the stability map with non-dimensional plane at 400 kPa with same other conditions as thermal-hydraulic tests. As can be seen, the boundary between the single-phase and two-phase natural circulation is still the line of $x_{core,exit} = 0$. This stability map confirms that void reactivity feedback can cause the power oscillations but not the change of the stability boundary. Because the DWO is not observed during the quasi-steady tests, the stability boundary considering the void reactivity feedback is not presented in this report.
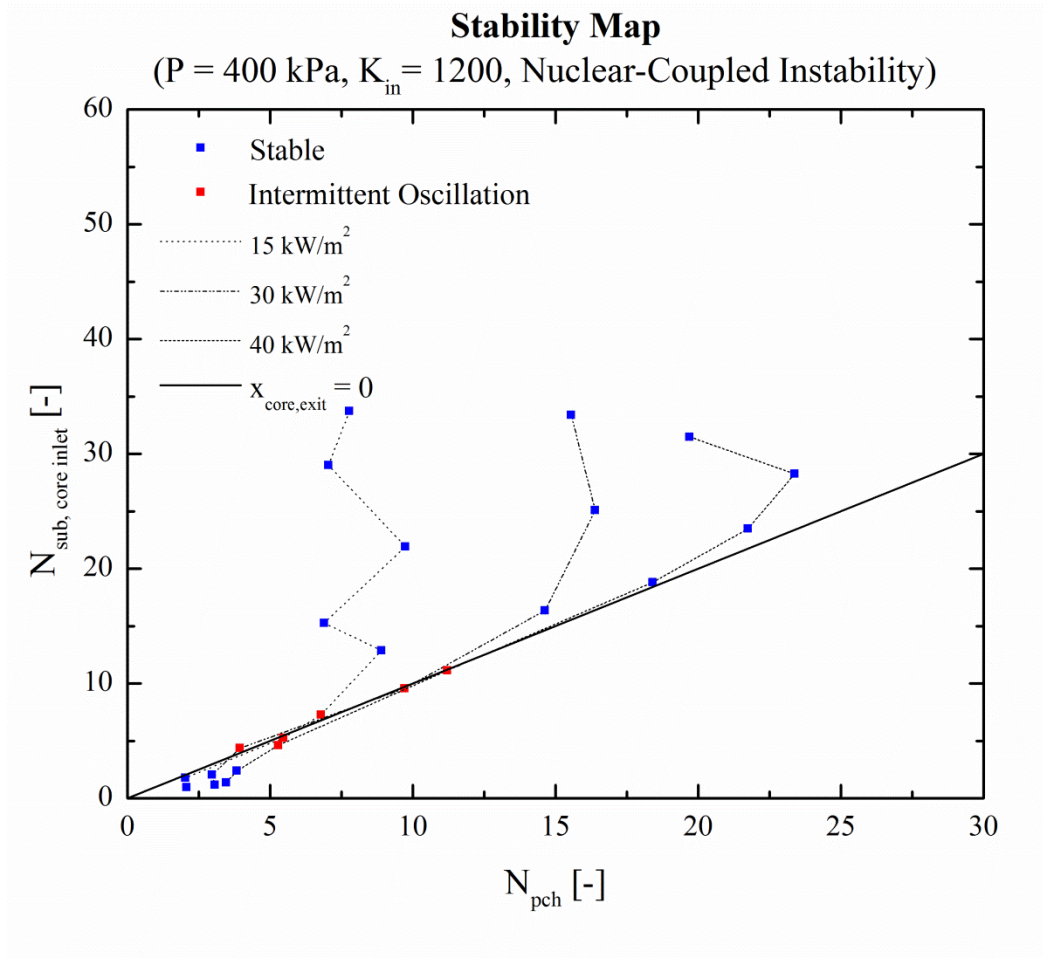
Figure 7-9 Stability Map with Non-dimensional Plane (N_{sub}-N_{pch}) with Nuclear-Coupling at 400 kPa

8.   PERDITION OF INSTABILITY OF BWR-TYPE SMR

The numerical prediction of the flow stability boundary in the frequency domain can be developed and benchmarked with the experimental data. Through small perturbation around the steady state, the transfer function between perturbations of total pressure drop and inlet velocity is obtained. The D-partition method is used to determine the roots of characteristic equation. The goal is to obtain numerical stability boundary or simple analytical criteria to predict the flow instability.

8.1. PREVIOUS THEORETICAL WORK ON PREDICTION OF STABILITY

Linear frequency domain stability analysis is a classical method to study the DWO. The system equations are linearized by small perturbation about steady-state and transfer functions is obtained between perturbed variables.

Teletov and Serov [32] were believed to be the first to formulate the dynamic problem in a two-phase flow system. They were the first to assume that density could be considered as a function of enthalpy only for low-frequency oscillations and thus the momentum equation was decoupled from the continuity equation and energy equation. However, their analysis limited to homogeneous flow model and thermodynamic-equilibrium condition. Later, Serov [33], [34] obtained the characteristic equations by integrating the momentum equation. The stability boundaries were solved from the characteristic equation using the D-partition method.

Boure [35] followed the similar methodology to Serov and integrated the momentum equation. He took account of the variation of the inlet flow and the displacement of the boiling boundary (which was neglected by Serov), but neglected the wall heat capacity (which was included by Serov). His analysis was applicable to thermodynamic equilibrium, homogeneous flow, and low-frequency flow oscillations.

Zuber [36] was the first to formulate the problem in terms of the drift-flux model accounting for the relative velocity between two phases. The formulation of the drift flux model included four constitutive equations and seven constitutive equations. By using small perturbation, a characteristic equation was obtained for a

distributed system. Following the formulation of Zuber, Ishii [4] obtained the similarity groups to characterize the phenomena. Various parameters, such as the heat flux, subcooling, inlet velocity, pressure, inlet and exit orificing, were investigated on the stability boundary. Furthermore, the effects of non-uniform heat flux, relative velocity, and static and dynamic friction factor were discussed.

Saha [37] extended Ishii's work and incorporated the effect of the thermal non-equilibrium. Compared to Ishii's thermal equilibrium model, the obtained stability boundary predicted a more stable system at low subcooling number and a more unstable system at high subcooling number. Babelli [38] incorporated the vapor generation due to flashing in the chimney to the model to predict the stability boundary of PUMA RPV. Kuran [5] took into account for the void reactivity feedback in the linear stability analysis for the NCBWR. However, the effect of flashing in chimney was neglected.

Yadigaroglu and Bergles [39] tried to explain the high-order DWO through frequency domain analysis. In single-phase region, transfer functions of the flow to enthalpy considered the effects of the wall heat storage and pressure variations on the shift of boiling boundary. While in two-phase region, the Lagrangian description of hydrodynamics was established to save great computation time. Lahey and Yadigaroglu [40] predicted the onset of DWO through method of characteristics in BWR including heater wall dynamics, boiling boundary dynamics, and nuclear kinetics.

Inada et al. [41], [42] investigated the thermo-hydraulic instability induced by flashing analytically, and the results were compared with the experimental data [43]. An analytical model using drift-flux model to analyze linear stability was developed.

Rui Hu [44] developed the FISTAB code in the frequency domain considering the flashing-induced stability. The SISTAB code prediction was benchmarked with the experimental results from the SIRIUS-N [45] test facility.

8.2. FORMULATION OF THE PROBLEM

In order to predict the observed flow instability in the experiments analytically, the mathematical model is developed following Ishii's formulation of the DWO [4]. The improved model aims to be capable of predicting the flashing instability and

DWO for the NMR-50. The system of interest basically consists of four components of the NMR-50 shown in Figure 8-1:

A) Single-phase upstream unheated section
B) Single-phase heated section
C) Two-phase heated section
D) Two-phase unheated section
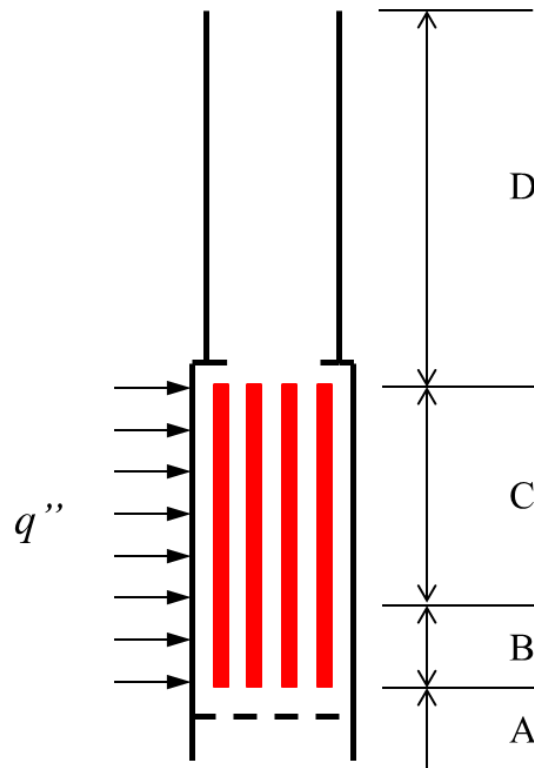
Figure 8-1 System Used for Analysis of Flow Instability

The kinematics and dynamics of the first three regions are addressed by Ishii [4] for the DWO without considering the flashing effects in the chimney at high pressure. However, the flashing effect is dominant at lower pressure, especially during the startup transients. The saturated water at the core exit becomes superheated under the reduced hydrostatic head in the chimney. The void fraction increases in the chimney section due to flashing. If this void fraction increase due to flashing is considered as uniformly heating source along the chimney, the method used for the heated mixture region (Region C) by Ishii [4] can be adopted to derive the kinematics of the downstream un-heated region (D). Before the derivation of the characteristic equation in the Region (D), two different methods, i.e. Lagrangian and Eulerian specification of the flow field, to describe the

145

enthalpy of the fluid particle are illustrated in Figure 8-2 and Figure 8-3. In Figure 8-2, the particle enters region (A), (B), (C), and (D) at τ_0, τ_1, τ_2, and τ_3, respectively. The residence time between two time points in is also called time lag, which is significantly related to the propagation of the disturbances. In Figure 8-3, the time lags are replaced by the space lags, which define the physical boundaries between two regions. One specially important space lag is the boundary between the single-phase liquid and two-phase mixture and is denoted by λ corresponding to the time lag τ_{12}.
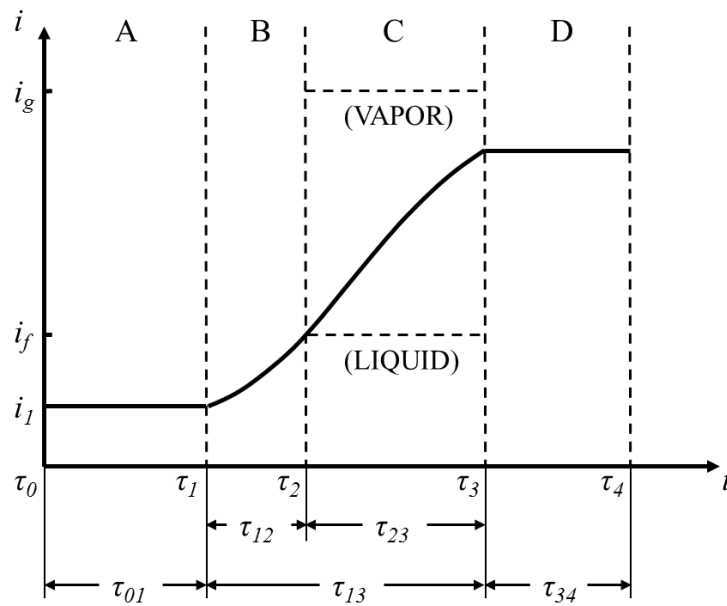
Figure 8-2 Lagrangian Description of Enthalpy

146
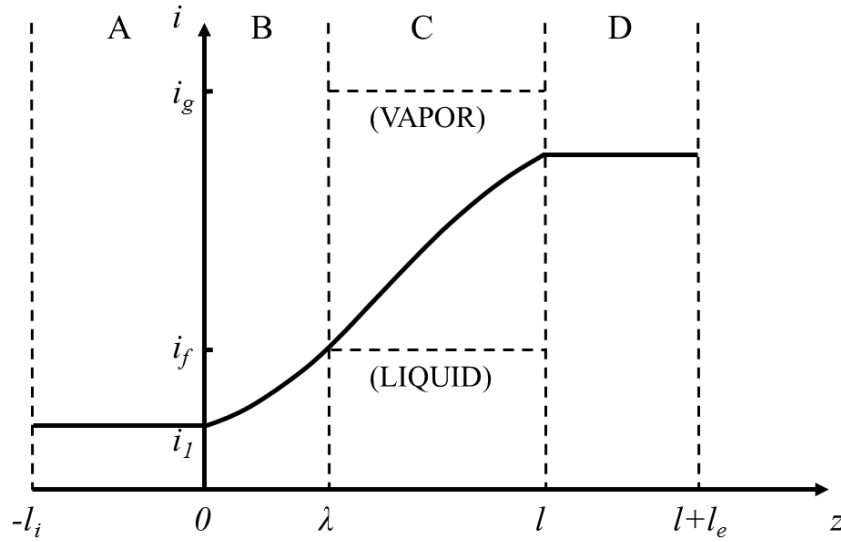
Figure 8-3 Eulerian Description of Enthalpy

8.3. CHARACTERISTIC EQUATION AND STABILITY BOUNDARY

The transfer function is obtained through small perturbation around steady state. The disturbance will be given in the form of a core inlet velocity perturbation. With proper initial and boundary conditions, the transfer function shown in Eq. (8.1) can be obtained between the perturbation of pressure drop and inlet velocity.

$$\delta v = \frac{1}{Q(s)} \delta \Delta P_{ex} \qquad (8.1)$$

where $Q(s)$ is the characteristic equation. According to control theory, the asymptotic stability of the system can be determined by nature of roots of the characteristic equation given by

$$Q(s) = 0 \qquad (8.2)$$

The characteristic equation can be formulated in a series of dimensionless numbers as

$$Q\left(s^*, \alpha_1, \alpha_2, \cdots, \alpha_n\right) = 0 \qquad (8.3)$$

where α_1 to α_n are independent dimensionless numbers. For the reactor stability analysis, the Zuber number and inlet subcooling number are chosen in the stability plane [4]. If the harmonic oscillations are considered, system response can be obtained by substituting $s^* = j\omega^*$ into Eq. (8.3) as

147

$$Q\left(j\omega^*, N_{Zu}, N_{sub}\right) = Q_{\mathrm{Re}}\left(\omega^*, N_{Zu}, N_{sub}\right) + jQ_{\mathrm{Im}}\left(\omega^*, N_{Zu}, N_{sub}\right) = 0 \tag{8.4}$$

Thus, Eq. (8.4) reduces to

$$Q_{\mathrm{Re}}\left(\omega^*, N_{Zu}, N_{sub}\right) = 0 \tag{8.5}$$

$$Q_{\mathrm{Im}}\left(\omega^*, N_{Zu}, N_{sub}\right) = 0 \tag{8.6}$$

Equations (8.5) and (8.6) give the harmonic frequency surfaces in the dimensionless plane of N_{sub}-N_{Zu}. The D-partition method states that the number of roots lying in the right half s^* plane for each region divided by surfaces do not change within a subdivision. Since the stability curve is determined, the stability of each region can be determined by testing the stability at any point in that region using certain stability criteria such as Mikhailov Criterion used by Ishii [4].

8.4. KINEMATICS OF THE DOWNSTREAM UN-HEATED REGION (D)

8.4.1. Volumetric Flux Equation and Density Propagation Equation

In this section, the mixture velocity and mixture property are given in the form of steady part and the perturbation part. The continuity equations, i.e., volumetric flux equation and density propagation equation, for this region are expressed in the following form

$$\frac{\partial j_e}{\partial z} = \Gamma_{g,fl} \frac{\Delta\rho}{\rho_g \rho_f} \tag{8.7}$$

and

$$\frac{\partial \rho_{me}}{\partial t} + C_{ke} \frac{\partial \rho_{me}}{\partial z} = -\Gamma_{g,fl} \frac{\Delta\rho\rho_{me}}{\rho_g \rho_f} \tag{8.8}$$

where

$$C_{ke} = j_e + V_{gje} \tag{8.9}$$

$$j_e = v_{me} + (\frac{\rho_f}{\rho_{me}} - 1)V_{gje} \tag{8.10}$$

$$\Gamma_{g,fl} = \frac{c_{pf}(T_3 - T_4)(1 - \overline{\alpha})\overline{v}_{m,l}\rho_f}{l_e \Delta i_{fg}} \tag{8.11}$$

j_e, C_{ke}, and V_{gje} is the volumetric flux of the mixture, kinematic wave velocity, drift velocity between two phases in this region, respectively. $\Gamma_{g,fl}$ is the vapor generation rate due to flashing in this region. T_3 and T_4 are the saturation temperatures corresponding to the pressures at the bottom and top of the chimney section, which are denoted by p_3 and p_4. $\overline{\alpha}$ and $\overline{v}_{m,l}$ are the steady state void fraction and mixture velocity at the exit of heated section. l_e is the axial length of the downstream un-heated section. The characteristic frequency is expressed as

$$\Omega_e = \Gamma_{g,fl} \frac{\Delta\rho}{\rho_g \rho_f} \tag{8.12}$$

8.4.2. Kinematic Wave Velocity

The integration of Eq. (8.7) gives

$$j_e(z,t) = j_e(l,t) + \Omega_e(z-l) \tag{8.13}$$

By expanding ρ_{me} into $\overline{\rho}_{me} + \delta\rho_{me}(t)$ at the exit of the heated section, the equations for C_{ke} becomes

$$
\begin{aligned}
C_{ke}(z,t) &= \overline{C}_{ke}(z) + \delta C_{ke}(t) \\
&= j_e(l,t) + V_{gje} + \Omega_e(z-l) \\
&= v_{me}(l,t) + (\frac{\rho_f}{\rho_{me}(l,t)} - 1)V_{gje} + V_{gje} + \Omega_e(z-l) \\
&= \overline{v}_{me}(l) + \frac{\rho_f}{\overline{\rho}_{me}(l)}V_{gje} + \Omega_e(z-l) + \delta v_{me}(l,t) - \frac{\rho_f}{[\overline{\rho}_{me}(l)]^2}V_{gje}\delta\rho_{me}(l,t)
\end{aligned}
\tag{8.14}
$$

where V_{gje} is assumed as a constant in this region. The steady state part and the perturbation part of C_{ke} can be written as

$$\overline{C}_{ke}(z) = \overline{v}_{me}(l) + \frac{\rho_f}{\overline{\rho}_{me}(l)}V_{gje} + \Omega_e(z-l) \tag{8.15}$$

$$\delta\overline{C}_{ke}(t) = \delta v_{me}(l,t) - \frac{\rho_f}{[\overline{\rho}_{me}(l)]^2}V_{gje}\delta\rho_{me}(l,t) \tag{8.16}$$

And the perturbation of mixture velocity and mixture density was given in Ishii's thesis [4].

$$\delta v_{me}(l,t) = \varepsilon e^{st}[\frac{A_c}{A_e}]\Lambda_5(l,s) \tag{8.17}$$

$$\delta \rho_{me}(l,t) = \varepsilon e^{st}\rho_f \Lambda_6(l,s) \tag{8.18}$$

so

$$\delta \overline{C}_{k,e}(t) = \varepsilon e^{st}\Lambda_{20}(l,s) \tag{8.19}$$

and

$$\Lambda_{20}(l,s) = [\frac{A_c}{A_e}]\Lambda_5(l,s) - [\frac{\rho_f}{\rho_{me}(l)}]^2 V_{gje}\Lambda_6(l,s) \tag{8.20}$$

8.4.3. Response of Mixture Density

By now the kinematic wave velocity is solved and can be substituted into Eq. (8.8) to obtain the density of the mixture. Usually a new variable is defined in this region as

$$\phi_e(z,t) = \ln[\frac{\rho_{me}(z,t)}{\rho_{me}(l)}] \tag{8.21}$$

So the density propagation Equation (8.8) becomes

$$\frac{\partial \phi_e}{\partial t} + C_{ke}(z,t)\frac{\partial \phi_e}{\partial z} = -\Omega_e \tag{8.22}$$

In order to apply perturbation method, we define

$$\phi_e(z,t) = \overline{\phi}_e(z) + \delta\phi_e(z,t) \tag{8.23}$$

and

$$\rho_{me}(z,t) = \overline{\rho}_{me}(z) + \delta\overline{\rho}_{me}(z,t) \tag{8.24}$$

By using the order of magnitude analysis, $\overline{\phi}_e(z)$ and $\delta\phi_e(z,t)$ can be expressed as

$$\overline{\phi}_e(z) = \ln[\frac{\overline{\rho}_{me}(z)}{\rho_{me}(l)}] \tag{8.25}$$

$$\delta\phi_e(z,t) = \frac{\delta\rho_{me}}{\overline{\rho}_{me}(z)} \tag{8.26}$$

Substituting Eq. (8.23) and (8.14) into Eq. (8.22) and using the perturbation method, the zeroth order and first order equations are expressed as

$$\overline{C}_{ke}(z)\frac{d\overline{\phi}_e}{dz} = -\Omega_e \tag{8.27}$$

150

and

$$\frac{\partial \delta\phi_e}{\partial t} + \overline{C}_{ke}(z)\frac{\partial \delta\phi_e}{\partial z} = \delta\overline{C}_{ke}(t)\frac{\Omega_e}{\overline{C}_{ke}(z)} \tag{8.28}$$

Integrating Equation (8.27) from l to z, then

$$\overline{\phi}_e(z) - \overline{\phi}_e(l) = -\Omega_e \int_l^z \frac{1}{\overline{C}_{ke}(z)}dz = -\int_l^z \frac{d\overline{C}_{ke}(z)}{\overline{C}_{ke}(z)} = -\ln[\frac{\overline{C}_{ke}(z)}{\overline{C}_{ke}(l)}] \tag{8.29}$$

Comparing Eq. (8.25) and (8.29), the following equation can be obtained.

$$\frac{\overline{\rho}_{me}(z)}{\overline{\rho}_{me}(l)} = \frac{\overline{C}_{ke}(l)}{\overline{C}_{ke}(z)} \tag{8.30}$$

The solution of the perturbed part for the mixture density can be solved by transforming Eq. (8.28) to Lagrangian form as

$$dt = \frac{dz}{\overline{C}_{ke}(z)} = \frac{\overline{C}_{ke}(z)d(\delta\phi_e)}{\delta C_{ke}(t)\Omega_e} \tag{8.31}$$

If the particle entering the bottom of the chimney at $t = \tau_3$, the first equality in Eq. (8.31) can be integrated as

$$t - \tau_3 = \int_l^z \frac{dz}{\overline{C}_{ke}(z)} \tag{8.32}$$

The right hand side of Eq. (8.32) is redefined as

$$E_e(z) = \int \frac{dz}{\overline{C}_{ke}(z)} \tag{8.33}$$

Thus Eq. (8.32) becomes

$$t = \tau_3 + E_e(z) - E_e(l) \tag{8.34}$$

The second equality of Eq. (8.31) can be written as

$$d(\delta\phi_e) = \frac{\delta C_{ke}(t)}{[\overline{C}_{ke}(z)]^2}d\overline{C}_{ke}(z) = \varepsilon e^{st}\Lambda_{20}(l,s)\frac{1}{[\overline{C}_{ke}(z)]^2}d\overline{C}_{ke}(z)$$

$$= \varepsilon e^{s\tau_3}e^{s[E_e(z)-E_e(l)]}\frac{\Lambda_{20}(l,s)}{[\overline{C}_{ke}(z)]^2}d\overline{C}_{ke}(z) \tag{8.35}$$

By defining $H_e(z,s)$ as

$$H_e(z,s) = \int e^{s[E_e(z)-E_e(l)]}\frac{1}{[\overline{C}_{ke}(z)]^2}d\overline{C}_{ke}(z) \tag{8.36}$$

Integrating Eq. (8.35) from l to z, the following equation can be obtained.

$$\delta\phi_e(z,\tau_3) - \delta\phi_e(l) = \varepsilon e^{s\tau_3}\Lambda_{20}(l,s)[H_e(z,s) - H_e(l,s)] \tag{8.37}$$

Thus $\phi_e(z,\tau_3)$ in the region (D) is expressed as

151

$$\phi_e(z, \tau_3) = \overline{\phi}_e(z) + \delta\phi_e(z, \tau_3)$$

$$= \ln[\frac{\overline{C}_{ke}(l)}{\overline{C}_{ke}(z)}] + \{\delta\phi_e(l) + \varepsilon e^{s\tau_3}\Lambda_{20}(l,s)[H_e(z,s) - H_e(l,s)]\} \tag{8.38}$$

And the boundary conditions for the $\phi_e(z,t)$ are given as

$$\phi_e(l, \tau_3) \approx 0 \tag{8.39}$$

Then

$$\delta\phi_e(l) = 0 \tag{8.40}$$

And $\delta\phi_e(z,t)$ in Eq. (8.38) can be written as

$$\delta\phi_e(z,t) = \varepsilon e^{st} e^{-s[E_e(z) - E_e(l)]}\Lambda_{20}(l,s)[H_e(z,s) - H_e(l,s)]\} \tag{8.41}$$

Finally, the response of mixture density $\rho_{me}(z,t)$ can be obtained from Eqs. (8.26), (8.30) and (8.41) as

$$\frac{\rho_{me}(z,t)}{\rho_{me}(l)} = \frac{\overline{\rho}_{me}(z)}{\overline{\rho}_{me}(l)} + \frac{\delta\rho_{me}}{\overline{\rho}_{me}(l)}$$

$$= \frac{\overline{C}_{ke}(l)}{\overline{C}_{ke}(z)} + \frac{\delta\rho_{me}}{\overline{\rho}_{me}(z)}\frac{\overline{\rho}_{me}(z)}{\overline{\rho}_{me}(l)} = \frac{\overline{C}_{ke}(l)}{\overline{C}_{ke}(z)} + \frac{\overline{C}_{ke}(l)}{\overline{C}_{ke}(z)}\delta\phi_e(z,t) \tag{8.42}$$

where

$$\frac{\delta\rho_{me}}{\overline{\rho}_{me}(l)} = \varepsilon e^{st}\Lambda_{21}(z,s) \tag{8.43}$$

and

$$\Lambda_{21}(z,s) = \frac{\overline{C}_{ke}(l)}{\overline{C}_{ke}(z)}e^{-s[E_e(z) - E_e(l)]}\Lambda_{20}(l,s)[H_e(z,s) - H_e(l,s)] \tag{8.44}$$

8.4.4. Center of Mass Velocity

In this section, the solution of the mixture velocity can be obtained after the solutions for the volumetric flux j_e and mixture density ρ_{me} in the previous section.

$$v_{me} = j_e - [\frac{\rho_f}{\rho_{me}} - 1]V_{gje} \tag{8.45}$$

Because $C_{ke} = j_e + V_{gje}$, then

$$v_{me}(z,t) = C_{ke}(z,t) - V_{gje} - [\frac{\rho_f}{\rho_{me}(z,t)} - 1]V_{gje}$$

$$= \overline{C}_{ke}(z) + \delta C_{ke}(z,t) - \frac{\rho_f}{\rho_{me}(z,t)}V_{gje}$$

$$= (\overline{C}_{ke}(z) - \frac{\rho_f}{\overline{\rho}_{me}}V_{gje}) + \{\delta C_{ke}(z,t) + \frac{\rho_f}{\overline{\rho}_{me}}\frac{\delta\rho_{me}}{\overline{\rho}_{me}}V_{gje}\}$$

$$= (\overline{C}_{ke}(z) - \frac{\rho_f}{\overline{\rho}_{me}(l)}\frac{\overline{\rho}_{me}(l)}{\overline{\rho}_{me}}V_{gje}) + \{\delta C_{ke}(z,t) + \frac{\rho_f}{\overline{\rho}_{me}(l)}\frac{\overline{\rho}_{me}(l)}{\overline{\rho}_{me}}\frac{\delta\rho_{me}}{\overline{\rho}_{me}}V_{gje}\}$$

$$= (\overline{C}_{ke}(z) - \frac{\overline{C}_k(l)\overline{C}_{ke}(z)}{\overline{C}_k(\overline{\lambda})\overline{C}_{ke}(l)}V_{gje}) + \{\delta C_{ke}(z,t) + \frac{\overline{C}_k(l)\overline{C}_{ke}(z)}{\overline{C}_k(\overline{\lambda})\overline{C}_{ke}(l)}\frac{\delta\rho_{me}}{\overline{\rho}_{me}(l)}\frac{\overline{\rho}_{me}(l)}{\overline{\rho}_{me}}V_{gje}\}$$

$$= (\overline{C}_{ke}(z) - \frac{\overline{C}_k(l)\overline{C}_{ke}(z)}{\overline{C}_k(\overline{\lambda})\overline{C}_{ke}(l)}V_{gje}) + \{\delta C_{ke}(z,t) + \frac{\overline{C}_k(l)\overline{C}_{ke}(z)}{\overline{C}_k(\overline{\lambda})\overline{C}_{ke}(l)}\frac{\delta\rho_{me}}{\overline{\rho}_{me}(l)}\frac{\overline{C}_{ke}(z)}{\overline{C}_{ke}(l)}V_{gje}\}$$

(8.46)

By noticing $\overline{C}_k(l) = \overline{C}_{ke}(l)$ at the boundary between region (C) and region (D), Eq. (8.46) can be written as

$$\frac{v_{me}(z,t)}{\overline{v}_{fi}} = \frac{\overline{C}_{ke}(z)}{\overline{C}_k(\overline{\lambda})} + \{\frac{\delta C_{ke}(z,t)}{\overline{v}_{fi}} + \frac{1}{\overline{v}_{fi}}\frac{\overline{C}_{ke}(z)}{\overline{C}_k(\overline{\lambda})}\frac{\overline{C}_{ke}(z)}{\overline{C}_{ke}(l)}\varepsilon e^{st}\Lambda_{21}(z,s)V_{gje}\}$$

$$= \frac{\overline{C}_{ke}(z)}{\overline{C}_k(\overline{\lambda})} + \frac{\varepsilon e^{st}}{\overline{v}_{fi}}\Lambda_{22}(l,s)$$

(8.47)

where

$$\Lambda_{22}(l,s) = \Lambda_{20}(l,s) + \frac{\left[\overline{C}_{ke}(z)\right]^2}{\overline{C}_k(\overline{\lambda})\overline{C}_{ke}(l)}\Lambda_{21}(z,s)V_{gje}$$

(8.48)

8.5. PRESSURE DROP OF THE DOWNSTREAM UN-HEATED REGION (D)

The pressure drop response in the un-heated region can be obtained by integrating the momentum equation in this region.

$$\Delta p_{34} = k_e\rho_{me}(l)v_{me}^2(l) + \int_l^{l+l_e}\{\rho_{me}[\frac{\partial v_{me}}{\partial t} + v_{me}\frac{\partial v_{me}}{\partial z}]$$

$$+ g_e\rho_{me} + \frac{f_{me}}{2D_e}\rho_{me}v_{me}^2 + \frac{\partial}{\partial z}[\frac{\rho_f - \rho_{me}}{\rho_{me} - \rho_g}\frac{\rho_f\rho_g}{\rho_{me}}V_{gje}^2]\}dz$$

(8.49)

In real reactor, such as NMR, other terms can be neglected except the exit throttling k_e and the gravitational term. The gravitational pressure drop is much

bigger than other terms due to long chimney section design in natural circulation BWR.

$$\Delta p_{34g} = \int_{l}^{l+l_e} g_e \rho_{me} dz = \int_{l}^{l+l_e} g_e [\overline{\rho}_{me} + \delta\rho_{me}] dz$$

$$= g_e \int_{l}^{l+l_e} \overline{\rho}_{me}(l) \frac{\overline{C}_{ke}(l)}{\overline{C}_{ke}(z)} dz + g_e \int_{l}^{l+l_e} \delta\rho_{me} dz$$

$$= g_e \overline{\rho}_{me}(l) \int_{l}^{l+l_e} \frac{\overline{C}_{ke}(l)}{\overline{C}_{ke}(z)} dz + g_e \int_{l}^{l+l_e} \overline{\rho}_{me}(l) \varepsilon e^{st} \Lambda_{21}(z,s) dz$$

$$= g_e \overline{\rho}_{me}(l)\{\int_{l}^{l+l_e} \frac{\overline{C}_{ke}(l)}{\overline{C}_{ke}(z)} dz + \varepsilon e^{st} \Lambda_{23}(z,s)\}$$

(8.50)

and

$$\overline{\Delta p}_{34g} = g_e \overline{\rho}_{me}(l) \int_{l}^{l+l_e} \frac{\overline{C}_{ke}(l)}{\overline{C}_{ke}(z)} dz$$

(8.51)

$$\delta\Delta p_{34g} = \varepsilon e^{st} \Lambda_{23}(z,s)$$

(8.52)

where

$$\Lambda_{23}(z,s) = g_e \overline{\rho}_{me}(l) \int_{l}^{l+l_e} \Lambda_{21}(z,s) dz$$

$$= g_e \overline{\rho}_{me}(l) \Lambda_{20}(l,s)\{\frac{l_e}{\overline{C}_{ke}(l) C_{re}^*} \frac{\Omega_e}{s-\Omega_e} - \frac{1}{s}[1-e^{-s\overline{\tau}_{34}}]\frac{\Omega_e}{s-\Omega_e}\}$$

(8.53)

and

$$C_{re}^* = \frac{\overline{\rho}_{me}(l)}{\overline{\rho}_{me}(l+l_e)} = \frac{\overline{C}_{ke}(l+l_e)}{\overline{C}_{ke}(l)}$$

(8.54)

$$\overline{\tau}_{34} = E_e(l+l_e) - E_e(l) = \frac{1}{\Omega_e} \ln C_{re}^*$$

(8.55)

The dimensionless form of Eq. (8.52) is given as

$$\frac{\delta\Delta p_{34g}^*}{\delta v^* v_{fi}^*} = \frac{1}{C_r^*} \frac{\Omega_e^*}{s^*-\Omega_e^*} \Lambda_{20}^* \{[\frac{1}{N_{Fr}} \frac{1}{[(\frac{1}{A_e^*})C_r^* + V_{gje}^* C_r^* + \frac{\Omega_e^* l_e^*}{v_{fi}^*}]}] + [\frac{g^*}{s^* v_{fi}^*}(1-e^{-s^*\overline{\tau}_{34}^*})]\}$$

(8.56)

and

$$\Lambda_{20}^* = \frac{1}{A_e^*} \Lambda_5^* - C_r^{*2} \frac{V_{gje}^*}{1+V_{gj}^*}[\frac{1}{s^*-1} \frac{1}{C_r^{*2}} \Lambda_3^* - e^{-[(s^*+1)\overline{\tau}_{23}^*+s^*\overline{\tau}_{12}^*]}]$$

(8.57)

$$\Lambda_5^* = \Lambda_3^* + \frac{1}{s^*-1} \frac{V_{gj}^*}{1+V_{gj}^*}[\Lambda_3^* - e^{-[(s^*-1)\overline{\tau}_{23}^*+s^*\overline{\tau}_{12}^*]}]$$

(8.58)

$$\Lambda_3^* = 1 - \frac{(1-e^{-s^*\overline{\tau}_{12}^*})}{s^*}$$

(8.59)

154

where the characteristic equations Λ_3^* and Λ_5^* are used by Ishii [4]. Also, some dimensionless parameters are defined as follows

$$\Delta p^* = \frac{\Delta p}{(\Omega l)^2 \rho_f} \tag{8.60}$$

$$C_r^* = \frac{\overline{C_k}(l)}{\overline{C_k}(\lambda)} \tag{8.61}$$

$$\Omega_e^* = \frac{\Omega_e}{\Omega} \tag{8.62}$$

$$s^* = \frac{s}{\Omega} \tag{8.63}$$

$$\Omega = \Omega_o = \frac{q_w'' \xi}{A_c \Delta i_{fg}} \frac{\Delta \rho}{\rho_g \rho_f} \tag{8.64}$$

$$N_{Fr} = \frac{\overline{v}_{fi}^2}{gl} \tag{8.65}$$

$$A_e^* = \frac{A_c}{A_e} \tag{8.66}$$

$$l_e^* = \frac{l_e}{l} \tag{8.67}$$

$$V_{gje}^* = \frac{V_{gje}}{\overline{v}_{fi}} \tag{8.68}$$

$$v_{fi}^* = \frac{\overline{v}_{fi}}{\Omega l} \tag{8.69}$$

$$g^* = \frac{g}{\Omega^2 l} \tag{8.70}$$

$$\overline{\tau}_{12}^* = \overline{\tau}_{12}\Omega = \frac{\lambda^*}{\overline{v}_{fi}^*} = \frac{\Delta i_{12}}{\Delta i_{fg}} \frac{\Delta \rho}{\rho_g} \tag{8.71}$$

$$\overline{\tau}_{23}^* = \overline{\tau}_{23}\Omega = \ln C_r^* \tag{8.72}$$

$$\overline{\tau}_{34}^* = \overline{\tau}_{34}\Omega \tag{8.73}$$

8.6. APPLICATION OF ANALYSIS

In the previous section, the application of kinematic and dynamic analyses to the stability problem considering the flashing effect in the chimney section has been explained. The stability boundary can be determined numerically by using the

155

D-partition method [4] on the dimensionless characteristic equation for the perturbations between the pressure drop and inlet velocity. And the theoretically obtained stability boundaries are compared with previous experimental data.

Figure 8-4 shows the flashing boundary at 200 kPa with different K_{in}. As can be seen, the flashing boundary is able to be predicted by treating the flashing as uniform heat source along the chimney. Also, the boundary for the DWO can also be seen in the stability plane in the region with high phase change number. The DWO boundary for $K_{in}=1200$ moves to the right part with higher phase change number, which exceed the limit of current dimensionless stability plane. In other words, the stable region is expanded by increasing the inlet flow resistance coefficient, which was also verified by Ishii [4].

However, the theoretical flashing stability boundary in Figure 8-4 does not agree very well with previous experimental data from the quasi-steady state tests, where the flashing boundary is above the zero quality line at the core exit. The reason is that the non-thermal equilibrium is not yet considered in current frequency domain analysis model. And the non-boiling length $\bar{\lambda}$ is over estimated in current frequency domain analysis.

Stability Map

(P = 200 kPa, Thermal Hydraulic Instability)
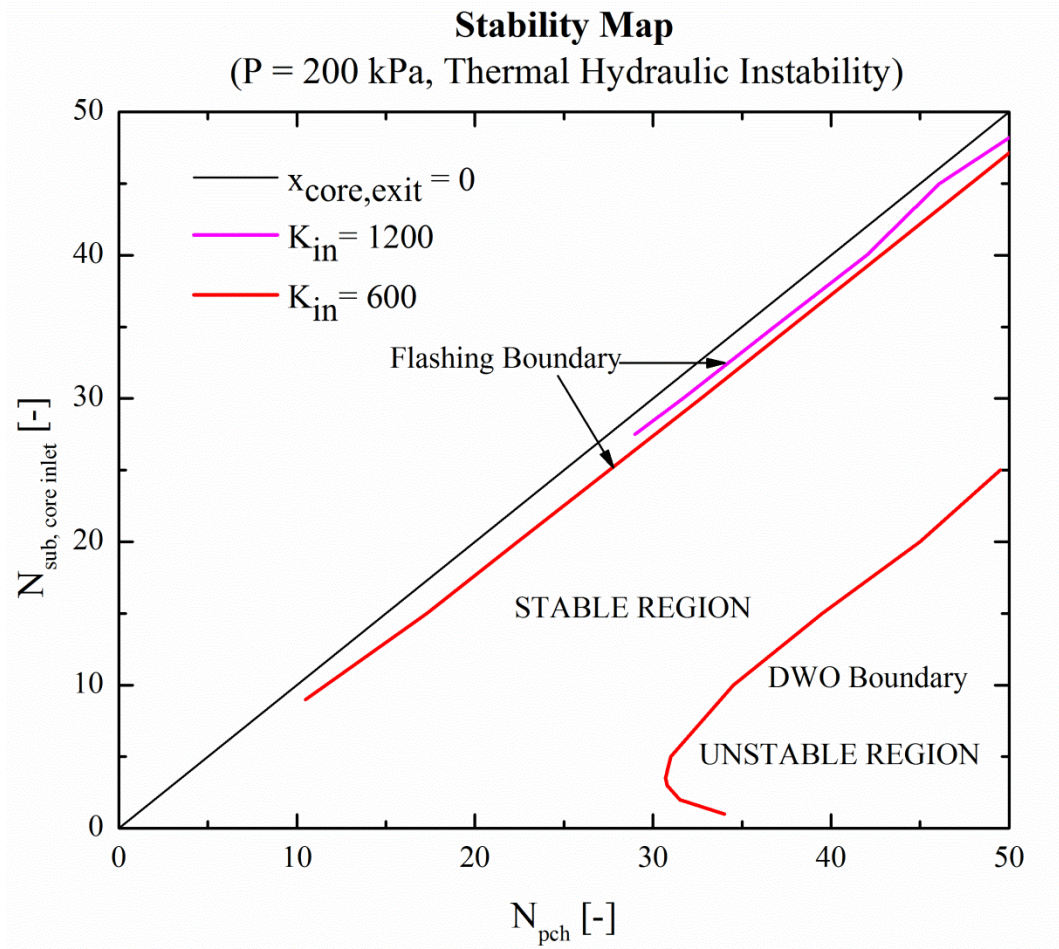
Figure 8-4 Stability Map at 200 kPa

The pressure effect on the theoretical stability boundary is also carried out in the frequency domain analysis. Figure 8-5 shows the stability boundary at the pressure of 400 kPa. As can be seen, only the DWO boundary can be predicted in the stability plane. And the pressure effect on the DWO boundary is not significant. The flashing boundary at high pressure can be indicated by the zero-quality line at the core exit by comparing with experimental data at 400 kPa.

Stability Map
(P = 400 kPa, Thermal Hydraulic Instability)
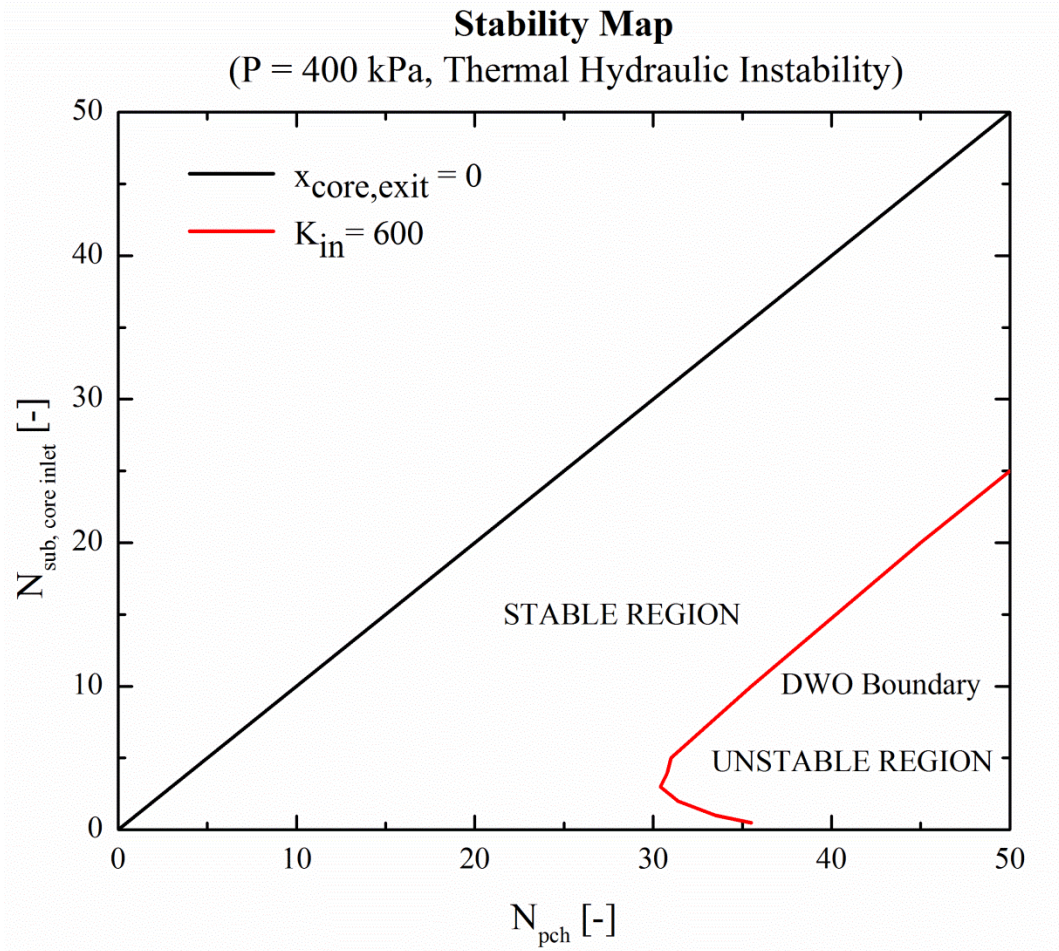
Figure 8-5 Stability Map at 400 kPa

8.7. SUMMARY AND CONCLUSIONS

Following Ishii's approach to obtain the DWO boundary, the flashing phenomena at the top of the chimney at low pressure is considered as axially uniform heat source in the frequency domain analysis. The kinematic and dynamics of the downstream unheated mixture region are obtained. The pressure response is also given in dimensionless equation by considering the gravitational term and flow resistance at the core exit. The stability boundary can be obtained by solving the characteristic equation between the perturbation of pressure drop and the perturbation of the core inlet velocity with D-partition method.

The predicted stability boundaries are compared with the previous quasi-steady state experimental data. The flashing boundary and density wave oscillations boundaries can be predicted in the dimensionless stability plane (N_{sub}-N_{pch}).

Although the theoretical flashing boundary shows some discrepancy with the experimental data, the effect of system pressure and inlet K factor can be correctly simulated. In the future, the thermal non-equilibrium conditions can be taken into account to improve the accuracy of the flashing boundary. Currently, the zero quality line at the chimney exit can be used as a simple analytical way to predict the flashing boundary during the startup procedure of the NCBWR.

9. INTRODUCTION OF NUSCALE REACTOR

The SMR two phase natural circulation instability study for PWR-type selected the NuScale Reactor as the simulation target and thus it is necessary to introduce NuScale reactor briefly here.

NuScale Power LLC is developing a PWR-type SMR technology which is designed with natural safety features. The NuScale small modular reactor uses natural circulation to operate normally and manage the design basis accidents. Every reactor module is self-contained and operates independently. Figure 9-1 shows the schematic design of NuScale reactor.
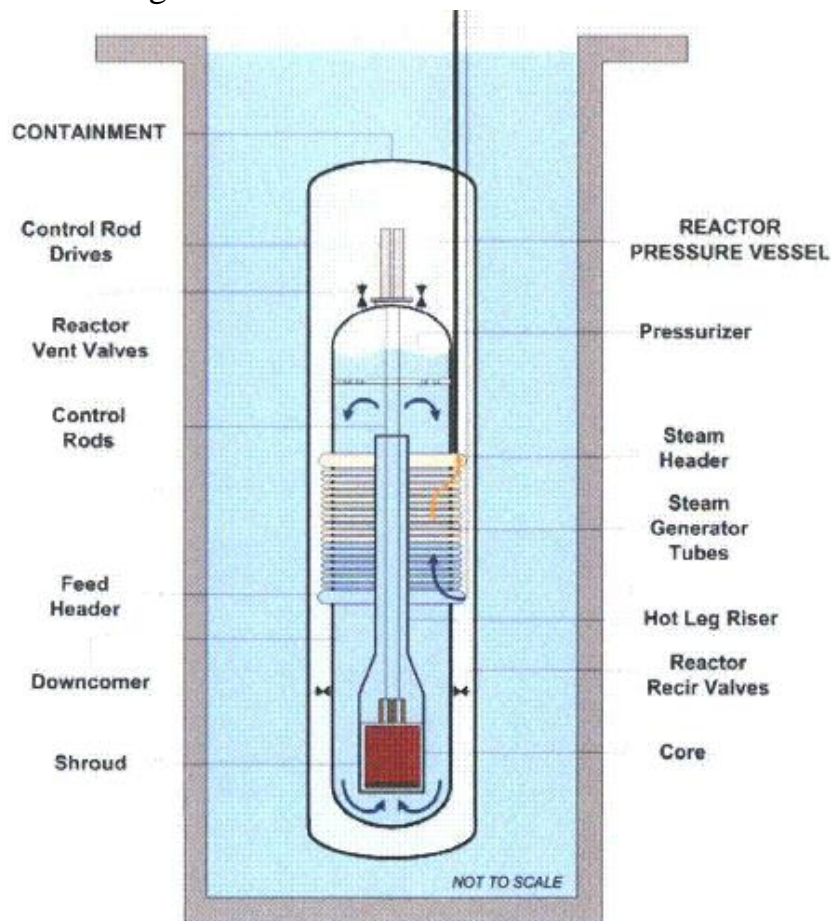
Figure 9-1 NuScale Reactor Design

The RPV is inside the containment vessel which is submerged in a water-filled pool. This pool of water is acting as the ultimate heat sink when accident happens. Unlike the regular PWR which all these components are separately apart, the core, steam generator and pressurizer are integrated in a single vessel for the NuScale

160

design. In normal operation and accidental scenarios, the NuScale reactor utilizes the principles of natural circulation. Water is heated after passing the core section and rises through the chimney because of the buoyancy caused by coolant density difference. Once the heated water reaches the top of the chimney, it is drawn downward by water that is cooled passing through the steam generator. The cooler water has a higher density thus it is pulled back down to the bottom of reactor by gravity, and then drawn over the core again. Because of the utilization of natural circulation, many large and complex systems required in regular PWR are no longer necessary in NuScale plant.

The whole primary loop is kept separate from water in the steam generator. As the hot water in the reactor system passes over the hundreds of tubes in the steam generator, heat is transferred through the tube walls and the water in the tubes turns into steam. The steam turns turbines which are attached by a single shaft to the electrical generator. After passing through the turbines, the steam loses its energy. It is cooled back into liquid form in the condenser then pumped by the feed water pump back to the steam generator where it begins the cycle again. Table 9.1shows some key design parameters of the NuScale reactor.

Table 9.1 Design Characteristics of the NuScale Reactor

Overall Plant	
Net Electrical Output	540 MW(e)
Plant Thermal Efficiency	30%
Number of Power Generation Units	12
Nominal Plant Capacity Factor	>90%
Power Generation Unit(Each Module)	
Number of Reactors	1
Net Electrical Output	45 MW(e)
Number of Steam Generators	2 independent tube bundles
Steam Generator Type	Vertical once-through helical tube
Steam Cycle	Superheated
Turbine Throttle Conditions	3.1 MPa
Steam Flow	71 kg/s
Feedwater Temperature	149ºC
Reactor Core	

Thermal Power Rating	160MWt
Operating Pressure	8.72 MPa(1850Psia)
Fuel	UO_2 (<4.95% enrichment)
Refueling /Inspection Interval	24 months

The NuScale Power Inc. has the proprietary rights of NuScale reactor design, therefore some of the design parameters cannot be accessed. Thus for the natural circulation instability analysis of the PWR-type SMR, the design of Multi-Application Small Light Water Reactor (MASLWR) are acted as the reference to NuScale. The MASLWR design [46] was conducted under the auspices of the Nuclear Energy Research Initiative (NERI) of the U.S. Department of Energy (DOE). Figure 9-2 shows the conceptual design of MASLWR. Table *9.2* gives the geometrical design parameter of the MASLWR. The biggest difference between the MASLWR design and the NuScale design is that the MASLWR design uses water to fill in the space between RPV and containment. The dimension and other design parameters between two reactor designs are very similar. The schematic design of RPV for both reactors is shown in Figure 9-3.
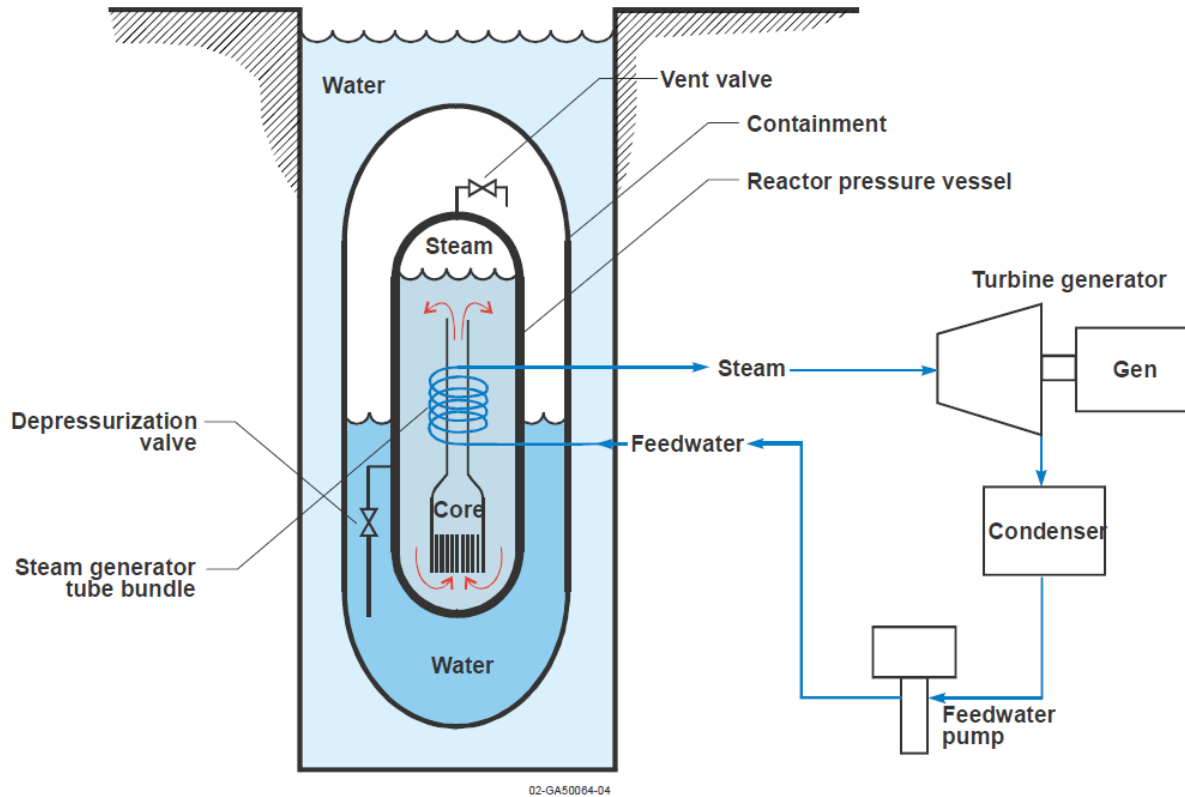
Figure 9-2 MASLWR Reactor Design (NuScale prototype) [46]

Table 9.2 Geometry Parameters of MASLWR RPV

Component	Specification	NuScale(MASLWR)
RPV	Total Height (mm)	13761
	I.D. (mm)	2440
	Wall Materials	Stainless Steel
	Wall thickness (mm)	150
Core	Number of rods	6336
	Rod diameter (mm)	9.5
	Rod cladding material	Zr. Clad
	Hydraulic diameter (mm)	11
	Flow area (m^2)	0.5904
	Core height (mm)	1767
	Active fuel length (mm)	1350
	Core shroud I.D. (mm)	1500
	Core shroud O.D. (mm)	1700
	Core shroud wall thickness (mm)	100
Chimney	Chimney shroud thickness (mm)	100

Component	Specification	NuScale(MASLWR)
	Chimney lower part height (mm)	2040
	Lower part area (m^2)	1.7219
	Lower part hydraulic diameter (mm)	348
	Chimney reducer height (mm)	250
	Chimney upper part height (mm)	6000
	Upper part area (m^2)	0.6109
	Upper part hydraulic diameter (mm)	136.1
	Top of chimney (mm)	11000
Downcomer	Downcomer upper part width (mm)	686
	Upper part area (m^2)	3.8792
	Upper part hydraulic diameter (mm)	1372
	lower part width (mm)	370
	lower part area (m^2)	2.4061
	lower hydraulic diameter (mm)	740
Steam Generator	Steam generator height (mm)	2591.2
	Tube O.D. (mm)	16
	Tube length (mm)	22250.4
	Tube thickness (mm)	0.9
	Number of tubes	1012
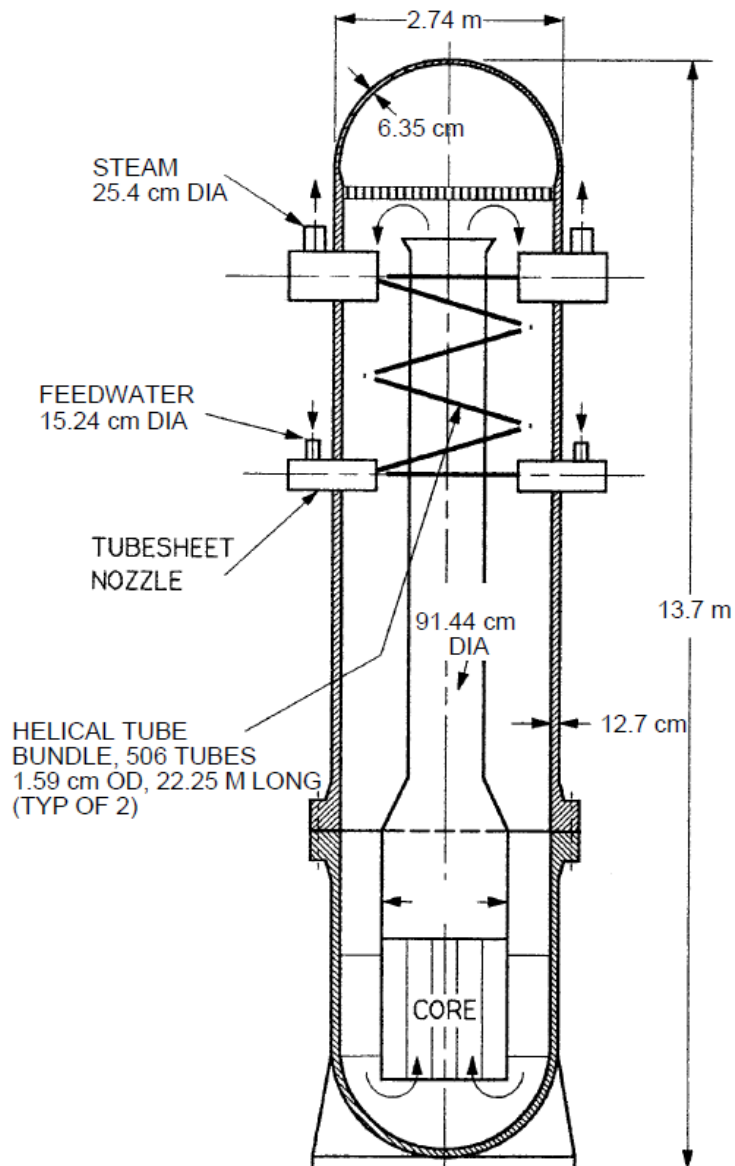
Figure 9-3 Schematic Design of NuScale (MASLWR) RPV [46]

10. SCALING ANALYSES OF NUSCALE FOR ISF

10.1. IDEALLY SCALED FACILITY DESIGN PARAMETERS

Based on the three-level scaling method developed for the design of Purdue University Multi-dimensional Integral Test Assembly by Ishii [28], the design of the Ideally Scaled Facility (ISF) for PWR-type SMR is performed. The ISF design is scaled from the geometry of the NuScale design. The ISF is scaled with the same fluid and under the same pressure (constant pressure scaling). Thus all the fluid properties can be considered identical for the prototype and the model:

$$\rho_R = \rho_{gR} = \beta_R = C_{pR} = k_R = \mu_R = \mu_{gR} = \Delta i_{fgR} = 1 \tag{10.1}$$

Then the length ratio and area ratio for the core geometrical scaling are selected based on the room space limitation remains in current laboratory. Ishii and Kataoka [48] introduced the scaling laws and non-dimensional numbers for thermal-hydraulic systems under single phase and two phase natural circulation. The natural circulation rate (velocity scale) can be derived from the Froude number. From the phase change number, the power ratio has the same value as the mass flow rate ratio. Another important number is the hydraulic diameter ratio, which comes from the time ratio number accounting for the transport time over conduction time. Under these scaling ratios, the time scale of events are shortened in the scaled-down ISF by a factor of $L_{0,R}^{1/2}$. The ratios for the ISF prototype pressure scaling are given as follows:

$$\text{Length ratio: } L_{0,R} = \frac{L_{0,ISF}}{L_{0,MASLWR}} = \frac{1}{4} \tag{10.2}$$

$$\text{Area ratio: } a_R = \frac{a_{ISF}}{a_{MASLWR}} = \frac{1}{100} \tag{10.3}$$

$$\text{Volume ratio: } V_R = \frac{V_{ISF}}{V_{MASLWR}} = \frac{1}{400} \tag{10.4}$$

$$\text{Velocity ratio: } u_{0,R} = \frac{u_{0,ISF}}{u_{0,MASLWR}} = \sqrt{L_{0,R}} = \frac{1}{2} \tag{10.5}$$

$$\text{Mass flow rate ratio: } \dot{m}_R = \frac{\dot{m}_{ISF}}{\dot{m}_{MASLWR}} = \rho_R u_{0,R} a_R = \frac{1}{200} \tag{10.6}$$

$$\text{Power ratio: } q_R = \frac{q_{ISF}}{q_{MASLWR}} = \frac{1}{200} \tag{10.7}$$

$$\text{Core hydraulic diameter ratio: } D_R = \frac{D_{ISF}}{D_{MASLWER}} = \sqrt{\frac{L_{0,R}}{u_{0,R}}} = \frac{1}{1.414} \tag{10.8}$$

$$\text{Time scale: } \tau_R = \frac{\tau_{ISF}}{\tau_{NMR-50}} = L_{0,R}^{1/2} = \frac{1}{2} \tag{10.9}$$

The geometry parameters of the ideal scaled facility can be listed in *Table 10.1*. A schematic drawing of test section is shown in Figure 10-1. As can be seen, the test facility includes the core, chimney, upper plenum, steam generator (SG), downcomer, and lower plenum in a loop. The containment is designed to use a single vessel which is connected to the test loop through ADS lines.

Table 10.1 Design of the Ideal Scaled Facility (ISF)

Component	Specification	NUSCALE	ISF	Ratio
RPV	Total height (mm)	13760	3440	0.25
Core	Core height (mm)	1767	412.0	0.25
	Fuel rod O.D. (mm)	9.522	0.950	0.1
Chimney	Lower section height (mm)	2040	510.0	0.25
	Lower section area (m^2)	1.722	0.017	0.01
	Lower section I.D	1500	150.0	0.1
	Chimney reducer height (mm)	250.0	63.00	0.25
	Upper section height (mm)	6000	1500	0.25
	Upper section area (m^2)	0.611	0.006	0.01
	Upper section I.D (mm)	914.4	91.44	0.1
Down comer	Upper section width (mm)	686.0	222.2	
	Upper section area (m^2)	3.879	0.004	0.01
	Lower section width (mm)	370.0	175.0	
	Lower section area (m^2)	2.406	0.002	0.01
Containment	Total height (mm)	17680	4420	0.25
	I.D.	4270	352.2	
	Volume (m^3)	172.3	0.431	0.0025

unit:m
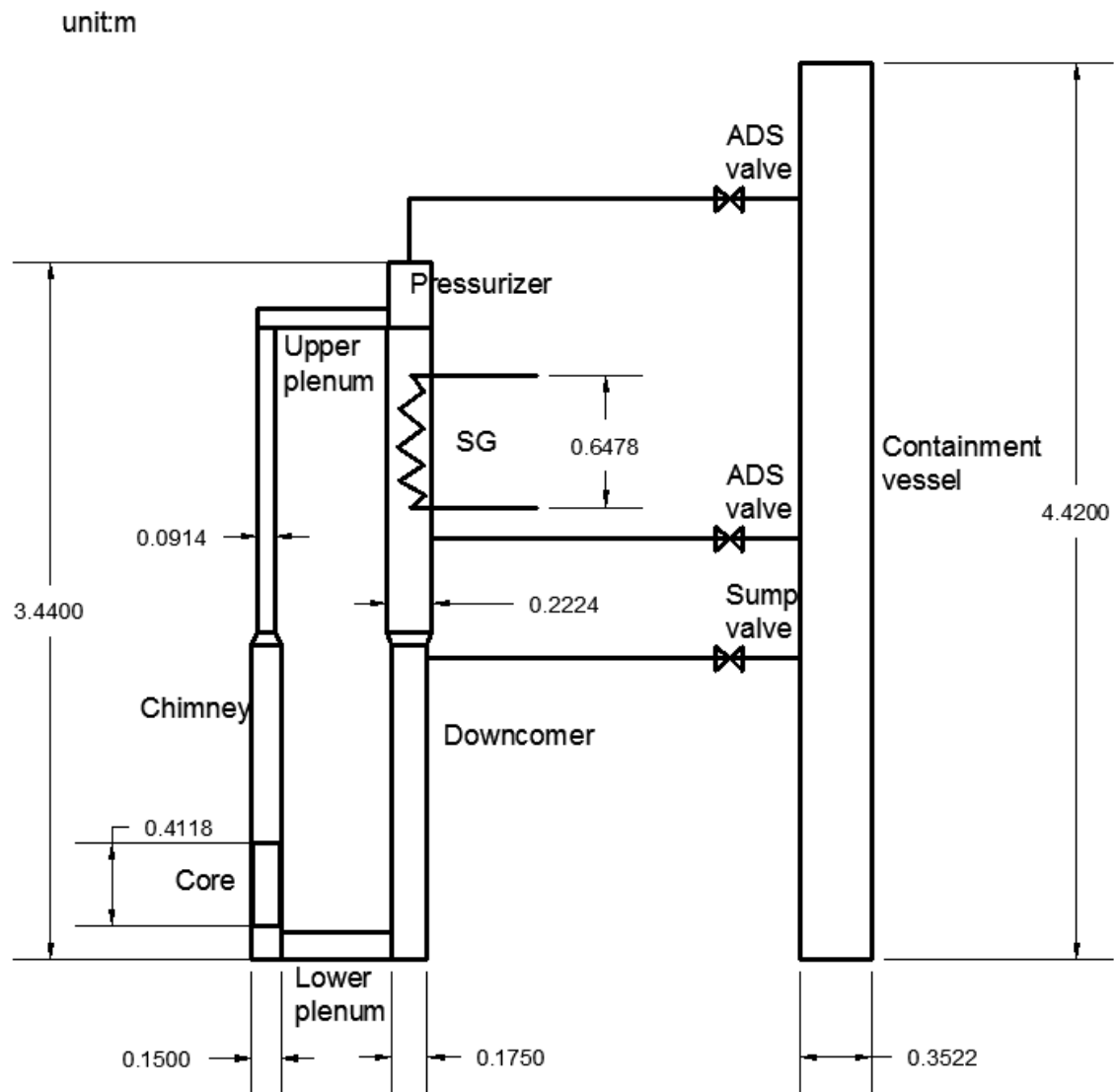
Figure 10-1 Schematic Design of ISF

The purpose of this section is to perform RELAP5 analyses for the NuScale plant and the Ideal Scaled Facility (ISF). Steady state and transient simulation are performed on both facilities using the RELAP5/MOD3.3 code [15]. For steady state simulation, the nominal operating conditions for NuScale plant is simulated firstly, then the same analyses are performed on the ISF as well. For transient accident analysis, since no direct accident performances of NuScale plant is available, the OSU-MASLWR facility test condition is simulated. This is by considering that the MASLWR is the prototype of NuScale reactor and transient tests have been performed in the OSU-MASLWR facility, the OSU-MASLWR tests should be able to represent the behavior of NuScale reactor under accident conditions. If the ISF acts similar to the OSU tests, the correctness of current ISF could be well verified. The simulation results are shown in the following section.

10.2.1. Nodalization and dimensions

The nodalization for the NuScale reactor is described in Figure 10-2. The right part of the nodalization represents the reactor pressure vessel (RPV) of the NuScale. The bottom region (124) connecting the down comer part (011-015) and core zone is represented with a BRANCH component in RELAP5. The core and the chimney are modeled with PIPE component. The upper plenum which separates the pressurizer and the ascending and descending side concentric regions is modeled with a single branch. The pressurizer (208) is simplified with single PIPE component.

The steam generator (300) is thermally connected with down comer using a heat structure. The helical coil SG is represented with a single pipe. The feed water tank (104) is composed with a TIME DEPENDENT VOLUME component at the inlet of SG. The secondary system pressure is controlled by turbine as another TIME DEPENDENT VOLUME at the outlet. The SG tubes are modeled using an inclination angle of real geometry thus horizontal flow regime is applied in the equivalent tubes.

Component 500 stands for the containment while component 600 represents the outer pool, which are both modeled as ANNULUS component. The

containment is connected to the RPV through the ADS lines, which includes a top ADS vent line, one middle ADS blowdown line and one sump line in the bottom. Each line has one trip valve to control the transient sequence. *Table 10.2* to *Table 10.4* list all the nodalization dimensions and component type for both NuScale reactor and the ISF.
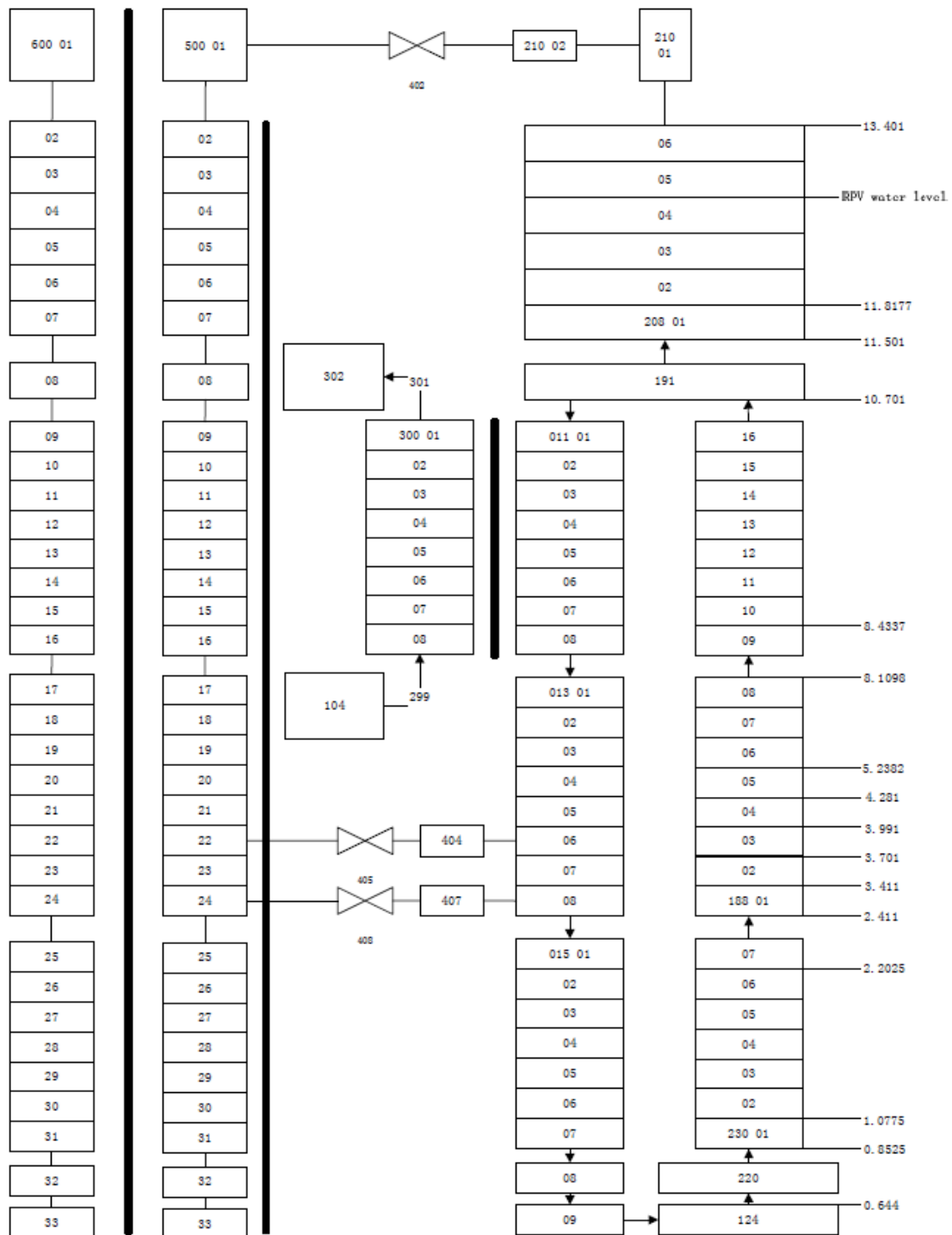
Figure 10-2 Nodalization for RELAP5 Code Simulation

Table 10.2 Primary Loop Nodalization Dimensions

Component	Unit	NuScale	ISF	Ratio (NS/ISF)
124 Lower plenum (Branch)				
Area	m^2	2.0340	0.0203	100
Length	m	0.6440	0.1610	4
Hydraulic dia.	m	1.6093	1.1381	1.414
220 Core plate (Branch)				
Area	m^2	0.5904	0.0059	100
Length	m	0.2085	0.0521	4
Hydraulic dia.	m	0.0110	0.0078	1.414
230 Core (Pipe)				
Area	m^2	0.5904	0.0059	100
length	m	1.3500	0.3375	4
Hydraulic dia.	m	0.0110	0.0078	1.414
18801 Chimney section-lower region (Pipe)				
Area	m^2	1.7219	0.0172	100
Length	m	1.0000	0.2500	4
Hydraulic dia.	m	0.3480	0.2461	1.414
18802-18804 Chimney section-reducer region (Pipe)				
Area	m^2	1.1442	0.0114	100
Length	m	0.8700	0.2175	4
Hydraulic dia.	m	0.2329	0.1647	1.414
18805-18816 Chimney section-upper region (Pipe)				
Area	m^2	0.6109	0.0061	100
Length	m	6.4200	1.6050	4
Hydraulic dia.	m	0.1361	0.0963	1.414
191 Upper plenum (Branch)				
Area	m^2	4.8087	0.0481	100
Length	m	0.8000	0.2000	4
Hydraulic dia.	m	0.8400	0.5941	1.414
208 Pressurizer (Pipe)				
Area	m^2	4.0850	0.0409	100
Length	m	1.9000	0.4750	4
Hydraulic dia.	m	0.735	0.5198	1.414
011 Down comer-SG (Annulus)				
Area	m^2	2.1312	0.0213	100
Length	m	2.5912	0.6478	4
Hydraulic dia.	m	0.0289	0.0204	1.414

Component	Unit	NuScale	ISF	Ratio (NS/ISF)
013 Down comer-Chimney (Annulus)				
Area	m²	3.8792/3.2991/2.4061	0.0388/0.0330/0.0241	100
Length	m	3.4088/0.25/2.04	0.8522/0.0625/0.51	4
Hydraulic dia.	m	1.3720/1.0790/0.7400	0.9703/0.7631/0.5233	1.414
015 Downcomer-Core (Annulus)				
Area	m²	2.4061	0.0241	100
Length	m	1.7670	0.4418	4
Hydraulic dia.	m	0.7400	0.5233	1.414

Table 10.3 Secondary Loop Nodalization Dimensions

Component	Unit	NuScale	ISF	Ratio (NS/ISF)
104 Feed water tank (Time Dependent Volume)				
Area	m²	1.0e6	1.0e4	100
Length	m	1.0	0.25	4
Hydraulic dia.	m	0.1	0.0707	1.414
300 Steam generator (Pipe)				
Area	m²	0.1580	0.0016	100
Length	m	2.7675	0.6919	4
Hydraulic dia.	m	0.0141	0.0100	1.414
302 Turbine (Time Dependent Volume)				
Area	m²	0.2003	0.0020	100
Length	m	1.0	0.25	4
Hydraulic dia.	m	1.0	0.7072	1.414

Table 10.4 Containment and Outer Pool Nodalization Dimensions

Component	Unit	NuScale	ISF	Ratio (NS/ISF)
500 Containment (Annulus)				
Area	m²	9.7440	0.0974	100
Length	m	17.68	4.42	4
Hydraulic dia.	m	1.53	1.082	1.414
600 outer pool (Annulus)				
Area	m²	68.4	0.684	100
Length	m	17.68	4.42	4
Hydraulic dia.	m	4.27	3.0193	1.414

10.2.2. Steady state analyses

In order to perform scaling analysis of the NuScale reactor, the steady state performance of NuScale reactor prototype should first be evaluated to make sure that all the nominal design parameters [11] can be matched in RELAP5 analysis. Then ideally scaled parameters are entered into the code to check if the prototype can be well scaled by current scaling method. In both cases the scaled parameters should match well.

During steady state simulation, all safety valves connected to the containment are separated and the RPV is the only part which was considered. The steady state normal operating conditions are listed in Table 10.5. These condtions are provided by previous reports [49] for NuScale reactor.

Table 10.5 Normal Operating Condition for NuScale Reactor

Normal operating condition	
Primary loop	
Pressure	7.8 MPa
Mass flow rate	596 kg/s
Core inlet tempreature	491.8 K
Core outlet temperature	544.4 K
Saturation temperature	567.4 K
Core thermal power	150 MW
Secondary loop	
Pressure	1.38 MPa
Mass flow rate	56 kg/s
Inlet temperature	310 K
Outlet temperature	477 K
Saturation temperature	467.5 K

According to the RELAP5 results, the steady state condtions all match with the given nominal operating parameters. We run the code for a relatively long period of time (8000 sec) and if the value doesn't change by time, the condition is considered to be in steady state. Figure 10-3 gives the steam dome pressure comparison between NuScale Prototype and ISF, while Figure 10-4 gives the scaled mass flow rate for both facility.
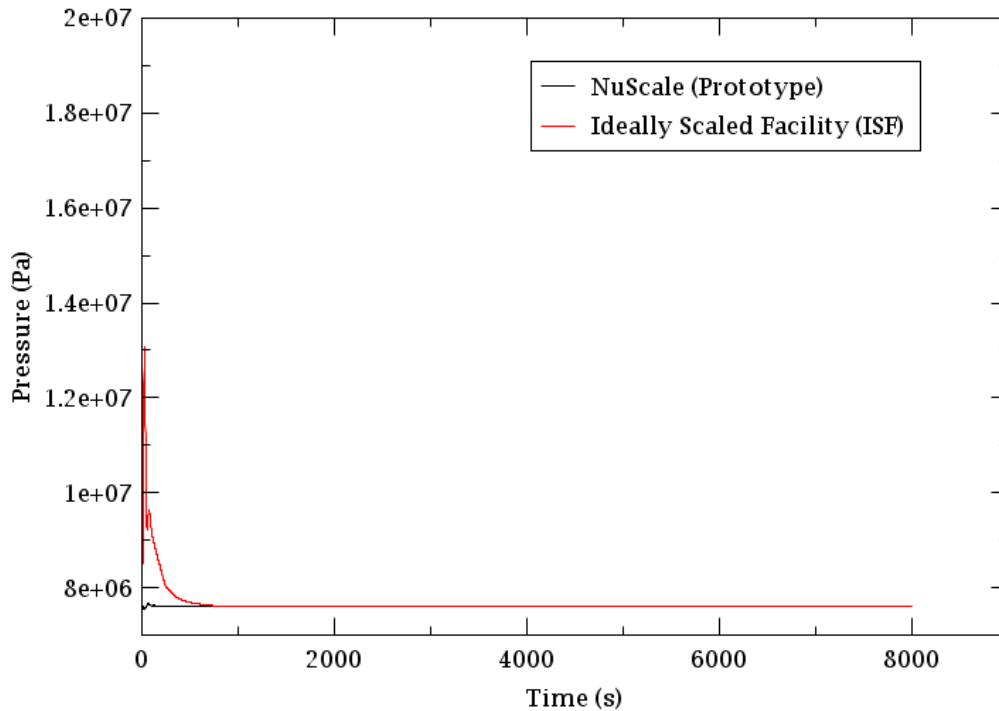
Figure 10-3 Steady State Steam Dome Pressure of the NuScale and the ISF by RELAP5

176
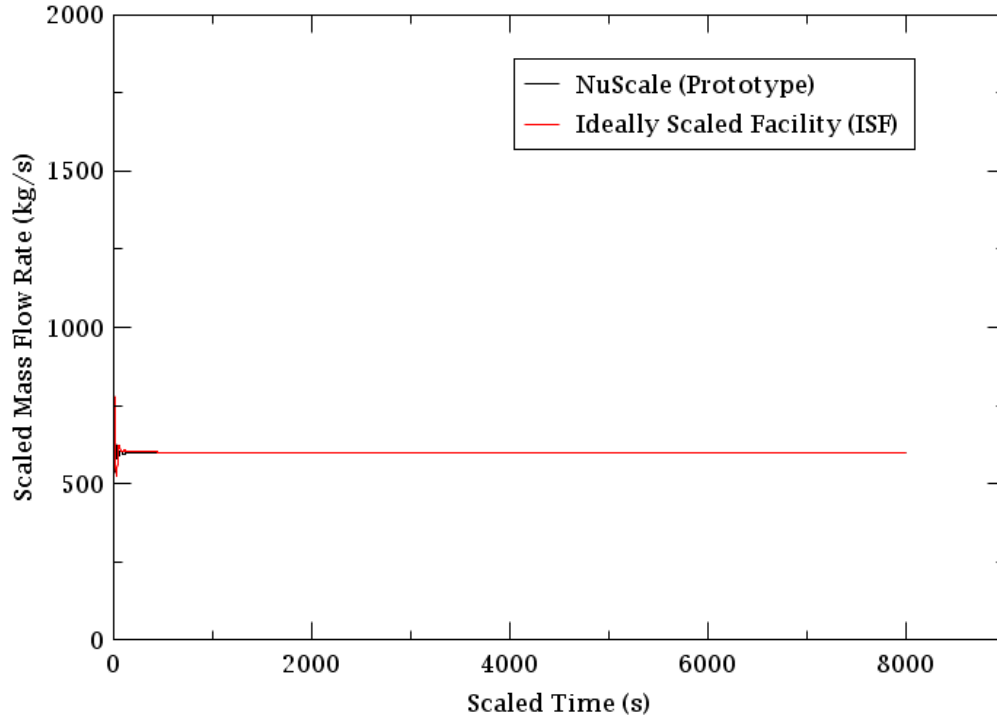
Figure 10-4 Steady State Mass Flow Rate Comparison of the NuScale and the ISF by RELAP 5

The flucturation at the very beginning is caused by initial setting of the RELAP5 code input and can be neglected. The results indicates that all the existing geometry and other design parameters for the ISF is well scaled to match the steady state normal operation performance of the prototype.

10.2.3. Transient analyses

Transient analyses are also performed on the NuScale reactor and ISF. Since limited transient data of the NuScale reactor was found in literature and its detailed accident scenerio and stragety belong to NuScale Power Inc.'s proprietary, the reference OSU-MASLWR facility test is simulated. Because the OSU facility is a full pressure and temperature scaled facility, its test results should be able to illustrate the transient behavior of the MASLWR reactor very well. With MASLWR being the design prototype of NuScale reactor, its transient behavior should thus somehow similar to, if not exactly the same, the transient behavior of NuScale reactor.

According to a publication from NuScale Inc. offical website[1], the NuScale also cooperates with OSU and run blowdown tests for safety anaylsis. Although NuScale didn't give the detailed pressure changing curve but only provided normalized pressure, the trend of pressure change is similar to the OSU-MASLWR 003b test. Figure 10-5 shows the RPV and containment pressure curve for NuScale and Figure 10-6 shows the OSU-MASLWR 003b test.
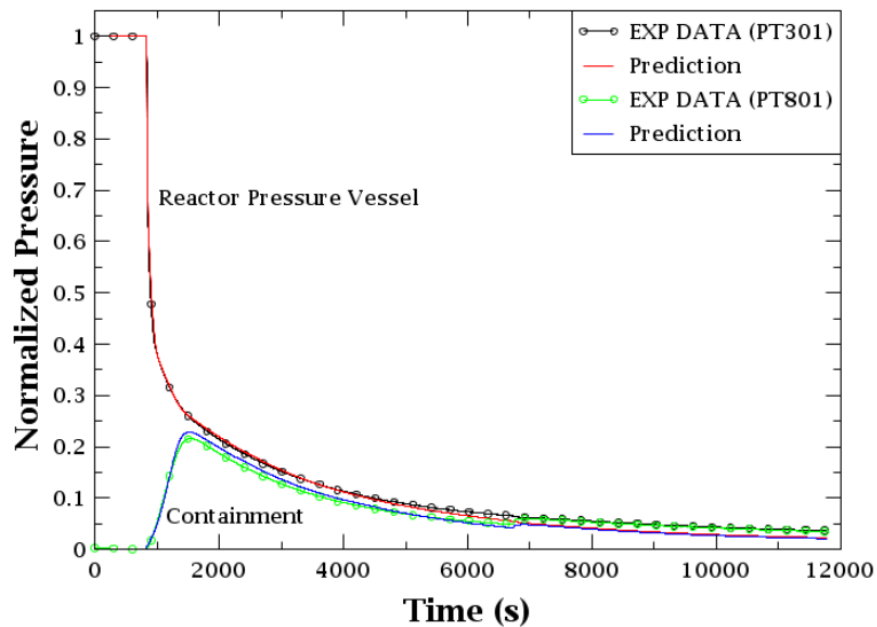

Figure 10-5 Blowdown pressure curve provided by NuScale Inc.

---

[1] http://nuscalepower.com/technicalpublications.aspx
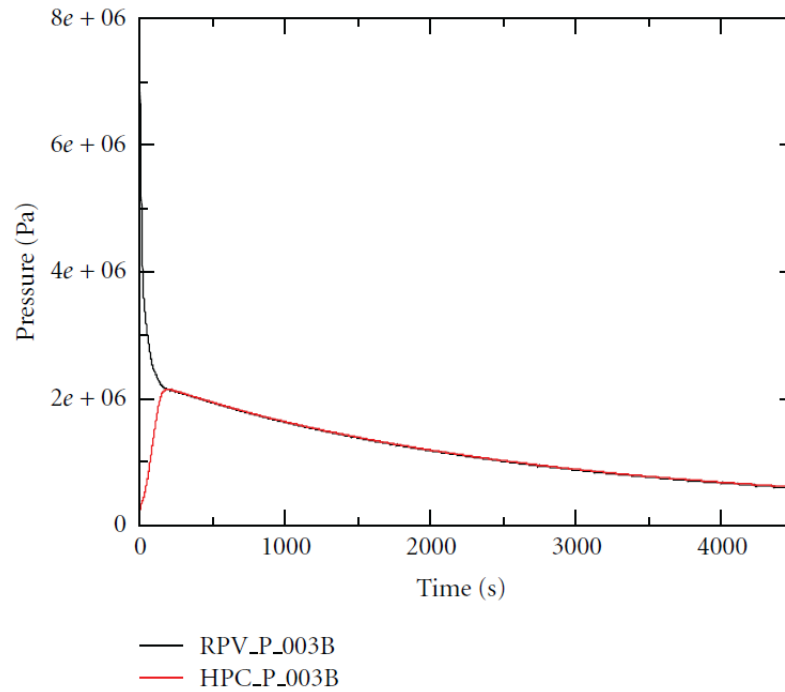
Figure 10-6 OSU-MASLWR 003b Test RPV and Containment Pressure Curve

Therefore, the OSU-MASLWR 003b test is selected as the simulation target. The OSU-MASLWR 003b test aims to show the behavior of RPV and containment pressure when top ADS valve is inadvertently actuated, which is considered as a beyond design basis accident for MASLWR concept design but a design basis accident for NuScale reactor. This is because the NuScale removes the middle ADS valves and only uses top ADS valves to reduce RPV pressure during an accident.

During this test, the top ADS valve is opened and the pressure with RPV and containment is monitored. The reactor is working under normal operation condition for the first 3000s. After that, the core trips to decay power mode and the steam generator is isolated. The top ADS valved is opened to start the blowdown process. Durring the blowdown process, the RPV pressure is decreasing significantly due to flow ejected into containment, which simulataneously rise up the containment pressure. The containment pressure reachs to a peak (about 2 MPa) at about 200s, then it decreases at a rate similar to that of RPV. After 6000s, the sump valve is opened to let the coolant in containment circulate back to RPV. During the whole process the core part never bares out and is always covered by coolant.

Top ADS blowdown event for both NuScale reactor and ISF are simulated by RELAP5 code. Figure 10-7 shows the comparison of blowdown pressure of both NuScale and ISF. It should be mentioned that the ISF has a time scale of 1/2 to the prototype. The time axis of figure is therefore adjusted to show the scaled time. It can be seen from the figure that very few difference exists between the prototype and ISF, which means the current ISF is well scaled.
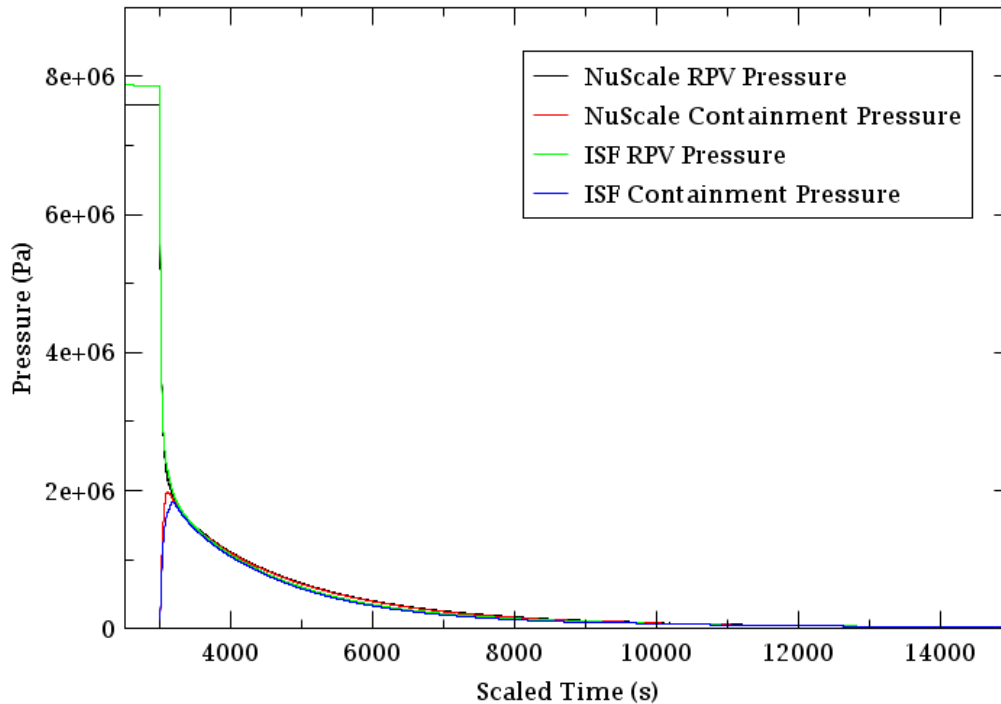
Figure 10-7 Blowdown Pressure Comparison for the NuScale and the ISF by RELAP 5

Figure 10-8 shows the collapsed water level of both two cases. The water level curves show great simularity. In both cases, water level never drops blow the height of core which means the core never bares out. After 6000s the sump valve is opened to enable the condensed water in containment circulate back to RPV. The fluctuation of water level curve may indicate existing of possible instability. However, since RELAP5 code is not capable of predicting the instablity and related phenomenon, the fluction may also caused by pressure fluctuation. Detailed phenomenon should be observed during the experiments later operated in the ESF.
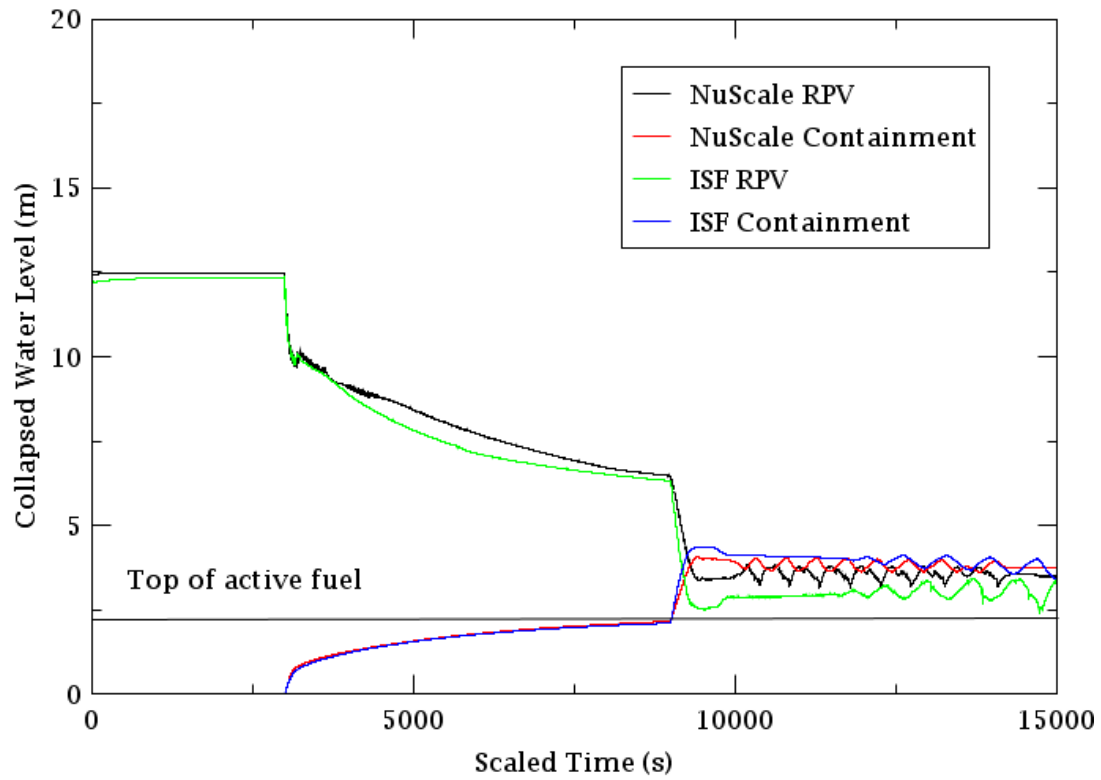
Figure 10-8 Collapsed Water Level Comparison for the NuScale and the ISF by RELAP 5

11. DESIGN OF ENGINEERING SCALED PWR-TYPE EXPERIMENTAL FACILITY

The ISF is strictly scaled down from the prototype based on those scaling ratios. However, it is impractical to build an ideally scaled facility without considering many restrictions. Due to the engineering limitations, it is unrealistic to customize arbitrary pipe size to fit the ideal scale. Besides, building a core consists of thousands of fuel rod with millimeters' diameter is also unrealistic. Therefore, the Engineering Scaled Facility (ESF) should thus be built not only based on the proper scaled ISF but also consider all the engineering limitations. Generally, the redesigned ESF would have some unavoidable scaling distortions although it shares the identical scaling ratio with ISF.

Due to safety considerations and existing conditions, the ESF is designed to work under the pressure of 1 MPa, which is much less than the nominal operation conditions of the NuScale reactor. However, current project aims to study the two-phase natural circulation instability in a PWR-type SMR under accident conditions. Therefore, it is unnecessary to build a full pressure scaled facility. The ESF with a design pressure of 1Mpa is considered enough to investigate the two-phase natural circulation instability under accident conditions. In the following sections, the design of main components including the RPV, steam generator, and containment and outer pool are introduced. In addition, the RELAP5 analyses has been performed to verify the scaling distortions of the ESF design.

11.1. RPV DESIGN

The ESF design simplifies the entire cylinder of NuScale RPV into a loop structure by replacing the annulus down comer part with a pipe structure. Standard schedule 10s stainless steel pipes are used to build the loop. The riser part is consist of 4 inch pipe for the core part and reduce to 3 inch for the chimney part. The steam dome is built with an eight inch pipe instead of a previous hemisphere cap. The down comer is built of a 6 inch pipe, connected with an expansion joint under the consideration that the entire loop may have a different thermal expansion

ratio. Figure 11-1 and Figure 11-2 show the front and top view of RPV loop.
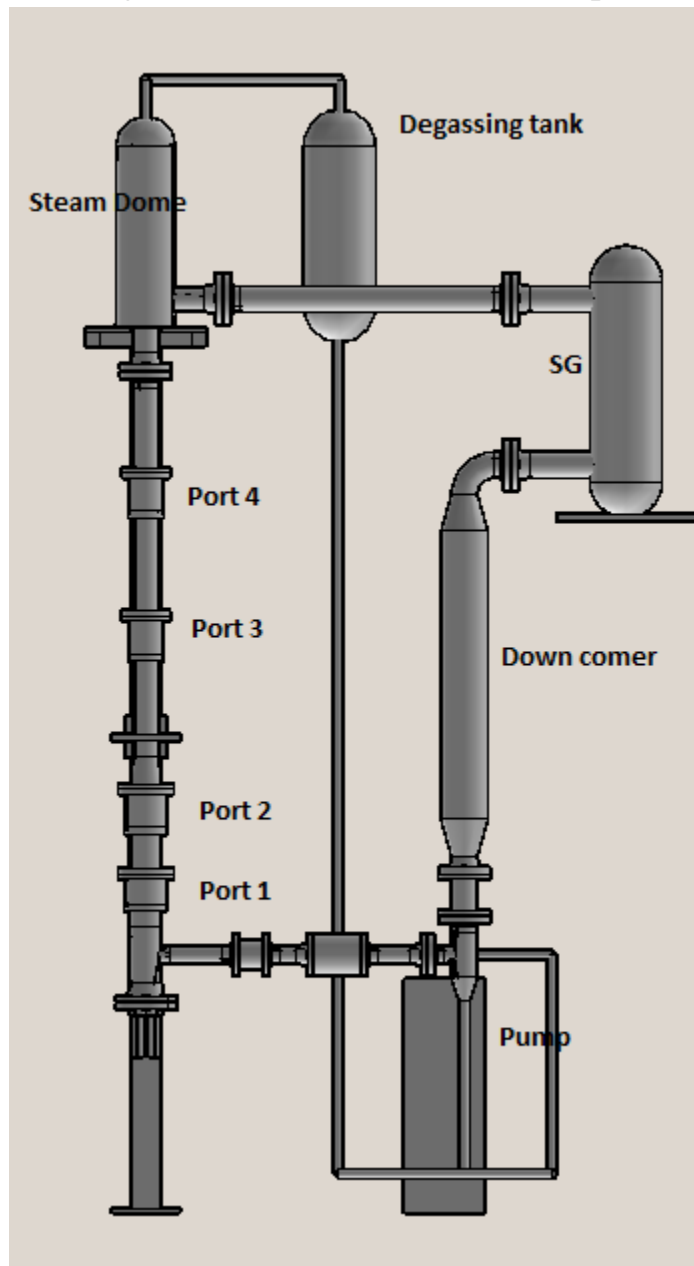
Figure 11-1 Front view of RPV loop
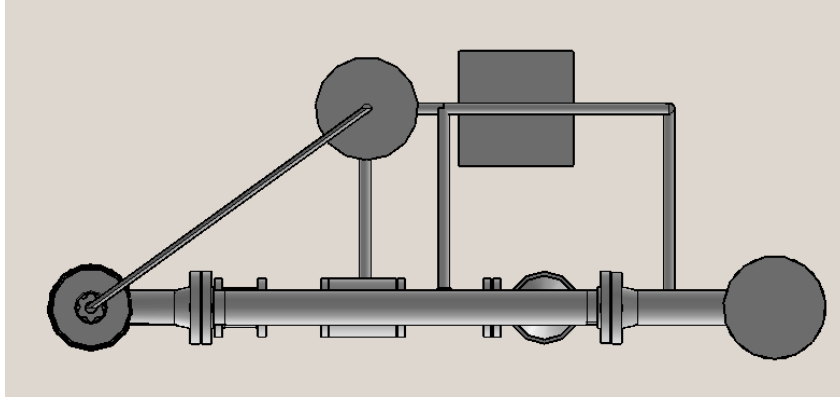
Figure 11-2 Top view of RPV loop

Six single phase electrical heater rods are installed to simulate the active core region in the reactor. The quantity 6 is selected to meet the core flow area scaling ratio as well as the requirement of electric three-phase connection in current working space. Partition plates will be installed to adjust the hydraulic diameters of core area and to prevent large slug bubbles. In addition, one impedance void meter will be installed on partition plates to measure the local void fraction in selected core area. Figure 11-3 shows the core heater assembly.
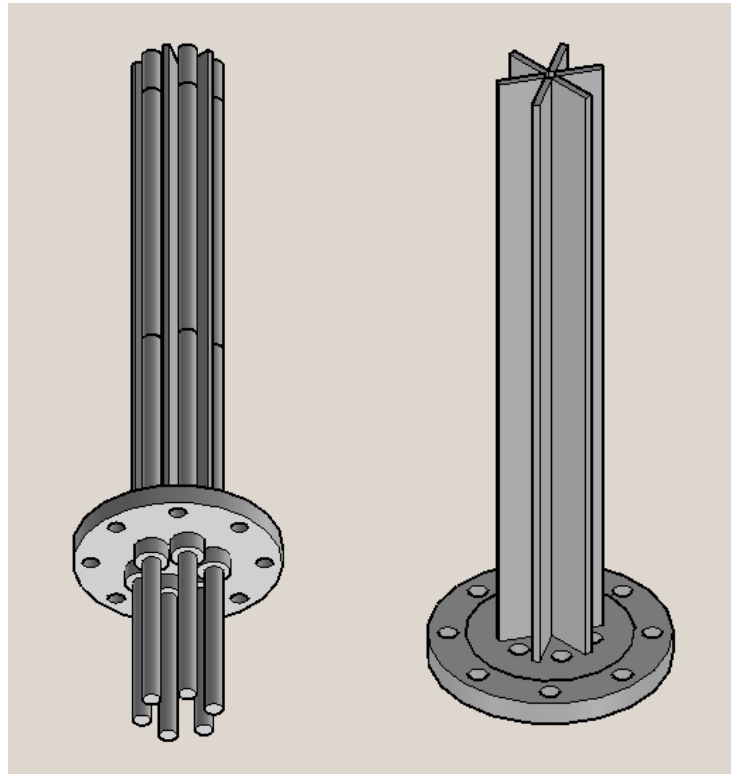
Figure 11-3 Heater rod assembly

Figure 11-4 shows the entire structure of riser part. There are 4 ports along the entire riser, with 4 ports in chimney and 1 port in core region, which are able to measure void fraction using impedance meter. Pressure transducers and thermal couples are also installed to collect pressure and temperature data. It should be noted that the entire loop is designed to work under 1 MPa and the water level is just below the steam generator for the test conditions. Therefore, the port at the top is designed to monitor the water level at the beginning of experiment. Once the top port impedance meter shows a pure gas reading but the DP between ports shows a pure liquid pressure difference, the water level is known to be at target position.
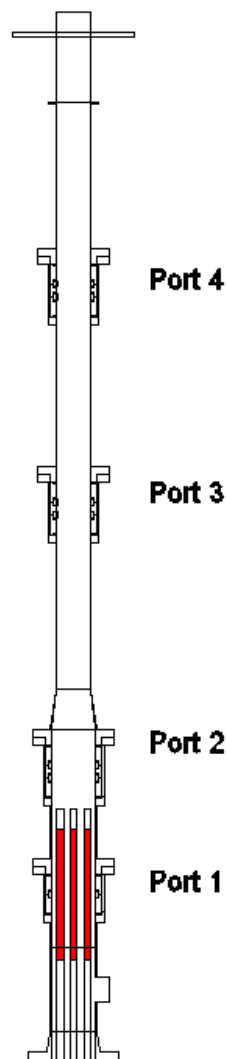
Figure 11-4 Riser part

There are two kind of impedance meter design in ESF. The chimney part uses a double ring structure [29]. The two rings can act as two electrodes and react to various flow regions to measure local void fractions. However, the double ring impedance meter are not feasible for the core part since the structure is much complicated. In addition, it is necessary to assume the flow pattern is symmetric and can be averaged into six equal part. Then if all the rods are acting as one electrode and one ring is installed and being the other electrode, the measured area averaged void fraction is still reasonable. The previous BWR type test facility also uses the same impedance design. Figure 11-5 and Figure 11-6 show two kind of impedance design respectively.
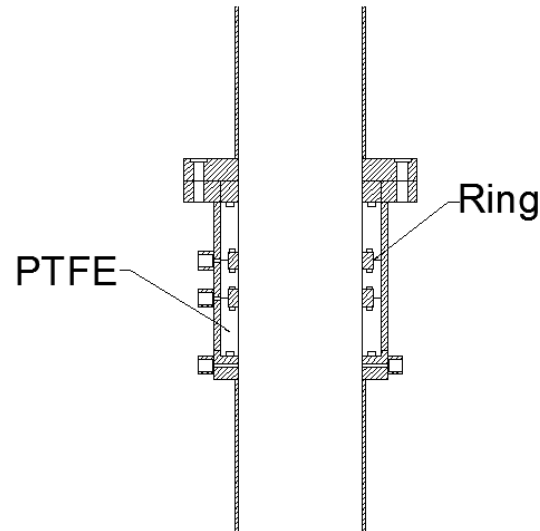
Figure 11-5 Chimney impedance port design
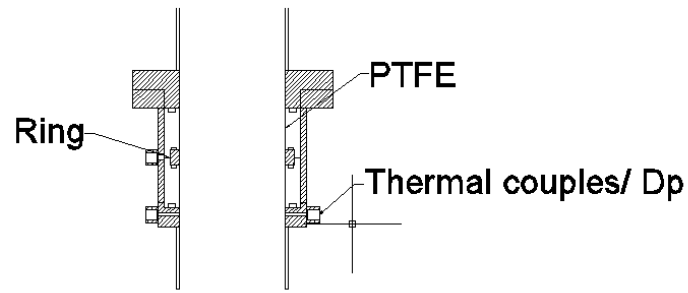
Figure 11-6 Core impedance port design

Table 10.1 shows the design parameters of ESF primary loop. Prototype and ISF parameters are also listed for comparison.

Table 1110.1 Design Parameters of ESF Primary Loop

Component	NuScale	ISF	Ratio (NuScale/ISF)	ESF	Ratio (ISF/ESF)
Lower plenum					
Area	2.034	0.020	100.0	0.006	3.169
Length	0.794	0.199	4.000	0.203	0.977
H.D.	1.609	1.138	1.414	0.031	36.813
Core					
Area	0.590	0.006	100.0	0.006	0.921
Length	1.350	0.338	4.000	0.330	1.022
H.D.	0.011	0.008	1.414	0.031	0.252
Chimney					
Area	1.722/0.611	0.017/0.006	100.0	0.009	1.87/0.663
Length	8.140	2.023	4.000	2.007	1.008
H.D.	0.348/0.136	0.246/0.096	1.414	0.108	1.848
Upper plenum					
Area	4.809	0.048	100.0	0.035	1.368
Length	1.000	0.250	4.000	0.254	0.984
H.D.	0.840	0.594	1.414	0.212	2.808
Pressurizer					
Area	4.085	0.041	100.0	0.035	1.164
Length	1.900	0.475	4.000	0.483	0.984
H.D.	0.735	0.520	1.414	0.212	2.457
Down comer (SG part)					
Area	2.131	0.021	100.0	0.056	0.377
Length	2.591	0.648	4.000	0.635	1.020
H.D.	0.029	0.020	1.414	0.014	1.457
Down comer (other part)					
Area	3.8792/2.4061	0.039/0.024	100.0	0.021	1.89/1.176
Length	6.492	1.623	4.000	1.626	0.999
H.D.	1.3720/0.7400	0.970/0.523	1.414	0.162	
Total RPV					
Height	13.60	3.400	4.000	3.404	3.996
Volume	52.64	0.132	400.0	0.126	1.046

11.2. STEAM GENERATOR DESIGN

The ESF uses a different steam generator design with the prototype due to the simplified design. The NuScale reactor uses helical tube arrangements to remove core heat and generate steam. The helical structure has been proved to be highly efficient in heat transfer. However, it is impractical to build such structure under current machinery condition in TRSL. In addition, our facility is supposed to work

188

under 1MPa only. Under accidental conditions, the core should be scrammed down already and steam generator should be isolated from the secondary loop. Because the whole secondary loop is isolated, the heat capacity of water remain inside SG is much more important than the convection heat transfer of SG tubes. Therefore, it is unnecessary to build a SG with similar geometry and structure as the prototype SG.

Current ESF design uses straight tubes to simulate the tubs in the SG. The total volume of steam generator is well scaled (1/400) to conserve the total heat capacity of water remains inside SG after the blow down phase in the accident. In addition, the location of inlet and outlet of steam generator should strictly follow the length scale. According to the safety strategy of the NuScale design. SG can also act as a part of decay heat removal system (DHRS) by exchanging core decay heat to outer pool shown in Figure 11-7. As can be seen, the helical SG is connected to two separate heat exchangers which are emerged into the outer pool. When accident happens and the SG is isolated from steam line, the heat exchangers start to work and transfer the core decay heat to the outer pool.
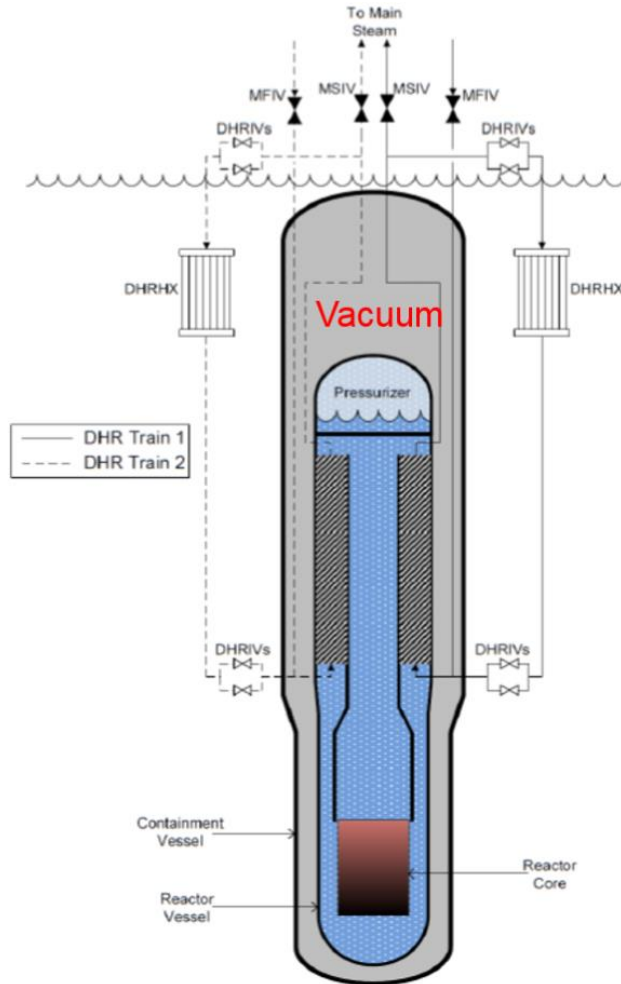
Figure 11-7 NuScale Decay Heat Removal System

The details of this system such as dimensions, operation scenario and design parameters are currently proprietary. However, the idea that the steam generator should still have the ability to transfer the decay heat after scram down should be considered in the ESF. Therefore, a secondary loop is connected to the steam generator to make it a once through straight tube heat exchanger.

In ESF design, the steam generator consists of fifty 0.75 inch stainless steel pipes weld together to a metal plate and enclosed into a 10 inch pipe. Steam passes from the shell of exchanger and cool water goes through inside tubes. The geometry of heat exchanger is shown in Figure 11-8.
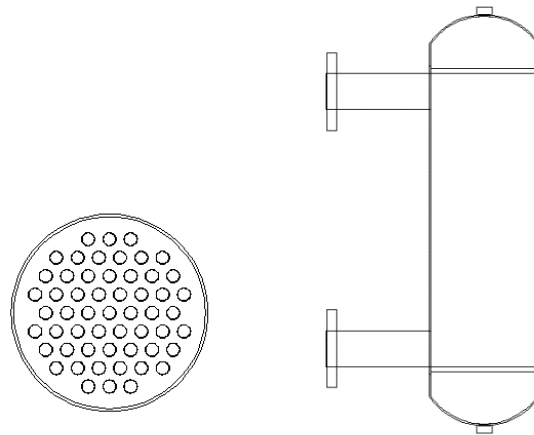
Figure 11-8 Design of ESF Steam Generator

It should be mentioned that the top and bottom of SG uses butt welding cap to seal the entire vessel. This is to ensure safety when operating. However, extra volume distortion is thus involved which may greatly affect the proper scaling of SG water volume. Therefore, PTFE balls with diameters of 1 inch and 0.75 inch are installed and fill the top and bottom caps to eliminate the extra volume. Also, PTFE balls can filter the flow so that the upcoming flow can pass averagely through every tube.

11.3. CONTAINMENT AND OUTER POOL SIMULATION

Current ESF design uses a single tank to simulate the containment. The tank should not only well scale the volume of prototype containment, but also have limit height less than the top of the lab ceiling. Therefore, the containment is comprised of 14 inch stainless pipe welded with two caps at both ends. The structure is also simplified to be a single cylinder, unlike the prototype case which has a larger cross section area in top part. Top ADS line and sump line are attached

directly to the containment by fittings. Orifice is installed in the ADS line, with a ratio of 1/200 for the scaling of the throat area. This area ratio equals to power ratio, which is because critical flow will happen in high pressure blowdown process and the flow velocity will be restricted to local sound speed. In order to assure correctly scale the energy inventory, it is necessary to reduce the throat area into half. Detailed derivations and verifications can be found in [8].

According to the NuScale design, the whole containment vessel is merged into an outer pool which serves as an ultimate heat sink. However, to build the experimental facility, it is impractical to merge the containment tank into another large water pool. Considering that the outer pool is designed to cool down the containment and absorb decay heat. It is reasonable to substitute the pool with an alternative heat sink.

The ESF design uses a build-in one inch pipe to simulate the outer pool. The pipe passes through the inside of containment and flows with cool city water. The flow rate can be adjusted by a ball valve attached to the loop. According to the tube heat exchanger heat transfer calculation, a 1 inch pipe with a length of 2.81 m will be enough.

11.4. RELAP 5 ANALYSES FOR ESF

11.4.1 Steady state analyses

Although ESF cannot run under full pressure normal operation condition, it is still necessary to run RELAP5 steady state analysis to help check the all the scaling distortions. As mentioned in the previous section, the steam generator has been changed significantly in the geometry. However, current design only aims to balance the thermal inertia and to provide an alternative method to remove core decay power. It is not designed to generate steam and balance the normal operation heat generation. Thus, ESF input deck remains the hydraulic component and heat structure of steam generator. The core part heat structure is also unchanged for the sake of energy balance.

In current ESF design, the cross section area of primary side of steam generator is distorted from the ISF. The flow area of ESF is larger than that of ISF.

This may cause the steady state pressure to increase because a faster flow rate will weaken the heat convection between down comer and SG. Thus, little adjustment has been made to the code. The SG flow area remains unchanged, and the distorted volume is compensated to the lower down comer part, where the heat transfer is not as significant. The simulation results match well with previous ISF results.

Figure 11-9 shows the steady state pressure comparison of ISF and ESF. There is fluctuation in first 2000s for both case which seems to be significant. However, this may because of the different input geometry. Since ISF and ESF use different flow area and heat structure, it is possible that the system fluctuate in the very beginning. However, after 2000s, both cases turn to be stable and enter the steady state.

Figure 11-10 shows the mass flow rate of the ESF. Although the flow area and hydraulic diameter have been changed for ESF, proper adjustment of inlet K factor can still help getting the same flow rate with ISF.
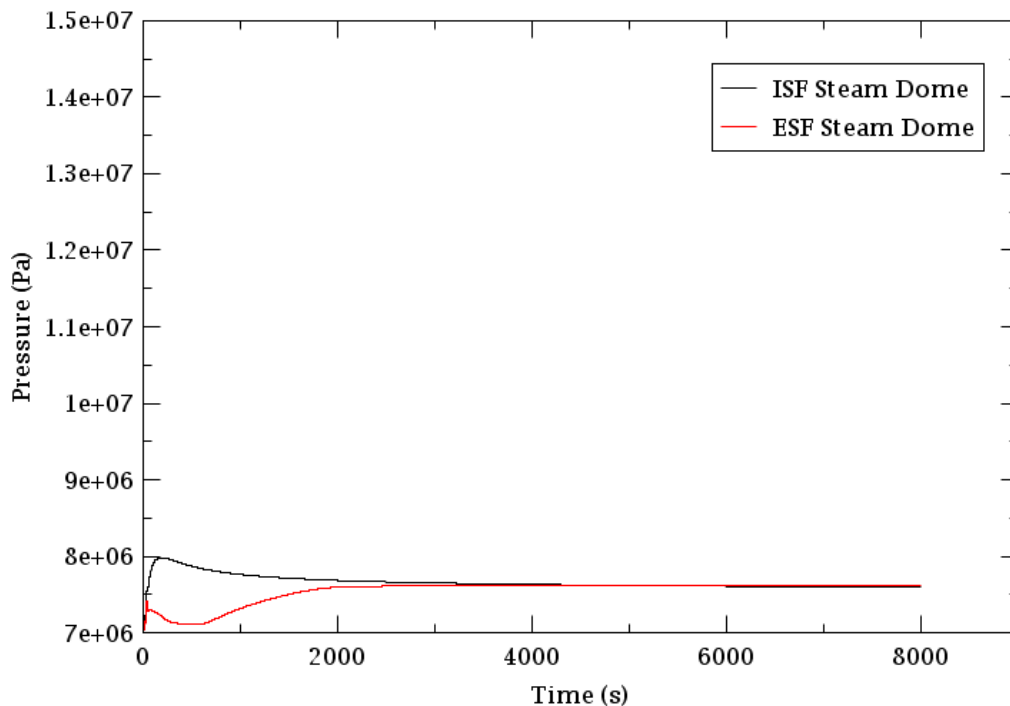
Figure 11-9 Steady State Steam Dome Pressure Comparison of the ISF and the ESF by RELAP 5
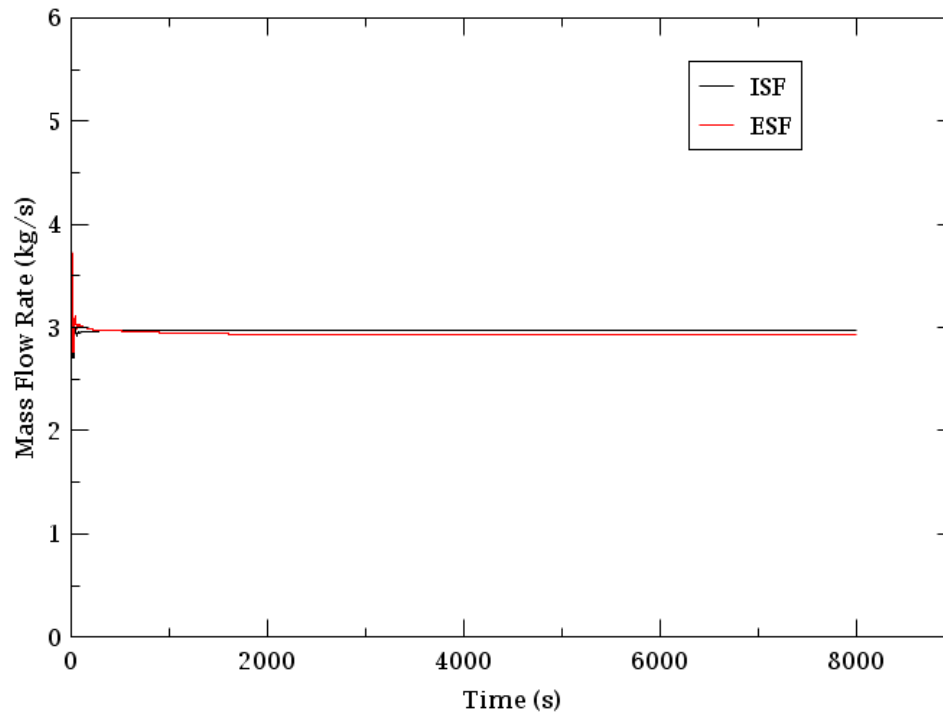
Figure 11-10 Steady State Mass Flow Rate Comparison of the ISF and the ESF by RELAP5

11.4.2 Transient analysis

Similar to that for ISF, blowdown transient performance is also simulated for the ESF case. Figure 11-11 shows the blowdown pressure curve for ESF, compared with ISF blowdown curve. As could be seen from the figure, the pressure curve fits well for ESF case. Very little difference can be seen which may because of the distortion of total volume of ESF.
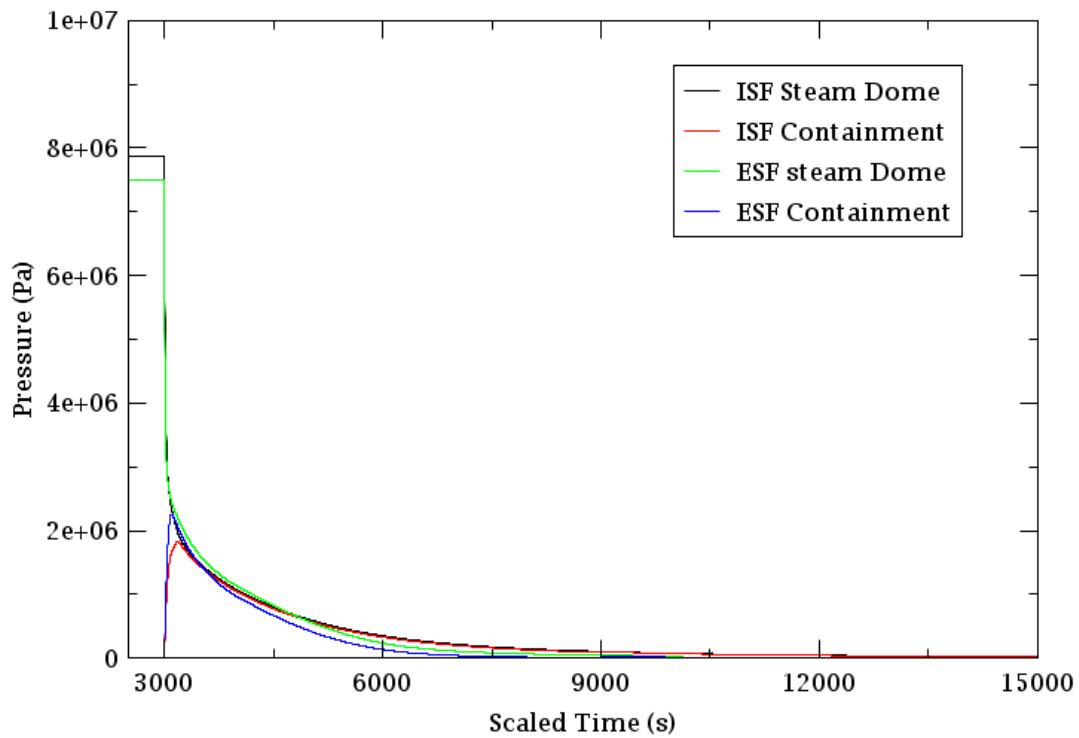
Figure 11-11 Blowdown Pressure Comparison for the ISF and the ESF by RELAP5

Collapsed water level of ESF is also compared with ISF, see Figure 11-12. Due to the distortion of the total volume, the level curve shows insignificant discrepancy between ISF and ESF. However, the idea that water level inside RPV would never decrease below the top of core always stands.
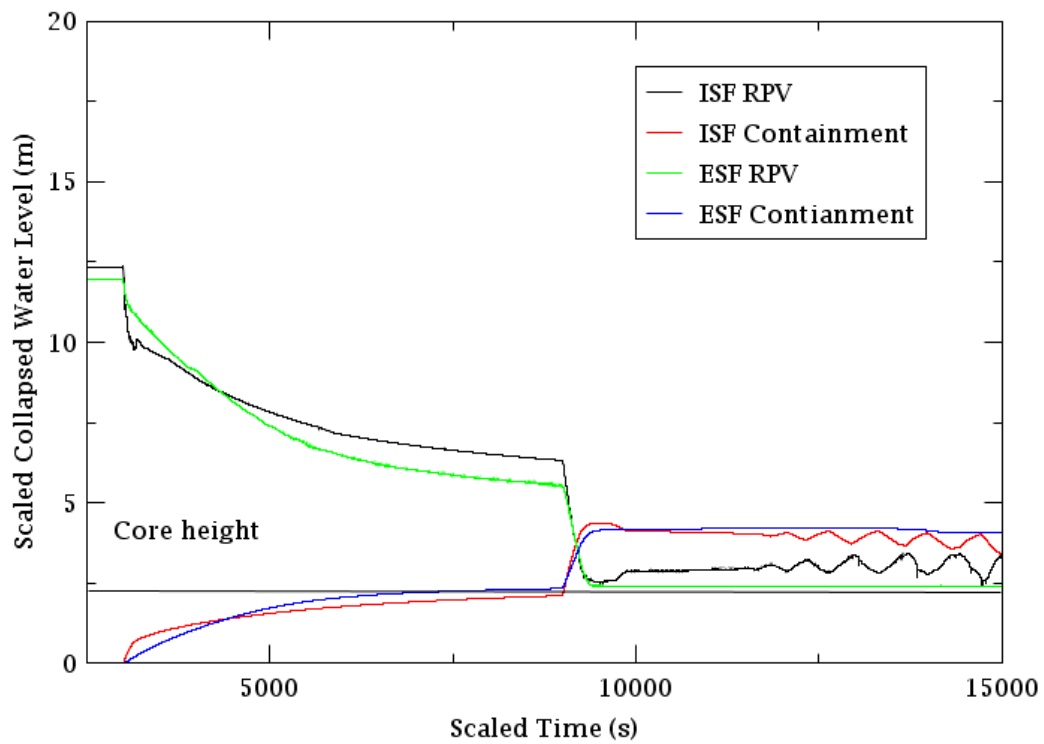
Figure 11-12 Collapsed Water Level Comparison for the ISF and the ESF by RELAP5

12. EXPERIMENTAL STUDY OF PWR-TYPE SMR

12.1 DESCRIPTION OF EXPERIMENT FACILITY AND INSTRUMENTATION

The detailed schematics of the facilities for the startup transient and quasi-steady tests are shown in Figure 12-1. The facility includes similar structures as the prototype (NuScale Reactor) such as

1. Lower plenum housing the unheated section of electric heater rods
2. Heated section (red part) simulating the core
3. Chimney section (riser)
4. Steam dome section
5. Steam generator section (simplified by using straight pipes)
6. Downcomer (simplified by using pipe)
7. Containment tank

Figure 12-1 Schematic Drawing of the Experimental Facility

The maximum power of the heater is 20 kW. It is powered with a three phase 480 V AC source. The time constant difference between the prototype fuel rods and electric heater rods are not important in the thermal hydraulic instability

analysis [26]. As shown in figure 12-1, the heat exchanger in upper part is designed for the degassing process which is necessary to remove non-condensible gases before heating tests.

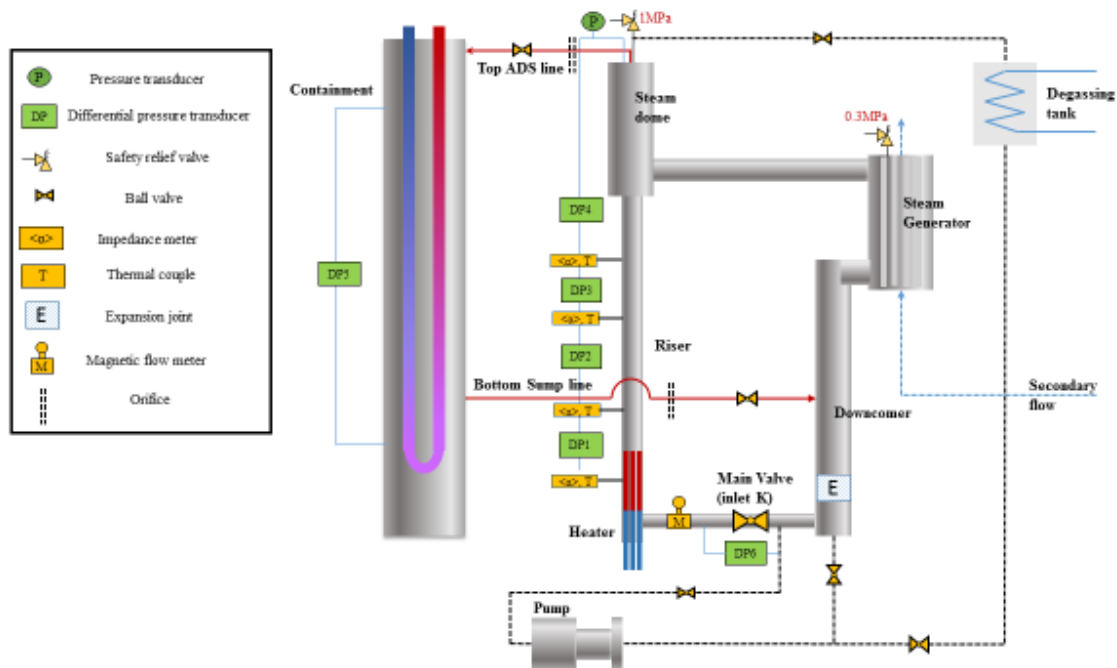Figure 12-2 is the photo of the test facility before insulating. The containment is at the left side of figure (a), while the steam generator is located at the ride side. The steam dome is next to the containment and is connected to containment and degassing loop at the top. And the core part can be found at the left side of figure (b).

(a)   (b)

Figure 12-2 Picture of the Test Facility before Insulation (a) Upper part (b) Lower part

Impedance meter, thermocouple, pressure transducer and magnetic flow meter were employed to measure the void fraction, temperature, pressure and flow rate of the system.

The design of impedance meter has been explained in previous chapter. The non-dimensional voltage measure by impedance meter was calibrated against the void fraction measured by differential pressure transducer and the results are shown in figure 12-3. The calibration process was conducted at adiabatic condition in still water. The IMP 1, 2, 3, 4 represent the result of impedance meter located at port 1, 2, 3, 4, respectively. These results show a good linear relation between the void fraction and the non-dimensional voltage thus proves the reliability of

impedance meter result. A calibration curve will be produced by fitting the non-dimensional voltage with the void fraction and this curve will be used in future experiment to convert the measured voltage to void fraction.
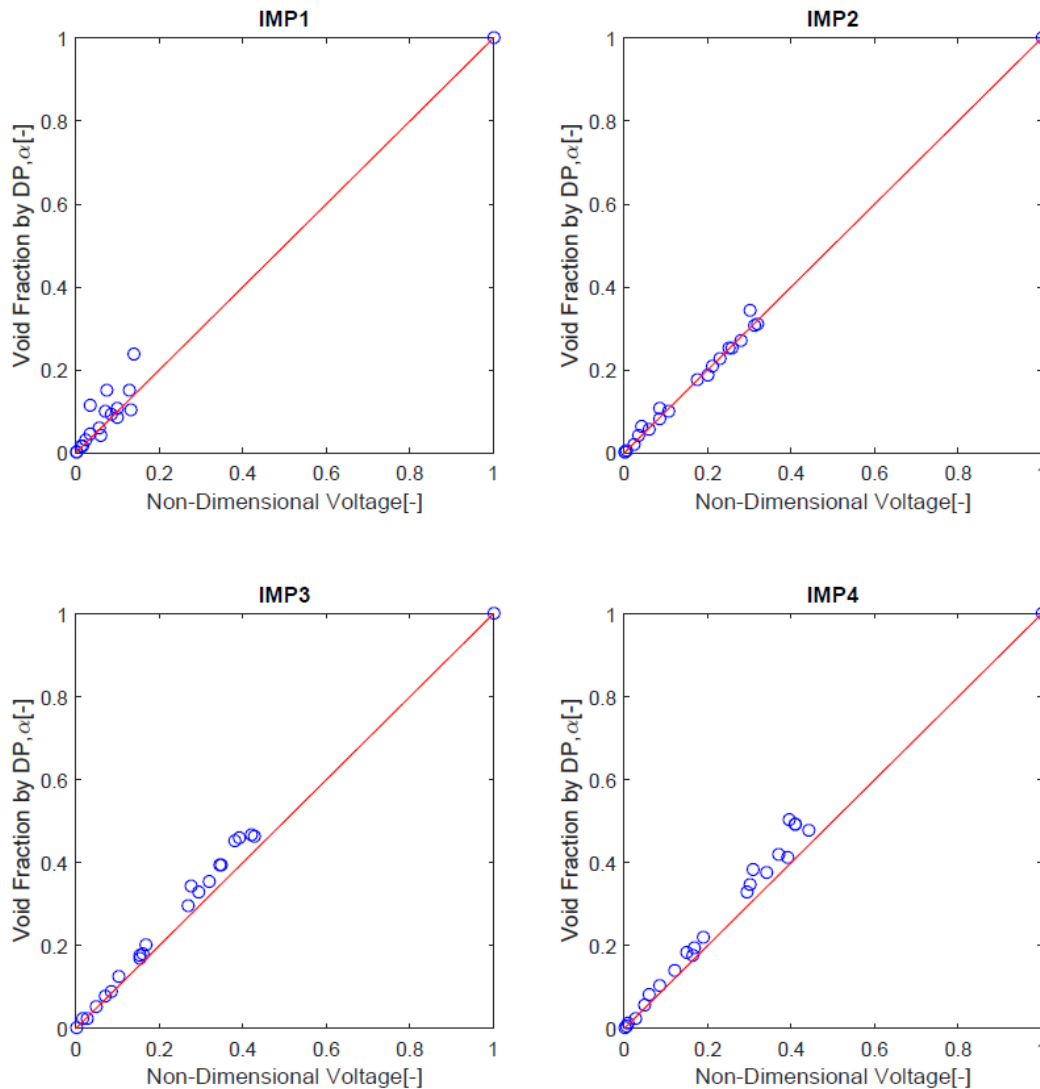
Figure 12-3 Result of Impedance Calibration

The pressure transducers used in this study are Honeywell pressure transducers with an accuracy of ±0.025% of the total measurement range. The range of the instruments has been set to 100 kPa in order to measure the full range of differential pressures seen in the experiment. The output of these instruments is a constant 4-20 mA current, which is converted into a 1-5 V signal by passing the current over a 250±1 ohm resistor.

The liquid flow rate is measured using electromagnetic liquid flow meters. These flow meters measure the distortion to an applied electromagnetic field. This distortion is caused by the slightly polar water molecules passing through the field, and is related to the velocity of the water molecules. Thus the distortion in the electromagnetic field can be calibrated against the liquid flow rate. The current flow meters (Honeywell MagneW 3000) have a diameter of 25 mm with an accuracy of ±1%. The flow meter output is a 4-20 mA signal, which is converted into a voltage by passing the output current over a 250 ohm resistor (±1 ohm). This voltage is then measured by the computer system, so that the final measurement has an error of ±1.1%.

Data is acquired from the instruments using a personal computer and a data acquisition system. The data acquisition board is a National Instruments AT-MIO-64E3. The board has a maximum acquisition rate of 500,000 samples per second for a single channel and 12-bit resolution. The board is configured for 64 single-ended or 32 differential analog inputs. The board input range is software selectable. The internal DAS board is connected to a SC-2056 adapter. Most signal-carrying wires are connected to this adapter. A 5B01 backplane is attached to the SC-2056 adapter. On this signal conditioning backplane, thirteen 5B37 Thermocouple Input Modules and two 5B39 Current Output Modules are installed.

The 5B37 Thermocouple Input Modules have input span limits of ±10 mV to ±0.5V and output range of 0 to +5V. The accuracy and nonlinearity of these input modules are ±0.05% of the span. The 5B39-01 Current Output Modules are used to control the heater and the preheater power. These output modules accept a high level signal at its input from the AT-MIO-64E3 analog output and provide a galvannically insolated 4-20 mA process current output signal.

The 5B39-01 Current Output Modules features high accuracy of ±0.05%, ±0.02% nonlinearity, and 1500 Vrms common mode voltage isolation protection. Data acquisition is written using LabVIEW for both the thermal hydraulic test and nuclear coupled test. A detailed DAS display for the thermal hydraulic test is shown in figure 11-4.
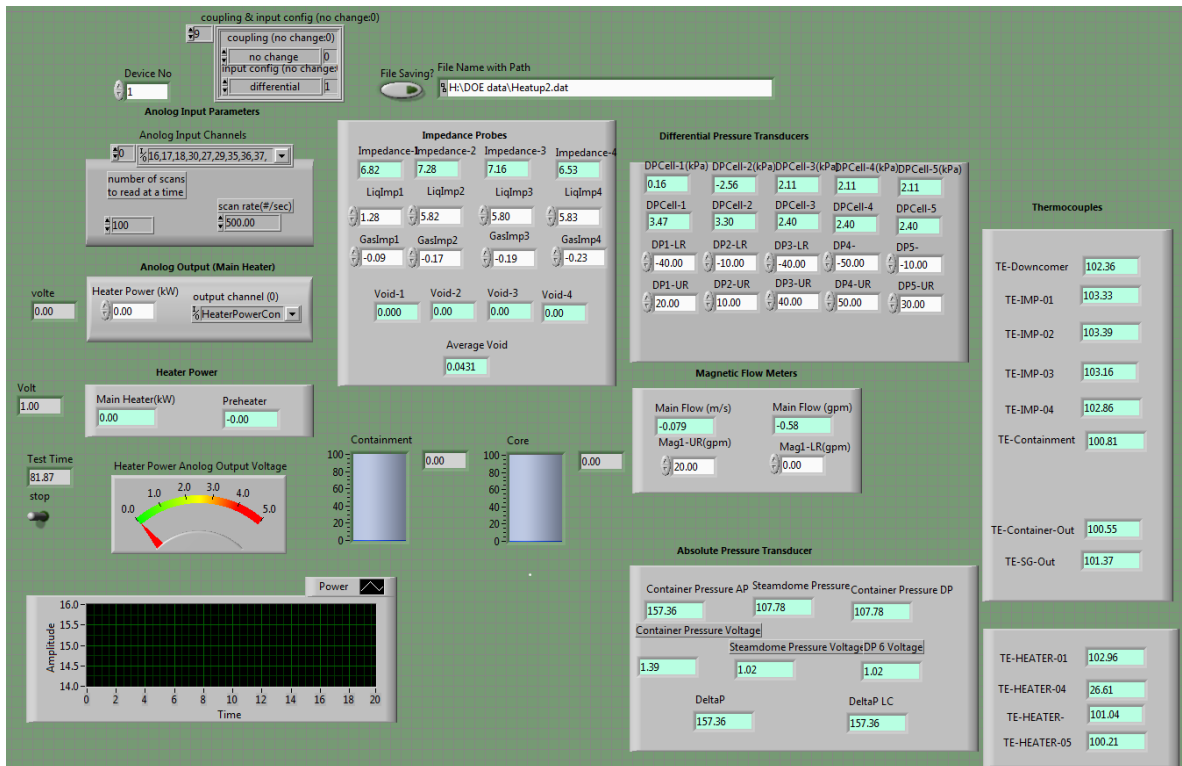
Figure 12-4 Display Panel for the Thermal Hydraulic test

Blowdown test procedure consists of a degassing procedure and heat-up test procedure. Before each test, general checks are performed. The steps are summarized as follows.

(1) Check valves positions: make sure the valve on the pump inlet line, outlet line and high ADS line are open, and make sure the valve on the drainage line, degassing line and low ADS line are closed

(2) Turn on the power for the DPs, AP and thermal couples, and impedance circuits

(3) Check the range of differential pressure transducer, including DP1 DP2 DP3 DP4 DP5 AP1 AP2.

(4) Purge each differential pressure transducer

(5) Check the DP and AP values and thermal couple readings, make sure the value is normal

(6) Collect the impedance data for full-air condition

(7) Set up the initial water level for the degassing procedure, make sure the water conductivity is less than 50 us

(8) Turn on the power supply for main heater and pump (for degassing)

201

(9) Turn on the pump, and set the heater power to 15 kW and heat the loop up to 85 ℃

(10) Stop the pump, run the degassing loop. Reduce the power of heater to 10 kW, open the valve on the bottom of containment, put the pipe inside a tank filled with water, degas the containment until the temperate of containment reaches 100 ℃, then close the containment bottom valve, close high ADS valve.

(11) Open the valve on the degassing pipe, insert the pipe inside a graduated cylinder with water, record the initial water level, heat the loop until no bubble appears in the cylinder

(12) Isolate the degassing line.

(13) Setup the initial water level

(14) Isolate the pump line from the loop

(15) Start the experiment

12.2 EXPERIMENT RESULTS OF BLOWDOWN TEST

Blow-down test are conducted by setting the RPV and containment to the initial conditions (pressure, temperature, water inventory) calculated by RELAP5 code and then opening the top ADS valve and the cool water supply valve of secondary loop of containment. During the blowdown test, the heat power curve was set according to the decay heat equation [50]:

$$\frac{P}{P_0} = 0.066[(\tau - \tau_s)^{-0.2} - \tau^{-0.2}] \tag{12.1}$$

where P is the decay power, P_0 is the nominal reactor, τ is the time since reactor startup and τ_s is the time of reactor shutdown measured from the time of startup. Here we take τ_s as 5 years in order to simulate the real situation. In fact, once τ_s is larger than 1 year, increasing of τ_s have little effect on the value of decay heat. The real-time power of the heater is shown in figure 12-5.

Table 12.1 Sequence of Events of Experiment

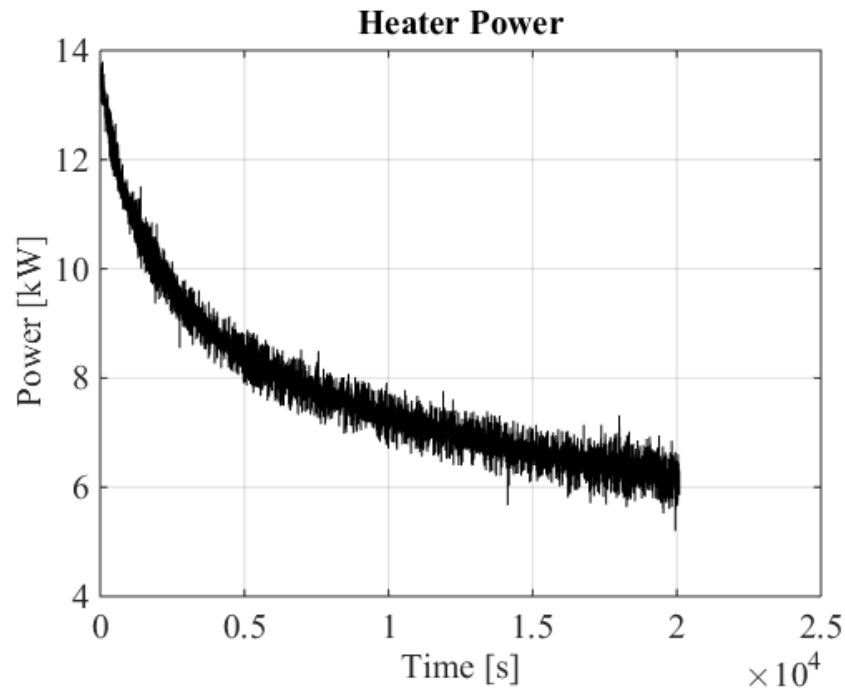| Time(s)	Events
71	Containment 2nd loop water supply valve open
71	Top ADS line open
2423	Bottom water supply line open

Figure 12-5 Decay Power Curve of Core

The steam dome pressure and containment pressure are measured during the experiment and the results are presented in figure 12-6. And the water level of the core and containment measured by differential pressure drop is shown in figure 12-7. The natural circulation flow rate can be found in figure 12-8. At the time 71s the valves of containment cooling system and ADS are opened, then both containment pressure and steam dome pressure decrease rapidly due to the condensing of the vapor. Meanwhile, the flow rate of natural circulation suddenly increases to 0.8 kg/s. This leap of flow rate results from the flashing phenomena: the decreasing of pressure in the main loop makes the coolant become overheated. Large amount of coolant vaporizes, which is so called flashing, and leads to the increasing of main loop flow rate. The vapor generated by flashing flows to the containment at the critical speed and then condenses in the containment. At the same time, the core water level decreases rapidly and the containment water level increases correspondingly. From figure 12-7 it can be found that the core water level keeps steady and increases a little during 18000s after the bottom water supply line open, and it is always higher that the heated core part, which corresponding the normalized water level 5%.
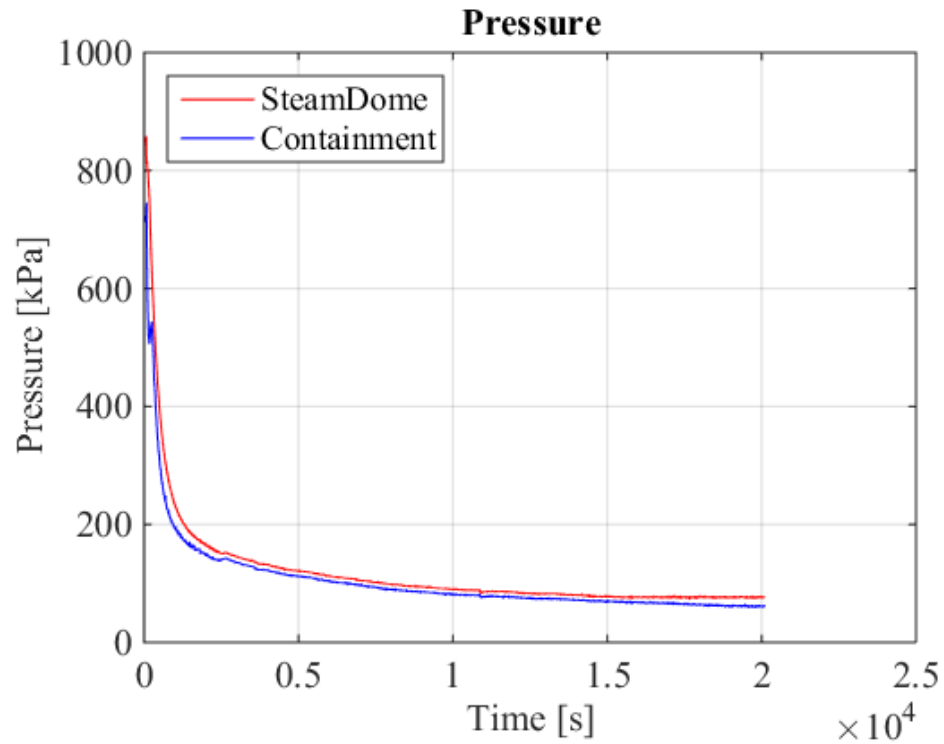
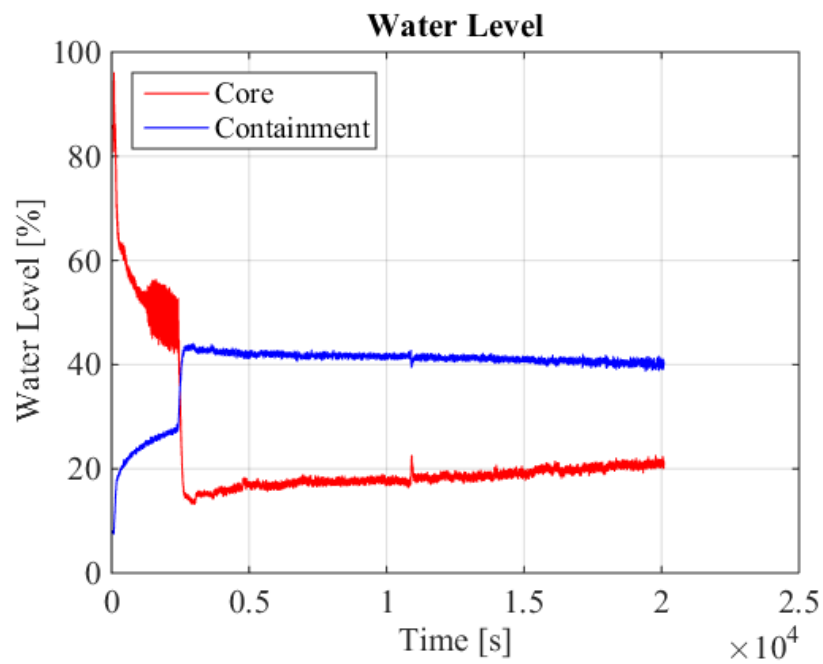*Figure 12-6 Pressure of Steam Dome and Containment*

Figure 12-7 Water Level of Core and Containment during the Blow-down Test
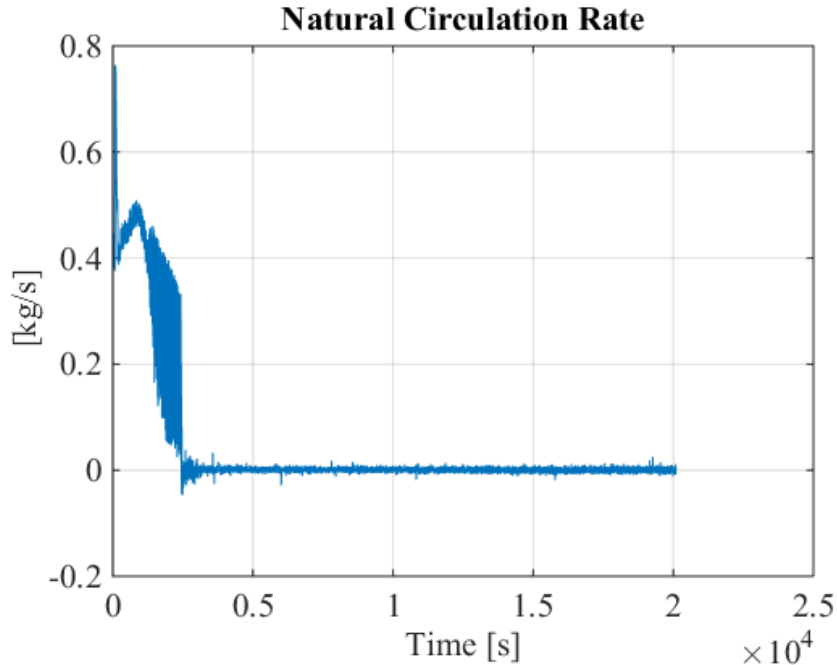
Figure 12-8 Natural Circulation Rate at the core during the Blow-down Test

However, strong oscillation of both core water level and flow rate is observed at about 2000s after blowdown, which haven't been reported in previous research of PWR-type small modular reactor [34]. Detailed natural circulation flow rate is shown in figure 12-9, 12-10, the frequency of which can be roughly estimated to be 0.2 Hz. The most possible reason is that the core water level decreases and becomes lower than the height of upper plenum. At the first 1000s the vapor bubbles generated in the core section move to the containment due to the low pressure in the containment, whereas the water flows through the upper plenum to the steam generator and down comer, hence the void fraction in down comer part is much smaller than that in chimney part, which results in a density difference and oscillates the flow. However, if the water level in the chimney keeps decreasing and becomes lower than the upper plenum, the water in the core can't flow back to the down comer and the flow rate will decrease significantly. The reducing of flow rate leads to the increasing of coolant enthalpy and produced more vaper in the core and chimney part. Then the increasing of void fraction will elevate the water level and make it higher than the upper plenum again, hence increase the flow rate and decrease the void fraction in the core, which forms self-sustained oscillations. At 2423s, the low water supply valve opens and the coolant in the core flow into

the containment due to the higher pressure and water level in the containment, leads to the rapid decreasing of the core water level and the liquid can no longer flow through the higher plenum and the flow rate decreases to near zero.
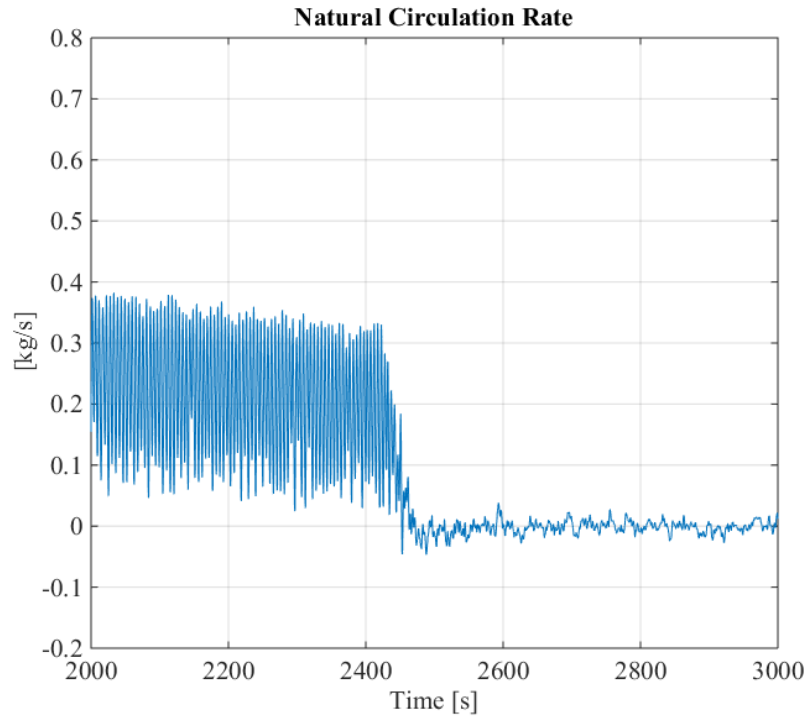

Figure 12-9 Detailed Natural Circulation Rate during 2000s to 3000s
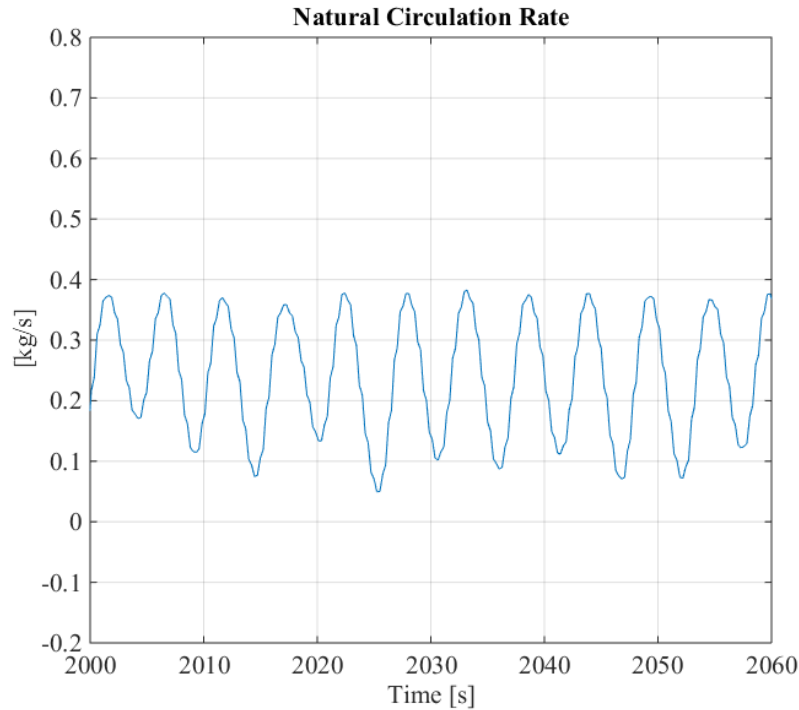
Figure 12-10 Detailed Natural Circulation Rate during 2000s to 2060s

In order to investigate this oscillation, the differential pressure, detailed differential pressure, void fraction and detailed void fraction results are shown is figure 12-11 to 12-15 respectively. The differential pressure measures the pressure differences between the bottom and the top of one specific vertical section, zero means that the pressure at the bottom of this section is same as the pressure at the top of this section, which can be concluded that there is no liquid in this section, the specific information of the locations of all five Dp can be found in figure 12-11. At the beginning of blowdown process, the pressure drop for all 4 Dp measurement ports at the RPV decreases, this is because the existence of vapor generated by flashing lower the average density of coolant. At around 1000s, the pressure drop starts to oscillate like the flow rate, which agrees with previous speculation.
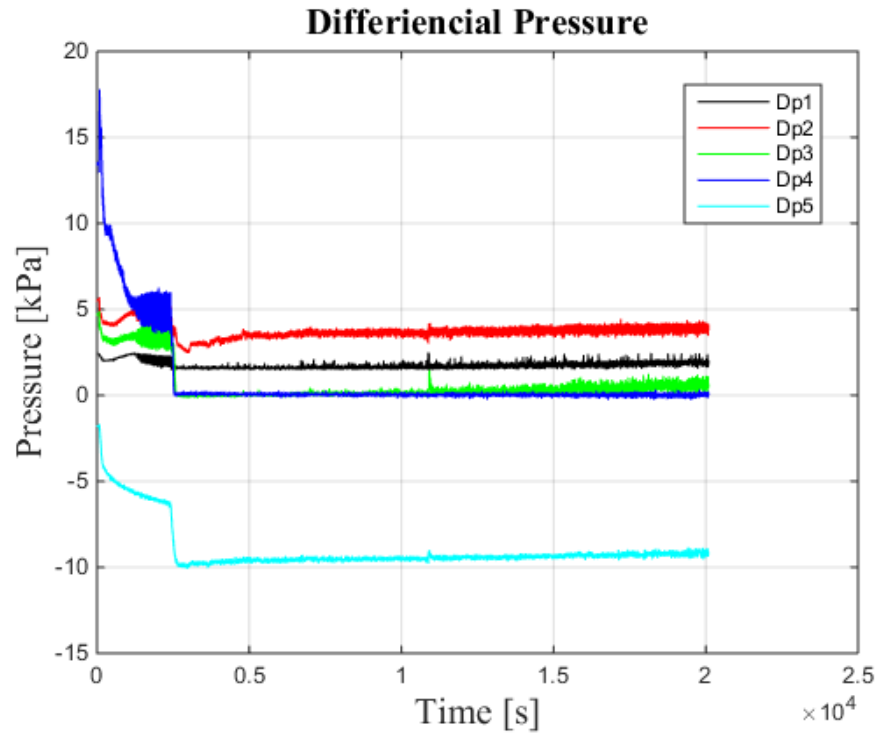
Figure 12-11 Pressure Drop Measurement Results during the Blow-down Test
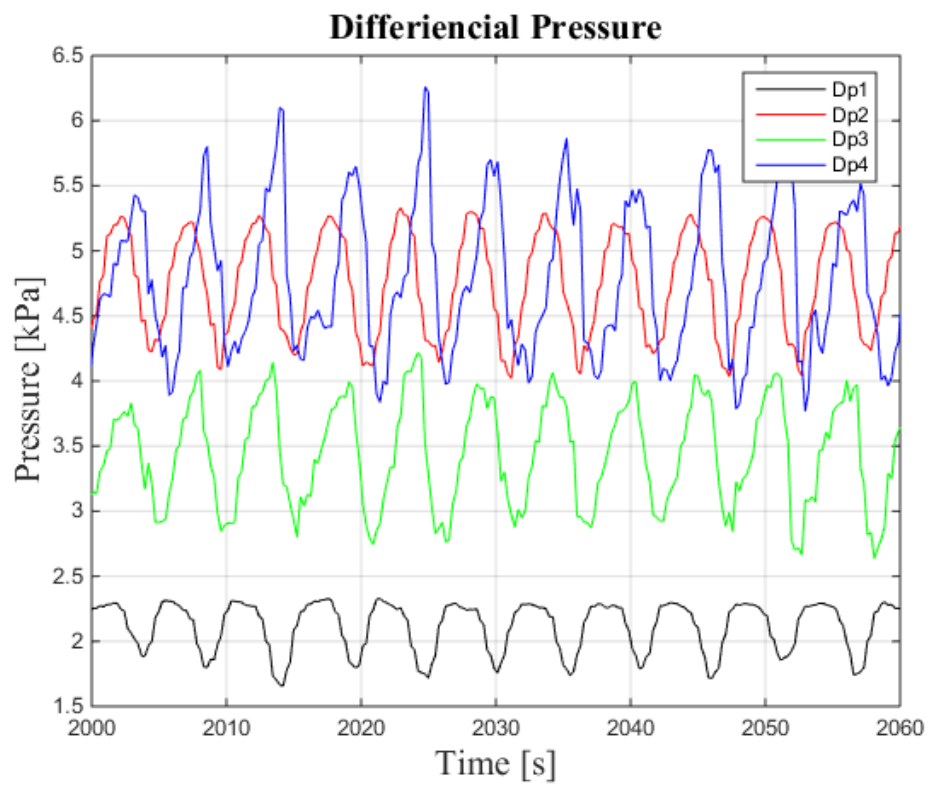
Figure 12-12 Detailed Pressure Drop Measurement Results during 2000 to 2060s

208

More detailed evidence can be found in the result of void fraction. Figure 12-15 shows the detailed void faction measurement result during 2000s to 2060s, which can be compared with figure 12-10, the detailed flow rate result during the same time. The Imp 1 2 3 4 means the void fraction measured at port 1 2 3 4, which can be found in figure 12-1. According to previous discussion, the when the flow rate is high, the void fraction becomes low hence reduce the core water level and hinder the water flow through upper plenum, so the void fraction-time plot should be opposite to the flow rate-time plot.

Figure 12-13 Impedance meter Measurement Results during the Blow-down Test
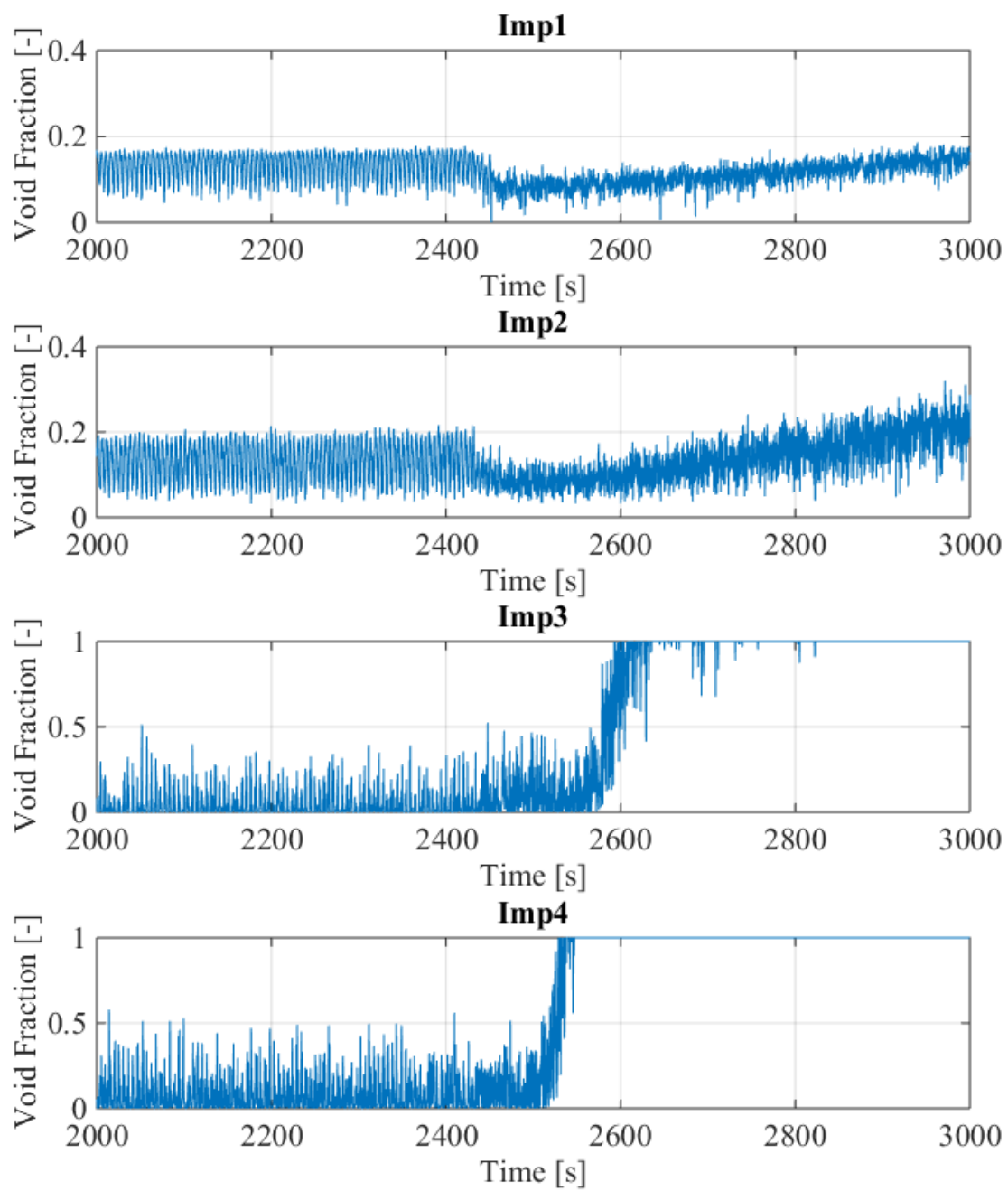
Figure 12-14 Impedance meter Measurement Results during 2000s to 3000s
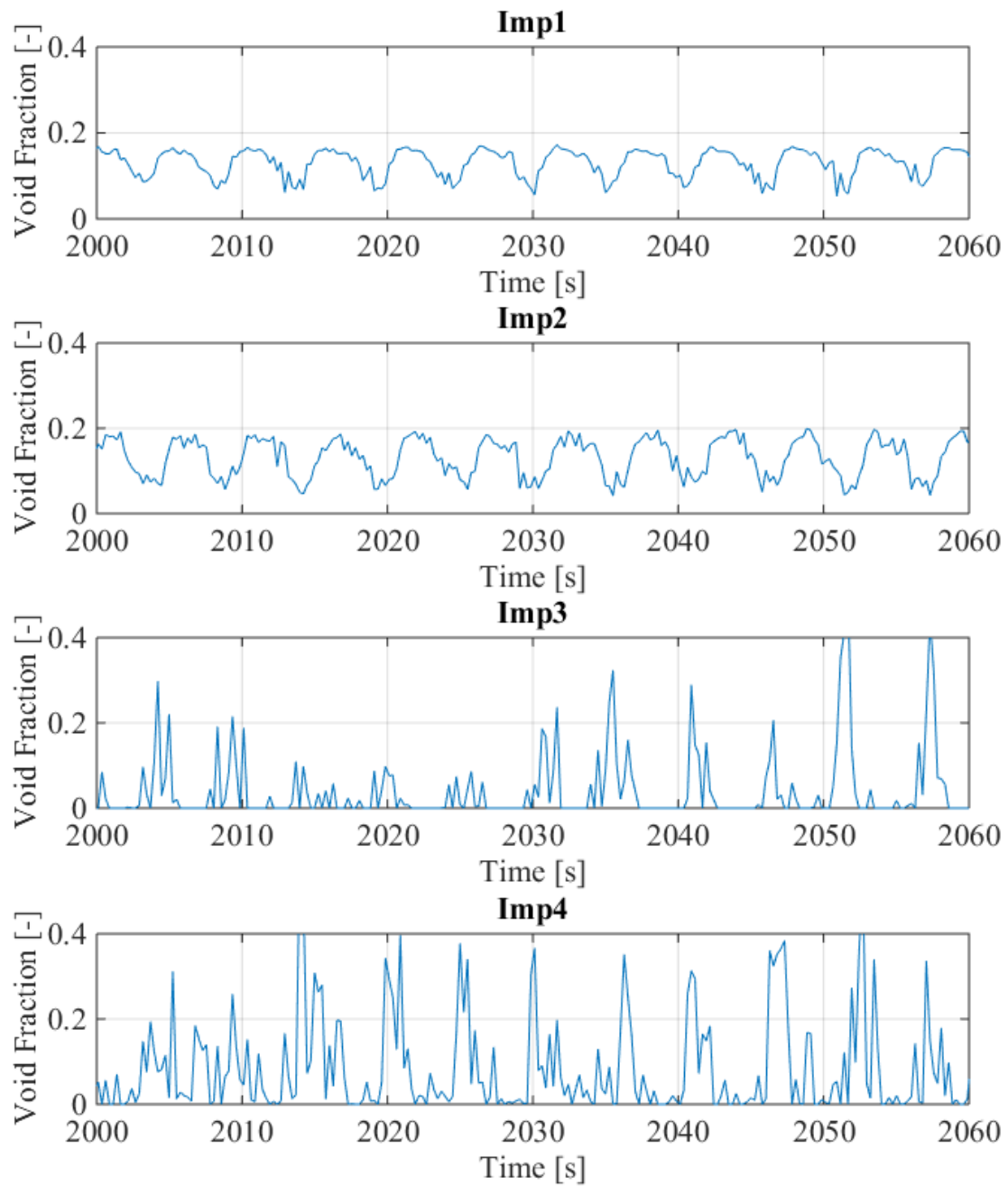
Figure 12-15 Detailed Impedance Measurement Results during 2000s to 2060s

The temperature measurement results is shown in figure 12-16, where the TeImp1 2 3 4 represents the temperature measured at port 1 2 3 4, respectively. TeContainmentOut means the temperature measured at the outlet of the secondary loop of containment. Once the ADS valve is op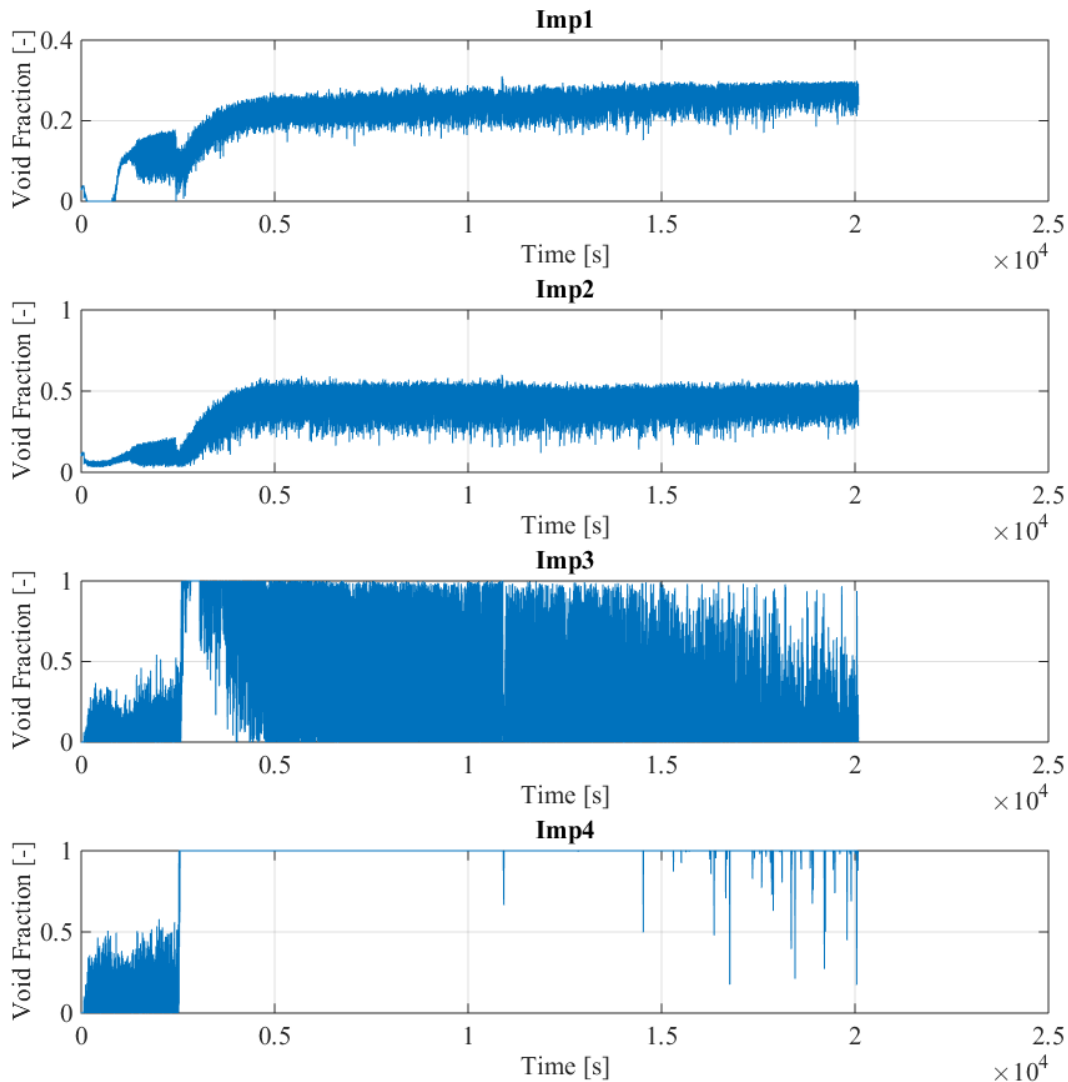ened, the containment secondary loop temperature increases from room temperature to above 100 ℃. And the secondary loop of containment is open to atmosphere, so the heat transfer change from single phase convection to two phase convection. Meanwhile, the main loop temperature decreases quickly because flashing took off a lot of heat from the main loop.
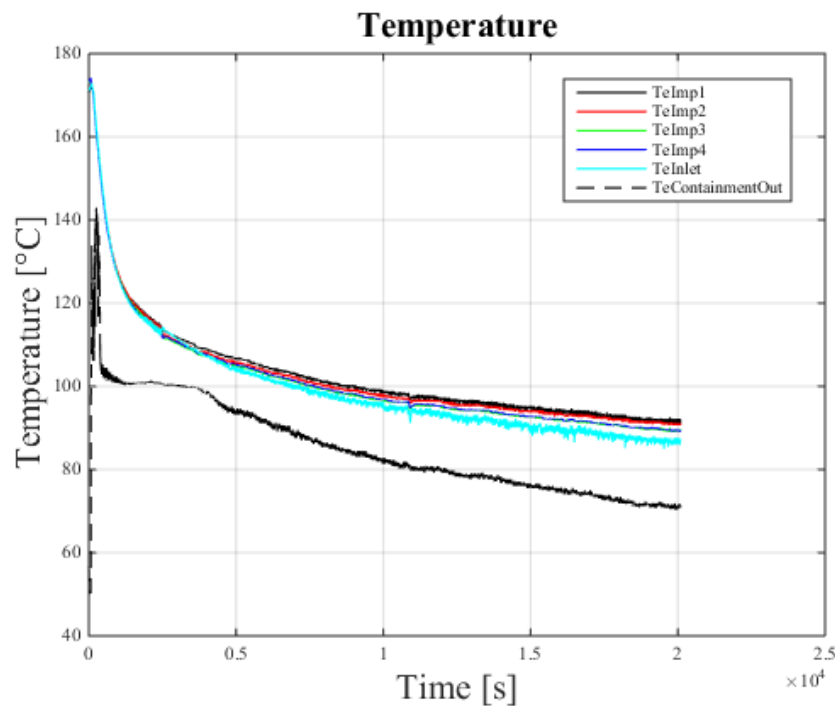
Figure 12-16 Temperature Measurement Results during the Blow-down Test

12.3 EXPERIMENT RESULT OF COLD BLOWDOWN TEST

Due to the limitation of pressure scope (1 MPa) of current test facility, a full pressure-scale blowdown event can't be simulated completely. In order to investigate the transients start from the opening of ADS valve in both experimental and numerical way, the cold blow-down experiment is conducted by setting the initial pressure of RPV to around 1 MPa and setting the initial pressure of containment to 50 kPa and then opening the ADS valve. This is similar to the

212

blowdown event except that the initial pressure of RPV is much lower than the normal operation condition (7.8 MPa). Such kind of accident can happen when the ADS valve inadvertent opens during the scram-down process. By comparing the experiment result and the code prediction on cold blowdown event, the capability of code in predicting detailed transients near the ADS valve opening can be evaluated.

During the experiment, the decay heat power is set to 10 kW. The sequence of events is presented in table 12.2. The pressure of RPV and containment is plotted in figure 12-17. The natural circulation rate and detailed figure is shown in figure 12-18 and 12-19. The collapsed water levels of both RPV and containment are presented in figure 12-20 and 12-21. At 100s the top ADS valve opens, the steam dome pressure suddenly decreases and leads to flashing of coolant in RPV. The density difference between hot part and cold part increases due to the flashing phenomena, hence the natural circulation increases, which can be seen from figure 12-18. The generated vaper vents into the containment and condenses due to the pressure gradient and lower temperature of containment, which results in the decrease of core water level and increasing of containment water level, as shown in figure 12-20.

Table 12.2 Sequence of Events of Experiment

Time(s)	Action
100	Top ADS line open
3600	Bottom water supply line open
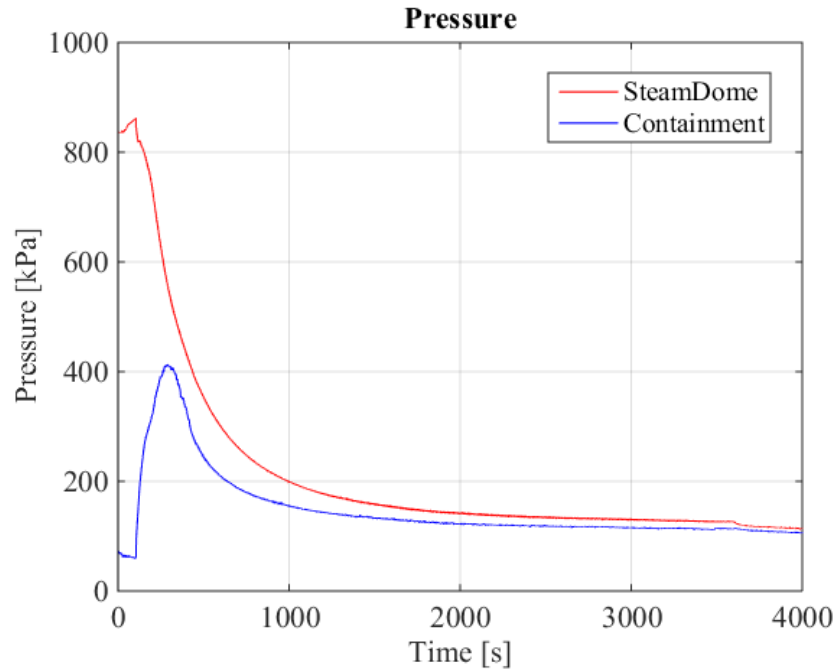
Figure 12-17 Pressure of Steam Dome and Containment
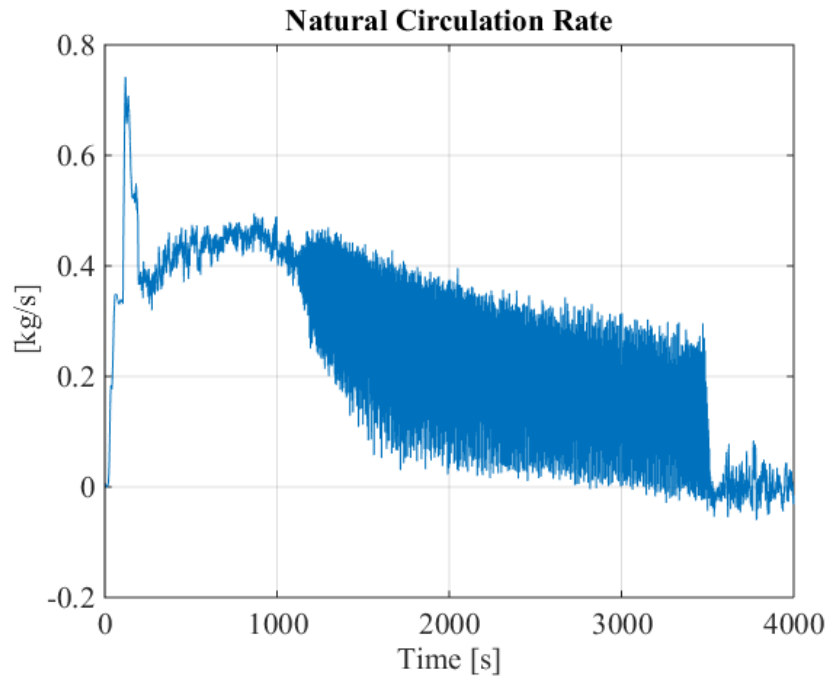
Figure 12-18 Natural Circulation Rate at the core during the Blow-down Test

However, oscillation of both core water level and flow rate is observed at 1100s after blowdown. This phenomena is also observed in previous blowdown test. The reason for this oscillation is explained in last chapter.
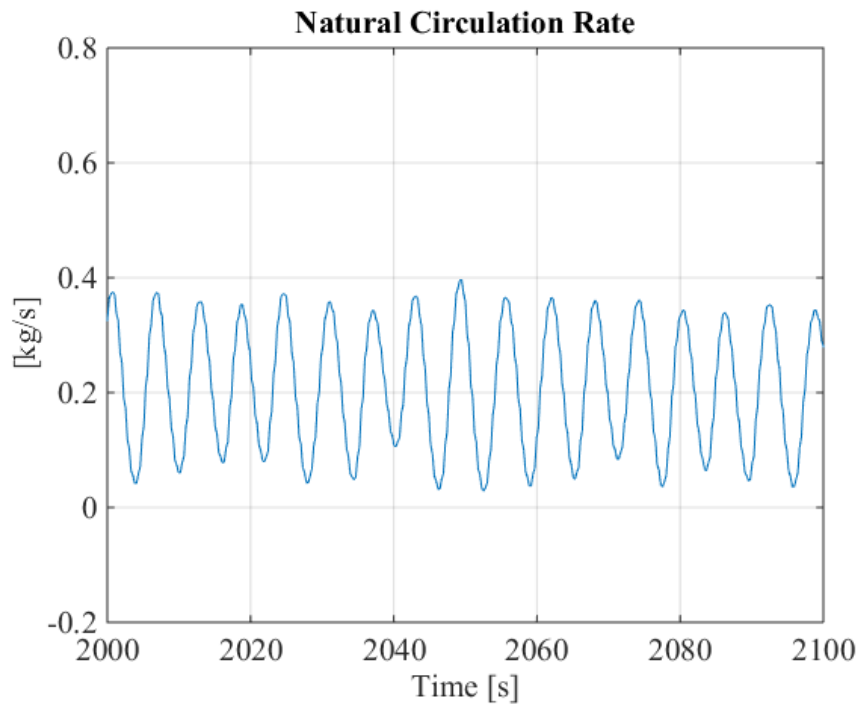
Figure 12-19 Detailed Natural Circulation Rate
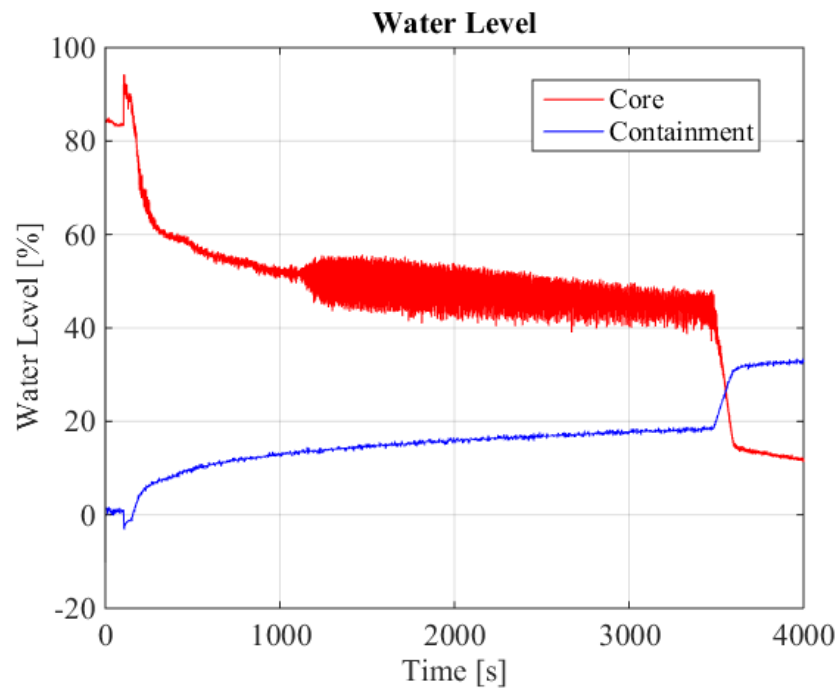
Figure 12-20 Water Level of Core and Containment

215
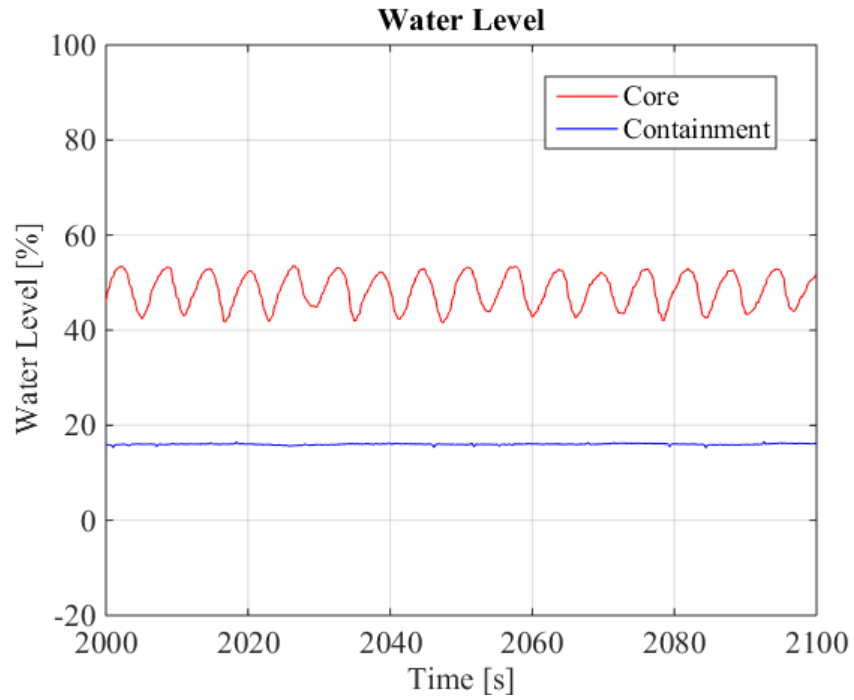
Figure 12-21 Detailed Water Level of Core and Containment
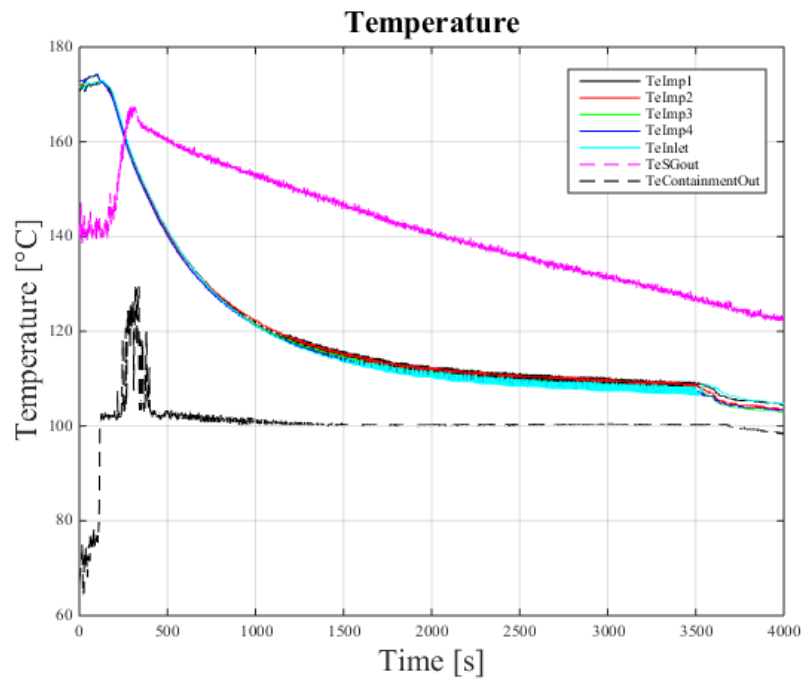
Figure 12-22 Temperature Measurement Results

The temperature measurement results is shown in figure 12-22, where the TeImp1 2 3 4 represents the temperature measured at port 1 2 3 4, respectively. TeSGout means the temperature measured at the outlet of the secondary loop of steam generator, and TeContainmentOut means the temperature measured at the outlet of the secondary loop of containment. Once the ADS valve is opened, the containment secondary loop temperature increases to above 100 ℃. And the secondary loop of containment is open to atmosphere, so the heat transfer change from single phase convection to two phase convection. Meanwhile, the main loop temperature decreased quickly because flashing took off a lot of heat from the main loop. Besides, the loss of water weaken the heat transfer of steam generator, so the steam generator becomes a heat source and its temperature is higher than main loop temperature.

The detailed plots of flow rate, pressure difference, temperatures, and steam dome pressure from 2000s to 2100s are shown in figure 12-23. When the water level is lower than the upper plenum, the flow rate reduces quickly and the boiling at the core is enhanced. Enhanced boiling generates more vaper and leads to the increasing of system pressure and the decline of gravity pressure drop, as well as the elevating of the water level. Once the elevated water level is higher than the upper plenum, the water can go through it and flows to the down comer part of RPV and forms natural circulation, which means the flow rate will increase. The increased flow rate weaken the boiling at the core and makes the water level decreases, which forms a self-sustained oscillation. This speculation can be verified by comparing the phase sequence of parameters shown in figure 12-23.
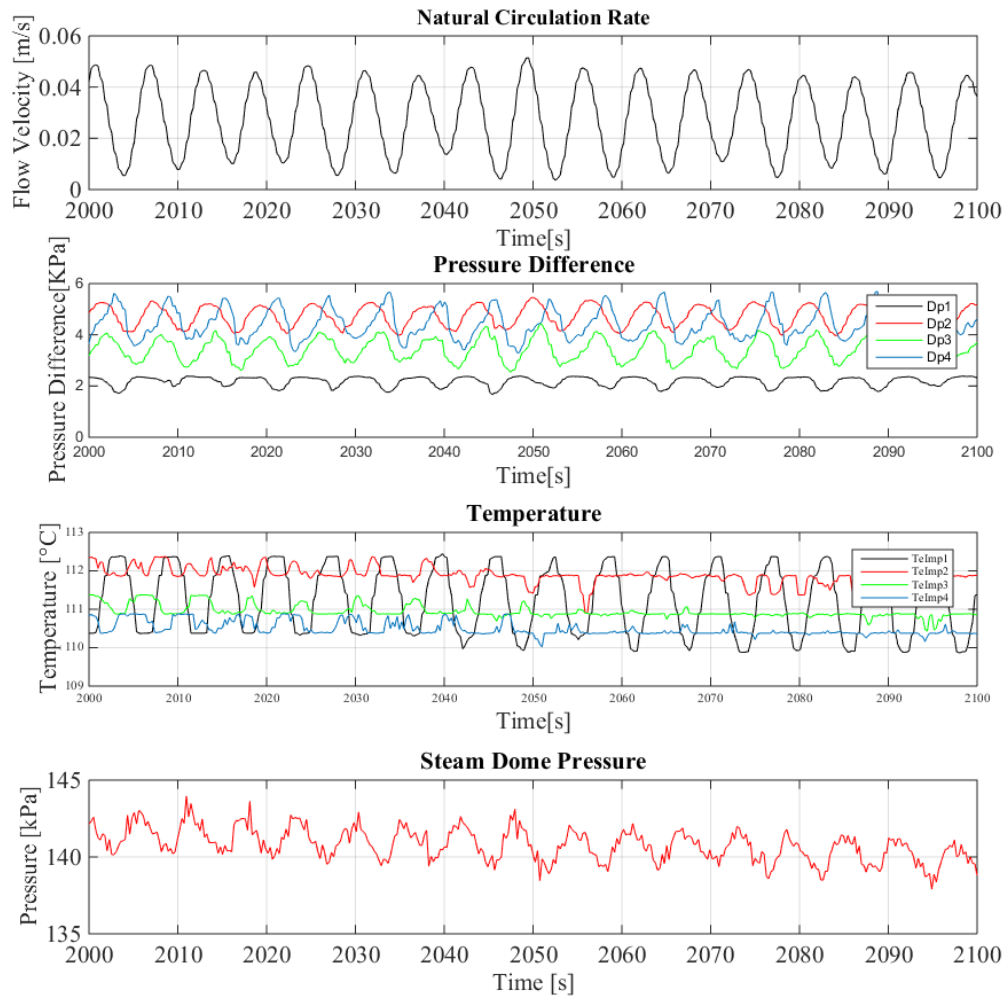
Figure 12-23 Detailed Figures of Pressure, Temperature, Flow rate between 2000s to 2100s

13. EVALUATION OF SAFETY ANALYSIS CODE

13.1 RELAP5 MODELING ON BLOWDOWN EVENT

In view of great importance of transient in blowdown event to the nuclear reactor safety, the RELAP5 code is used to predict the behavior of the transient during blowdown process. The results of system pressure prediction, core mass flow rate

prediction and water level prediction is shown in figure 13-1, 13-2, 13-3, respectively. The sequence of events can be found in table 13.1.

Table 13.1 Sequence of Events

Event	Time (s)
Steady state operation	0-1500
ADS valve open	1500
Reactor trip to decay power mode	1501
Isolate SG	1505
Bottom water supply valve open	4725

As shown by figure 13-1, the pressure of steam dome decreases very rapidly from the normal operation condition (7.5 MPa) when the automatic depressurization system (ADS) valve open, while the containment pressure increases. Such increase is due to the critical flow of coolant from reactor pressure vessel (RPV) to the containment as well as flashing caused by sudden depressurization. Eventually the system pressure becomes stable at about 0.1 MPa, which shows the capability of the reactor cooling and depressurization system.
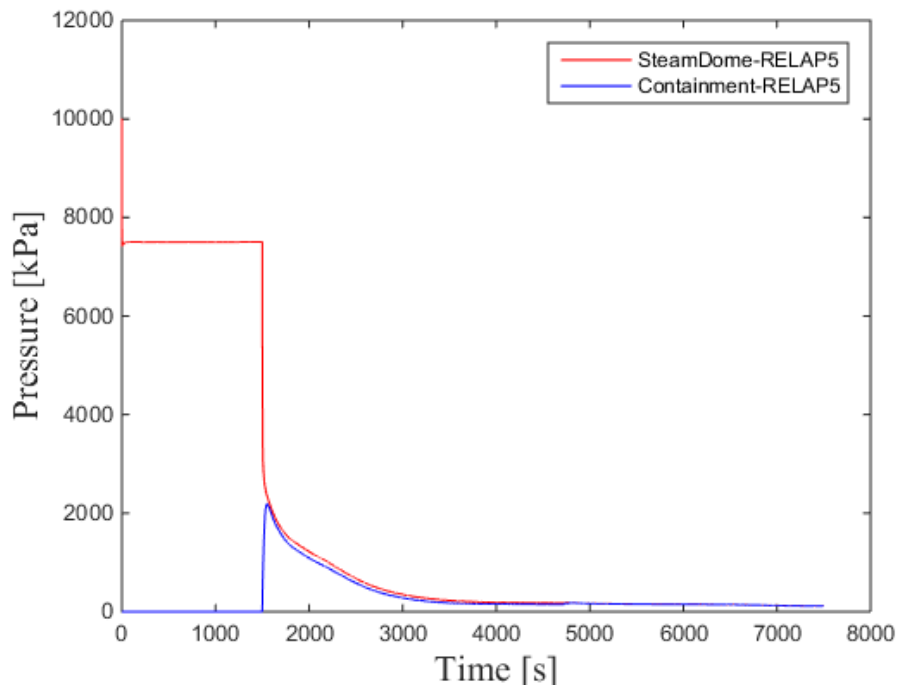
Figure 13-1 Pressure Prediction for Blowdown Event

219

The mass flow rate prediction is shown in figure 13-2. At the first 1500s the mass flow keeps normal operation condition, and when the ADS valve opens at 1500s, the flow rate decreases rapidly and oscillates between 0-1 kg/s. This is because the decreasing of RPV pressure leads to the flashing of coolant at both chimney and down comer part of RPV, which reduces the coolant density difference between chimney part and down comer part and affects natural circulation rate. However, due to the existence of core decay heat, the core part is boiling continuously. When the flashing phenomenon recedes and the coolant in downcomer part becomes subcooled, the density driven force increases and results in the augment of flow rate, which can be seen from figure 3-3 and the time around 1800s.
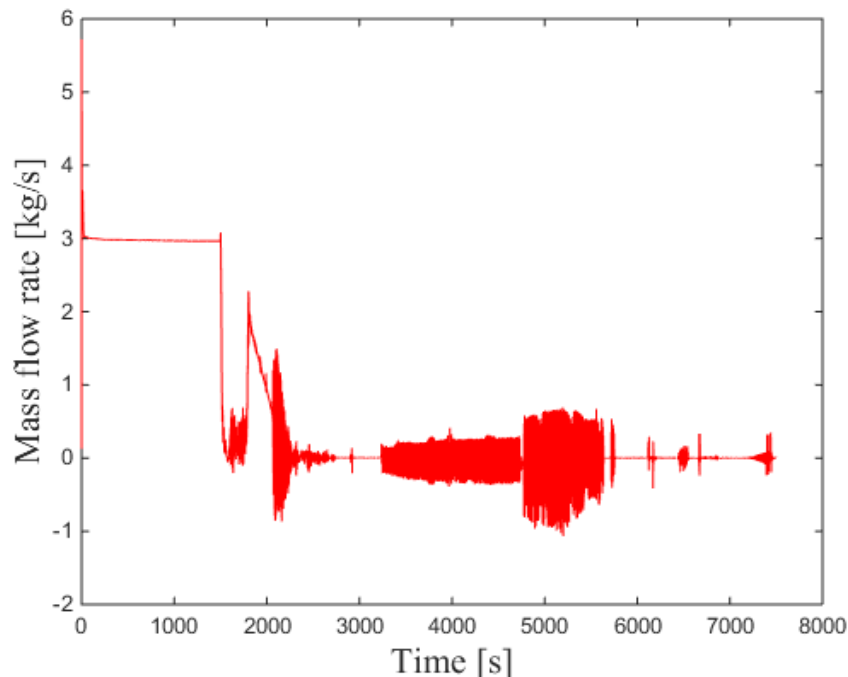
Figure 13-2 Flow Rate Prediction for Blowdown Event

Figure 13-3 presents the water level variation of both the core and containment. When the blowdown events begins, the core water level reduces due to the flashing and critical flow of coolant from the core to the containment. And the containment water level increases correspondingly. At 4725s, the bottom water supply valve opens to provide a natural circulation path from the lower containment through the core. The core water level decreases due to the higher

water level and pressure compare to the containment. Then both the core and containment water level keeps stable.
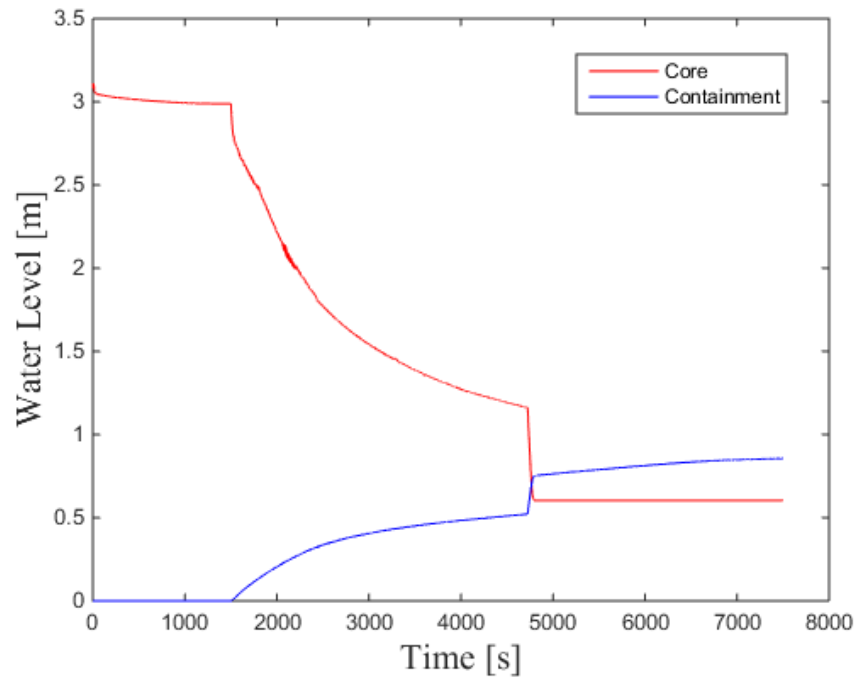
Figure 13-3 Water Level Prediction for Blowdown Event

13.2 EVALUATION OF CODE PERFORMANCE ON BLOWDOWN EVENT PREDICTION

It is desirable to compare the experiment result with the code prediction. Given that the initial conditions of previous experiments are set based on the code calculation and the capability of the test facility, the comparison is easy to realize. Figure 13-4 to 13-7 present comparison between measurement and code prediction of pressure, flow rate, temperature and water level, respectively. The time is set to zero when the test facility reaches desired initial conditions. The bottom water supply valve opens at 2177s at the new time scale.

By comparing the pressure transients of experiment result and code prediction, it can be found that the code prediction agrees well with the experiment result for both steam dome pressure and containment pressure. When the bottom water supply valve opens, the containment pressure increases suddenly and the pressure difference between steam dome and containment becomes very small. This is because the steam dome pressure is higher than containment due to the decay heat, and opening the bottom valve will lead to the coolant in the core flow

into the containment at first. It should be note that not only the containment pressure, the steam dome pressure also increases a little after the bottom valve open for both experiment and code prediction. For the experiment result, the increase of steam dome pressure can be explained by the flow rate change. Before the bottom water supply valve open, the natural circulation rate is sustained at a relatively high rate, even though the strong oscillation exists. When the valve open, the flow rate suddenly decrease to near zero, which can be seen from figure 13-5, leads to the decrease of convection heat transfer and increase of boiling heat transfer, which will generate more vaper and increase the system pressure. However, for the code prediction, the increasing of steam dome pressure more likely results from both the decrease of mass flow rate and the numerical instability. As we can see from figure 13-2 and 13-5, the mass flow rate is oscillating even before the water supply line open, and the average value is close to zero. After the opening of water supply line, the oscillating range becomes lager and the average value decrease to negative values. The oscillation of mass flow rate most likely comes the numerical instability due to no similar phenomena is observed during the experiment. Given that the of numerical instability of flow rate calculation exists before the bottom valve open, the prediction of transient could include the error of instability and may not be reliable.
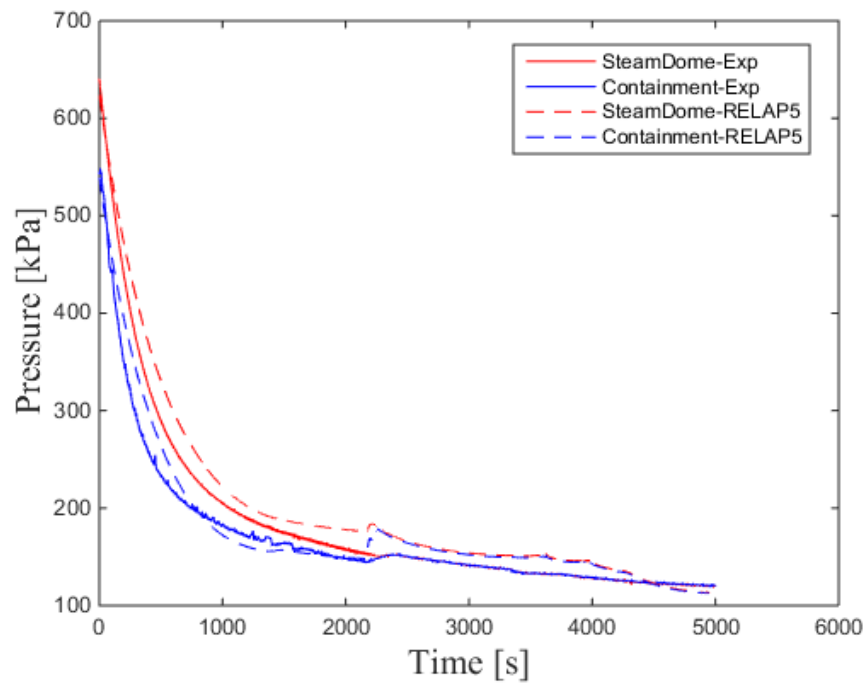
Figure 13-4 Comparison of System Pressure between Experiment and Code Prediction
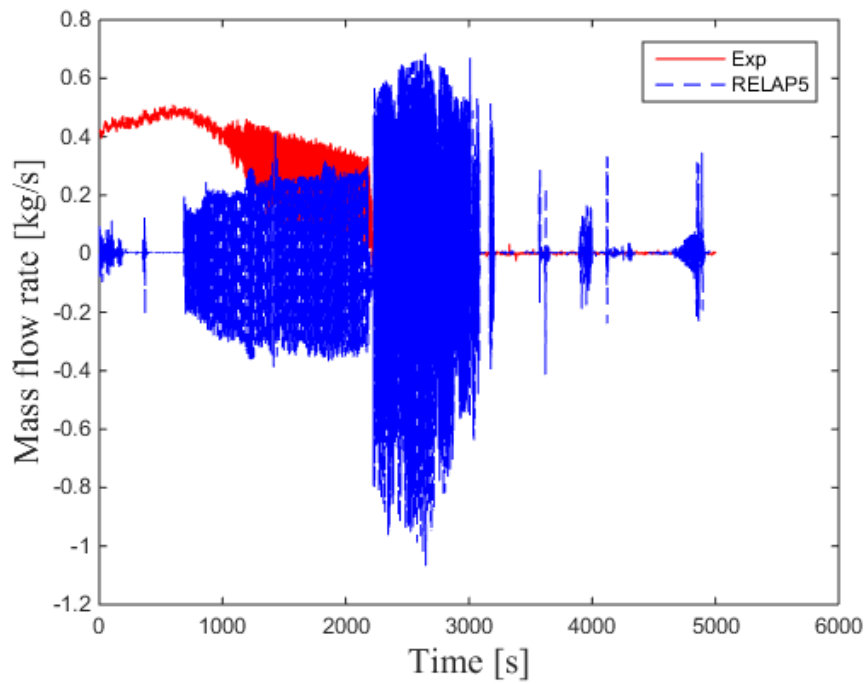
Figure 13-5 Comparison of flow rate between Experiment and Code Prediction

The temperature transient comparison between the measurement result at port 2 and the code prediction at the same location is shown in figure 13-6. Both the absolute value and the decreasing trends between the experiment result and the prediction agree well.

The measured collapse water level is compared with the water level calculated by code and the result is shown in figure 13-7. At 2177s the bottom water supply valve opens and coolant flow from the core to the containment at first, then keeps stable, both the experiment and code prediction show the trends like this, which is also reported by pervious research conducted by NuScale [51]. It is interesting to note that the measured core water level oscillates with a magnitude of about 0.3m during 1000s to 2000s, while the code predicted water level is stable. This oscillation can be explained by the instability mentioned previously. Therefore the code needs to be improved in predicting such kind of water level related flow instability. Besides, small deviation of the absolute value of initial water level exists between the experimental value and predicted value. This deviation results from experimental difficulties in setting the initial conditions (temperature, pressure, water level) exactly same as the code prediction.
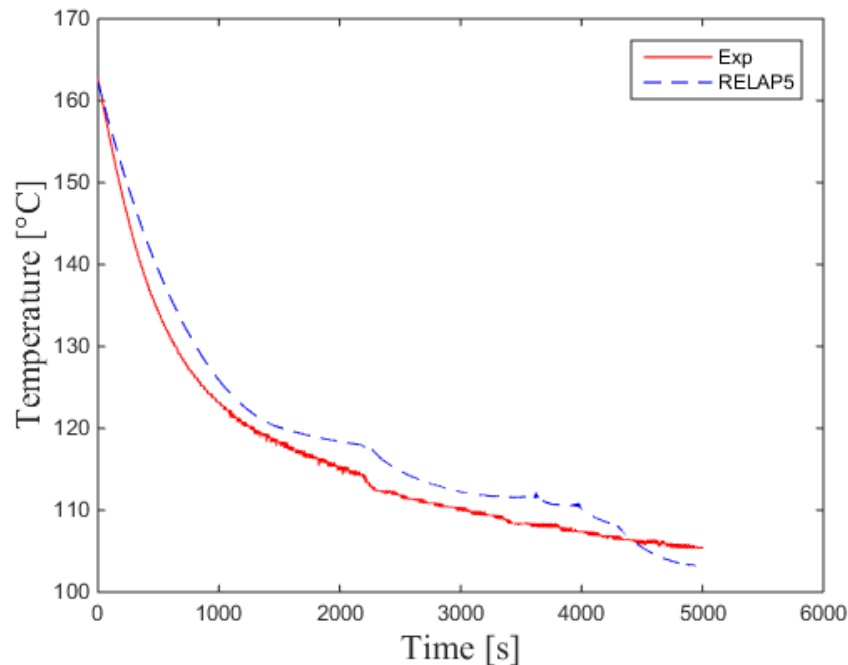
Figure 13-6 Comparison of Temperature
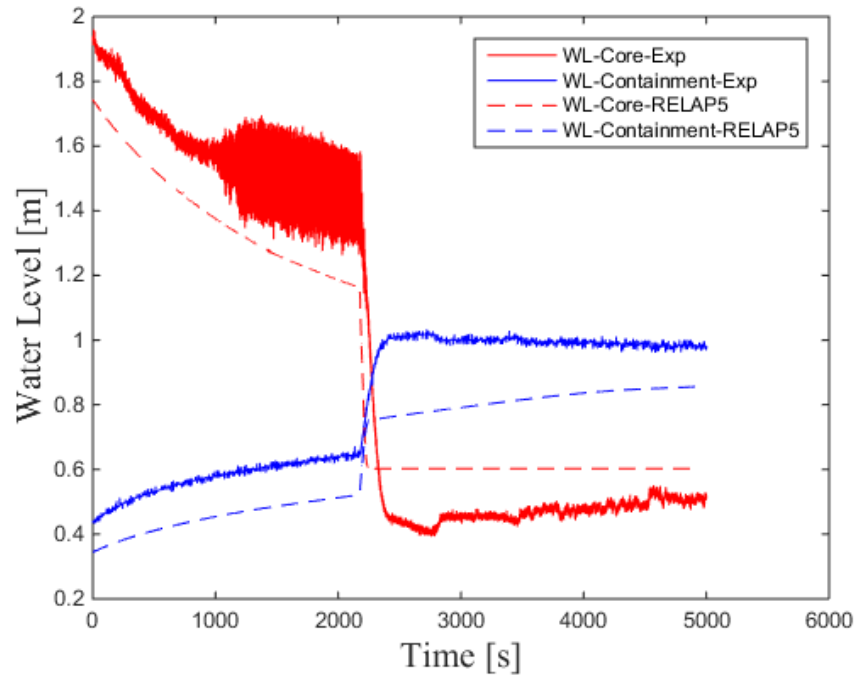
Figure 13-7 Comparison of Water Level

13.3 EVALUATION OF CODE PERFORMANCE ON COLD BLOWDOWN EVENT PREDICTION

The RELAP5 calculation results of cold blowdown events are compared with the experimental results and the comparison of system pressure, natural circulation rate, collapsed water level, temperature and void fraction are shown in figure 13-8 to 13-12, respectively.

From the pressure transients comparison, it can be found that the final stable value of both steam dome pressure and containment pressure are well predicted by the code, although discrepancy exists during the pressure decreasing process. This discrepancy indicates that the code prediction in the heat transfer or mass transfer from the core to containment may be different from experiment. The most possible reason could be error in prediction of boiling heat transfer. When the ADS valve opens, the temperature of secondary loop of containment, which is designed to simulate the pool outside the containment, increases rapidly and the water inside the secondary loop starts boiling. Given that two-phase heat transfer is complicated and small error in vapor generation could lead to large deviation of heat transfer amount, the discrepancy of pressure transient can be considered as acceptable.

225
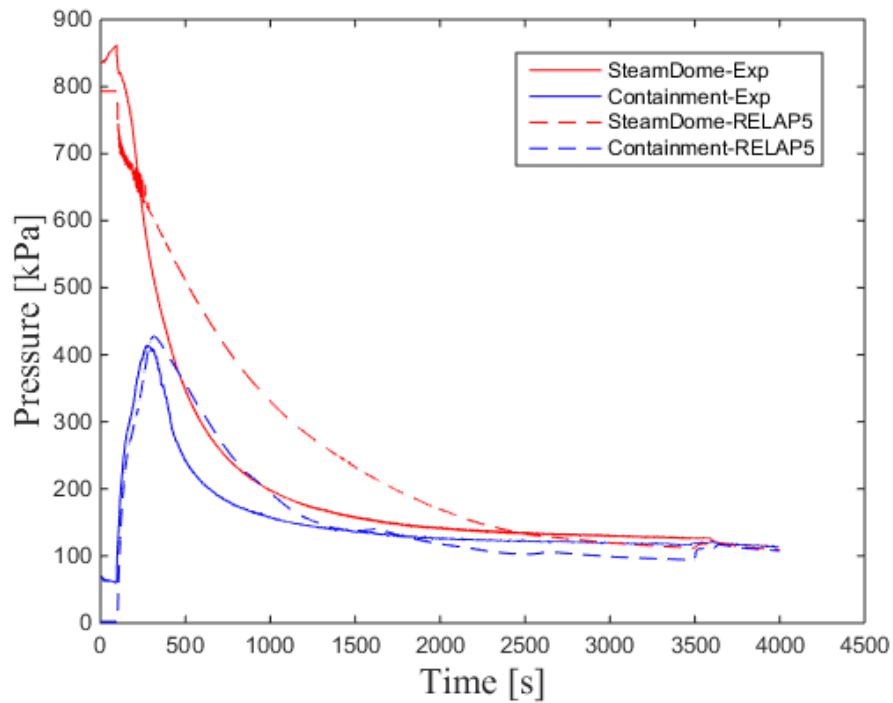
Figure 13-8 Comparison of System Pressure between Experiment and Code Prediction

The mass flow rate transient predicted by the code is different from the experiment result. According to the experiment, the natural circulation rate increases after the ADS valve opening and starts oscillating after 1100s, and reasons are explained in previous chapter. However the code indicates that the flow rate decreases to zero and oscillates around zero at around 1500s. This is because current code lack of capability in predicting such kind of two phase flow instability. Further investigation is necessary to fix this issue.
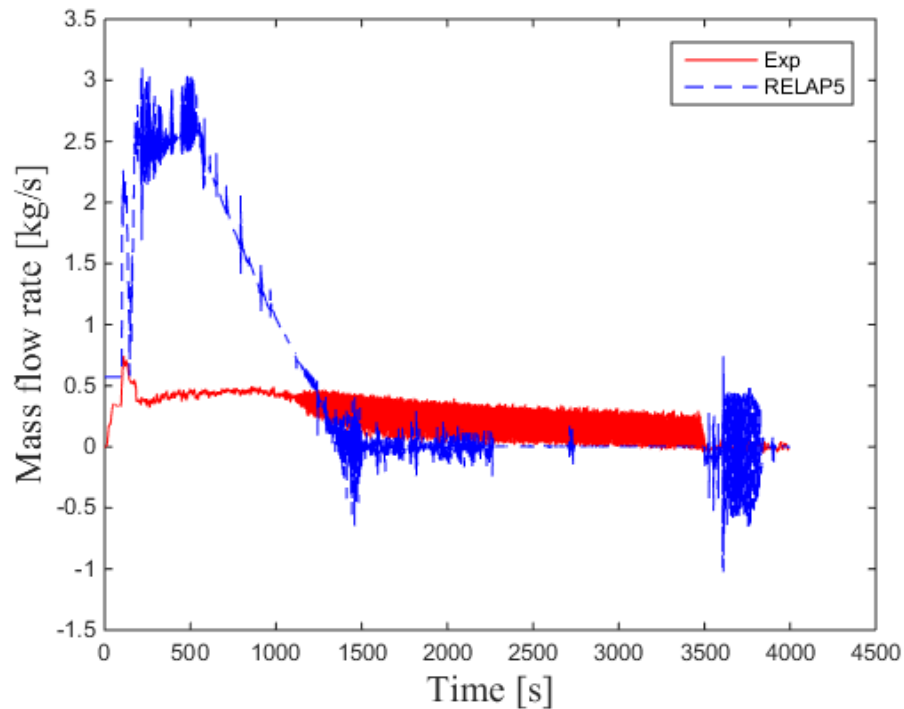
Figure 13-9 Comparison of Flow Rate between Experiment and Code Prediction

The measured collapse water level is compared with the water level calculated by code and the result is shown in figure 13-10. It is interesting to note that the measured core water level oscillates with a magnitude of about 0.3m during 1000s to 3500s, whereas the code predicted water level is stable. This oscillation is related to the flow rate and pressure drop, and proves that the code needs to be improved in predicting such kind of water level related flow instability.

The temperature transient comparison between the measurement result at port 2 and the code prediction at the same location is shown in figure 13-11. The trends are similar to the pressure comparison in figure 13-8.

The void fraction comparison between experiment and code prediction at port 2 is shown in figure 13-12. The trends of void fraction can be accurately predicted by the code and the absolute value agrees to the measurement at most time. However, the oscillation of void fraction in code prediction is more likely caused by the numerical instability because it is less regular in the frequency and amplitude than the oscillation of void fraction observed in the experiment.

227
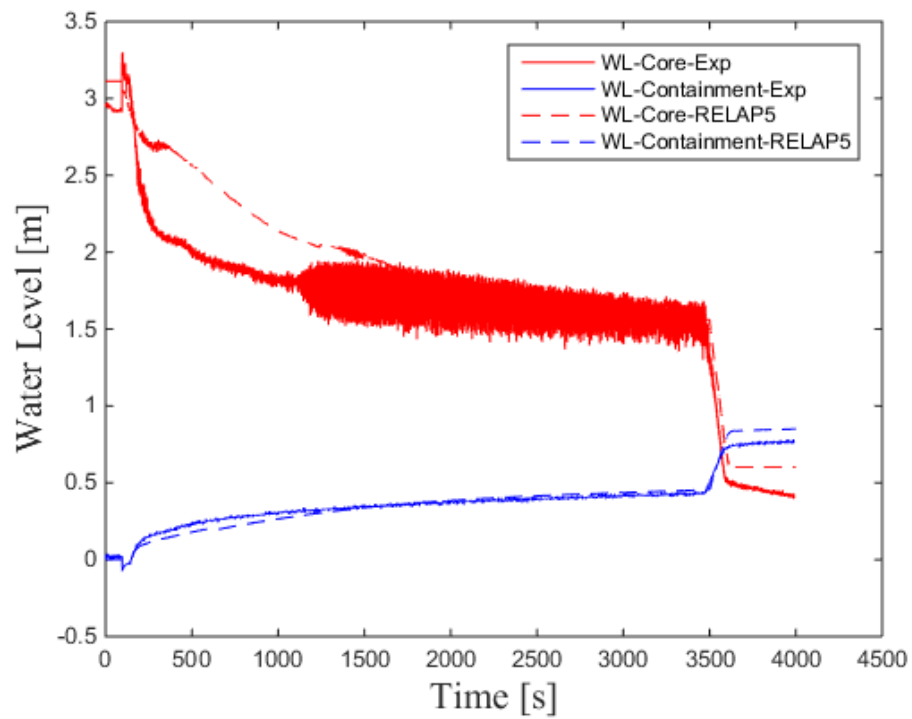
Figure 13-10 Code Prediction of Collapsed Water Level
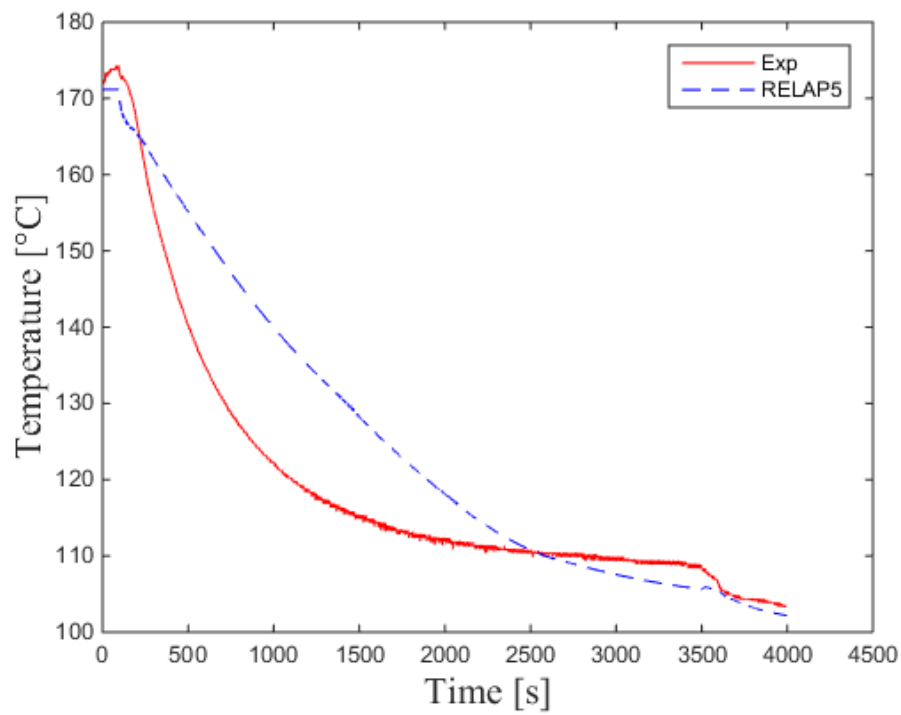
Figure 13-11 Code Prediction of Temperature at Port 2
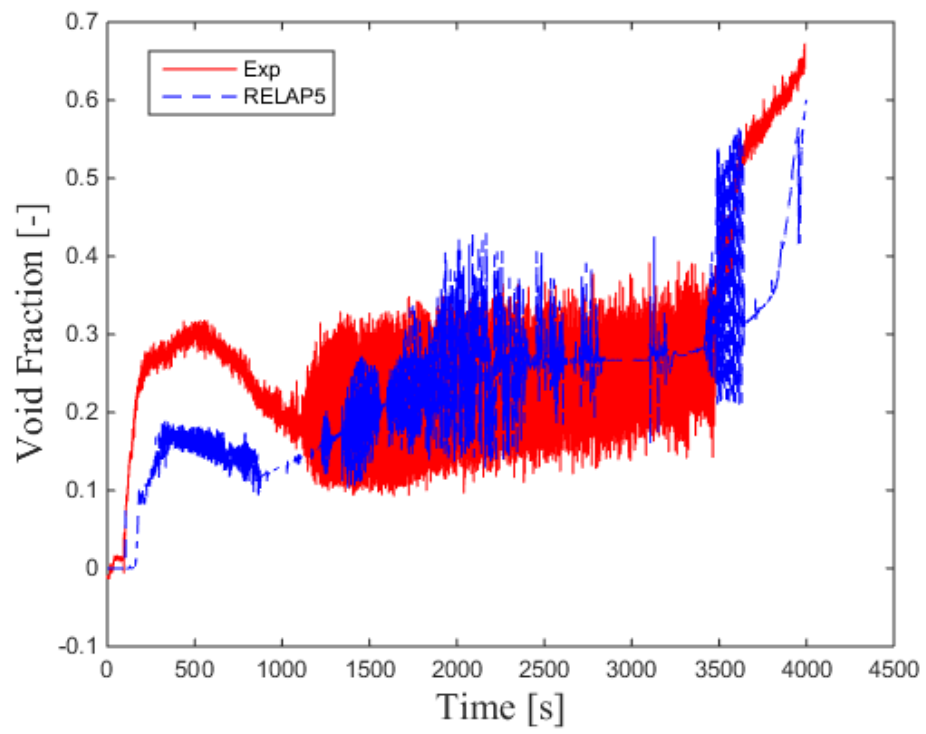
Figure 13-12 Code Prediction of Void Fraction at Port 2

14. CONCLUSIONS

In contrast to the forced circulation of conventional light water reactor, SMRs usually operate under natural circulation in both normal and accidental scenarios. This research sponsored by Depart of Energy (DOE) studies possible instabilities which could occur in SMRs at low temperature and pressure conditions. The NMR-50 is the prototypical reactors for the BWR-type natural circulation SMR.

Through a systematic three-step optimization approach, an optimum fuel assembly design was developed for the NMR-50. This fuel assembly design with an average fuel enrichment of 4.61 wt% yields a 10.2-year cycle length. Seven gadolinia fuel rods within an assembly were chosen with an average Gd enrichment of 6.17 wt%. The MCPR and MFLPD during the cycle are 1.99 and 18.25 kW/m, respectively, showing that the thermal design constraints are satisfied with large margins. The reactivity feedback coefficients were sufficiently negative, and a sufficient cold shutdown margin of 1.7 %ρ was provided. The possibility of xenon oscillation is always present, but the induced power oscillation is heavily damped because of a large negative VC, a small size core, and a low operating thermal neutron flux. This could provide NMR-50 with enhanced xenon stability characteristics. The reduced power density and increased leakage allow for a lower EOC fast neutron fluence on the structural materials as well as lower cycle burnup.

NMR-50 peak fast neutron fluence at the channel box is $8.8 \times 10^{21} \, \text{n/cm}^2$ and average and maximum cycle burnup is around 32 and 40 GWd/tU. Thus, from extensive plant data records, channel distortion is not a major concern from a radiation damage point of view.

The initial startup procedures for the natural circulation boiling water reactor are prone to the flashing instability at low pressure and low power conditions. Based on the previous research, the flashing instability can happen during the net vapor generation phase, which is also the transition from the single-phase flow to two-phase flow. Two startup procedures are proposed to avoid the startup instability.

1. Using very slow power ramp rate at the beginning of the initial startup procedure until the two-phase natural circulation is generated. The initial startup procedure might take one or two days before the full power is reached. In current report, a three phase power ramp rate, i.e., initially very small power ramp rate,

middle constant power, and later small power ramp rate, is presented to the very slow startup transient. Flashing oscillations can be stabilized by using very small power for long time heating during the startup. The flow oscillations caused by flashing disappear after the pressure reaches about 0.35 MPa. In real natural circulation BWR reactor, there are several power channels with different heat flux. So the amplitude of flow oscillations in the real reactor could be further reduced to an acceptable range.

2. Pressurized startup procedures can be adopted for the initial startup procedure to avoid the flashing instability. The pressurized startup procedures include the initial pressurization with the non-condensable gas to 0.3 MPa. When the system pressure reaches 0.5 MPa, a venting process is needed to eject the non-condensable gas. This venting process causes the evaporation in the reactor and generates the two-phase natural circulation. The pressurized startup procedures are investigated for the initial startup procedure under three different power ramp rates. The results show that the initial pressurization can not only eliminating the flashing instability in the single-phase region, but also suppress the flashing in the net vapor generation phase. So the pressurized startup procedure is a practical choice if flow instabilities occur during the startup for NCBWR.

Experimental stability maps are obtained by performing quasi-steady tests at different flow conditions. The experimental flashing instability boundary at lower pressure is above the zero quality line at the core exit and is close to the zero quality line at the chimney exit. In other words, the flashing phenomenon mainly occurs in the upper section of the adiabatic chimney, while the coolant in the core section could be subcooled. The flashing boundary moves to the zero quality line at the core exit when the system pressure increases. Therefore, increasing system pressure can effectively suppress the flashing instability and stabilize the system.

By increasing inlet flow resistance the density wave oscillations in normal boiling water reactor can be largely stabilized according to previous research. This method is proved to be also effective in the natural circulation system. However, the natural circulation rate is reduced due to increased inlet flow resistance, which would diminish the positive effects of this method to some extent.

The void reactivity feedback on the flow instability boundary is not very significant for the NMR-50. The reason is the void fraction in the core section is still small when flashing occurs in the chimney. Therefore, the power oscillations

caused by flashing instability or density wave oscillations are not large enough to alter the flow regime during the period of thermal hydraulic oscillation.

A theoretical stability boundary is obtained by performing linear stability analysis in the frequency domain. The flashing effect due to reduced hydrostatic head in the adiabatic chimney is considered as axially uniform heat source based on Clausius-Clapeyron relation. The improved model is able to predict the flashing boundary and density wave oscillation boundary. Parametric study shows that the flashing instability can be stabilized by increasing system pressure and core inlet flow resistance coefficient. And the density wave oscillation boundary moves to the right region in the dimensionless stability plane by increasing core inlet flow resistance coefficient. However, the density wave oscillation boundary is not very sensitive to the system pressure. Currently, the void reactivity feedback is not considered in the frequency domain analysis. By comparing with quasi-steady state tests, the theoretical flashing boundary shows some discrepancy with the experimental data. One possible reason is that the non-boiling length could be overestimated under thermal equilibrium conditions. However, the accuracy of flashing boundary can be improved by taking account of the thermal non-equilibrium into the frequency domain analysis in the future.

Besides, the PWR-type SMR instability study is also in progress. NuScale reactor design concept is explained briefly. Difficulties occurred when collecting the design parameter and accident scenario Because of NuScale design's proprietary rights. Therefore, being the NuScale reactor's design prototype, MASLWR's design parameters are utilized wherever NuScale parameters are unavailable. RELAP5 simulation of NuScale reactor's normal operation condition and blowdown event has been performed to ensure the accuracy of existing knowledge of NuScale design.

The three-level scaling method is then applied to design the Ideally Scaled Facility (ISF) for the PWR-type SMR. RELAP5 steady state and transient simulation have been performed for ISF and the results match well with that for the NuScale design. Based on the ISF, the Engineering Scaled Facility (ESF) is designed by considering all engineering considerations. The steam generator is designed differently from prototype regarding that current experiment only perform in low pressure and low power conditions, in which the secondary loop has been isolated and the heat capacity of water remains inside steam generator is more important. The RPV is separated from the containment and the containment

is insulated instead of merging thoroughly into a water pool. An additional heat exchanger is designed to function as the ultimate heat sink. Similar RELAP5 code analyses have been performed on the ESF. Both steady state and accident blowdown performance of ESF code prediction shows great agreement with the ISF, which means the current ESF design should be capable of simulating the flow instability behavior of NuScale reactor during the accident conditions.

PWR-type SMR experiments are performed in a well-scaled test facility to investigate the potential thermal hydraulic flow instability during the blowdown events, which might occur during the loss of coolant accident (LOCA) and loss of heat sink accident (LOHS) of the prototype PWR-type SMR. Two kinds of experiments, normal blowdown event and cold blowdown event, are experimental simulated and compared with code prediction. The normal blowdown event was experimentally simulated since an initial condition where the pressure is lower that the designed pressure of the experimental facility, while the code prediction of blowdown starts from the normal operation condition. For cold blow down event, different from setting both reactor pressure vessel (RPV) and containment at high temperature and pressure, only RPV is heated close to the highest designed pressure and then open the ADS valve, same process is predicted using code. By doing cold blowdown experiment, the entire transients from the opening of ADS can be investigated by code and benchmarked with experimental data. Important thermal hydraulic parameters including reactor pressure vessel (RPV) pressure, containment pressure, local void fraction and temperature, pressure drop and natural circulation flow rate are measured and analyzed during the blow-down event. The oscillations of natural circulation flow rate, water level and pressure drop are observed during the blow-down transients. Specific reasons and mechanisms of the observed instability phenomena are discussed. The safety analysis code RELAP5 is used to predict the blowdown transient and the results are compared with experimental data. The comparison reveals that the RELAP5 code can successfully predict the pressure and temperature transient during the blown down event with limited error, but numerical instability exists in predicting natural circulation flow rate. Besides, the code is lack of capability in predicting the water level related flow instability, which is observed in experiments.

15. PROJECT PUBLICATION

Journal Publications

- S. Shi, M. Ishii, "Modeling of Flashing-induced Flow Instabilities for a Natural Circulation Driven Novel Modular Reactor", Annals of Nuclear Energy, vol. 101, pp. 215-225, Mar. 2017
- Odeh, Faisal Y., and Won Sik Yang. "Core design optimization and analysis of the Purdue Novel Modular Reactor (NMR-50)," Annals of Nuclear Energy, vol. 94, pp. 288-299, Aug. 2016
- S. Shi, T. Hibiki, M. Ishii, "Startup Instability in Natural Circulation Driven Nuclear Reactors", Progress in Nuclear Energy, vol. 90, pp. 140-150, Mar. 2016
- Z. Wu, W.S. Yang, S. Shi, and M. Ishii, "A Core Design Study for a Small Modular Boiling Water Reactor with Long-Life Core", Nuclear Technology, vol. 193, Mar. 2016
- M. Ishii, S. Shi, W. S. Yang, Z. Wu, S. Rassame, Y. Liu, "Novel Modular Natural Circulation BWR Design and Safety Evaluation," Annals of Nuclear Energy, vol. 85, pp. 220-227, Nov. 2015
- S. Shi, J.P. Schlegel, C.S. Brooks, Y.-C. Lin, J.H. Eoh, Z. Liu, Q. Zhu, Y. Liu, T. Hibiki, M. Ishii, "Experimental Investigation of Natural Circulation Instability in a BWR-type Small Modular Reactor," Progress in Nuclear Energy, vol. 85, pp. 96-107, Nov. 2015
- S. Shi, Z. Wu, Z. Liu, J.P. Schlegel, C.S. Brooks, J.H. Eoh, Y. Yan, Y. Liu, W. S. Yang, M. Ishii, "Experimental Investigation of Natural Circulation Instability with Void Reactivity Feedback During Startup Transients for a BWR-type SMR," Progress in Nuclear Energy, vol. 83, pp. 73-81, Aug. 2015

Journal Publication in Preparation

We currently working on 2 manuscript drafts for journals such as: Annals of Nuclear Energy, Nuclear Engineering and Design, etc.

Conference Proceedings

- Yan, Yikuan, Shanbin Shi, and Mamoru Ishii. "Scaling Analysis and Facility Design for Stability Investigation during Accidents in a PWR-Type SMR." 2016 24th International Conference on Nuclear Engineering. American Society of Mechanical Engineers, 2016
- Shi, S., et al. "Experimental stability maps for a BWR-type small modular reactor." the 16th International Topical Meeting on Nuclear Reactor Thermal Hydraulics (NURETH-16), Chicago, IL. 2015
- Z. Wu, W. S. Yang, S. Shi, M. Ishii, "Core Design Studies for a BWR-Based Small Modular Reactor with Long-Life Core," in 2015 ANS Annual Meeting, San Antonio, TX, Jun. 2015
- Shi, Shanbin, et al. "Pressurized Startup Transient Analyses for the BWR-type NMR-50." ANS Winter Meeting and Nuclear Technology Expo, Anaheim, CA. 2014

REFERENCES

[1] S. Shi, F. Odeh, M. Ishii, W. S. Yang, Y. Yan, and Y. Lin, "Investigation of Natural Circulation Instability and Transients in Passively Safe Small Modular Reactors - 2014 Annual Report," PU-NE-14-08, Oct. 2014.

[2] M. Ledinegg, "Instability of flow during natural and forced circulation," *Warme*, vol. 61, no. 8, pp. 891–898, 1938.

[3] G. B. Wallis, *One-dimensional two-phase flow*, vol. 1. McGraw-Hill New York, 1969.

[4] M. Ishii, "Thermally induced flow instabilities in two-phase mixtures in thermal equilibrium," Dissertation, Georgia Institute of Technology, 1971.

[5] S. Kuran, "Modeling and simulation of coupled flow/power behavior in low pressure natural circulation systems," Purdue University, West Lafayette, IN, 2006.

[6] S.-Y. Lee and M. Ishii, *Simulation Experiments on Two-phase Natural Circulation in a Freon-113 Flow Visualization Loop*. The Commission, 1988.

[7] M. Ishii, T. Hibiki, W. S. Yang, J. Schlegel, S. Shi, S. Rassame, and Y. Lin, "Scientific design of Purdue University novel modular reactor (NMR-50)," PU/NE-12-27, 2012.

[8] K. Ekberg, B.-H. Forssén, D. Knott, J. Umbarger, and M. Edenius, "CASMO-4: A FUEL ASSEMBLY BURNUP PROGRAM," 1995.

[9] T. Downar, Y. Xu, V. Seker, and N. Hudson, "PARCS v3.0 – U.S. NRC Core Neutronics Simulator," University of Michigan, Ann Arbor, MI, 2010.

[10] U.S. NRC, "RELAP5/MOD3.3 Code Manual, vol. 1-8," U.S. NRC, 2006.

[11] E. R. Bradley and G. P. Sabol, *Zirconium in the Nuclear Industry: Eleventh International Symposium, Issue 1295*. ASTM International, 1996.

[12] Y. Xu and T. Downar, "GenPMAXS-V6 Code for Generating the PARCS Cross Section Interface File PMAXS," 2012.

[13] a. Worrall, *Core and fuel technologies in integral pressurized-water reactors (iPWRs)*. Woodhead Publishing Limited, 2015.

[14] J.-P. A. Renier and M. L. Grossbeck, "Development of improved burnable poisons for commercial nuclear power reactors," Oakridge, TN, 2001.

[15] P. J. Turinsky, "Core Isotopic Depletion and Fuel Management," in *Handbook of Nuclear Engineering*, New York: Springer, 2010, pp. 1241–1312.

[16] S. Kirkpatrick, C. D. Gelatt, and M. P. Vecchi, "Optimization by Simulated Annealing," *Science*, vol. 220, no. 4598, pp. 671–680, 1983.

[17] N. Metropolis, A. W. Rosenbluth, M. N. Rosenbluth, A. H. Teller, and E. Teller, "Equation of State Calculations by Fast Computing Machines," *J. Chem. Phys.*, vol. 21, no. 6, p. 1087, 1953.

[18] E. Aarts and J. Korst, *Simulated Annealing and Boltzmann Machines*. John Wiley & Sons, 1989.

[19] R. J. Cacciapouti, R. J. Weader, and J. P. Malone, "PWR burnable absorber evaluation," *Nucl. Energy*, vol. 34, no. 5, 1995.

[20] "ABWR Design Control Document," GE Nuclear Energy, 1997.

[21] L. S. Tong, *Principles of design improvement for light water reactors*. New York, NY (USA): Hemisphere Publishing, 1988.

[22] Y. Oka, *Nuclear Reactor Design*. TOkyo: Springer, 2010.

[23] Y. Oka and K. Suzuki, *Nuclear Reactor Kinetics and Plant Control*. 2013.

[24] F. Garzarolli, R. Adamson, A. Strasser, and P. Rudling, "BWR Fuel Channel Distortion," Molnlycke, Sweden, 2011.

[25] Karl O. Ott, *Introductory nuclear reactor dynamics*. La Grange Park, USA: American Nuclear Society, 1985.

[26] K. Woo, "Experimental and analytical study of stability characteristics of natural circulation boiling water reactors during startup transient," Purdue University, West Lafayette, IN, 2008.

[27] U. S. Rohatgi, H. S. Cheng, H. J. Khan, and K. W. Wulff, "Preliminary Phenomena Identification and Ranking Tables (PIRT) for SBWR start-up stability," Nuclear Regulatory Commission, Washington, DC (United States). Div. of Systems Technology; Brookhaven National Lab., Upton, NY (United States), 1997.

[28] M. Ishii, S. T. Ravankar, and R. Dowlati, "Scientific design of Purdue University Multi-Dimensional Integral Test Assembly (PUMA) for GE SBWR," Apr. 1996.

[29] A. Dixit, "Stability of two-phase natural circulation reactor during start-up procedures," Purdue University, West Lafayette, IN, 2010.

[30] M. Ishii and H. K. Fauske, "Boiling and Dryout Behavior in a Liquid-Metal Fast Breeder Reactor Subassembly Bundle Under Low Heat Flux and Low Flow Conditions," *Nucl Sci Eng U. S.*, vol. 84:2, Jun. 1983.

[31] M. Ishii, T. Hibiki, W. S. Yang, J. Schlegel, Z. Wu, S. Shi, Y. Lin, C. S. Brooks, C. Clark, Y. Yan, Q. Zhu, and C. Macke, "Investigation of Natural Circulation Instability and Transients in Passively Safe Small Modular Reactors - Scaling Analysis of NMR-50 for Scaled BWR Experimental Facility," PU/NE-13-03, Apr. 2013.

[32] E. P. Serov, "The operation of once-through boilers in variable regimes," *Tr. Mosk Energ Inst*, vol. 11, 1953.

[33] E. P. Serov and L. PASHKOV, "Analytical Investigation of Boundary Conditions for Formation of Pulsation in Steaming Pipes During Forced Circulation," *High Temp.*, vol. 3, no. 4, p. 545, 1965.

[34] E. P. Serov, "Transient processes in steam generators," *Teploenergetika*, vol. 13, no. 9, p. 50, 1966.

[35] J. A. Boure, "The oscillatory behavior of heated channels–An analysis of density effects," *CEAR3049 Cent. Etude Nucleaires Grenoble Fr.*, 1966.

[36] N. Zuber, "Flow excursions and oscillations in boiling, two-phase flow systems with heat addition," in *Symposium on Two-phase Flow Dynamics, Eindhoven EUR4288e*, 1967, pp. 1071–1089.

[37] P. (Pradip) Saha, "Thermally induced two-phase flow instabilities, including the effect of thermal non-equilibrium between the phases," Dissertation, 1974.

[38] I. M. M. Babelli, "Flow instabilities under low-pressure and low flow conditions with application to the simplified boiling water reactor," Ph.D., Purdue University, United States -- Indiana, 1996.

[39] G. Yadigaroglu and A. E. Bergles, "An experimental and theoretical study of density-wave oscillations in two-phase flow.," DTIC Document, 1969.

[40] R. T. J. Lahey and G. Yadigaroglu, "Lagrangian analysis of two-phase hydrodynamic and nuclear-coupled density-wave oscillations," 1974.

[41] F. Inada, M. Furuya, A. Yasuo, H. Tabata, Y. Yoshioka, and H. T. Kim, "Thermo-hydraulic instability of natural circulation BWRs at low pressure star-up. Experimental estimation of instability region with test facility considering scaling law," in *Proceedings of the 3rd JSME/ASME joint international conference on nuclear engineering*, 1995, vol. 1, pp. 173–178.

[42] F. Inada, M. Furuya, and A. Yasuo, "Thermo-hydraulic instability of boiling natural circulation loop induced by flashing (analytical consideration)," *Nucl. Eng. Des.*, vol. 200, no. 1–2, pp. 187–199, Aug. 2000.

[43] M. Furuya, F. Inada, and A. Yasuo, "Density wave oscillations of a boiling natural circulation loop induced by flashing," in *The 7th International Topical Meeting on Reactor Thermal Hydraulics*, 1995, pp. 923–932.

[44] R. Hu and M. S. Kazimi, "Flashing-Induced Instability Analysis and the Start-Up of Natural Circulation Boiling Water Reactors," *Nucl. Technol.*, vol. 176, no. 1, pp. 57–71, Oct. 2011.

[45] M. Furuya, F. Inada, and T. H. J. J. Van der Hagen, "Development of SIRIUS-N facility with simulated void-reactivity feedback to investigate regional and core-wide stability of natural circulation BWRs," *Nucl. Eng. Des.*, vol. 235, no. 15, pp. 1635–1649, Jul. 2005.

[46] S. M. Modro, J. Fisher, K. Weaver, P. Babka, J. Reyes, J. Groome, and G. Wilson, "Generation-IV Multi-Application Small Light Water Reactor (MASLWR)," pp. 837–843, Jan. 2002.

[47] I. Kataoka and M. Ishii, "Drift flux model for large diameter pipe and new correlation for pool void fraction," *Int. J. Heat Mass Transf.*, vol. 30, no. 9, 1987.

[48] M. Ishii and I. Kataoka, "Scaling laws for thermal-hydraulic system under single phase and two-phase natural circulation," *Nucl. Eng. Des.*, vol. 81, no. 3, pp. 411–425, Sep. 1984.

[49] S. M. Modro, J. E. Fisher, K. D. Weaver, J. N. Reyes, J. T. Groome, P. Babka, and T. M. Carlson, "Multi-application small light water reactor final report," *DOE Nucl. Energy Res. Initiat. Final Rep. Ida. Natl. Eng. Environ. Lab.*, 2003.

[50] Neil E. Todreas and Mujid S. Kazimi, Nuclear Systems I, Thermal Hydraulic Fundamentals, Hemisphere Publishing Corporation, 1990.

[51] B. Wolf, M. Kizerian, S. Lucas, "Analysis of Blowdown Event in Small Modular Natural Circulation Integral Test Facility," Trans Am Nucl Soc, 109, 1754-1757, Nov. 2013.

[52] Ishii, M., & Jones Jr, O. C. (1976). Derivation and application of scaling criteria for two-phase flows. In *Two-phase flows and heat transfer, vol. 1,* 163–185.

[53] Kocamustafaogullari, G., & Ishii, M. (1987). Scaling of two-phase flow transients using reduced pressure system and simulant fluid. *Nuclear Engineering and Design*, *104*(2), 121–132.

[54] M. Ishii, S. Shi, W. S. Yang, Z. Wu, S. Rassame, Y. Liu, "Novel Modular Natural Circulation BWR Design and Safety Evaluation," Annals of Nuclear Energy, vol. 85, pp. 220-227, Nov. 2015.